

SELF-CONSISTENT FIELD THEORIES FOR THE SURFACE  
AND BULK THERMODYNAMICS OF BLENDS OF  
NONLINEAR AND LINEAR POLYMERS

by  
Renfeng Hu

© Copyright by Renfeng Hu, 2013

All Rights Reserved

A thesis submitted to the Faculty and the Board of Trustees of the Colorado School of Mines in partial fulfillment of the requirements for the degree of Doctor of Philosophy (Chemical Engineering).

Golden, Colorado

Date \_\_\_\_\_

Signed: \_\_\_\_\_

Renfeng Hu

Signed: \_\_\_\_\_

Dr. David T. Wu  
Thesis Advisor

Golden, Colorado

Date \_\_\_\_\_

Signed: \_\_\_\_\_

Dr. David W. M. Marr  
Professor and Head  
Department of Chemical and Biological Engineering

## ABSTRACT

Theoretical understanding of the surface and bulk thermodynamic properties of nonlinear macromolecules is desirable with rapid advances in the synthesis and application of polymers with complex architectures. This thesis focuses on the study of the surface and bulk in polymeric systems containing nonlinear species as two individual topics. Polymers with nonlinear architectures, such as branched or cyclic polymers, can segregate to both surfaces and interfaces when blended with linear polymer. A self-consistent field theory (SCFT) was developed to understand the segregation of blends of a linear polymer with various nonlinear polymer molecules, and was carried out in close collaboration with experiments on a series of nonlinear molecules with exquisitely controlled architectures. The theory predicts how the composition density profiles vary with the architecture of the nonlinear species and the volume fraction of two components, as well as the total density. The dependence on composition of the total surface excess of nonlinear species is compared with both linear response theory and experimentally determined surface excesses of star, branched, comb and ring polymers. The comparison between experiments and theories indicates that SCFT can capture the effects of the branch points, the lengths of side branches and the topologies on the surface enrichment in those blends containing nonlinear and linear polymers. As the second topic, the bulk conformations of nonlinear polymers are studied using a novel two-chain SCFT developed in this thesis. The two-chain theory is designed to capture the intra- and intermolecular correlations in melts and solutions of linear and branched polymers that are not present in conventional SCFT. The intra- and intermolecular density correlations are calculated using SCFT by breaking translational symmetry and holding a given monomer fixed. The two-chain theory is shown to be capable of describing the crossover from self-avoiding walk at short distances, to screened random walk at long distance in a semi-dilute solution or melt of linear and branched molecules, and to predict dependence on the excluded

volume parameter. End-branched polymers varying in branch functionality and length are studied by SCFT, and indicate that the branching architectures enhance the swelling of polymers in melts, and show stretching effects at short distances from the core. The mean field Helmholtz free energy can be evaluated in both canonical and grand-canonical ensemble within the two-chain theory. The effective Flory interaction parameter in the two-chain SCFT is obtained from an approximate evaluation of the mixing free energy, which is dependent on excluded volume. The calculations show qualitative agreement with the Gaussian field theory by Fredrickson and co-workers and with neutron scattering experiments.

In summary, my original contributions to the knowledge in this field are:

- 1) SCFT studies of surface segregation in blends of new branched and linear polymers.
- 2) SCFT studies of surface segregation in blends of linear and cyclic polymers, and tests of linear response theory predictions.
- 3) Numerical algorithms to handle a variety of complex architectures for SCFT.
- 4) Development of a novel two-chain SCFT for various branched polymers to capture bulk intra- and intermolecular correlations, with application to stars, end-branched and pom-pom molecules.
- 5) Evaluation of the mixing free energy for homogeneous polymer blends containing complex branched architectures by two-chain SCFT.

Most importantly, close collaboration with experimentalists has proven that SCFT can give good agreement with experiments on both surface and bulk thermodynamics. Therefore, the theory provides an efficient and useful tool in directing future experiments and hopefully the commercialization of nonlinear polymers.

## TABLE OF CONTENTS

ABSTRACT . . . . .	iii
LIST OF FIGURES . . . . .	ix
LIST OF TABLES . . . . .	xviii
ACKNOWLEDGMENTS . . . . .	xix
CHAPTER 1 INTRODUCTION . . . . .	1
CHAPTER 2 BACKGROUND . . . . .	9
2.1 Surface segregation of nonlinear and linear polymer blends . . . . .	9
2.1.1 Experiments on the surface segregation of polymer blends . . . . .	9
2.1.2 Theory and simulation of surface segregation in polymer blends . . . . .	18
2.2 Bulk conformations and thermodynamics of polymer solutions, melt and blends . . . . .	24
2.2.1 Scaling analysis of self-avoiding walk in polymer solutions . . . . .	24
2.2.2 Experiments on bulk conformations and thermodynamics of polymers . . . . .	26
2.2.3 Theories of bulk conformations and thermodynamics of nonlinear polymer melts and mixtures . . . . .	32
CHAPTER 3 SELF-CONSISTENT FIELD THEORY (SCFT) . . . . .	36
3.1 SCFT for nonlinear/linear polymer blends near surfaces . . . . .	38
3.1.1 The statistical weight functions of branched polymers: example of stars . . . . .	45
3.1.2 The statistical propagators of cyclic molecules . . . . .	45
3.1.3 The statistical weight functions of combs . . . . .	48

3.2	Linear response theory for branched and linear blends . . . . .	49
3.3	Surface SCF potential on specific functional groups in branched polymers attracted or repelled from a surface . . . . .	51
CHAPTER 4 SURFACE SEGREGATION OF LINEAR AND NONLINEAR POLYMER BLENDS . . . . .		53
4.1	Surface segregation of star/linear blends . . . . .	54
4.2	Surface segregation of blends of end-branched and linear polymers . . . . .	59
4.3	Surface segregation of 6-pom/linear blends: comparison between theory and experiments . . . . .	64
4.4	Surface segregation in cyclic and linear polymer blends . . . . .	65
4.4.1	Surface segregation in equal and differing molecular weight cyclic/linear blends . . . . .	67
4.4.2	Comparisons between SCFT calculations and NR experiments for isotopic blends of cyclic/linear polystyrene . . . . .	70
4.5	Surface segregation in blends of comb and linear polymers . . . . .	75
4.5.1	SCFT calculations for the surface segregation in comb/linear blends . . . . .	75
4.5.2	Surface segregation in blends of linear polymer and densely branched combs . . . . .	78
4.6	Surface segregation of branched/linear blends with surface potentials on ends and branch points . . . . .	81
4.7	Linear response theory on the surface segregation of branched and linear polymer blends . . . . .	83
4.7.1	Surface segregation of two families of branched polymers . . . . .	85
4.7.2	Surface segregation of densely branched combs . . . . .	91
4.8	Summary . . . . .	95
CHAPTER 5 THE INTRA- AND INTERMOLECULAR CORRELATIONS IN LINEAR AND BRANCHED POLYMER MELTS AND BLENDS . . . . .		98

5.1	Two-chain SCFT for polymer bulk properties in melts and blends . . . . .	100
5.1.1	Modified diffusion equation in a spherically symmetric coordinate system . . . . .	101
5.2	Dilute solutions of linear and branched polymers . . . . .	104
5.3	The end-end distance distribution of a branched molecule . . . . .	109
5.4	Branched chain conformations in semi-dilute solutions and melts . . . . .	111
5.4.1	Intermolecular and total density distribution functions . . . . .	111
5.4.2	The swelling of linear molecules in semi-dilute solutions and melts . . . . .	111
5.4.3	The scaling analysis . . . . .	114
5.4.4	The swelling of branched polymers in semi-dilute solutions and melts . . . . .	116
5.4.5	Stretching of molecules due to branching . . . . .	118
5.4.6	Structure factors of polymers in solutions and melts . . . . .	121
5.5	The intra- and intermolecular correlations in branched/linear polymer blends . . . . .	125
5.5.1	Swelling in homogeneous star and linear polymers blends . . . . .	126
5.5.2	The intermolecular correlation functions and static structure factors . . . . .	128
5.6	The free energy of binary blends by two-chain SCFT . . . . .	131
5.6.1	The mixing free energy of branched/linear blends in canonical ensemble . . . . .	132
5.6.2	The mixing free energy in semi-grand canonical ensemble . . . . .	136
5.6.3	Gaussian field theory on the approximation of Flory-Huggins parameter for comb/linear blends . . . . .	141
5.7	Summary . . . . .	143
CHAPTER 6 CONCLUSIONS AND FUTURE WORK . . . . .		146
REFERENCES CITED . . . . .		151

APPENDIX A - THE NUMERICAL ALGORITHMS IN SCFT . . . . .	165
A.1 Numerical method for modified diffusion equation . . . . .	165
A.1.1 The explicit and implicit method . . . . .	165
A.1.2 The Crank-Nicolson algorithm . . . . .	166
A.2 Discretization of the modified diffusion equation . . . . .	166
A.3 The boundary conditions . . . . .	167
A.4 The Picard method and Newton-Broyden algorithm . . . . .	168
APPENDIX B - GAUSSIAN STRUCTURE FACTORS OF BRANCHED AND COMB POLYMERS . . . . .	173
B.1 Structure factors of branched molecules . . . . .	173
B.2 Structure factors of comb molecules . . . . .	175
APPENDIX C - PARALLELIZATION OF SELF-CONSISTENT FIELD CALCULATIONS . . . . .	178
C.1 Parallel scheme for 1-D diffusion equation using explicit method . . . . .	178
C.2 The implementation of parallelized SCFT for cyclic molecules . . . . .	180

## LIST OF FIGURES

Figure 1.1	An illustration of the surface and interface segregation in a binary polymer blend film (left), and its corresponding composition profile (right). The filled areas show the interfacial excess above the hypothetical uniform bulk composition (dashed line) . . . . .	2
Figure 1.2	Schematic of a star molecule near an interface under the influence of the interfacial potentials predicted by linear response theory. The joint is entropically repelled and ends attracted by the interface. . . . .	3
Figure 1.3	Schematic of the general idea of solving for a many chain system by a self-consistent field. . . . .	4
Figure 2.1	Illustration of a neutron reflectivity experiment on a polymer film surface and interface. . . . .	10
Figure 2.2	Neutron reflectivity spectrum of a blend of 20vol% 6-pom hPS with linear dPS. The inset shows the composition profile of 6-pom versus film depth resulting from fitting the spectrum. . . . .	16
Figure 2.3	Scattered neutron beams from two particles of the sample. . . . .	26
Figure 3.1	(a) An illustration of a polymer melt near a wall. (b) The self-consistent field approximation for a system of many chains near a wall. The test molecule feels an external field (the filled area) by averaging the densities of all the other molecules. . . . .	37
Figure 3.2	An illustration of the calculation for the unnormalized density on the $t^{\text{th}}$ bead of a linear chain. . . . .	42
Figure 3.3	An illustration of calculating the unnormalized density at the joint of a 3-arm structure. . . . .	46
Figure 3.4	An illustration of calculating the statistical weight of a ring polymer in terms of the propagators $G(z', z; 0, t)$ from the $0^{\text{th}}$ site at $z'$ to the $t^{\text{th}}$ site at $z$ . . . .	47
Figure 3.5	An illustration of calculating $q$ and $q^\dagger$ for a comb structure. . . . .	48
Figure 4.1	Schematic illustration and names of star, multiple-end branched, pom-pom, cyclic and comb polymers studied. . . . .	54

Figure 4.2	Excess density profiles of star species for different compositions of star monomers in various 4-star/linear blends. The molecular weight of the star is $N_{\text{star}} = 100$ . (a) A binary blend containing shorter linear molecules $N_{\text{linear}} = 10$ . (b) A binary blend with equal molecular weights of linear and star. $N_{\text{linear}} = 100$ . (c) A binary blend with longer linear chains $N_{\text{linear}} = 1000$ . $\bar{v} = 0.1$ and $\bar{\rho}_b = 1$ . . . . .	55
Figure 4.3	Comparison of integrated surface excess of the 4-star/linear binary blends shown in Figure 4.2. the solid curve on plots of case $N_{\text{linear}} = 100$ represents the corresponding 2nd order polynomial fit. . . . .	57
Figure 4.4	The excess density of a series of 4-star/linear blends of symmetric molecular weight. $\phi_{\text{star}} = 0.2$ , $\bar{v} = 0.1$ and $\bar{\rho}_b = 1$ . . . . .	59
Figure 4.5	The integrated surface excess of star/linear blends versus number of star arms. Each arm has length $N_{\text{arm}} = 25$ . $N_{\text{linear}} = 1000$ , $\bar{\rho}_b = 1.0$ , $\phi_{\text{star}} = 0.2$ , $\bar{v} = 0.1$ . . . . .	60
Figure 4.6	The integrated surface excess of 4-star/linear blends for different star arm lengths. $N_{\text{linear}} = 1000$ , $\bar{\rho}_b = 1.0$ , $\phi_{\text{star}} = 0.2$ , $\bar{v} = 0.1$ . . . . .	61
Figure 4.7	The surface density profiles of the 9-end polymer in 9-end/linear blends by SCFT, broken down into the contributions of the inside arms and outside branches. $N_{9\text{end}} = N_{\text{linear}} = 1000$ , $N_{\text{arm}} = 183$ and $N_{\text{branch}} = 50$ . In these calculations, $\bar{\rho}_b = 1.0$ , $\bar{v} = 0.1$ , and $\phi_{9\text{end}} = 0.5$ . . . . .	61
Figure 4.8	Excess density profiles of end-branched polymers in $n$ -end/linear blends by SCFT. (a) Blends containing 9-end structures with $N_{9\text{end}} = N_{\text{linear}} = 1000$ . (b) Blends of $n$ -end polymers with increasing number of branches and fixed number and length of inside arms. The molecule contains 3 arms and each arm has $N_{\text{arm}} = 183$ . $N_{\text{branch}} = 50$ . In all calculations, $\bar{\rho}_b = 1.0$ , $\bar{v} = 0.1$ . . . .	63
Figure 4.9	The integrated surface excess of the $n$ -end polymers in blends with linear molecules. All $n$ -end species have three equal inside arms, $N_{\text{arm}} = 183$ . Two series of calculations are considered, one with fixed linear molecular weight $N_{\text{linear}} = 1000$ , and the other one with equal molecular weight, $N_{n\text{-end}} = N_{\text{linear}} = 1000$ . For all calculations, $\bar{\rho}_b = 1.0$ , $\bar{v} = 0.1$ , and $\phi_{n\text{-end}} = 0.2$ . . . . .	64
Figure 4.10	A comparison of integrated surface excess derived from neutron reflectometry measurements and SCFT calculations. $\phi_{\text{pom}} = 0.2$ and $N_{\text{linear}} = N_{\text{pom}} = 360$ ; for SCFT, $\bar{v} = 0.1$ , $\bar{\rho}_b = 1$ . . . . .	66

Figure 4.11	Surface density of cyclic molecules blended with linear polymer. $N_{\text{linear}} = 100$ , $N_{\text{cyclic}} = 5, 10, 20, 50$ , and $100$ . $\phi_{\text{cyclic}} = 0.01$ , $\bar{v} = 0.1$ and $\bar{\rho}_b = 1$ . . . . .	68
Figure 4.12	Surface density profiles of cyclic/linear blends with fixed $N_{\text{cyclic}} = 1000$ in low cyclic concentrations. (a) Density profiles of cyclic at $\phi_{\text{cyclic}} = 0.01$ . (b) Density profiles of linear molecules at $\phi_{\text{cyclic}} = 0.01$ . (c) The density profiles of cyclics with initial bulk $\phi_{\text{cyclic}} = 0.05$ and (d) The linear density profiles with initial bulk $\phi_{\text{cyclic}} = 0.05$ . All calculations use $\bar{v} = 0.1$ , $\bar{\rho}_b = 1$ and $\bar{z} = 100$ . . . . .	69
Figure 4.13	Surface excess density profile of cyclic molecules blended with linear molecules of equal and much shorter molecular weight. (a) $\phi_{\text{cyclic}} = 0.01$ , (b) $\phi_{\text{cyclic}} = 0.05$ . $N_{\text{cyclic}} = 1000$ . $\bar{v} = 0.1$ and $\bar{\rho}_b = 1$ . . . . .	71
Figure 4.14	The excess surface density of cyclic polymers in cyclic/linear blends for various compositions of cyclic monomers. $N_{\text{linear}} = N_{\text{cyclic}} = 100$ . $\bar{v} = 0.1$ , $\bar{\rho}_b = 1$ . . . . .	72
Figure 4.15	The effect of the excluded volume parameter on the cyclic excess density blended with linear chains, with $N_{\text{linear}} = N_{\text{cyclic}} = 100$ and $\phi_{\text{cyclic}} = 0.2$ , $\bar{\rho}_b = 1$ . . . . .	72
Figure 4.16	The integrated surface excess of cyclic molecules normalized by the bulk density plotted versus $\sqrt{N_{\text{cyclic}}}$ in blends with linear chains of fixed length. $N_{\text{linear}} = 100$ , $\bar{v} = 0.1$ and $1$ , $\phi_{\text{cyclic}} = 0.01$ and $0.05$ , respectively. . . . .	73
Figure 4.17	The depth profile for hydrogenous macrocyclic CPS37k blended with deuterated linear PS37k in 20/80 wt%. $\phi_H$ corresponds to the volume fraction of the CPS37k, with molecular weight $\approx 37\text{kg/mol}$ . The surface is at $z \approx 0$ and the interface is at $z \approx 800\text{\AA}$ . . . . .	74
Figure 4.18	Excess density profiles of combs in comb/linear blends with $\phi = 0.5$ . $N_{\text{comb}} = 190$ with $L = 10$ , $M = 10$ and $p = 10$ . . . . .	76
Figure 4.19	Excess density profiles of combs in comb/linear blends with equal degrees of polymerization. $N = 190$ and the comb has parameters $L = 10$ , $M = 10$ and $p = 10$ . . . . .	77
Figure 4.20	The comb density profiles for a blend of shorter comb molecules with longer linear chains. $N_{\text{comb}} = 190$ , $N_{\text{linear}} = 1000$ , and the comb has parameters $L = 10$ , $M = 10$ and $p = 10$ . . . . .	77

Figure 4.21	The integrated comb excess profiles for comb/linear blends with equal and different molecular weights at different compositions. The degree of polymerization of the comb is fixed at $N_{\text{comb}} = 190$ , with $L = 10$ , $M = 10$ , $p = 10$ . . . . .	78
Figure 4.22	The integrated excess profiles of comb polymers with different structures blended with linear chains of fixed length $N_{\text{linear}} = 1000$ . (a) Varying number of teeth, $p$ , with $L = 10$ and $M = 10$ . (b) Varying length of teeth, $M$ , with $p = 10$ and $L = 10$ . (c) Varying length between teeth, $L$ , with $M = 10$ and $p = 10$ . In all calculations, $\bar{v} = 0.1$ , $\phi_{\text{comb}} = 0.2$ , and $\bar{\rho}_b = 1.0$ . . . . .	79
Figure 4.23	The excess density of densely branched comb molecules in a blend with linear chains. $N_{\text{comb}} = 1099$ , $L = 1$ , $M = 10$ and $p = 100$ . The linear chain has the same molecular weight as that of the combs, $N_{\text{linear}} = 1100$ , $\bar{\rho}_b = 1$ , and $\bar{v} = 0.1$ . . . . .	80
Figure 4.24	The excess density of comb molecules in a blend with linear chains. $N_{\text{comb}} = 1099$ , $L = 1$ , $M = 10$ and $p = 100$ . $N_{\text{linear}} = 100$ , $\bar{\rho}_b = 1$ , and $\bar{v} = 0.1$ . . . . .	81
Figure 4.25	The surface density profiles of 4-star/linear blends with varying strengths of the surface attractive potential for chain ends. $N_{\text{star}} = N_{\text{linear}} = 100$ , $\bar{v} = 0.1$ , $\bar{\rho}_b = 1.0$ and $\phi_{\text{star}} = 0.2$ . Surface potentials for ends range from $U_e = -0.1kTb$ to $-1.0kTb$ . . . . .	82
Figure 4.26	(a) The integrated surface excess of $n$ -star/linear blends versus number of star arms by introducing an attractive surface potential $U_e = -0.1kTb$ for chain ends. (b) The percent increase in the integrated surface excess density of stars in the same $n$ -star/linear blends. $N_{\text{arm}} = 25$ and $N_{\text{linear}} = 100$ . $\bar{v} = 0.1$ , $\bar{\rho}_b = 1$ , and $\phi_{\text{star}} = 0.2$ . . . . .	84
Figure 4.27	The effect of a repulsive surface potential $U_a$ for branch points on the surface density profiles of a 4-star polymer blended with linear polymer. $N_{\text{star}} = N_{\text{linear}} = 100$ , $\bar{v} = 0.1$ , $\bar{\rho}_b = 1$ and $\phi_{\text{star}} = 0.2$ . . . . .	85
Figure 4.28	The chemical structures and nomenclature of the functional groups of joints on the branched molecules studied by Lee <i>et al.</i> . . . . .	86
Figure 4.29	The composition profiles for a family of blends of hydrogenous branched chain structures having 6 ends with linear dPS. The bulk volume fraction is 20 vol% hydrogenous branched PS. The air/polymer surface is at $z = 0$ and polymer/substrate interface is at $z \approx 900\text{\AA}$ . Dashed line: Linear/dPS. Dash-dot-Dashed line: 6-star/dPS. Dotted line: 6-pom/dPS. Solid line: 6-end/dPS. . . . .	86

Figure 4.30	The composition profiles for a family of blends of hydrogenous end-branched chain structures having 4 branch points with linear dPS. The bulk volume fraction is 20 vol% hydrogenous branched PS. The air/polymer surface is at $z = 0$ and polymer/substrate interface is at $z \approx 950\text{\AA}$ . Dashed line: 6-end/dPS. Dotted line: 9-end/dPS. Solid line: 13-end/dPS. . . . .	87
Figure 4.31	Excess density profiles of the branched/linear blends with 20 vol% branched component by linear response theory normalized by bulk density $\rho_b$ . Surface and interface potentials on joints and ends in Table 4.2 are applied. (a) Excess density profiles at the air/polymer surface. (b) Excess density profiles at the interface. Note also that the linear response theory assumed there were 15 ends on the 13-end molecule, as 15 was the nominal target synthetically. . . . .	90
Figure 4.32	The excess density profile, in units of $(\xi/b)$ , predicted by linear response theory for a comb/linear blend accounting for the entropic surface potential for joints ( $U_j = 0.19kT\xi$ ) and ends ( $U_e = -0.31kT\xi$ ). The mole fraction of comb polymer is $\phi_{\text{comb}} = 0.2$ . $N_{\text{linear}} = 360$ , $p = 28$ , $M = 24$ , and $L = 1$ . . . . .	93
Figure 4.33	Comparison of the excess concentration profiles of comb polymer for the comb/linear blend by linear response theory fitting the surface potential of joints and ends. The mole fraction of comb polymer is $\phi_{\text{comb}} = 0.2$ . $N_{\text{lin}} = 360$ , $p = 28$ , $M = 24$ , and $L = 1$ . . . . .	94
Figure 5.1	An illustration of two-chain SCFT on a star molecule fixing the joint at origin (black dot) which feels a mean-field from surrounding chains. $\omega(r)$ is the intramolecular monomer-monomer correlations, $g_{11}(r)$ means the intermolecular correlations between a given monomer on a different star (white dot) and the fixed joint. $g_{12}(r)$ is the intermolecular correlation between a monomer (white dot) of linear chain and the joint. . . . .	102
Figure 5.2	An illustration to calculate the local monomer density of a 3-star structure. In this example, the molecule is fixed at $t_{\text{fix}}$ . As $q3$ is solved from the end of the chain and reaches $t_{\text{fix}}$ , $q3$ is reset to an initial condition $q3(r; t = t_{\text{fix}}; t_{\text{fix}}) = \delta(r)$ . . . . .	103
Figure 5.3	The flowchart of a two-chain SCFT algorithm. . . . .	104
Figure 5.4	The intramolecular density profiles of a single linear molecule for different values of excluded volume $\bar{v}$ . (a) The intramolecular density profiles of a linear molecule from the center. (b) The intramolecular density profiles of a linear molecule from the end. The length of the molecule is $N = 50$ . . . . .	105

Figure 5.5	The intramolecular density profiles of a 4-star single molecule for different value of excluded volume $\bar{v}$ in log-log scales. (a) The intramolecular density profiles of a 4-star molecule from the joint. (b) The intramolecular density profiles of a 4-star from the end. $N_{\text{arm}} = 25$ . . . . .	107
Figure 5.6	Comparisons of density distributions of $f$ -star in a dilution solution condition with different numbers of arms. $N_{\text{arm}} = 25$ , $\bar{v} = 0.1$ . (a) Density profiles from the joint and (b) Density profiles from the end. $N_{\text{arm}} = 25$ , $N_{\text{star}} = 100$ . . . .	108
Figure 5.7	The single chain end-to-end distribution function of a linear molecule ( $N = 50$ ) and a 4-star ( $N = 100$ ) by SCFT. (a) The end-to-end distribution function of a linear molecule ( $N = 50$ ) and the comparison with Gaussian and des Cloizeaux models. (b) The end-to-end distribution function of a 4-star molecule ( $N = 100$ ) and the comparison with the Gaussian model. The reduced distance $x = \frac{r}{\sqrt{\langle R^2 \rangle}}$ . . . . .	110
Figure 5.8	Density profiles of a linear melt from the center of the molecule, the molecular weight $N = 50$ , and $\bar{\rho}_b = 0.2$ . The thin solid, dash and dash-dot lines correspond to the total, intra- and intermolecular density profiles with $\bar{v} = 1$ , respectively. The thick solid, dash and dash-dot lines are the total, intra- and intermolecular density profiles with $\bar{v} = 100$ , respectively. . . . .	112
Figure 5.9	The intramolecular density profiles in linear polymer solutions from the center of the molecule. (a) $\bar{\rho}_b = 0.2$ , $\bar{v}$ varies from 0.01 to 100. The slope of the density profile in the log-log scale is between $-4/3$ and $-1$ at $\bar{r} \approx 0.1$ . (b) $\bar{v} = 1$ , bulk monomer density $\bar{\rho}_b$ increases from 0.02 to 2. The dot line shows the expected exponent for SAW. . . . .	113
Figure 5.10	Scaling analysis of the monomer density and correlation lengths versus the excluded volume in melts of linear polymers. (a) The scaling relationship between scaled monomer density $\bar{\rho}(\bar{r})/\bar{r}^\alpha$ and excluded volume $\bar{v}$ at $\bar{r} = 0.1$ in linear solutions with $\bar{\rho}_b = 0.2$ and $N = 50$ . (b) The scaling dependence of the correlation length $\bar{\xi}$ on $\bar{v}$ for linear solutions. The circles are obtained from intramolecular densities of solutions corresponding to the examples in Figure 5.9a. Crossed points are obtained assuming the intramolecular density profile in a melt is the same as in the dilute solution (as shown in Figure 5.4). The scaling exponent results agree with Equation 5.9 for $\bar{v} > 1$ . The inset in case (b) shows the result when using the criterion $\rho(\bar{\xi}) = \bar{\rho}_b$ from the intramolecular density profiles to obtain $\bar{\xi}$ . The dashed line: density profile of $\bar{v} = 10$ , $\bar{\rho}_b = 0.2$ . The solid line: density profile of a dilute chain, $\bar{v} = 10$ . . . . .	115
Figure 5.11	The density profiles from the joint of pure component 4-star chains. $N = 100$ . (a) For varying excluded volume $\bar{v} = 0.1$ , $\bar{v} = 1$ and $\bar{v} = 10$ ; $\bar{\rho}_b = 0.2$ . (b) For varying density $\bar{\rho}_b = 0.02$ , 2, and 10; $\bar{v} = 1$ . . . . .	117

Figure 5.12	The mean squared end-to-end distances $\langle \bar{R}^2 \rangle$ of $f$ -stars ( $N_{\text{arm}} = 100$ , $f = 4, 6, 8, 12$ ) by Grayce <i>et al.</i> using PRISM theory. $\eta$ is the packing density of the monomer representing the concentration of the solutions. . . . .	118
Figure 5.13	The mean squared end-to-end distances $\langle \bar{R}^2 \rangle$ of $f$ -stars ( $N_{\text{arm}} = 25$ , $f = 4, 8, 10, 16$ ) in dilute and semi-dilute solutions. The 2-star is the linear chain with $N = 50$ . For dilute solutions, $\bar{v} = 1$ . . . . .	119
Figure 5.14	The intramolecular density profiles of various branched polymer melts from the inside joint. ( $\bar{v} = 1$ and $\bar{\rho}_b = 0.2$ ) (a) The density profiles of 9-end melts with the inside arm length of $N_{\text{arm}} = 70$ and with varying lengths of the outside branches. (b) Density profiles of branched molecules with varying numbers of outside branches by fixing the length of the inside arm $N_{\text{arm}} = 70$ and the outside branch, $N_{\text{branch}} = 10$ . (c) Density profiles of different 9-end molecules by changing the length of the outside branch $N_{\text{branch}}$ with fixed degree of polymerization of $N = 300$ . The lengths of the inside arms are $N_{\text{arm}} = 1$ for $N_{\text{branch}} = 33$ and $N_{\text{arm}} = 10$ for $N_{\text{branch}} = 30$ . (d) The difference of density profiles of 6, 9 and 15-end by fixing the total degree of polymerization $N = 300$ and the length of the inside arms $N_{\text{arm}} = 70$ . . . . .	120
Figure 5.15	The intramolecular $\omega(k)$ and intermolecular $h(k)$ structure factors of 4-star molecules ( $N_{\text{star}} = 100$ ). (a) Comparison with the Gaussian chain, with a chain in dilute solution with $\bar{v} = 1$ , and with 4-star solutions with $\bar{\rho}_b = 0.2$ and 10, respectively, and $\bar{v} = 1$ . (b) Comparison with various $\bar{v}$ and $\bar{\rho}_b$ . . . . .	123
Figure 5.16	Structure factors of 4-star molecules in different solutions. $N_{\text{star}} = 100$ . . . . .	124
Figure 5.17	The Kratky plots of the intramolecular structure factors $\omega(k)$ of 4-star molecules ( $N_{\text{star}} = 100$ ). Comparisons are performed among the Gaussian chain, the single chain in dilute solution with $\bar{v} = 1$ , and 4-star in different solutions with $\bar{v} = 1$ , $\bar{\rho}_b = 0.2$ and 2, respectively. $\bar{v} = 0.1$ , and $\bar{\rho}_b = 2$ . . . . .	125
Figure 5.18	The Kratky plots of the intramolecular structure factors $\omega(k)$ of $f$ -star solutions. $N_{\text{arm}} = 25$ , $\bar{v} = 1$ and $\bar{\rho}_b = 0.2$ . . . . .	126
Figure 5.19	Comparisons of the intramolecular density profiles of a 4-star polymer in a melt and a 4-star/linear blend, $\Delta\bar{\rho}_{\text{star}}$ . Density profiles are calculated by fixing the joint at the origin. $N_{\text{star}} = 100$ and $N_{\text{linear}} = 50$ . (a) The comparison of $\Delta\bar{\rho}_{\text{star}}$ in different compositions. The total monomer density $\bar{\rho}_b = 0.2$ and $\bar{v} = 1$ . (b) The intramolecular density of the 4-star components in the 4-star/linear blend by varying excluded volume parameters. The composition of the star monomers, $\phi_{\text{star}} = 0.5$ , $\bar{\rho}_b = 0.2$ . . . . .	127

Figure 5.20	A comparison of the intramolecular density profiles between 4-star/linear blends and the 4-star melt. (a) Comparisons of $\Delta\bar{\rho}_{\text{star}}$ from the joint and end in the 50/50 blend. $N_{\text{star}} = N_{\text{linear}} = 100$ . (b) Comparison of $\Delta\bar{\rho}_{\text{star}}$ from the joint of star polymer by changing the molecular weight of the linear polymer. In both cases, $\bar{\rho}_b = 0.2$ and $\bar{v} = 1$ . . . . .	129
Figure 5.21	A comparison of the intramolecular 9-end density profiles between various 9-end/linear blends and the 9-end melt. The plots locate the joint of the 9-end molecule at the origin. The polymerization index of the 9-end and linear molecules are fixed to be $N = 300$ . The 9-star is equivalent to a 9-end molecule with $N_{\text{arm}} = 0$ . $\bar{\rho}_b = 0.2$ and $\bar{v} = 1$ . . . . .	130
Figure 5.22	The intra- and intermolecular density distribution function of a 4-star/linear binary blend from the joint of a 4-star by SCFT. $N_{\text{star}} = 100$ and $N_{\text{linear}} = 50$ . $\bar{\rho}_b = 2.0$ , $\bar{v} = 1$ , and $\phi = 0.5$ . . . . .	130
Figure 5.23	The structure factors of a series of 4-star/linear binary blends for various molecular weights. $\bar{v} = 1$ , $\bar{\rho}_b = 0.2$ , and $\phi = 0.5$ . . . . .	131
Figure 5.24	The excess free energy $\Delta\bar{F}$ of the 4-star/linear homogeneous blend in semi-grand canonical SCFT. $N_{\text{star}} = 100$ , and $N_{\text{linear}}$ are 50, 100 and 200, respectively. $\bar{v} = 1$ , and $\bar{\rho}_b = 0.2$ . The size of the system, $\bar{r}_{\text{max}} = 100$ . . . . .	139
Figure 5.25	The excess free energy $\Delta\bar{F}$ of n-end/linear homogeneous blends in semi-grand canonical SCFT. $N = 360$ , $\bar{v} = 1$ , $\bar{\rho}_B = 0.2$ , and the size of the system, $\bar{r}_{\text{max}} = 200$ . . . . .	141
Figure 5.26	The effective interaction parameter $\chi_{\text{eff}}$ in the n-end/linear homogeneous blends by semi-grand canonical two-chain SCFT, Gaussian field theory and SANS experiments. The experimental $\chi_{\text{eff}}$ is determined by SANS at $120^\circ\text{C}$ . The uncertainty in $\chi_{\text{eff}}$ of $\pm 0.3 \times 10^{-4}$ for characterizing a linear/linear blend using the same method is reported. Gaussian field theory assumes the statistical segment length $b = 6.2\text{\AA}$ . In SCFT, $\bar{v} = 1$ , $\bar{\rho}_b = 0.2$ . . . . .	142
Figure 5.27	The effective thermodynamic interaction parameters $\chi_{\text{eff}}$ of blends of linear and densely branched comb polymers calculated by Gaussian field theory. The segment length is assumed to be $b = 6.2\text{\AA}$ as previously reported for branched polystyrene. . . . .	144
Figure 6.1	Cyclic, balloon, dumbbell, and rings on a rope topologies. . . . .	150
Figure A.1	The flowchart of SCFT iterations by Picard method. . . . .	171
Figure A.2	The flowchart of SCFT iterations by Newton-Broyden method. . . . .	172

Figure C.1	An illustration of the domain decomposition algorithm using ghost points for an explicit method scheme on 4 CPUs. . . . .	179
Figure C.2	The speedup test for solving the 1-D diffusion equation using parallel explicit method. . . . .	180
Figure C.3	The schematic illustration of a parallel matrix of function $G(z', z''; 0, t)$ . The first dimension $z'$ is split into eight steps and split into four processors. The filled area represents a separate solution of diffusion equation at a specified $z$	181
Figure C.4	The values to be gathered in the array of $G(z', z''; 0, t)$ . . . . .	182
Figure C.5	The flowchart of an SCFT program for cyclic molecules. . . . .	183
Figure C.6	CPU wall time of SCF calculations in parallel of a cyclic/linear ( $\phi = 0.5$ ) blend. $N_{\text{ring}} = N_{\text{linear}} = 100, \bar{v} = 1$ . . . . .	184
Figure C.7	The speedup of parallel computation of a cyclic/linear ( $\phi = 0.5$ ) blend in the calculations in Figure C.6. . . . .	184
Figure C.8	The efficiency of the parallel computation of a cyclic/linear ( $\phi = 0.5$ ) blend. The dimension of the matrix is the same as Figure C.6. . . . .	185
Figure C.9	Sequential fraction $f$ in parallel computation of a cyclic/linear ( $\phi = 0.5$ ) blend. The dimension of the matrix is the same as Figure C.6. . . . .	185

## LIST OF TABLES

Table 4.1	The integrated surface and interface excess of the hydrogenous branched PS molecule blended with deuterated linear PS by NR . The uncertainties are $\pm 1\text{\AA}$ . . . . .	88
Table 4.2	The surface and interface potentials of functional groups of branched and linear polymers from linear response theory, under the assumptions that $U_{j4} = U_{j3'}$ and $U_{j2} = U_{j3}$ . . . . .	91
Table 4.3	The decay lengths of surface density profiles in branched/linear blends from linear response theory and experiments. Surface and interface potentials in Table 4.2 are applied. . . . .	92
Table 5.1	The effective Flory-Huggins interaction parameters of different 4-star/linear blends with equal monomer compositions, based on the free energy diagrams in Figure 5.24. . . . .	139
Table 5.2	The molecular characterization of n-end/linear blends in two-chain SCFT. . . . .	140
Table 5.3	The molecular characterization of comb polymers for Gaussian field theory. . . . .	143

## ACKNOWLEDGMENTS

First and foremost, I sincerely appreciate my advisor Prof. David T. Wu, for his insightful guidance and support throughout my PhD research. I would never attain my goals without his patient supervision and encouragement. I would also like to thank Prof. Mark D. Foster, for his helpful guidance from the experimental prospective in understanding the results of numerical modeling during our five years of collaboration. I would like to thank Prof. Mahadevan Ganesh, for his advice in numerical computing. I truly appreciate Prof. Amadeu K. Sum, Prof. John Dorgan, and Prof. Matthew Liberatore for their support as committee members throughout my graduate study.

I am deeply grateful to my collaborators, Prof. Roderic P. Quirk, Dr. Shih-Fan Wang, Dr. Boxi Liu, Dr. Jaesik Lee and Dr. Sewoo Yang from the University of Akron, for sharing views and discussions in the research project. I would like to thank current and former colleagues in the molecular modeling and theory research groups, Dr. Eric Grzelak, Caleb Tormey, Benjamin Zeidman, Patrick Lafond, Dr. Brian Barnes, and Dr. Francesca Stanzione for discussion and advice on theories and simulations.

I truly appreciate Prof. David Marr, Prof. Colin Wolden, and Prof. James Ely for their encouragement and support to complete my study.

Many thanks to Dr. Timothy Kaiser, Steve Toleque and Prof. Mark Lusk in the Golden Energy Computing Organization, for offering me great opportunities to learn high performance computing and participate in the building and testing of the supercomputers. The knowledge and experience they shared with me is my precious treasure. Specially, I would like to express my sincere gratitude to Dr. Hans-Heinrich Carstensen, Dr. Amanda Lewis, Dr. Bin Liu, Dr. Huayang Zhu, Huashan Li, and all my friends.

The research project is supported by the National Science Foundation. Golden Energy Computing Organization HPC group provided computing resources and technical support

for the project.

Finally and mostly, I want to dedicate this dissertation to my parents for their endless love and support.

# CHAPTER 1

## INTRODUCTION

Blending has become one of the most widely applied methods to enhance properties of polymer materials. It is used to improve performance by tuning specific properties such as viscosity, solubility, biodegradability and mechanical properties [1, 2]. Polymer blends are currently used in textile, medical and electronic industries, among many others [3].

Although polymer blends are being used commercially, not much is known about the surface and bulk properties of blends made with nonlinear architectures, such as branched and cyclic polymers. According to Ober *et al.* [4], one of the future challenges in polymer science and engineering is to improve synthesis techniques of complex architectures and to apply them to industrial uses. The surface and bulk properties of polymers are of renewed interest with progress in synthesizing branched and cyclic polymers with complex architectures [5–13]. Such novel synthesized nonlinear branched structures can be made with fine control over the functionality of branch points and the degree of polymerization of the branches. Blends synthesized using the same monomers but with different complex structures also exhibit good miscibility and stability to prevent phase separation.

The difference in surface free energy between components in polymer mixtures can cause *surface* (i.e., the interface between polymer and air) and *interface* (i.e., the interface between polymer and substrate) segregation for low surface free energy species. For instance, linear polymers with fluorinated molecular ends in polymer blends have been proven to segregate to the surface [14, 15]. However, nonlinear architectures are also known to segregate to the surface of a blend containing nonlinear and linear polymers composed of the same type of repeat units. There are thermodynamic driving forces for surface enrichment caused by steric and conformational entropies in addition to any enthalpic driving forces. Nonlinear architectures introduce an alternative route to surface modification without including special

groups that are difficult to synthesize or that could reduce bulk stability. This phenomena in a binary polymer blend film is illustrated by Figure 1.1 [16], and the surface and interface segregation is characterized by measuring the composition depth profile (vertical to the substrate) in terms of the integrated excess.

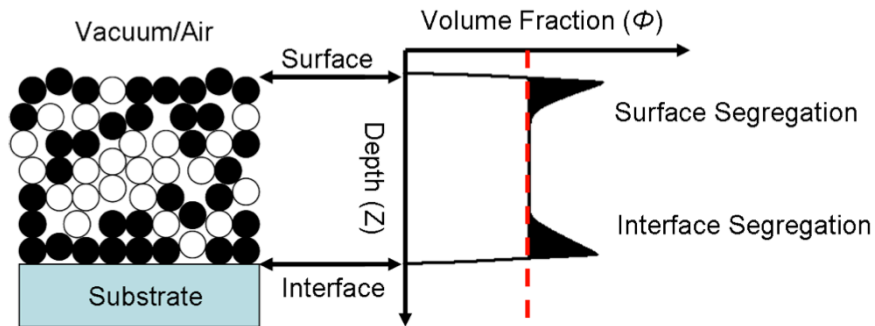


Figure 1.1: An illustration of the surface and interface segregation in a binary polymer blend film (left), and its corresponding composition profile (right). The filled areas show the interfacial excess above the hypothetical uniform bulk composition (dashed line) [16].

Controlling the surface segregation in blends containing nonlinear architectures is thus a potential route to modify polymer surface properties. A pioneering application of this strategy for surface modification was used in the design of anti-fouling membranes by adding highly-branched comb molecules into linear hosts to create segregated layers at the surface [17]. The current and potential applications of adding nonlinear polymers to linear hosts stimulate the drive to advance fundamental understanding of architecturally-driven segregation in both experiments and theory.

The Foster and Quirk groups at the University of Akron have carried out synthesis and experimental studies of blends of various novel branched and cyclic molecules mixed with their linear analogs. They found that when mixing nonlinear and linear polymers composed of the same monomers, such as styrene or butadiene, and having similar degrees of polymerization, there is typically surface enrichment of the nonlinear component [16, 18–20]. Previous understanding for surface segregation driven by molecular architecture differences was given in the work of Wu and Fredrickson [21], where linear response theory was used to

explain the enrichment of branched architectures in terms of the effective surface potentials of end and branch points. According to the linear response theory, the conformational entropy contributes a repulsion for joints and an attraction for end groups towards the surface or interface. A hypothetical chain conformation of a star molecule reflecting these entropic interactions with an interface is schematically shown in Figure 1.2.

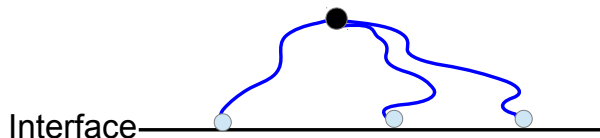


Figure 1.2: Schematic of a star molecule near an interface under the influence of the interfacial potentials predicted by linear response theory. The joint is entropically repelled and ends attracted by the interface.

However, recent research by Yang [20] on the effect of junction placement in a series of pom-pom branched polymers shows the limitations of the linear response theory. The experiments blend linear polystyrene with a series of 6-pom polystyrenes with the same total molecular weight but different lengths between the two joints. Yang's results indicate that the integrated excess decreases as the distance between the two joints increases. This contradicts the linear response theory, which predicts that the integrated excess depends only on the number and type of end and branch groups, and should thus remain constant as the joint separation changes. The discrepancy between linear response theory and experiments requires us to develop a theory beyond the assumption of linear response, to model not only the effects of branch groups, but also the total chain conformations including the effect of junction placement within the molecule.

As a well-established theory, self-consistent field theory (SCFT) has been successfully applied to study the surface and interface of polymers mixtures [21–31]. SCFT reduces a

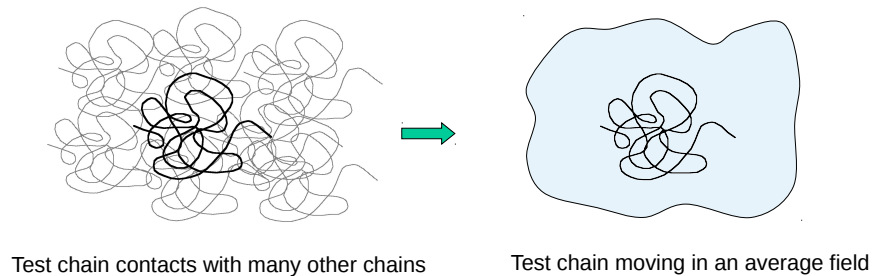


Figure 1.3: Schematic of the general idea of solving for a many chain system by a self-consistent field.

many-body problem to a one-body problem by focusing on a test chain in a polymer melt or blend. The fluctuating environment is replaced by an average field. To get the field, the average density profile of the test chain is calculated self-consistently. The general idea of SCFT for polymers is shown in Figure 1.3. The SCFT algorithm for a given polymer architecture can be implemented by assuming the conformations are those of a Gaussian chain in an external field. Gaussian conformations are a good model for long chain molecules, but less accurate for short rings because of the non-random walk conformation due to short-ranged interactions such as packing. The various example nonlinear architectures to be modeled in SCFT are introduced in Chapter 3 of this dissertation. In addition, cyclic chains are also driven to the surface and interface due to conformational entropy [21]. A relevant experimental study was performed by Wang in the Foster group for high molecular weight cyclic polystyrene [32]. I developed a SCFT to test the predictions of linear response theory and to compare with Wang's results on long-chain mixtures.

This theoretical research is done in close collaboration with synthesis and experimental studies by the Foster and Quirk groups at the University of Akron. The goal of this project is to advance the theory of polymer blends containing nonlinear molecules and perform direct comparisons between the experiments and theories on surface segregation phenomena of

nonlinear/linear blends. We expect the theory can guide the design of blends with nonlinear polymers including star, end-branched, comb, and cyclic architectures. The experimental studies in the Foster group have focused on bulk conformation and thermodynamics of various branched and cyclic molecules mixed with linear structures. They found that when mixing nonlinear polymers with their linear analogs, while there is typically surface enrichment of the nonlinear component, a stable single phase is formed in the bulk [18–20]. For densely branched comb polymers, the stability of comb/linear blends cannot be guaranteed due to the strongly crowded topology and large number of ends. Good bulk miscibility is important in blends to improve bulk performance, to form a stable product with uniform properties. For instance, the rheology of branched and cyclic polymers has been shown to differ dramatically from that of linear chains with the same types of monomers [16, 32, 33]. Thus they can be potentially added into linear hosts to modify the bulk rheology of the linear melts.

The second goal of my research focuses on developing a new algorithm to extend the SCFT to capture the intra- and intermolecular correlations to study the molecular conformations in polymer solutions and blends. The bulk conformation of polymer systems has been previously described with scaling theory by de Gennes and others, and the analytical Gaussian model by Edwards [22, 34]. Molecular simulations have also been used to study the bulk property of polymers with complex structures [35].

In this thesis, a new two-chain theory is developed to capture the screening of a polymer in a nonlinear polymer melt and in nonlinear/linear polymer blends. The conventional one-chain SCFT cannot model the chains in the bulk because it neglects correlations so that the test chain experiences a featureless mean environment. Due to translational symmetry, the one-chain algorithm only results in an averaged uniform bulk densities. The development of the two-chain SCFT in my research extends conventional one-chain SCFT to a two-body problem by focusing on two test chains. One of them is fixed at the origin of space, breaking translational symmetry. The new algorithm allows locating the coordinates of the test chain in a non-uniform environment, and showing correlations within and between the test chains.

This project applies the novel two-chain SCFT to study the bulk conformations of branched molecules in solutions and blends to understand swelling and stretching effects of branching.

Moreover, the two-chain algorithm provides the free energy of mixing in polymer blends and the segment-segment interaction parameter  $\chi$  beyond mean-field theory. For instance, in Flory-Huggins mean-field theory [36,37], the interaction free energy between monomers is approximately a parabolic function of the volume fraction and the coefficient  $\chi$  is considered a measure of miscibility of the blends. The random phase approximation (RPA) theory using linear response assumptions showed that  $\chi$  can be estimated by the excess free energy, and relates the change in chain structures before and after blending [22]. Gaussian structure factors are assumed in RPA theory. RPA theory is widely accepted in neutron scattering experiments to estimate  $\chi$ , with a measured scattering structure factor and given single chain structure factors for two pure components. The Gaussian field theory by Fredrickson *et al.* [38] captures the entropic contribution to the excess mixing free energy for incompressible molecules. The excess free energy is approximated by a field of densities satisfying a Gaussian distribution. Both RPA and Gaussian field theories neglect the swelling effect because the conformations of the components are held Gaussian. Scaling analysis of experiments indicates that molecules change conformations in solutions and blends, but this effect is beyond RPA and Gaussian field theories. In the case of nonlinear polymers of crowded architectures, e.g., high-arm star molecules, the swelling effect should be considered as an aspect affecting  $\chi$ . The experimental  $\chi$  (by RPA theory) and Gaussian field  $\chi$  has been found inconsistent in star and linear polybutadiene blends by Martter *et al.* [39] The inconsistency, such as different trends of  $\chi$  in symmetric molecular weight blends of linear and stars containing various number of arms, implies possible non-universal factors in  $\chi$ .

My research exploits the ability of the two-chain SCFT for capturing swelling and crowding of molecules in the bulk, and to calculate the free energy of mixing, and thus provide an estimated interaction parameter  $\chi$  for nonlinear/linear blends. In contrast to the Gaussian field theory, the free energy profile in SCFT is approximated by the saddle point value,

while Gaussian field theory uses a Gaussian function for the free energy profile. However, the molecular correlations by two-chain SCFT introduces conformational contributions to the excess free energy. Hence, the two-chain SCFT is expected to be a helpful method in predicting  $\chi$  with swelling effects.

This thesis is organized as follows. Chapter 2 provides background on state of the art experimental and theoretical studies on the surface segregation behavior of nonlinear architectures when mixed with linear molecules. It summarizes characterization of polymer bulk thermodynamics using neutron scattering technology and theories, such as scaling theory, mean-field theory, polymer liquid state theory and simulations. Chapter 3 presents a review of SCFT for the study of a polymer blend near a surface. This chapter discusses the derivation of compressible SCFT for various nonlinear polymers such as end-branched, cyclic and comb polymers. Linear response theory and the concept of effective surface potentials for polymer ends and joints in an SCFT calculation are also discussed in Chapter 3.

Calculations using SCFT to study the surface enrichment due to branching and cyclic topologies are presented in Chapter 4. In this chapter, the surface excess of specific nonlinear/linear blends are calculated and compared with available experiments. The SCFT calculations allow answering several questions regarding the surface enrichment of nonlinear polymers due to conformational entropy in nonlinear/linear blends. A variety of nonlinear topologies are studied in Chapter 4, including star, pom-pom, multiple end-branched, comb and cyclic polymers. Extra surface potentials on junction groups and ends are also studied by SCFT beyond the entropy influencing surface segregation. Linear response theory predictions on particular blends are also provided for comparison.

Chapter 5 introduces the development of a two-chain SCFT algorithm to study the bulk conformations of branched polymer solutions, melts and blends. The two-chain algorithm captures the intra- and intermolecular correlations due to the steric and entropic driving forces, normally not accessible within conventional SCFT theory, and is helpful in understanding the conformations of branched polymer solutions. The application of the two-chain

SCFT to bulk thermodynamics for branched molecule solutions and melts are presented in this chapter. Particularly, in Section 5.4, the swelling of linear and branched chains are captured by two-chain SCFT and compared with the scaling analysis for solutions and melts. The plots of pair correlation functions of the branched and linear species in solutions and melts, as well as the static structure factors are also shown.

In Section 5.5, the stretching and swelling for branched polymer blends are discussed. By using two-chain SCFT in semi-grand canonical ensemble, the free energy of the star/linear blends and their approximate free energy of mixing are evaluated in Section 5.6. I propose an approximation for the Flory interaction parameter  $\chi$  based on a self-consistent field assumption. The two-chain SCFT  $\chi$  parameter accounts for the excluded volume, the effective interaction free energy, and the change of configurational entropy. The effective interaction parameters for a preliminary test using semi-dilute condition values for the excluded volume parameter  $v$  in Section 5.4 for different 4-star/linear blends are qualitatively consistent with the Flory-Huggins theory and Gaussian field theory. However, comparisons of  $\chi$  in a series of multiple end-branched polystyrene and linear blends do not always show a consistent order of magnitude between RPA and two-chain SCFT, as well as between the Gaussian field theory and two-chain SCFT. Therefore, an improvement of the theory is needed to find appropriate excluded volume parameters for a real polymer blend. The Gaussian field theory for several densely branched comb and linear blends are performed to support the SANS experiments from the University of Akron.

The appendices include several additional materials. Firstly, the numerical methods for conducting the SCFT iterations on nonlinear structures are provided as the supplementary information for Chapter 3. Secondly, the derivation of the Gaussian structure factors for various branched molecules are given, and they are applied in linear response theory and the Gaussian field theory. Finally, the parallelization performance of the SCFT algorithm for solving the differential equations in SCFT is presented.

## CHAPTER 2

### BACKGROUND

In this chapter, the theories and experiments relevant to understanding surface segregation in blends of linear and nonlinear polymers are reviewed in section 2.1. Previous studies on the characterization of bulk thermodynamic properties in polymer blends are then discussed in section 2.2, including experimental and theoretical perspectives.

#### **2.1 Surface segregation of nonlinear and linear polymer blends**

As discussed in Chapter 1, surface segregation in homogeneous polymer blends can be entropically and enthalpically driven. This section reviews the studies on surface segregation of polymer blends in experiments and theory.

##### **2.1.1 Experiments on the surface segregation of polymer blends**

A variety of experimental techniques are available to characterize the surface segregation of polymeric systems such as neutron reflectivity (NR), surface enhanced Raman scattering (SERS), secondary ion mass spectrometry (SIMS), nuclear reaction analysis (NRA), forward-recoil spectrometry (FRES) and X-ray photoelectron spectroscopy (XPS). Surface characterization of different types of polymer blends have shown that various factors can affect surface segregation, including isotopic labeling, polymer molecular weight, end groups type, annealing and molecular architecture. I discuss these below, and highlight especially the connection between prior experimental work on molecular architecture with the motivation for the work in this thesis.

As one of the most successful and widely applied techniques for studying the near-surface structure of materials, NR is briefly introduced and illustrated in Figure 2.1. In an NR experiment, an incident beam of neutrons strikes the flat surface of the sample at a small angle  $\theta$ .

The intensity of radiation reflected from the sample surface at an angle equal to the incident angle is measured by a detector. This reflected intensity varies with incident angle in a manner characteristic of the variation in scattering length density with depth in the sample, for example that at the polymer film/substrate interface.

NR data is recorded as the reflectivity, which is the reflected intensity divided by the incident intensity,  $R = I_R/I_0$  versus the momentum transfer vector  $\mathbf{q}$ . For reflectivity it is only the  $z$ -axis (vertical to the surface) component of the vector  $\mathbf{q}$  that is pertinent, and it depends on the neutron wave length and  $\theta$  according to

$$|\mathbf{q}| = \frac{4\pi}{\lambda} \sin(\theta). \quad (2.1)$$

The scattering of the beam from the sample depends on the depth dependent scattering length density (SLD), which is defined as

$$\rho_{\text{SLD}}(z) = \frac{\sum_i^n b_i}{V}, \quad (2.2)$$

where  $V$  is the reference volume containing  $n$  atoms representative of the material (e.g., one repeat unit for a polymer) and  $b_i$  is the scattering length of atom  $i$ . NR can probe

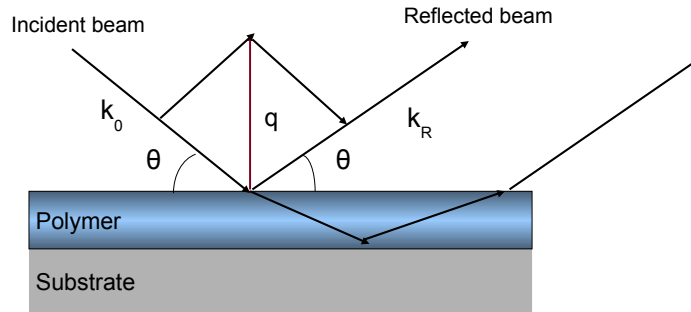


Figure 2.1: Illustration of a neutron reflectivity experiment on a polymer film surface and interface.

the neutron scattering length density at depths of up to several thousand Ångströms with an effective depth resolution of a few Ångströms (10-20Å). Blend samples are prepared by dissolving the polymers in a mutual solvent and then spin casting on a silicon substrate. The thickness of the film can typically be several hundreds of Ångströms (on the order of several  $R_g$ , i.e., the radius of gyration). The SLD depth profile can be inferred from fitting the neutron reflectivity curve by nonlinear regression of the data using a parameterized model of the SLD depth profile.

The reflectivity depends on the contrast of scattering length density between components and an isotopic labeling on specific molecules is often used in NR to obtain strong contrast. One polymer component is usually fully deuterated for distinguishing the components. However, the slight differences in the bond lengths and polarizabilities between C-D bonds and C-H bonds can introduce molar volume and surface free energy differences between hydrogenous and deuterated melts [40]. The deuteration also creates a small enthalpic exchange interaction between the deuterated and hydrogenous molecules. Bates *et al.* [41, 42] discussed the isotopic effect in binary polymer mixtures, in particular, the mixing free energy due to deuteration. They concluded that the isotopic labeling changed the chain segment volume and the van der Waals interaction between polymers; and therefore it changed the monomer-monomer (segment-segment) exchange interaction parameter. Accounting for the corrected interaction parameters achieved good agreement with the neutron scattering results. Hariharan *et al.* [43] performed NR and SIMS measurements of annealed deuterated polystyrene/hydrogenous polystyrene (dPS/hPS) blends with symmetric molecular weights. The results for mixtures of low molecular weight and high molecular weight polystyrenes indicated that the segregation of dPS to the air/polymer surface is a purely energetic effect due to isotopic differences. The experimental results agreed well with the lattice-SCFT calculations published earlier by Hariharan and coworkers [44, 45]. Zhao *et al.* [46] attempted to measure the surface preference of ends in dPS-*b*-hPS-*b*-dPS tri-block copolymers using neutron reflectivity. The deuterated blocks were found to segregate to the surface of the

polymer melt. However, the results failed to distinguish the entropic driving force acting on ends and the effect of deuteration on the surface segregation.

Norton *et al.* [47] applied NR to investigate the isotopic effect on the surface segregation in a thin film blend of deuterated and hydrogenous poly (ethylene-propylene) (dPEP/hPEP,  $N_{\text{PEP}} \sim 2000$ ). A strong enrichment of the dPEP at the air/polymer surface was seen in NR data. The composition of dPEP decayed exponentially with depth. Norton and coworkers concluded that the surface segregation is due to the surface energy difference between hydrogenous and deuterated molecules. Norton *et al.* focused only on the segregation at the free surface and neglected the change at the interface between the substrate and polymer. In particular, their study indicated that dPEP can segregate to the air/polymer surface with a surface concentration eight times that in the bulk. Hopkinson *et al.* [48] used SIMS and NR to characterize the surface compositions of dPMMA ( $M_w \approx 12, 25, 130, \text{ and } 420 \text{ kg/mol}$ )/PMMA ( $M_w \approx 30 \text{ kg/mol}$ ) blends and concluded that the surface segregation for dPMMA is insignificant. Compared to the experiments using dPS/hPS blends, the difference in the surface energy between dPMMA and PMMA is too small to cause measurable segregation.

The isotopic effect interferes with NR experiments for studying surface segregation in blends of chains of different architectures. It is often neglected in theoretical studies of the surface enrichment in polymer blends that mainly focus on conformational entropy effects [27, 28]. Linear response theory [21] indicated that the surface segregation of branched molecules can be understood in terms of effective surface potentials for end and joint monomers. The surface potentials of specific groups can be both entropic and enthalpic. Similarly, SCFT can also be extended beyond entropic effects to include enthalpic contributions to the end and joint surface potentials. A review of linear response theory is presented in the next section, and the effect of extra end and joint enthalpic surface potentials is discussed in Chapter 4.

The annealing of polymer samples above the glass transition temperatures of the components releases internal stress in the molecules, with accompanying relaxation in the mor-

phology and composition. Sokolov *et al.* [49] and Jones *et al.* [50] showed that linear dPS ( $M_w \approx 1030$  kg/mol)/hPS ( $M_w \approx 1800$  kg/mol) blend films (with thickness  $\sim \mathcal{O}(10^3)\text{\AA}$ ) exhibit significant surface enrichment of dPS after annealing at  $184^\circ\text{C}$  for several ( $\sim 3$ -5) days, while the blends showed no segregation before annealing. Sokolov *et al.* also compared the relative surface segregation (i.e., the ratio of surface composition to the bulk composition) among blends in different dPS compositions, and indicated that increasing the bulk volume fraction of dPS from 0.1 to 0.5 could increase the surface segregation of the deuterated component. Jones and coworkers [50] performed FRES measurements on blends of the same high molecular weight polystyrenes to study long chain surface segregation caused by the deuteration of one component. The dPS molecules were found enriched at the surface after annealing. Jones indicated that the total surface excess increased approximately linearly with increasing dPS composition from  $\phi = 0.025$  to 0.15. Steiner *et al.* [51] studied a bilayer polyolefin film with a deuterated layer on the substrate and a hydrogenous layer at the air/polymer surface. The NRA results showed that the deuterated polymers could be transported from the bottom layer to the air/polymer surface by increasing the annealing time, and the thickness of the segregated regime at the surface increased with annealing time.

In addition, for very thin films, the film thickness is also considered an important factor affecting the surface composition. Hong [52] found that by increasing the thickness of polymer films, the surface concentration of dPS increased linearly with the thickness of films. Walton [53] also indicated that thick ( $\sim 2000\text{\AA}$ ) coated films of P(MMA-r-MnG)/PMMA blends ( $\phi_{\text{P(MMA-r-MnG)}} \leq 20\%$ ) showed that the surface composition of P(MMA-r-MnG) approaches 100% at the air/polymer surface, while films of half that thickness resulted in lower P(MMA-r-MnG) surface compositions.

The surface free energy of a polymer depends on the polymer end group type. Jalbert *et al.* [54] measured the surface tension of polydimethylsiloxane (PDMS) with different ends including amine-, hydroxyl-, and methyl groups. The experiments were performed to un-

derstand the effect of end groups on the molecular conformations at the surface. The study concluded that the difference of surface tensions between backbone monomers and ends are important factors in controlling the molecular surface tension. Therefore, modifications of the end groups of polymers can provide different enthalpic contributions to the surface enrichment. Affrossman *et al.* [55] measured the surface concentration of end-modified polystyrene copolymers using SIMS. Polymer samples studied included dPS-hPS diblock, dPS-hPS-dPS and hPS-dPS-hPS triblock structures. The deuterated ends were found to be enriched at the surface. Ends with protons were also enriched at the surface, although the segregation was weaker than that for the deuterated ends.

Polymer blends containing a component modified with lower surface energy chemical groups have been studied [14, 15, 56]. Schaub *et al.* [14] characterized the surface compositions of PS modified with an oligo-tetrafluoroethylene(TFE) end. The polymer films were composed of short dPS-TFE molecules and long hPS chains. The TFE ends on the dPS polymers enhanced the surface segregation compared to the linear dPS without TFE end modification. This can be explained by the lower surface energy of the fluorinated groups. However, blends using hPS-TFE and regular dPS showed that the chains with fluorinated groups had a stronger preference for the surface than did the deuterated chains. Thus, no segregation of the dPS component was detected at the surface. It is notable that the TFE end did not increase the PS enrichment as much at the substrate interface as at the air/PS surface. Mason and coworkers [15] studied the surface free energy and surface segregation of fluorinated end-capped PS films for different degrees of polymerization of PS molecules. The end effect on surface segregation is significant not only for low molecular weight molecules ( $M_w \approx 5$  to 20 kg/mol), but also for high molecular weight PS ( $M_w \approx 150$  kg/mol). The fluorinated groups at the surface were also found to reduce the surface tension of the molecules. For instance, a 3% increase in the number of low-energy end groups reduced the surface tension by approximately 39%. Tanaka *et al.* [56] had similar findings showing that the fluorinated ends segregate to the surface. The PS films were prepared by

end-capping fluoro-alkyl groups and characterized by XPS and NR. The end segregation was shown to be dependent on the PS backbone length, and the shorter backbone resulted in stronger surface excess of the end groups.

Both experiment [52] and theory [57] have shown that lengths of chains can affect the surface segregation in symmetric molecular weight linear polymer blends. In general, symmetric blends with long chains exhibit stronger surface segregation. However, in blends of chains differing in molecular weight, shorter molecules have a preference to segregate to the surface and interface entropically rather than long molecules [43,45]. The disparate molecular weight effect becomes stronger as the difference in molecular weights between the short and long chains increases. Hong *et al.* [52] emphasized that the isotopic effect can overwhelm the entropic preference due to molecular weights. In the measured surface compositions of a blend with short hPS and long dPS by Hong and coworkers, the long dPS segregated to the surface instead of the short hPS.

Pioneering work on the effect of side chains on surface segregation was conducted in polyolefin blends and copolymers containing short side branches and showed that molecules with more side branches can segregate to the air/polymer surface regardless of the isotopic effect, although they were not always found to be enriched at the substrate [58–60]. Surface segregation due to long chain branching was studied by Walton and coworkers [53] using NR experiments on blends of linear PMMA and branched random copolymer of methyl methacrylate and methoxy poly(ethylene glycol) monomethacrylate, P(MMA-r-MnG). The P(MMA-r-MnG) species, which has higher surface free energy than PMMA, segregated to the surface and interface due to branching. The measurement of the surface composition profiles of blends of low molecular weight symmetric star polymers ( $M_w \approx 160$  kg/mol) with linear analogs ( $M_w \approx 230$  kg/mol) was carried out by Foster *et al.* [61] Blends of linear and deuterated 6-star polystyrene were characterized using dynamic SIMS. The star polymers segregated to both the air surface and the substrate interface.

Recent work has focused on synthesizing branched polymers with highly controlled architecture and careful characterization of the surface and interface of binary blends containing complex architectures. Lee [18] performed NR experiments on a series of end-branched ( $M_w \approx 37$  kg/mol) and linear polystyrene blends symmetrically in molecular weight. Lee's study focused on the effect of functionality of branched polymers on surface segregation. For linear and branched molecules with similar degrees of polymerization, surface enrichment was enhanced by changing the branch architecture. One series of molecules had an increasing number of branch points with a fixed total number of ends, while a second series had an increasing number of end groups with a fixed number of branch points. The branched architectures enhanced surface segregation to different degrees. An NR spectrum of a 6-pom hPS/dPS blend and the corresponding density profile of the 6-pom molecules are given in Figure 2.2. As discussed below, the overall magnitude and some trends agreed with a Gaus-

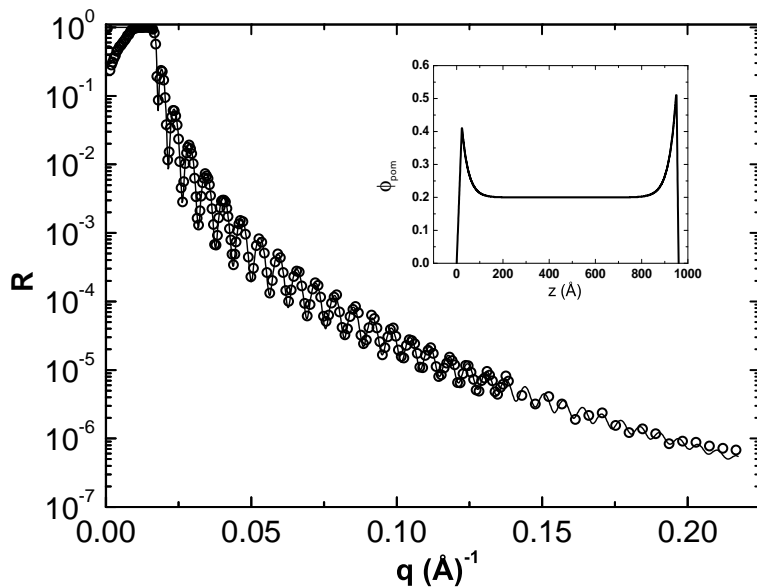


Figure 2.2: Neutron reflectivity spectrum of a blend of 20vol% 6-pom hPS with linear dPS. The inset shows the composition profile of 6-pom versus film depth resulting from fitting the spectrum [18].

sian field theory with no fitted parameters. There was evidence that discrepancies were due

to enthalpic effects associated with differing end groups. In addition, the discrepancy between the Gaussian field theory and experiment appears larger for greater number of arms, suggesting the possibility that the Gaussian assumption for chain conformations breaks down with increased crowding. This was a significant motivation for pursuing the development of the two-chain SCFT approach in this thesis.

Yang [20] focused on the effect of junction placement on surface segregation, keeping all end and branch groups the same in a series of pom-pom molecules. NR experiments were performed on blends of linear PS and a series of 6-pom PS molecules with various lengths of central linear portions between the joints, but at fixed total molecular weight. The strength of the air/polymer surface segregation, in terms of the integrated surface excess, increases with decreasing length of the linear portion between the joints of the 6-pom, rather than depending on only the number and type of functional groups as approximated by linear response theory [21]. This provides strong motivation to go beyond linear response theory, and for my research in using SCFT to account for these effects.

Surface segregation of cyclic molecules is also of interest for a number of scientific and technological reasons. High molecular weight cyclic molecules have traditionally been difficult to make in large quantities, but new synthetic methodologies are emerging. Cyclic molecules are topologically distinct, which gives rise to unusual rheological properties, and also presents a challenge for theory. They have no ends or joints, and so any surface segregation mechanism would be distinct from that for linear or branched molecules. Indeed, linear response theory [21] predicts that in blends of cyclics and infinitely long linear hosts, the surface composition is exactly twice that in the bulk due to differences in conformational entropy of purely topological origin. The synthesis of large molecular weight cyclic polymers [32] provides opportunities of testing the surface enrichment in cyclic/linear blends. Wang performed NR experiments on molecular weight symmetric cyclic/linear PS blends with relatively high molecular weight ( $M_w \approx 37$  kg/mol) [32, 62]. The depth profile indicated an approximately 80% increase of the surface composition above that in the bulk. However, the linear response

theory assumption of infinite linear length does not correspond to the actual molecular weight in experiments. I apply SCFT here to examine the theoretical prediction of the enrichment of cyclics in blends with finite length linear chains.

### **2.1.2 Theory and simulation of surface segregation in polymer blends**

The theoretical treatment of surface segregation in polymer blends in general is a broad area, and follows the theory of inhomogeneous polymer systems that describes composition variations resulting from entropic and enthalpic driving forces. As such, the self-consistent field theory (SCFT) for inhomogeneous polymer systems introduced by Helfand and Tagami [23–26], treating the polymer as a coarse-grained Gaussian chain in a self-consistent potential, was a key development, and one that has provided the most widely used framework for understanding polymer surface segregation. As I will discuss SCFT more extensively in the following chapter, I highlight here the theoretical and simulations studies most directly related to surface segregation in nonlinear polymer blends. In particular, I will review the coarse-grained SCFT-based theories related to long-chain branched architectures and short-chain branched architectures (often characterized by the related property of chain stiffness), atomic-scale theories of these systems based on liquid-state theory, and molecular simulations.

Wu and Fredrickson [21] solved the SCFT for blends of linear and nonlinear polymers analytically within a linear response approximation, and in the limit of incompressibility. The analytical solution allowed the interpretation of the entropic driving force for surface segregation, due to gradients in the conformational entropy, as producing effective surface potentials for ends and branch points. It concluded that for branched/linear blends in the absence of enthalpic effects, chain ends (on both linear and branched molecules) are attracted and joints of branched arms are repelled from the surface. Branched molecules can segregate to the surface when mixing with linear molecules of the same or larger degree of polymerization. If the linear chain is much shorter, it is still possible that the linear chain segregates to the surface because of the entropic preference for short molecules at

the surface. While these analytical results are conceptually useful, they are limited by the range of validity of the linear response and incompressibility approximations. As mentioned above, Yang’s NR study of segregation in 6-pom/linear blends [20] were not consistent with the linear response description in terms of surface potentials only, and suggested a more complete SCFT study is needed.

Minnikanti and Archer modified the linear response theory by introducing energetic factors such as the monomer-monomer interaction into the response function [63]. The modified theory was developed to improve the connection between the theoretical prediction of surface segregation and experiments. The deuteration effect on surface enrichment of polymer blends was modeled and compared with the lattice-SCFT. The SCFT results on star/linear polymer blends supports the experimental conclusions that the existence of isotopic ends on linear species can cause the linear components to be enriched at the surface. Minnikanti *et al.* [64] applied the lattice-SCFT to study the surface tension of a branched polymer. Calculations showed that in the limit of a high degree of polymerization, the surface tension of a polymer is a linear function of the reciprocal of the degree of polymerization. The slope of the surface tension vs. inverse molecular weight contained contributions from ends and joints to the surface segregation.

Hariharan *et al.* [44] developed an SCFT to investigate the effect of polymer molecular weight and surface free energy on the surface enrichment in homogeneous linear polymer blends. The shorter species segregated to the surface entropically in short chain/long chain blends. The integrated surface excess of the short chain peaked at compositions greater than  $\phi = 0.5$  and also depended on the ratio of the molecular weight  $N_{\text{short}}/N_{\text{long}}$ . In symmetric molecular weight blends, species with lower absorption energy was shown to be surface enriched [45]. A ground state analytical solution of SCFT for the polymer adsorption on a hard surface was given by Ploehn *et al.* [65] as a comparison with SCFT by Scheutjens and Fleers for polymer adsorption on the surface [66, 67]. The adsorption of a polymer within SCFT at the surface was analogous to surface segregation problems of a polymer blend by

controlling the adsorption free energy and the solubility of polymers in the solvent. The adsorbed polymer density profile was shown to decay exponentially with increasing distance from the surface. Later, van der Linden *et al.* [68] showed an exponential decay length of the density profile to be less than  $3R_g$  for long chain adsorption at a high adsorption preference. Stratouras [69] derived the analytical density profiles of a Gaussian ring interacting with an attractive surface. The adsorption of a ring was found to be more affected by the surface than a linear chain due to their compact architecture. The linear response theory [21] also predicted that the entropic preference of a cyclic structure could cause surface segregation for dilute additives in a pure melt. For a dilute short cyclic and long linear polymer blend, the surface density of ring monomers is predicted to be double the bulk density purely as a consequence of the topology of the ring.

The monomer stiffness of components in binary blends has been addressed as an important factor causing surface segregation. These theories were taken to be models of chains with varying stiffness resulting from different degrees of short-chain branching. Possible explanations showed contradicting conclusions depending on different molecular models and surface potentials. Fredrickson [70] derived the free energy profile of binary polymer blends with a hard surface using density functional theory. The contribution of the surface free energy was assumed to originate from within a range on the order of  $R_g$  from the surface. They indicated that the more flexible species (i.e., molecules with shorter statistical length) had a stronger preference for the surface. The analytical SCFT on incompressible polymer blends by Wu *et al.* also concluded that the flexibility of chains played an important role in surface segregation [71]. Within a Gaussian chain model, the more flexible component segregated to the surface.

Research on the surface enrichment of copolymer and polyolefin blends by Donley *et al.* [72, 73] showed that the athermal blends had no segregation or weak segregation for flexible polymers due to the cancellation between the packing and configurational effect. However, attractive interactions within polyolefin blends led to a significant preference for

the surface enrichment of the more flexible components. The mixing free energy had a trivial effect on the surface segregation of polyolefins. However, an opposite result was obtained by Carignano and Szleifer [74] using SCFT for surface segregation in strongly stretched diblock copolymer and homopolymer blends. The stiffer component was found to segregate to the surface in the stiff/flexible mixtures while segregation in diblock copolymers was attributed to packing entropy effects where the block with short segments preferred to segregate. Regarding this contradiction, Donley and coworkers argued that the enrichment occurred in weakly stretched copolymers and even when the packing efficiency was weak [73].

Walton and Mayes applied the lattice-SCFT to study entropic effects on surface segregation in blends of linear polymers and polymers with side branches [28]. The dependence on chain architecture, molecular weight, and number of branches were considered in their effect on the degree of the surface segregation. They concluded that with no enthalpic interactions between the polymers and walls, the conformational entropy can cause branched species to segregate to the surface more than linear molecules. This prediction is in an agreement with the linear response theory by Wu *et al.* [21] The number of branched ends enhanced the surface segregation as all side chains can behave similarly as unconnected shorter linear chains.

Recently, theories on polymers with nonlinear architectures have gained interest as experiments progressed. Qian *et al.* [75] focused on the surface tension of star, comb and highly branched dendrimer architectures in a linear polymer host using lattice-SCFT. The lattice-SCFT considered the entropic effects in athermal blends. All these non-linear architectures exhibit surface enrichment due to the entropic driving forces to the chain ends. Star polymers with more branches showed stronger surface segregation, which agreed with the linear response theory. When the number of arms and the polymerization degree of the branched polymer were fixed, increasing the length of outside branches could result in stronger surface segregation. Generally, the star architecture exhibited the strongest surface segregation compared to asymmetric stars, dendrimers and combs.

Overall, SCFT has been widely used to study surface and interface composition and chain conformations of linear polymer blends, as well as several preliminary studies on nonlinear or copolymer structures. The most recent progress in surface segregation of well-defined nonlinear polymers should be systematically and directly compared with these theories. The SCFT is nonetheless a coarse-grained theory, and the applicability is limited by the Gaussian molecular model. For non-Gaussian conformations, such as in small branches or molecules, liquid-state theories allow capturing non-Gaussian effects such as packing. I turn now to some key liquid-state theory studies on polymer surface segregation.

The wall-PRISM theory was developed to study the properties of polymer melts and blends near the surface driven by entropy including packing and configurational contributions [76–78]. As such, wall-PRISM theory provides good predictions by accounting for monomer level correlations and packing effects for molecules near the surface. Yethiraj [78] studied the surface density profile of star and linear symmetric blends using wall-PRISM and found that the packing efficiency for linear chains caused a preference for linear chains at the immediate vicinity of the surface. This packing effect was missing in SCFT. At long distances from the surface, the conformational entropy was the dominating factor for segregation, creating for instance an enriched regime of star polymers with depth on the order of  $R_g$  from the wall. The total surface excess increased strongly with increasing the number or the length of arms. However, for a highly dense short-arm star, a negative surface segregation of the star molecule was obtained due to the competition between packing and configurational entropy.

The wall-PRISM-Monte Carlo hybrid simulations [76, 77] showed that the local stiffness (controlled by the bending energy of the coarse-grained bond) could affect surface segregation in polymer blends. The stiffer chain was found to partition to the surface at high concentration independent of the molecular weight, which was mainly because of better packing at the surface. At low concentration, the flexible chain was favored at the surface but the stiffer species was still found in the vicinity of the surface. Increasing the disparity of the stiffness could increase the segregation of the stiffer polymer, but the PRISM theory became

less accurate compared to molecular simulation for very large stiffness disparity due to the neglect of local conformational change at the surface.

Nath *et al.* [79] studied the density distribution of linear polymer melts near the surface by comparing a modified SCFT and wall-PRISM calculations. The comparison provided a bridge between PRISM and SCFT, and showed comparable results between the two theories. The density profile in contact with a hard wall by SCFT showed no segregation while the modified SCFT incorporating density functional theory produced a damped density profile by setting a wall contact number within the SCFT equations.

Finally, direct Monte Carlo simulation is a useful tool to study the surface properties of polymers near the surface. Cifra *et al.* [80] used lattice-Monte Carlo simulations on homogeneous linear polymer melts and found that the density distributions of the end monomers was enriched at the free surface and the wall. This agrees with SCFT predictions. Monte Carlo simulations for miscible binary linear polymer blend by Cifra and coworkers [81, 82] also indicated that lowering the surface interaction energy of one of the components (i.e., adjusting the surface preference of the components) can cause surface segregation of the corresponding species.

Yethiraj [83] investigated branched and linear polymer blends using Monte Carlo simulations. The molecules consisted of hard-sphere beads confined between two parallel walls. There were also wall-polymer attractions and polymer-polymer attractions. The Monte Carlo simulations indicated that in an attractive polymer blend, the branched species was preferred rather than the linear chain at the wall. This work explained the surface segregation of polymer blends in terms of enthalpic effects such as polymer-polymer interactions and polymer-surface interactions. However, the simulations also indicated that the surface enrichment of the branched species could exist because of the polymer-polymer attraction. The linear molecules were shown to segregate to the surface in the absence of the intermolecular attraction.

In summary, the coarse-grained SCFT has produced a consistent understanding of the larger-scale driving forces for surface segregation that can account for enthalpic and entropic driving forces that to a large degree can be understood in terms of surface potentials for end and branched groups. As the branching becomes shorter and monomer scale effects such as packing or stiffness become important, liquid-state theories reveal new mechanisms for surface segregation. Monte Carlo simulation has provided results which are in qualitative agreement with both coarse-grained and atomic scale theories. However, the existing theories have limitations related to approximations invoked, such as incompressibility, linear response or Gaussian chain conformations. One important limit where non-Gaussian chain conformations are relevant to nonlinear molecules is the situation of swelling due to steric crowding, particularly for highly branched molecules. I discuss chain conformations and swelling in the section below.

## **2.2 Bulk conformations and thermodynamics of polymer solutions, melt and blends**

The conformation within a polymer molecule can be strongly influenced by enthalpic interactions, steric repulsions and conformational entropy. In particular, for a large number of arms emanating from a branch point, or for branch points in close proximity, crowding can lead to stretching of arms near the branch points, which swells the molecule. The conformation of a single molecule can influence how it interacts with surrounding molecules. These intramolecular correlations influence interpenetration and miscibility in blends, but can also be expected to influence entanglements and chain dynamics. The theoretical and experimental studies on the bulk thermodynamic properties of nonlinear polymeric systems are reviewed in this section.

### **2.2.1 Scaling analysis of self-avoiding walk in polymer solutions**

In semi-dilute polymer solutions in good solvent, the polymer conformations undergo a crossover from self-avoiding walk (SAW) to random walk statistics at a length scale corre-

sponding to the blob (mesh) size  $\xi$  [22, 84, 85]. In the Daoud and Cotton [86] model for star polymers, the blob size  $\xi(r)$  increases with increasing distance from the core to the outside, up to the concentration blob size when the internal concentration matches the solution concentration.

Daoud *et al.* [84] characterized the crossover of linear polymer semi-dilute solutions using SANS and concluded that at  $r < \xi$  the SAW was dependent on the excluded volume, and at larger distances,  $\xi < r < R_g$  the Gaussian random walk dominated. The scaling law of density distribution as a function of distance, within a linear chain is approximately

$$\rho(r) \cong r^\alpha \quad (2.3)$$

where  $\alpha = -1$  is the ideal chain exponent that the polymers are random walking without intermolecular correlation. For swelling chains,  $\alpha = -\frac{4}{3}$ , and it obeys the self-avoiding walk. The scaling relationship between  $R_g$  and polymerization degree  $N$  for a Gaussian chain is  $R_g \sim \sqrt{N}$ , while for the swollen chain it is  $R_g \sim N^{0.6}$ .

In a semi-dilute solution, the monomers are screened by intermolecular interactions [87]. The screened regime relates to the correlation length (screening length) depends on the bulk density  $\rho_b$  and the excluded volume  $v$ .

$$\xi_E = \frac{b}{\sqrt{12v\rho_b}} \quad (2.4)$$

De Gennes [22] comments that the Edwards correlation length does not reveal the correct scaling law for polymer solutions with finite concentrations. The screening length of a real chain satisfies

$$\xi_{\text{real}} \cong (\rho_b)^{-3/4} v^{-1/4} b, \quad (2.5)$$

where  $b$  is the segment statistical length. Within the length scale of  $\xi$ , monomers obeys self-avoiding walk, beyond the length scale of  $\xi$ , the intermolecular correlations screen the self-avoiding walk so that the chain is Gaussian.

### 2.2.2 Experiments on bulk conformations and thermodynamics of polymers

The characterization of polymer conformations in homogeneous polymer solutions, melts and blends has been widely studied using scattering techniques, such as Small Angle Neutron Scattering (SANS) [88–92]. A brief illustration of a neutron beam with wavelength  $\lambda$  scattered by particles is represented in Figure 2.3:

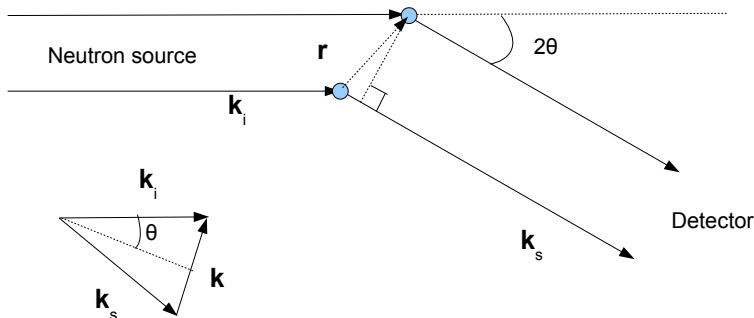


Figure 2.3: Scattered neutron beams from two particles of the sample.

The scattering wavevector  $\mathbf{k}$  (or  $\mathbf{q}$ ) is defined as

$$\mathbf{k} = \mathbf{k}_i - \mathbf{k}_s, \quad (2.6)$$

and it can be obtained by Equation 2.1.

Screening in dilute and semi-dilute polystyrene solutions was studied by Wendt *et al.* [93]. The dependence of screening length on the molecular weight was determined by SANS data and compared with scaling theory, which gave a relationship,  $\xi \sim N^{0.6}$ , where  $N$  is the degree of polymerization. Boothroyd *et al.* [90] studied the bulk conformation of star-shaped polyethylene polymers. In a  $\theta$ -solution the star molecules were still swollen. The swelling was enhanced with increasing the number of arms but was not enhanced with increasing arm length.

Richter *et al.* [94] used Low Angle Laser Light Scattering and SANS to measure the intramolecular correlations of star-shaped polybutadiene (PB) in a dilute solution ( $\phi < 0.5\%$ ). The polymers had varying length of arms from 100 monomers to 700. The molecular size was estimated by a power function of the concentration and given as  $R_g \sim \rho^{-1/8}$ . The structure factor obtained by SANS indicated that the star solutions behaved as a liquid near the overlap concentration but stars with many arms behaved as a solid.

The miscibility of a homogeneous polymer blend is given as a mean-field approximation for the mixing free energy within Flory-Huggins theory:

$$\frac{\Delta G}{kT} = \frac{\phi_1}{N_1} \ln \phi_1 + \frac{\phi_2}{N_2} \ln \phi_2 + \chi_{\text{FH}} \phi_1 \phi_2, \quad (2.7)$$

where  $\Delta G$  is the mixing free energy in a constant total volume.  $\phi_i$  and  $N_i$  are the volume fraction and the number of monomers of  $i$  and  $\chi_{\text{FH}}$  is the Flory-Huggins segment-segment exchange interaction parameter. By assuming the interaction free energy,  $\chi_{\text{FH}} \phi_1 \phi_2$ , is parabolic in  $\phi$ ,  $\chi_{\text{FH}}$ , a measure of the polymer miscibility, is independent of composition. An empirical linear function of  $\chi_{\text{FH}}$  versus the temperature  $T$  is written as

$$\chi_{\text{FH}} = a + \frac{b}{T}, \quad (2.8)$$

where the coefficients  $a$  and  $b$  can be fit using experimental  $\chi_{\text{FH}}$  at different temperatures.

Experimentally, the miscibility of polymer blends is often studied using neutron scattering and interpreted using the random phase approximation (RPA) [22]. For long-chain polymers of varying architectures, coarse-grained descriptions of the conformations have been successfully utilized to study both surface and bulk properties. In particular, the model of conformations as a Gaussian chain is useful. The RPA theory gives

$$\frac{1}{S(k)} = \frac{1}{N_1 \phi_1 S_1(k)} + \frac{1}{N_2 \phi_2 S_2(k)} - 2\chi_{\text{FH}}. \quad (2.9)$$

In RPA theory, the structure factor  $S_i(k)$  of component  $i$  is often considered as a Gaussian single chain structure factor.  $S(k)$  is the total structure factor of the blends which can be measured by scattering techniques.

The isotopic groups were found to cause weak inhomogeneity of polymer melts. Warner *et al.* [95] and Bates *et al.* [96–98] performed SANS experiments on deuterated (dPB) and hydrogenous polybutadiene (hPB) blends to show evidence for the isotopic effect in blends. Several mixtures of dPB/hPB blends were found to be unstable at low temperature due to isotopic substitution. For those blends, the RPA equation for homogeneous blend failed to fit the SANS spectra. Additionally, increasing the molecular weight of each component also caused phase separation. The labeling induced inhomogeneity was studied by Graessley *et al.* [99] as well and an estimation of the interaction parameter in hydrogenous binary blends was suggested to average the results of labeling one species and then switching the labeled species. In SANS experiments focusing on the architecturally induced bulk thermodynamics, such as linear and nonlinear polymer blends, the isotope effect is removed by characterizing  $\chi_{FH}$  in a linear polymer melt with partially deuterated analogs [19].

The asymmetry of segment length in affecting the mixing entropy was not included in the mean-field Flory-Huggins mixing free energy. However, Bates and coworkers [100] measured binary polymer blends with asymmetric statistical segment length by SANS and showed a dependence between the interaction parameter  $\chi_{FH}$  and segment length. They concluded that the difference between the segment lengths of two species correlated positively with the interaction parameter. The conclusion that increasing difference of segment lengths could increase  $\chi_{FH}$  was supported later by Krishnamoorti *et al.* [101] in SANS experiments on both randomly and regularly branched polymer blends. Gaussian field theory [38] for entropic contributions of excess free energy of mixing takes account of the dissimilarity of different monomer volumes, and is able to consider the difference between segment length of the components.

Experiments also found that the interaction parameter  $\chi_{FH}$  is dependent on composition, rather than being a composition independent parameter according to Flory-Huggins theory. Londono *et al.* [102] studied the interaction of mixing in isotopically labeled polymer melts. The non-isotopic polymer molecules, such as poly(vinyl ethylene)(PVE), poly(ethyl

ethylene)(PEE) and polystyrene (PS) exhibited notable interaction parameters when mixing with the same polymers with deuterated groups.  $\chi_{FH}$  obtained by the RPA equation is maximized for equal mixtures. Bates *et al.* [103] showed that in a homogeneous diblock polymer melt,  $\chi_{FH}$  obtained by SANS was different depending on the compositions of components. Londono *et al.* [102] also reported a minimum  $\chi_{FH}$  for polyethylene isotope blends at  $\phi = 0.5$  but a maximum value for polystyrene isotope blends at  $\phi = 0.5$ .

Russell *et al.* [104] evaluated the binary PS blend composed of 4-star and linear architectures. The RPA equation using Gaussian model structure factors can fit the SANS data well.  $\chi_{FH}$  in dPS/PVME (poly(vinyl methylether) blend varied with composition and decreased linearly with increasing temperatures. Hammouda *et al.* [91] also studied the temperature dependence of the scattering intensity for PS/PVME blends and found that increasing temperature did not always increase the scattering intensity at low  $k$ . At high  $k$ , the scattering density was independent of the temperature. In the following publication by Hammouda and coworkers [105], the measurement of the interaction parameters in pressurized dPE/hPVME blends was carried out using SANS. Their results indicated that by increasing pressure the scattering intensity at  $q=0$  could decrease. The interaction parameters depended weakly on pressure.

Brereton *et al.* [106] performed SANS experiment on a series of binary blends. The RPA estimate showed that the molecular weight of polymers influences the measured interaction parameter. The Zimm plot of the SANS data (i.e.,  $1/S(k)$  vs.  $k^2$ ) often produced a constant slope as a function of the molecular size at different temperatures. The calculation also showed an anomalous temperature dependence in Polytetramethyl Carbonate (PTMC)/dPS blends, because the Zimm plots depicted largely varying slopes which indicated rapid changes in molecular size when heating the blend. Brereton also suggested that  $\chi_{FH}$  might be spatially dependent. Cabral *et al.* [107] investigated the same blends containing PTMC and deuterated PS recently. The SANS data did not have inconsistent slopes in the Zimm plot as found by Brereton [106] after undergoing heat treatments such as quenching or annealing. The

author suggested that the anomalous behavior seen by Brereton could be accounted for by incomplete equilibration. In addition, the PTMC/dPS blends exhibited phase separation with strong  $\chi_{FH}$  values but no evidence of spatial dependence at all.

For polymers with nonlinear architectures, an understanding of the bulk thermodynamics is important to avoid bulk phase separation. Alamo *et al.* [108,109] and Agamalian *et al.* [110] highlighted the branching effect on the miscibility of binary polymer blends containing short branched polymers. They indicated that the blends could be stable as a melt if the number of branches was low but an increasing number of branches on the backbone could cause phase separation from a homogeneous melt. Chen *et al.* [111] characterized mixtures of high molecular weight ( $M_w \sim \mathcal{O}(10^5)$  g/mol) linear PE and different comb-branched PB. Single phase blends were possible for low molecular weight combs ( $M_w \sim \mathcal{O}(10^4)$  g/mol). However, when the combs had similar or higher molecular weight compared to linear PE, a separated phase was found in the blend. SANS on star/linear blends by Martter *et al.* [39] also found increasing the concentration of stars could decrease  $\chi_{FH}$ .

Greenberg *et al.* [112] studied the interaction parameters in  $f$ -star/linear PS blends using SANS.  $\chi_{FH}$  was estimated using RPA and compared with Gaussian field theory [38]. The experimental  $\chi_{FH}$  for star/linear blends did not agree with the theoretical prediction. Compared among various star-shaped polymers with the styrene monomer, the interaction parameters of comb/linear blends were found to be stronger than  $f$ -star/linear blends. Martter *et al.* [39] later characterized star and linear PB blends using SANS. The contributions of the functionality and the molecular weight of arms to  $\chi_{FH}$  were studied by RPA theory.  $\chi_{FH}$  was larger in samples with higher number of arms while it did not vary monotonically with increasing functionality when the total molecular weight is fixed. In particular, a 12-star/linear blend exhibits a greater  $\chi_{FH}$  than the 4-star/linear blend but blends containing 6-star or 8-star exhibit a smaller  $\chi_{FH}$  than in blends containing 12-star or 4-star. However, increasing the length of arms could increase  $\chi_{FH}$ . In addition, their experiments also showed that increasing the linear molecular weight caused an increasing  $\chi_{FH}$  that could not be pre-

dicted by Gaussian field theory. It can be potentially be compared with predictions by the two-chain SCFT I develop in this thesis.

Recently, Lee *et al.* [19] characterized a series of end-branched PS with symmetric architectures in blends with linear PS by focusing on how branch points and ends affect the interaction parameters. The interaction parameters determined by the RPA equation increased with increasing number of branch points if the total number of ends were fixed. A comparison of blends with fixed branch points and increasing number ends indicated that the magnitude of  $\chi_{\text{FH}}$  increased as well and agreed qualitatively with Gaussian field theory. Particularly,  $\chi_{\text{FH}}$  increases rapidly from increasing the branched polymer from 9 branches to 13 branches. However, their results showed that the Gaussian field theory is not in agreement for predicting  $\chi_{\text{FH}}$  for branched/linear blends for fixed number of ends but varying functionality. Lee showed that for a series of molecules with six total ends,  $\chi_{\text{FH}}$  decreases as the number of branch groups increases from 6-star (one joint) to a 6-end (one joint and three branch points). However, Gaussian field theory predicts a reverse trend, which implies that the theory is limited by assuming Gaussian structure factors for swollen molecules in the blends. Both experiments and Gaussian field theory showed qualitatively consistent orders of magnitude for  $\chi_{\text{FH}}$  values and indicate stable single-phase mixtures.

In general, SANS experiments on bulk thermodynamics of branched/linear blends with identical monomers have shown good bulk miscibility, supporting their possible use for bulk property modification applications. However, the Gaussian field theory did not produce trends of the interaction parameter  $\chi_{\text{FH}}$  that are consistent with SANS. An important reason is neglecting the swelling effect on the bulk chain conformations. A new SCFT is developed for capturing the swelling and stretching in highly crowded branched polymers. This method provides a new way to calculate the interaction parameter  $\chi$  with real chain conformations, as a comparison with Gaussian field and mean-field theory.

### 2.2.3 Theories of bulk conformations and thermodynamics of nonlinear polymer melts and mixtures

In spite of the Flory-Huggins theory and the random phase approximation, theories to understand the conformation of polymer melts and blends have been widely developed in the past decades. In SCFT [22–26, 29], the Gaussian model is extended to account for the influence of surrounding chains by a self-consistent mean-field. Although SCFT has enjoyed wide success in explaining the compositional distributions of a wide variety of inhomogeneous polymer systems, one drawback of conventional SCFT is that correlations between monomers are only accounted for by this mean-field. One-chain SCFT has been successfully applied for polymer melts and blends to capture surface effects [30, 31, 71, 113]. However, the translational symmetry always results in a uniform bulk density if the test chain is in the bulk, without capturing any intra- or intermolecular correlations describing the chain conformations. For highly crowded branched polymers, the correlations become more significant, and it is desirable to extend conventional SCFT to account for such correlations, even in homogeneous systems. The way to allow the averaged field is to break the translational symmetry by fixing the test molecule. For instance, Wolterink *et al.* [114, 115] modeled a star-shaped polyelectrolyte using numerical SCFT with Scheutjens-Fleer algorithm [66]. Their study focused on the role of the ionic interactions and the branched functionality to enhance the swelling of single polyelectrolyte conformation. To study the bulk conformations of polymer melts and blends, a complete two-chain SCFT algorithm is developed with two test chains. One chain has a fixed monomer at the origin, leaving the other chain freely moving.

A well-developed method in the study of polymeric bulk properties is the polymer reference interaction site model (PRISM) theory and the self-consistent PRISM [116–127]. The PRISM theory calculates the intermolecular correlation function from a known intramolecular distribution function. For linear polymers, the size of molecules was found to decrease with increasing monomer density [123]. Curro *et al.* [121] applied PRISM to study the inter-

molecular correlations of polyolefin blends containing short side-branches modeled by specific sites different from backbones. PRISM results indicated that the backbone monomers were screened because of the crowding of monomers on side branches. This side-branch packing effect increased with the size of side-branches. The structure factor of the blends exhibited a low-angle peak in the low  $q$  regime which was not present in a polyethylene linear melt. This peak could shift to lower  $q$  regime as the size of branches increase.

Grayce *et al.* [125] performed PRISM calculations on star polymers to model the swelling in solution and melt. The stretching of arms was found near the branch point because of the long-range excluded volume effect crowding around the core region. Because of the swelling, the radius of gyration of the stars decreases as the monomer density increases. Patil *et al.* [128] studied star and comb polymer melts with the PRISM theory. The results indicated that swelling was enhanced when increasing the number of arms or branches. For a comb with a small number of long branches, the intermolecular correlation function showed that the monomer packing behaved similar to a linear structure with the same degree of polymerization as the backbone. However, the intermolecular correlation function of a highly branched comb with short branches was found to be significantly different from that of a linear chain. The swelling in such a comb molecule was more enhanced than a linear chain and was qualitatively similar to the conformation in star melts. The PRISM calculations have successfully revealed the stretching of the branched polymers that differs from that of the linear chains, while the non-Gaussian single chain structure factor input to PRISM may require a large amount of calculations by Monte Carlo simulations.

Fredrickson *et al.* [38] developed the Gaussian field theory to estimate the entropic mixing free energy and thermodynamic interaction parameters of polymer binary blends. The theory assumes density is fixed and that the bulk molecular structure factor is Gaussian. As discussed previously, predictions of  $\chi_{FH}$  for blends of star, branched and linear molecules in Gaussian field theory have shown inconsistent agreement with SANS experiments [19,39,112]. Comparisons between the Gaussian field theory and two-chain SCFT are performed for end-

branched/linear blends in this thesis to study the interaction parameters in different assumptions. In principle, the two-chain SCFT and Gaussian field theory both model the polymer blends as chains in an external field. In Gaussian field theory, the polymer holds the ideal chain random walk conformation, and the fluctuations in the field are assumed to be a continuous Gaussian distribution. In two-chain SCFT, the free energy is approximated by the saddle point maximum. The swelling and stretching of the polymer are included, and thus the non-ideal conformations can be modeled using the two-chain SCFT in this thesis.

In addition to theoretical understanding of the bulk thermodynamics of nonlinear polymers, molecular simulations were carried out for individual nonlinear polymers showed SAW bulk conformations consistent with scaling theory. Grest *et al.* [35] performed molecular dynamics for a dilute solution of coarse-grained stars with different arms. The conformation of the star polymer is shown to be SAW and agreed with scaling theory. Murat and Grest [129] later studied the dendrimer structures and reported that the size of a dendrimer is  $R_g \sim N^{1/3}$  for a highly compact conformation. Rouault *et al.* [130] used bond fluctuation model (BFM) [131–133] Monte Carlo simulation to simulate comb-branched polymers in good solvent, measuring correlations in the orientation of the backbone as well as the molecule size. They observed that the conformations of highly branched combs strongly depend on the length of the side branches and the spacing between neighboring branches. A BFM simulation of star polymers in a good solvent by Cecca *et al.* [134] also showed that the intramolecular density distribution corresponds to SAW statistics to the arms. Yethiraj [135] studied a single highly branched molecule by Monte Carlo simulation using a molecular model consisting of hard sphere monomers connected by semi-flexible bonds. The conformations of the backbone and branches are both nearly self-avoiding. The persistence length of a side chain is found to be greater than that of an isolated chain with the same number of beads while it is insensitive to the length and stiffness of the backbone. The crowding on branches increases the branch persistence length but the crowding effect became weak if the monomers on branches or the backbone are stiffer. The crowding of branches also affects the confor-

mation of the backbone. The author concluded that increasing the number or the length of branches without changing the backbone length would increase the stiffness of backbone significantly, but increasing branch stiffness does not always increase the backbone stiffness. The limitation of using atomic level molecular simulations to study the bulk polymer conformations is that the simulation of a large system containing many chains requires extensive computing resources. Theories are more efficient in understanding general concepts of the swelling of branched topologies and comparing to scaling theory and experiments.

## CHAPTER 3

### SELF-CONSISTENT FIELD THEORY (SCFT)

Over the past few decades, SCFT has been a successful approach for determining polymer bulk and surface properties [21–31, 34, 66, 87]. A typical SCFT assumes that the conformations of any molecule in the system can be equivalent to those of a specific chain feeling an external potential from other polymer chains. The test chain satisfies Gaussian statistics in an averaged or mean chemical potential field. When approximating the free energy as a quadratic function of the density (for instance for small perturbations about an equilibrium density), this mean-field is taken to be proportional to the averaged total density. Figure 3.1 shows a brief illustration of the self-consistent field approximation of polymers near a polymer/air surface and a polymer/substrate interface. A neutral hard substrate is represented by a wall with infinite potential at which the density goes to zero. While a more exact treatment of the free (air) surface would involve a non-quadratic free energy, a simplistic approximation is to require the density to go to zero at a specified distance—in effect using a hard wall to mimic the effect of a free air surface. Any attractive or repulsive interactions in the case of an actual solid substrate can be included with an additional potential.

SCFT has been widely applied to various types of polymers including polymer brushes, block copolymers and polymer blends. In recent years, however, researchers have become interested in polymeric systems containing a wide variety of polymer architectures. For instance, Wu *et al.* [21] developed a linear response theory using self-consistent field theory solutions to describe the surface composition change of branched or cyclic polymer additives with linear molecules. The lattice-SCFT algorithm has been applied to study the conformation of star-shaped colloid particles [114, 115, 136] and combs [137–139] in dilute polyelectrolyte solutions. Qian *et al.* [75] studied the surface segregation and surface free energies of binary blends containing linear and highly branched molecules using lattice-SCFT.

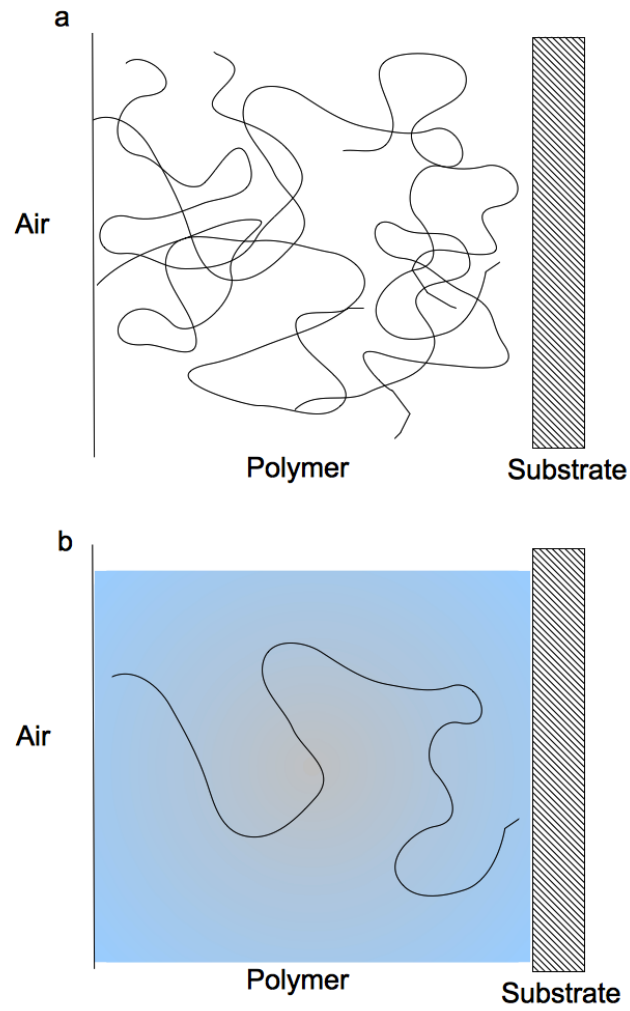


Figure 3.1: (a) An illustration of a polymer melt near a wall. (b) The self-consistent field approximation for a system of many chains near a wall. The test molecule feels an external field (the filled area) by averaging the densities of all the other molecules.

Entropic and steric effects cause surface enrichment phenomena when mixing different polymer architectures. Such phenomena can be captured by conventional SCFT and compared with experimental results. This chapter presents the derivation of the conventional self-consistent field theory using a Gaussian chain polymer model and linear response theory for the study of nonlinear architectures.

### 3.1 SCFT for nonlinear/linear polymer blends near surfaces

The analytical development of self-consistent field theory to study polymer conformation originates from the single chain problem given by Edwards and coworkers [34, 87, 140]. Helfand *et al.* [23–26] extended the SCFT to treat inhomogeneous polymer systems. In these coarse-grained models, the ideal chain conformations undergo a Gaussian random walk and are described by the Wiener distribution

$$\begin{aligned}
 P(\mathbf{r}_\alpha) &\propto \exp [H_0[\mathbf{r}_\alpha]] \\
 &\propto \exp \left[ -\frac{3}{2b^2} \int_0^N dt \left| \frac{d\mathbf{r}_\alpha(t)}{dt} \right|^2 \right],
 \end{aligned}
 \tag{3.1}$$

where  $\mathbf{r}_\alpha(t)$  is the position of monomer index  $t$  on chain  $\alpha$ , and  $N$  is the total number of monomer segments. The unit of energy is taken to be  $kT$  and  $b$  is the Gaussian step length.

The concept of the Gaussian step length  $b$  and its use for comparison with experiment deserve some comment. A mathematically exact infinite Gaussian random walk is a fractal, and has no intrinsic length scale. In this case, the choice of  $b$  is an arbitrary length scale. In other words, we could “zoom” in by a factor  $\lambda$  and the polymer would visually look the same. This is also apparent in the mathematical description of the Wiener distribution, where we could have a change of variable from  $b$  to  $b/\lambda$ , where  $\lambda$  rescales our length scale. To preserve the distribution, we would then also rescale  $t$  to  $\lambda^2 t$ , and  $N$  to  $\lambda^2 N$ . Note that for a finite Gaussian random walk, the only length scale is the size of the polymer,  $\sim \sqrt{N}b$ , which is invariant to scale transformation. Since the SCFT models polymer conformations by a finite Gaussian random walk, within the SCFT, the choice of  $b$  is indeed arbitrary as long as the other parameters are rescaled accordingly. Thus in this thesis, length scales are

typically non-dimensionalized in units of  $b$ .

A real polymer chain, however, is not Gaussian at the monomer scale, but on a longer length scale, the chain conformation approaches a Gaussian random walk. This justifies the use of a Gaussian random walk to model a polymer chain on a coarse-grained level. There is then the question of which value of  $b$  to choose. The most common convention, and the one I primarily adopt in this thesis when choosing numerical values, is to pick  $b$  to correspond to a “monomer” or a chemical repeat unit. This is convenient when working with theories that use the concept of a “monomer” and its properties, such as the volume. With the definition and thus number of monomers chosen,  $b$  can then be assigned to be the “Kuhn length” or “statistical segment length”, which is the bond length of a freely jointed chain consisting of the same number of monomers that gives the same end-to-end distance as the real molecule. (For instance, for polystyrene, the statistical segment length is  $\sim 6 - 7\text{\AA}$ , depending on conditions.) We should keep in mind, however, that for SCFT results, it may be convenient to leave results in units of  $b$  with the idea that we have freedom to choose a different convention for  $b$  if desired.

The monomer-monomer interaction can be modeled in terms of the excluded volume energy functional

$$\hat{W}[\mathbf{r}_\alpha(t)] = \frac{v}{2} \int d\mathbf{r} \hat{\rho}(\mathbf{r})^2, \quad (3.2)$$

where  $\hat{\rho}(\mathbf{r})$  is the microscopic density operator at point  $\mathbf{r}$  and is defined as

$$\hat{\rho}(\mathbf{r}) = \sum_{\alpha=1}^n \int_0^N dt \delta(\mathbf{r} - \mathbf{r}_\alpha(t)), \quad (3.3)$$

where  $n$  is the number of polymer chains.

The partition function in canonical ensemble is therefore written as

$$\begin{aligned} \mathcal{Z}_C &= \int \prod_{\alpha=1}^n \mathcal{D}\mathbf{r}_\alpha P(\mathbf{r}_\alpha) \exp(-\hat{W}) \\ &= \int \prod_{\alpha=1}^n \mathcal{D}\mathbf{r}_\alpha \exp \left[ -\frac{3}{2b^2} \int_0^N dt \left| \frac{d\mathbf{r}_\alpha(t)}{dt} \right|^2 \right] \times \exp \left[ \frac{-v}{2} \int d\mathbf{r} \hat{\rho}(\mathbf{r})^2 \right]. \end{aligned} \quad (3.4)$$

Given the fact that

$$\int \mathcal{D}\rho \delta[\rho - \hat{\rho}] = 1, \quad (3.5)$$

Equation 3.4 can be expressed as an integral over fields

$$\begin{aligned} \mathcal{Z}_C &= \int \mathcal{D}\rho \int \prod_{\alpha=1}^n \mathcal{D}\mathbf{r}_\alpha P(\mathbf{r}_\alpha) \exp \left[ -\frac{3}{2b^2} \int_0^N \left| \frac{d\mathbf{r}_\alpha(t)}{dt} \right|^2 \right] \delta[\rho - \hat{\rho}] \\ &\quad \times \exp \left[ \frac{-v}{2} \int d\mathbf{r} \rho(\mathbf{r})^2 \right]. \end{aligned} \quad (3.6)$$

Recalling the functional delta function identity

$$\delta[\rho - \hat{\rho}] = \int_{-i\infty}^{i\infty} \mathcal{D}\mu \exp \left[ \int d\mathbf{r} \mu(\mathbf{r}) (\rho(\mathbf{r}) - \hat{\rho}(\mathbf{r})) \right] \quad (3.7)$$

allows us to introduce the conjugate potential field  $\mu(\mathbf{r})$  by substituting Equation 3.7 and Equation 3.3 into Equation 3.6. The partition function then becomes

$$\begin{aligned} \mathcal{Z}_C &= \mathcal{Z}_0 \int \mathcal{D}\rho \mathcal{D}\mu \exp \left[ \frac{-v}{2} \int d\mathbf{r} \rho(\mathbf{r})^2 \right] \times \exp \left[ \int d\mathbf{r} \mu(\mathbf{r}) \rho(\mathbf{r}) \right] \\ &\quad \times \int \prod_{\alpha=1}^n \mathcal{D}\mathbf{r}_\alpha \exp \left[ \frac{3}{2b^2} \int_0^N dt \left| \frac{d\mathbf{r}_\alpha(t)}{dt} \right|^2 \right] \exp \left[ - \int_0^N dt \mu[\mathbf{r}_\alpha(t)] \right] \\ &= \mathcal{Z}_0 \int \mathcal{D}\rho \mathcal{D}\mu Q_0^n[\mu] \exp \left[ \frac{-v}{2} \int d\mathbf{r} \rho(\mathbf{r})^2 + \int d\mathbf{r} \mu(\mathbf{r}) \rho(\mathbf{r}) \right], \end{aligned} \quad (3.8)$$

where  $\mathcal{Z}_0 = V^n/n!$  ( $V$  is the volume of the system).  $Q_0[\mu]$  is the single chain partition function in an external field  $\mu$ . The canonical ensemble effective Hamiltonian of the polymer melt is thus

$$H_C = \frac{v}{2} \int d\mathbf{r} [\rho(\mathbf{r})^2 - \mu(\mathbf{r})\rho(\mathbf{r})] - n \ln Q_0[\mu], \quad (3.9)$$

and the canonical Helmholtz free energy functional reads

$$F_C = \frac{v}{2} \int d\mathbf{r} [\rho(\mathbf{r})^2 - \mu(\mathbf{r})\rho(\mathbf{r})] - n \ln V Q_0[\mu] + n \ln(n) - n. \quad (3.10)$$

The partition function can be written in terms of the summation of density propagators  $G(\mathbf{r}, \mathbf{r}'; t, t')$  representing the statistical weight of a monomer  $t$  at  $\mathbf{r}$  connected by the chain

to another monomer  $t$  at  $\mathbf{r}'$ ,

$$\begin{aligned}\mathcal{Z}_C &= \iint d\mathbf{r}' d\mathbf{r}'' G(\mathbf{r}', \mathbf{r}''; N, 0) \\ &= \iiint d\mathbf{r} d\mathbf{r}' d\mathbf{r}'' G^\dagger(\mathbf{r}', \mathbf{r}; N, t) G(\mathbf{r}, \mathbf{r}''; t, 0),\end{aligned}\quad (3.11)$$

where the density propagator  $G$  in terms of a Green's function is written as

$$G(\mathbf{r}, \mathbf{r}'; t, t') = \frac{\int \mathcal{D}\mathbf{r} P(\mathbf{r}) \exp(-W(\mathbf{r})) \delta(\mathbf{r}(t) - \mathbf{r}) \delta(\mathbf{r}(t') - \mathbf{r}')}{\int \mathcal{D}\mathbf{r} P(\mathbf{r}) \delta(\mathbf{r}(t) - \mathbf{r})}, \quad (3.12)$$

and similarly for  $G^\dagger$ . Simplifying the above integrals by defining weight functions:

$$q(\mathbf{r}; t) = \int d\mathbf{r}'' G(\mathbf{r}, \mathbf{r}''; t, 0) \quad (3.13)$$

and

$$q^\dagger(\mathbf{r}; t) = \int d\mathbf{r}' G^\dagger(\mathbf{r}', \mathbf{r}; N, t), \quad (3.14)$$

as the statistical weight of a chain of length  $t$  and a chain of length  $N - t$  to be found at position  $\mathbf{r}$ , respectively.  $q$  and  $q^\dagger$  satisfy the modified diffusion equation:

$$\frac{\partial q(\mathbf{r})}{\partial t} = \frac{b^2}{6} \nabla^2 q(\mathbf{r}) - \mu(\mathbf{r}) q(\mathbf{r}), \quad (3.15)$$

The polymer statistical segment length  $b$  is the step length of the Gaussian chain model. In the SCFT calculations presented here,  $b$  is used as the unit of length, e.g., to report the dimension of a molecule or the system size. The external potential,  $\mu(\mathbf{r})$ , can be estimated by using a saddle point approximation on Equation 3.8, i.e., by taking the functional derivative of Equation 3.9 with respect to  $\mu$  and  $\rho$  to be equal to zero, i.e.,

$$\frac{\partial H_C}{\partial \mu} = \frac{\partial H_C}{\partial \rho} = 0. \quad (3.16)$$

The saddle-point approximation results in a self-consistent equation for the external field  $\mu$ :

$$\mu(\mathbf{r}) = v\rho(\mathbf{r}), \quad (3.17)$$

in terms of the averaged local probability density  $\rho(\mathbf{r})$ , which can be evaluated by

$$\rho(\mathbf{r}) = \mathcal{N} \frac{\int_0^N dt q(\mathbf{r}; t) q^\dagger(\mathbf{r}; t)}{\int_0^\infty d\mathbf{r} q(\mathbf{r}; N) q^\dagger(\mathbf{r}; N)}, \quad (3.18)$$

where  $\mathcal{N}$  is a normalization constant. The integrand of the numerator is the unnormalized density distribution, which is shown briefly in Figure 3.2.

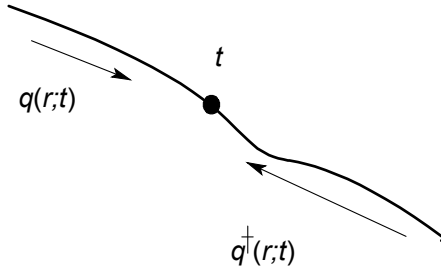


Figure 3.2: An illustration of the calculation for the unnormalized density on the  $t^{\text{th}}$  bead of a linear chain.

Equation 3.15, Equation 3.17 and Equation 3.18 are a complete set of self-consistent equations. An initial guess of  $\mu$  is required when starting the self-consistent iterations.

At the surface or interface of a polymeric system, the problem can be cast as a solution of the one-dimensional modified diffusion equation:

$$\frac{\partial q(z, t)}{\partial t} = \frac{b^2}{6} \frac{\partial^2 q(z, t)}{\partial z^2} - \mu(z) q(z, t), \quad (3.19)$$

where  $z$  is a distance normal to the surface, starting from the surface at  $z = 0$  and reaching a maximum at  $z = z_{\text{max}}$  at the other surface. The system is thus constrained between two parallel walls, with one of the walls possibly representing the condition of zero density at an air surface. The initial condition at  $t = 0$  (corresponding to monomers of length approaching zero) is the uniform distribution,  $q(z; t = 0) = 1$ , because zero-length chains feel no potential.

The generalization to blends is straightforward. In an athermal blend containing species  $A$  and  $B$ , the SCF potential is written as

$$\mu(z) = v (\rho_A(z) + \rho_B(z)). \quad (3.20)$$

The number density  $\rho_i$  of polymer of type  $i$  ( $i = A$  or  $B$ ), in units of monomers per volume, can then be written as

$$\rho_i(z) = \rho_{i_0} \frac{z_{\max} \int_0^{N_i} dt q_i(z; t) q_i^\dagger(z; t)}{N_i \int_0^{z_{\max}} dz q_i(z; N_i) q_i^\dagger(z; N_i)}, \quad (3.21)$$

where  $\rho_{i_0}$  is the bulk monomer density of species  $i$  and  $N_i$  is the degree of polymerization, and the boundary conditions satisfy  $q(z \leq 0; t) = q^\dagger(z \leq 0; t) = 0$  and  $q(z \geq L; t) = q^\dagger(z \geq L; t) = 0$ .

The density of the polymer blend goes smoothly to zero at  $z = 0$  and  $z = z_{\max}$  for compressible models (i.e., finite excluded volume parameter  $v$ ). For an incompressible polymer, the density jumps discontinuously from the bulk value to zero at the wall.

For a compressible description of polymers, the definition of the integrated surface excess used to quantify the magnitude of surface segregation needs to be generalized from that used in the incompressible blend. For the incompressible blend, the surface excess of component  $A$  is defined as

$$Z_A^* = \rho_b \int (\phi_A(z) - \phi_{A_0}) dz, \quad (3.22)$$

where the total density  $\rho_b = \rho_{A_0} + \rho_{B_0}$  is simply the bulk density.  $\phi_{A_0}$  is the bulk mole fraction of  $A$  monomers. This definition is applicable for incompressible blends because  $\rho_b$  is a constant, and the density of the component is proportional to the mole fraction, i.e.,  $\rho_A(z) = \rho_b \phi_A(z)$ . However, in compressible blends,  $\rho_A(z) \neq \rho_b \phi_A(z)$ , and the total density,  $\rho_A(z) + \rho_B(z)$  will change as a function of  $z$ . Equation 3.22 can be generalized for a compressible blend as

$$Z_A^* = \int [\rho_A(z) - \phi_{A_0}(\rho_A(z) + \rho_B(z))] dz, \quad (3.23)$$

i.e., it is the integrated excess density of  $A$  relative to that expected had the mole fraction remained constant even as the density changes. This can be simplified as

$$Z_A^* = \int [\phi_{B_0}\rho_A(z) - \phi_{A_0}\rho_B(z)]dz, \quad (3.24)$$

where  $\rho_A$  and  $\rho_B$  are the monomer densities of species  $A$  and  $B$  at  $z$ , and  $\phi_{A_0}$  and  $\phi_{B_0}$  are the bulk mole fractions of  $A$  and  $B$ , which are

$$\phi_{A_0} = \frac{\rho_{A_0}}{\rho_{A_0} + \rho_{B_0}} \quad (3.25)$$

and

$$\phi_{B_0} = \frac{\rho_{B_0}}{\rho_{A_0} + \rho_{B_0}}, \quad (3.26)$$

and  $\rho_{A_0}$  and  $\rho_{B_0}$  are the bulk densities of species  $A$  and  $B$ , respectively. The integrand of Equation 3.24,  $\phi_{B_0}\rho_A(z) - \phi_{A_0}\rho_B(z)$ , is defined as the *excess density* of  $A$  monomers in compressible blends. Note that since the densities of  $A$  and  $B$  go to zero at the boundary, the excess density must converge to zero at the boundaries as well. The compressible bulk density,  $\rho_b = \rho_{A_0} + \rho_{B_0}$ , can be estimated from the value at the plateau region of the density profiles (i.e.,  $z = 0.5z_{\max}$ ).

It can be shown that Equation 3.24 is equivalent to Equation 3.22 in the limit of incompressible blends:

$$\begin{aligned} Z_A^* &= \int \phi_{B_0}\rho_A(z) - \phi_{A_0}\rho_B(z)dz \\ &= \int \phi_{B_0}\rho_b\phi_A - \phi_{A_0}\rho_b(1 - \phi_A)dz \\ &= \rho_b \int (\phi_{A_0} + \phi_{B_0})(\phi_A - \phi_{A_0})dz \\ &= \rho_b \int (\phi_A - \phi_{A_0})dz. \end{aligned} \quad (3.27)$$

I turn now to the SCFT equations generalized for branched polymers, covering stars (end-branched and pom-poms are direct extensions), cyclic, and comb polymers below. The flowcharts for the SCFT programs for nonlinear/linear blends are given in Appendix A.

### 3.1.1 The statistical weight functions of branched polymers: example of stars

I consider the large class of branched polymers without any loops. Each monomer on this molecule is either on a linear section or a branch point. Along the linear sections, the statistical weight functions  $q(r, t)$  are propagated according to the modified diffusion Equation 3.15, just the same as for linear polymers. Because there are no loops, the direction of propagation is well-defined, and is taken to be from the outer ends to the point of interest. When a branch point is reached, the statistical weight functions are multiplied together, which is a consequence of the statistical independence of each branch in SCFT, before being propagated further along the linear section towards the point of interest. In this way, for every monomer on a linear section, there are two statistical weights,  $q$  and  $q^\dagger$ , representing the statistical weight from the two pieces that come from the two directions towards that monomer. Thus, the only new aspect of the calculation relative to the linear case is the product of statistical weights at a branch point.

As an example, for symmetric star structures with  $m$  arms, the probability density of the  $m$ -arm joint (branch point) is written as

$$q_{i;\text{joint}}(r; t_{\text{joint}})q_{i;\text{joint}}^\dagger(r; t_{\text{joint}}) = \prod_{j=1}^m q_{i;j}(r; t_{\text{joint}}), \quad (3.28)$$

where  $q_{i;\text{joint}}$  is diffusing from every end of the branch to the joint. An example for calculating the density of a 3-arm joint is given in Figure 3.3.

In this way, the density of every monomer of a branched polymer (without loops) can be calculated.

### 3.1.2 The statistical propagators of cyclic molecules

All monomers on a ring homopolymer are equivalent since the molecule has no ends. To determine the monomer density, we divide the loop into two portions from 0 to  $t$  and  $t$  to  $N$ . The cyclic topology implies that the head and end must be at the same position  $z' = z''$ .

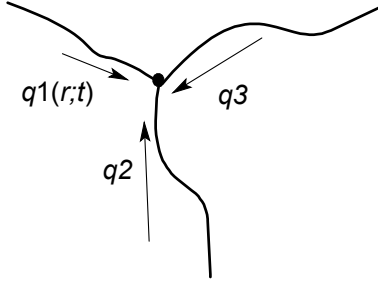


Figure 3.3: An illustration of calculating the unnormalized density at the joint of a 3-arm structure.

The partition function for a ring can therefore be written in terms of the propagators as

$$\mathcal{Z} = \iiint dz dz' dz'' G(z', z; 0, t) G^\dagger(z, z''; N, t) \delta(z' - z''), \quad (3.29)$$

where the delta function controls the closure of the loop. (Note I have formally kept two propagators  $G$  and  $G^\dagger$  in my notation, although due to symmetry in the case of cyclic molecules, they are the same function.) Similarly, the monomer density is defined as

$$\rho(z) = \frac{\int_0^N dt \iint dz' dz'' G(z', z; 0, t) G^\dagger(z, z''; N, t) \delta(z' - z'')}{\int_0^{z_{\max}} dz \iint dz' dz'' G(z', z; 0, N) G^\dagger(z, z''; N, N) \delta(z' - z'')}. \quad (3.30)$$

This expression can be simplified using the convolution property of propagators, that is, given that for any monomer  $t$  on the ring,  $G(z', z; 0, t) G^\dagger(z, z''; N, t) = G(z', z; 0, 0) G^\dagger(z, z''; N, 0)$ .

Thus,

$$\rho(z) = \frac{N \int dz' G(z', z; 0, 0) G^\dagger(z, z'; N, 0)}{\int_0^{z_{\max}} dz \int_0^{z_{\max}} dz' G(z', z; 0, N) G^\dagger(z, z'; N, N)}. \quad (3.31)$$

Figure 3.4 illustrates  $G$  on a loop from the 0th site at position  $z'$  to the  $t^{\text{th}}$  site at position  $z$  in the calculation of the statistical weight for the ring polymer. Since  $G(z', z; t, t) = \delta(z - z')$  for any  $t$ , the monomer density can be simplified to

$$\rho(z) = N \frac{G^\dagger(z, z; N, 0)}{\int_0^{z_{\max}} dz G^\dagger(z, z; N, 0)} \quad (3.32)$$

$$= N \frac{G(z, z; 0, N)}{\int_0^{z_{\max}} dz G(z, z; 0, N)}. \quad (3.33)$$

The derivation eliminates the index of the starting point. It shows that for a loop, the density probability only depends on the whole path looping back to the same position.

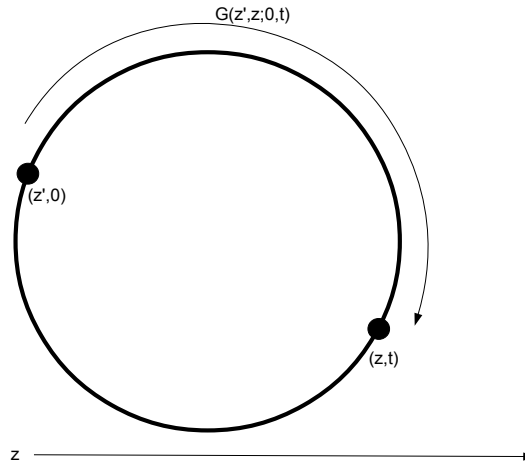


Figure 3.4: An illustration of calculating the statistical weight of a ring polymer in terms of the propagators  $G(z', z; 0, t)$  from the  $0^{\text{th}}$  site at  $z'$  to the  $t^{\text{th}}$  site at  $z$ .

Thus, the numerical SCFT for a cyclic molecule requires a numerical integration with respect to the time step  $t$  because only  $G$  at the last step  $N$  is needed. However, this calculation requires a larger allocation of memory because of the three dimensional array needed to store  $G(z, z'; 0, t)$ . The diffusion equation is solved sequentially along the  $z$  direction with a fixed  $z'$ . The performance can be improved if using a parallel algorithm to split work among many processors. The details for the parallelization are given in Appendix C.

### 3.1.3 The statistical weight functions of combs

In SCFT, the evaluation of the statistical weight function  $q(z; t)$  for a comb is straightforward. Figure 3.5 introduces the scheme for calculating the weight functions of a comb. Assuming a comb has  $p$  teeth and each tooth is  $M$  sites long, with  $L$  monomers between adjacent teeth on the backbone. The joints can be considered as a 3-arm structure except for the two joints, 0 and  $p - 1$ .  $q$  begins from the left joint  $i = 0$ , and diffuses towards the joint  $i = p - 1$ . Meanwhile, the corresponding  $q^\dagger$  diffuses from the opposite direction starting at joint  $p - 1$ .

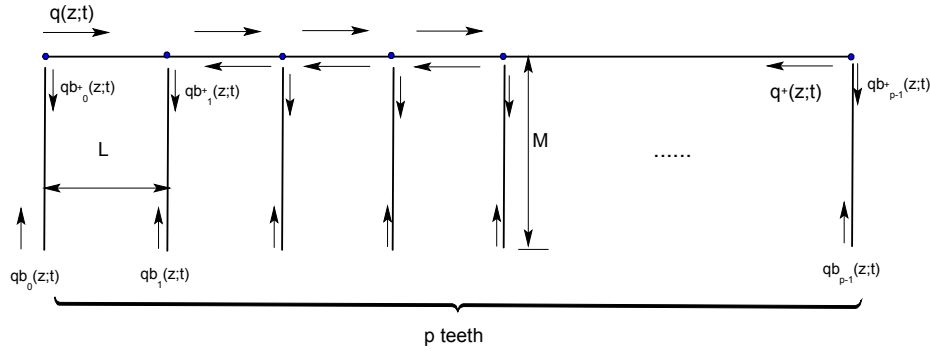


Figure 3.5: An illustration of calculating  $q$  and  $q^\dagger$  for a comb structure.

The weight functions of each tooth are also needed. They can be defined by introducing the tooth index  $i$ .  $qb_i$  and  $qb_i^\dagger$  correspond to weight functions of the  $i$ th tooth counting from 0 to  $p - 1$ . Note that all  $qb_i$  are the same, but  $qb_i^\dagger$  depends on the initial value  $qb_i^\dagger(z; 0) = q_{\text{joint}}(z; t_i)$ . For this 3-arm structure, the probability density at the joint is

$$\rho_{\text{joint}}(z, t_i) = q(z, t_i)q^\dagger(z, t_i)qb_i(z, t_i), \quad (3.34)$$

and furthermore  $qb_i^\dagger(z; t_i) = q(z; t_i)q^\dagger(z; t_i)$ . The complete solution of the modified diffusion equation must contain  $p$  outer iterations to update the  $q$  and  $q^\dagger$  at those joints. Each iteration solves the equation from  $t = t_i$  to  $t = t_{i+1}$ , which counts the sites between two adjacent joints.

### 3.2 Linear response theory for branched and linear blends

The linear response theory for polymers about the self-consistent field solution is developed by introducing the response function  $S(\mathbf{r}, \mathbf{r}') = \langle \delta\rho(\mathbf{r})\delta\rho(\mathbf{r}') \rangle$ , describing the correlation of local density fluctuations  $\delta\rho$  at  $\mathbf{r}$  and at  $\mathbf{r}'$ . By the fluctuation-dissipation theorem, it also gives the change in the average density at position  $\mathbf{r}$

$$\Delta\rho(\mathbf{r}) = - \int d\mathbf{r}' S(\mathbf{r}, \mathbf{r}') U(\mathbf{r}'). \quad (3.35)$$

in response to a weak potential field  $U(\mathbf{r}')$ . Because  $S(\mathbf{r}, \mathbf{r}')$  only depends on the relative distance  $|\mathbf{r} - \mathbf{r}'|$ , it has a simple form after a Fourier transform:

$$\Delta\rho(\mathbf{q}) = -S(\mathbf{q})U(\mathbf{q}). \quad (3.36)$$

Wu and Fredrickson [21] extended the linear response theory to study the surface segregation due to the surface potentials of joints and branched groups in the blends of linear and nonlinear polymers. For a binary blend with linear  $A$  and branched  $B$ , the effective surface potentials on joints and ends lead to a change in monomer density of  $B$ , which is written as

$$\Delta\rho^B(\mathbf{r}) = - \int d\mathbf{r}' S_{\rho_e}^B(\mathbf{r}, \mathbf{r}') U_e^B(\mathbf{r}') + S_{\rho_j}^B(\mathbf{r}, \mathbf{r}') U_j^B(\mathbf{r}'), \quad (3.37)$$

where the end density and joint density response function for branched species are written respectively, in terms of

$$S_{\rho_e}^B(\mathbf{r}, \mathbf{r}') = \langle \delta\rho^B(\mathbf{r})\delta\rho_e^B(\mathbf{r}') \rangle \quad (3.38)$$

and

$$S_{\rho_j}^B(\mathbf{r}, \mathbf{r}') = \langle \delta\rho^B(\mathbf{r})\delta\rho_j^B(\mathbf{r}') \rangle. \quad (3.39)$$

The effective surface potential field  $U(\mathbf{r})$  is given as a delta function at a given infinitesimal distance  $z$  from the surface, in terms of enthalpy and entropy:

$$U(\mathbf{r}) = U\delta(z) = \Delta h - T\Delta S, \quad (3.40)$$

where the conformational entropy contribution to  $S$  is written as

$$-T\Delta S = -\xi kT\delta(z) \int_0^\infty [\tanh^p(z) - \tanh^2(z)]dz, \quad (3.41)$$

where  $\xi = b/\sqrt{3v\rho_b}$  is the Edwards screening length, and  $p$  is the functionality of the branch point.

The excess monomer density in the limit of incompressibility ( $v \rightarrow \infty$ ), for branched molecules in a branched/linear blend is written as

$$\Delta\rho(\mathbf{q}) = \left( \frac{S_{\rho\rho}^B(\mathbf{q})}{S_{\rho\rho}(\mathbf{q})} \right) S_{\rho\rho}^L(\mathbf{q})U_e^L - \left( \frac{S_{\rho\rho}^L(\mathbf{q})}{S_{\rho\rho}(\mathbf{q})} \right) (S_{\rho e}^B(\mathbf{q})U_e^B + S_{\rho j}^B(\mathbf{q})U_j^B). \quad (3.42)$$

In this equation,  $S_{\rho\rho}^B$  represents the monomer-monomer correlation functions for the branched molecules and  $S_{\rho\rho}^L$  is for the linear.  $U_e^L$  is the potential on the end of linear species; similarly for  $U_e^B$  on branched ends. The excess density profiles from the surface can be obtained by taking the 1-D Inverse Fourier transform on Equation 3.42. The integrated total surface excess is therefore given by

$$\int_0^\infty dz\Delta\rho(z) = \rho_b \left[ \frac{1}{\phi_B N^B} + \frac{1}{(1-\phi_B)N^L} \right]^{-1} \left( \frac{2}{N^L}U_e^L - \frac{n_j^B}{N^B}U_j^B - \frac{n_b^B}{N^B}U_e^B \right), \quad (3.43)$$

where  $N^B$  is the polymerization degree of the branched polymer,  $N^L$  is the polymerization degree of the linear chain, and  $\phi_B$  is the mole fraction of the branched species. The total bulk monomer density  $\rho_b = \rho_L + \rho_B$  is a constant. Linear response theory shows that the joint and branch points are entropically repulsed by the surface however the ends of molecule are entropically preferred to stay at surface. It predicts that conformational entropy effects, if acting alone, will cause the branched species to be enriched at the surface when mixed with long linear chains. The enthalpic potentials of the specific chemical groups, which can be simply added to the entropic potentials within linear response theory, also affect the surface enrichment and this prediction is helpful in experimental studies on branched/linear blends. However, the linear response theory gives a result for the integrated surface excess that depends only on the number and type of branch and end points, and thus fails to predict

variations in surface segregation when the branch and end group type and numbers are held fixed, but the intervening lengths are varied.

### 3.3 Surface SCF potential on specific functional groups in branched polymers attracted or repelled from a surface

Linear response theory has shown that the effect of surface potentials of ends and joints on surface enrichment. The specific surface potentials acting on joints and ends can also be implemented within conventional SCFT. The modification is described as below.

Assuming a branched molecule contains two types of joints  $j_a$ ,  $j_b$  and one end  $e$ , with surface potentials  $\mu_{j_a}$ ,  $\mu_{j_b}$  and  $\mu_e$ , respectively. The surface potentials have an effective given cutoff range  $z_{\text{eff}}$  from the surface. The branched molecule as a whole can feel an external field  $\mu(z; t)$ , which is written as

$$\mu(z; t) = \rho(z)v, (t \neq \text{end, joint}), \quad (3.44)$$

and the surface potentials near the wall on the joints and ends satisfy

$$\begin{aligned} \mu(z; \text{end}) &= \rho(z)v + \mu_e(z), \\ \mu(z; \text{joint}_a) &= \rho(z)v + \mu_{j_a}(z), \\ \mu(z; \text{joint}_b) &= \rho(z)v + \mu_{j_b}(z). \end{aligned} \quad (3.45)$$

The surface potentials are then incorporated during the solution to the modified diffusion equation:

$$\frac{\partial q'}{\partial t} = \frac{b^2}{6} \nabla^2 q' - \mu q'. \quad (3.46)$$

The solution of  $q'$  at different  $t$  depends on the specific potentials on the end or joint. Thus, the initial conditions are changed to be  $q(z; 0) = \exp[-\mu_e(0)]$  and  $q^\dagger(z; N) = \exp[-\mu_e(0)]$ .

At the joint containing  $m$  branches, the unnormalized density is written as

$$\begin{aligned} \rho(z) &= \exp(-\mu_{j_b})q_1(z; \text{joint})q_2(z; \text{joint})q_3(z; \text{joint})\dots q_{m-1}(z; \text{joint})q^\dagger(z; \text{joint}) \\ &= \exp(-\mu_{j_b})q_1^{m-1}(z; \text{joint})q^\dagger(z; \text{joint}), \end{aligned} \quad (3.47)$$

where  $q_i(z; \text{joint})$  is the solution of the modified diffusion on the  $i^{\text{th}}$  branch, and the second equation applies as we consider the case of all equal length branches. The weight function of the joint is defined as

$$q'(z; \text{joint}) = \exp(-\mu_{j_b})q_1^m(z; \text{joint}). \quad (3.48)$$

The simplest form of the surface potentials  $\mu_e$ ,  $\mu_{j_a}$  and  $\mu_{j_b}$  is the finite square-well potential:

$$\begin{aligned} \mu_{j_a} &= \frac{U_a}{z_{\text{eff}}}, (z \leq z_{\text{eff}}), \\ \mu_{j_a} &= 0, (z > z_{\text{eff}}), \end{aligned} \quad (3.49)$$

where  $U_a$  is the area of the squared well in units of  $kTb$  ( $b$  is the Gaussian step length). Similarly,  $\mu_e$  and  $\mu_{j_b}$  are defined in terms of  $U_e$  and  $U_{j_b}$  as square-well potentials. The cutoff distance  $z_{\text{eff}}$  can be taken to be the screening length  $b/\sqrt{3v\rho_b}$ , where  $v$  is the excluded volume and  $\rho_b$  is the bulk density [21].

## CHAPTER 4

### SURFACE SEGREGATION OF LINEAR AND NONLINEAR POLYMER BLENDS

This chapter focuses on the surface segregation of nonlinear molecules in blends of nonlinear and linear polymers. A variety of architectures are studied, such as star, pom-pom, n-end, comb, and cyclic polymers. These nonlinear structures has been shown a preference of segregation when mixing with linear molecules in Chapter 2. Linear response theory predicted that surface segregation can be understood as surface potentials of entropic and enthalpic origins. The influence of surface potentials for different branch groups is tested using linear response theory and SCFT, by separately varying number of ends and of branch points, at fixed molecular weights. As the number and type of ends and joints are fixed across the series of pompoms, the pom-pom molecules address a question to the effect of the length of side branches on the surface enrichment. However, linear response is insufficient to address pom-poms, since it neglects the difference of the molecular weight in branches and linear backbones. SCFT is applied in this chapter and compared with the experimental results. The cyclic structures are interesting because of the topology without ends. The surface enrichment of the cyclic molecules in the blend with linear cannot be explained by potentials of functional groups; however, linear response theory predicts a factor of two enhancement compared to its bulk concentration at the surface due to topological entropy. Compressible SCFT calculations are given as tests of linear response theory and comparison with experiments. Finally, the surface segregation of a series of blends with densely branched combs and linear polymers are of interest and studied by both linear response theory and SCFT, to predict that a highly branched molecule show strong entropic preference to the surface, and compare with experiments.

Figure 4.1 gives examples of the various symmetrically branched molecules studied. These molecular architectures were based on branched, cyclic and comb polystyrene molecules

synthesized and experimentally studied by Foster and co-workers [9, 16, 20, 32].

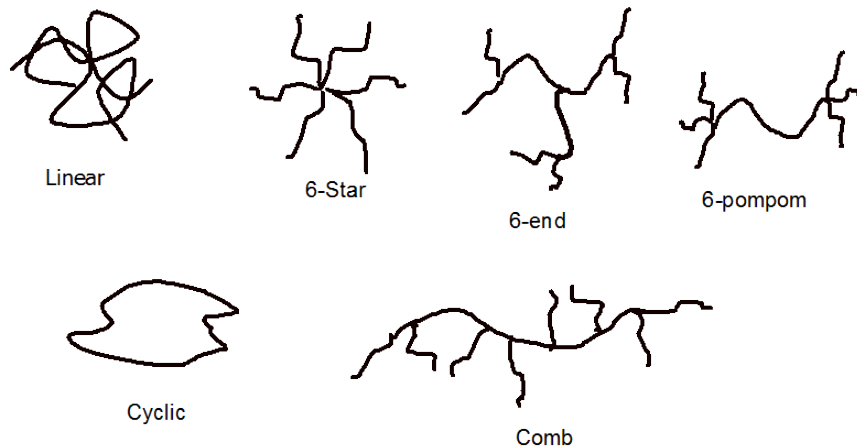


Figure 4.1: Schematic illustration and names of star, multiple-end branched, pom-pom, cyclic and comb polymers studied.

I present SCF theory calculations for blends of each of these nonlinear polymers with their linear analogs, and where available, compare with experimental data.

#### 4.1 Surface segregation of star/linear blends

In this section, a series of SCFT calculations on blends of 4-star and linear polymers are performed to study the surface enrichment of the star molecules. The 4-star chains studied have fixed total polymerization degree of  $N_{\text{star}} = 100$ , while three different polymerization degrees of the linear component,  $N_{\text{linear}} = 10, 100$  and  $1000$ , are used to study the effect of molecular weight differences. The simulation box size is  $z_{\text{max}} = 100b$  where  $b$  is the Gaussian step length, and the total monomer density is fixed at  $\bar{\rho} = 1.0$ . Figure 4.2 presents the excess density profiles of star molecules in the blend with varying the degree of polymerization of linear components. Dimensionless variables,  $\bar{z} = z/b$ ,  $\bar{v} = vb^{-3}$  and  $\bar{\rho} = \rho b^3$  are defined and used in these SCFT calculations. The excess density is dimensionless in terms of the reduced density  $\bar{\rho}$ . The parameter  $\phi_i$  represents the initial monomer mole fraction of the component  $i$  in a blend.

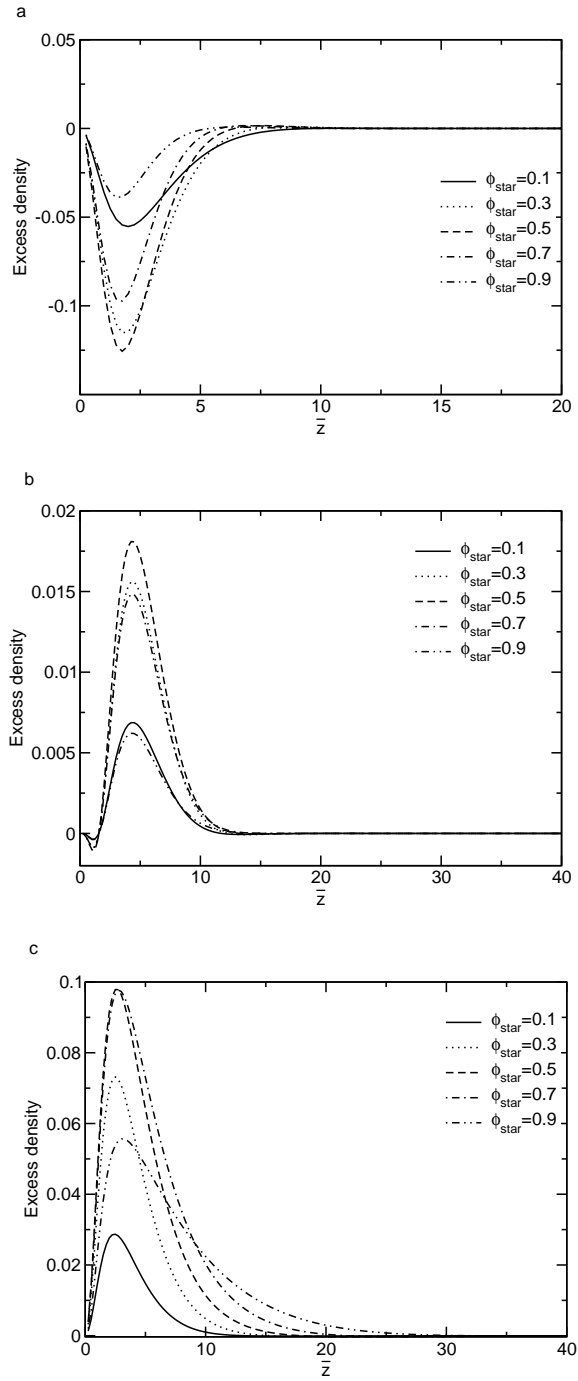


Figure 4.2: Excess density profiles of star species for different compositions of star monomers in various 4-star/linear blends. The molecular weight of the star is  $N_{\text{star}} = 100$ . (a) A binary blend containing shorter linear molecules  $N_{\text{linear}} = 10$ . (b) A binary blend with equal molecular weights of linear and star.  $N_{\text{linear}} = 100$ . (c) A binary blend with longer linear chains  $N_{\text{linear}} = 1000$ .  $\bar{v} = 0.1$  and  $\bar{\rho}_b = 1$ .

In Figure 4.2a, the stars ( $N = 100$ ) are repelled from the surface in a low molecular weight linear host ( $N = 10$ ). In this case, the driving force for lower molecular weight species to go to the surface dominates over architectural effects.

For the symmetric molecular weight case in Figure 4.2b, stars segregate near the surface over the range scaling as  $R_{g,\text{star}} \sim \sqrt{N_{\text{star}}} \approx 10b$  as expected by the linear response theory, but the linear can still slightly segregate at the surface. It is notable that the segregation profiles are nearly symmetrical with respect to the composition of star monomers: the excess density profiles for  $\phi_{\text{star}} = 0.3$  and  $0.7$  are very similar, as are the blends of  $\phi_{\text{star}} = 0.1$  and  $0.9$ , and the excess density profile reaches maximum around  $\phi_{\text{star}} = 0.5$ . Panel a and c both show that the decay length of the excess density decreases as the composition of the small molecule decreases. The decay length for the excess of branched polymer is seen to change with the composition. This is also seen and first explained in the linear response theory [21]: the decay length is a function of the sizes ( $R_g$ ) of both components, which may differ. The relative weight of each size in contributing to the determination of the overall decay length varies with composition, and hence so does the decay length itself.

$R_g$  for a polymer near the surface can vary from the Gaussian model,  $R_g \sim \sqrt{N}$ , because the conformation changes that ends are entropically attracted but joints are repelled.  $R_g$  near the surface can be calculated by two-chain SCFT. The algorithm for particularly  $R_g$  calculations in two-chain SCFT is more complicated than the algorithm developed in Chapter 5. It can be expected that when a star molecule approaches to the surface from the bulk, the molecule should be firstly stretched because of the surface attraction of the ends, but then compressed when the molecule is too close to the surface. The study of  $R_g$  near the surface is not discussed in the thesis.

As discussed by linear response theory, the depth between the surface and peaks due to compressibility is proportional to the screening length  $\xi$ . Figure 4.2a and c clearly show that this compressibility regime varies with compositions. However, there is no clear explanation for the details of the composition dependence of this length scale.

For the case where the linear molecules are higher in molecular weight than the stars, an even greater enrichment of star species will be found at the surface, as can be seen in comparing panels b and c. This reflects the combined effects of molecular weight and architectural driving forces for surface segregation. Figure 4.2c also shows that excess profiles for  $\phi_{\text{star}} = 0.5$  and  $\phi_{\text{star}} = 0.7$  have the same maximum excess density. However, in the blend of  $\phi_{\text{star}} = 0.7$ , the decay length of the excess profile is wider. Therefore the integrated excess is greater than for  $\phi_{\text{star}} = 0.5$ . The corresponding integrated excesses as a function of compositions of star monomers are plotted in Figure 4.3. The linear excess for  $N_{\text{linear}} = 10$  peaks at  $\phi_{\text{star}} = 0.3$  while the star excess in a blend with long linear molecules peaks at  $\phi_{\text{linear}} = 0.7$ . The integrated excess in the symmetric blends present a parabolic function of composition, which is symmetric to  $\phi = 0.5$ . This trend agrees with the prediction by Wu and Fredrickson using linear response theory on 10-star/linear blends [21].

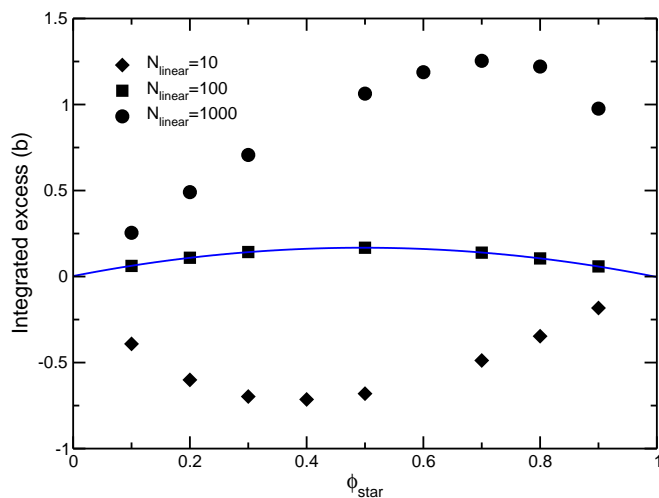


Figure 4.3: Comparison of integrated surface excess of the 4-star/linear binary blends shown in Figure 4.2. the solid curve on plots of case  $N_{\text{linear}} = 100$  represents the corresponding 2nd order polynomial fit.

I show here that this symmetry with respect to the composition of monomers results from a simple assumption that the density profile  $\rho_A(z)$  for a given species A in the blend

retains the same shape as  $\phi_A$  varies, and is simply proportional to the bulk density  $\rho_{A_0}$  of that species, namely that

$$\rho_A(z) = \rho_{A_0} f_A(z), \quad (4.1)$$

and similarly

$$\rho_B(z) = \rho_{B_0} f_B(z), \quad (4.2)$$

where  $f_A(z)$  and  $f_B(z)$  are the functions defining the shape of the profiles. The bulk composition of A and B monomers are  $\phi_{A_0} = \rho_{A_0}/\rho_b$  and  $\phi_{B_0} = \rho_{B_0}/\rho_b$ , respectively, with  $\rho_b = \rho_{A_0} + \rho_{B_0}$  being the total bulk density. Recall the excess densities for compressible blends are defined to be

$$\Delta\rho_A(z) = \phi_{B_0}\rho_A(z) - \phi_{A_0}\rho_B(z), \quad (4.3)$$

and

$$\Delta\rho_B(z) = \phi_{A_0}\rho_B(z) - \phi_{B_0}\rho_A(z). \quad (4.4)$$

Thus, Equation 4.4 can be written as

$$\begin{aligned} \Delta\rho_B(z) &= (\rho_{A_0} + \rho_{B_0})\phi_{A_0}\phi_{B_0}[f_B(z) - f_A(z)] \\ &= \rho_0\phi_{B_0}(1 - \phi_{B_0})[f_B(z) - f_A(z)]. \end{aligned} \quad (4.5)$$

The integrated excess of component B is

$$Z_B^* = \rho_0\phi_{B_0}(1 - \phi_{B_0}) \int (f_B(z) - f_A(z)) dz. \quad (4.6)$$

The integrated excess is thus predicted to be parabolic in the composition if  $f_B(z) - f_A(z)$  is independent of  $\phi$ . However, the SCFT solution shows  $\phi(z)$  depends on the molecular weight  $N$  so that in symmetric blends the integrated excess can be parabolic. The excess density profiles of a series of symmetric molecular weight 4-star/linear blends are plotted in Figure 4.4, for presenting that the small amount of linear molecules at the surface is decreasing as the molecular weight increases.

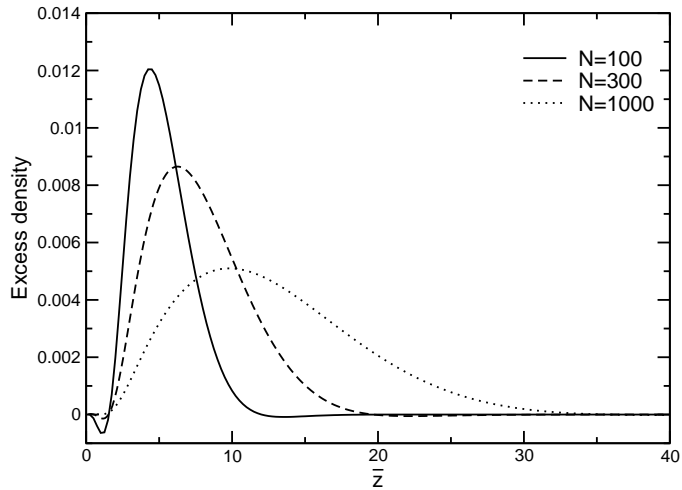


Figure 4.4: The excess density of a series of 4-star/linear blends of symmetric molecular weight.  $\phi_{\text{star}} = 0.2$ ,  $\bar{v} = 0.1$  and  $\bar{\rho}_b = 1$ .

I now consider how the number of arms on the star affects surface segregation. In a blend of linear molecules with  $N_{\text{linear}} = 1000$  and star molecules having arms of length  $N_{\text{arm}} = 25$ , the integrated excess of star is plotted versus the number of arms in the star in Figure 4.5. All blends have identical bulk composition,  $\phi_{\text{star}} = 0.2$ . The total bulk density is  $\bar{\rho}_b = 1.0$ . The results in Figure 4.5 show that the total surface excess of stars increases approximately linearly with number of arms. The effect of the length of the star arms can also be considered. The results for a 4-star/linear blend with varying arm lengths  $N_{\text{arm}} = 25, 125$  and  $250$  are shown in Figure 4.6, indicating that the integrated excess of stars decreases approximately linearly with increasing  $N_{\text{arm}}$ .

## 4.2 Surface segregation of blends of end-branched and linear polymers

The surface density profiles of polymer blends involving more complicated branched structures are studied to determine the effect of branching points on the surface segregation. In the previous discussion, shorter linear components are enriched at the surface when mixed with a longer linear molecule and certain longer nonlinear molecules. The current study

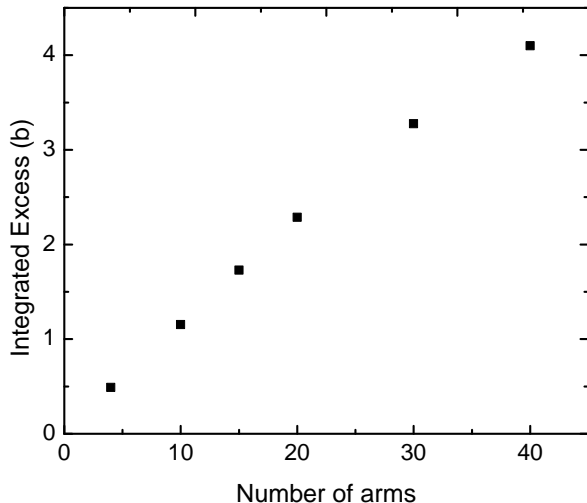


Figure 4.5: The integrated surface excess of star/linear blends versus number of star arms. Each arm has length  $N_{\text{arm}} = 25$ .  $N_{\text{linear}} = 1000$ ,  $\bar{\rho}_b = 1.0$ ,  $\phi_{\text{star}} = 0.2$ ,  $\bar{v} = 0.1$ .

focuses on the blend symmetric in molecular weight (degree of polymerization) and long linear/short branched blends, i.e.,  $N_{\text{nonlinear}} \leq N_{\text{linear}}$ .

Figure 4.7 depicts the contributions of the inner arms (between the central branch point and the 3 outer branch points) as well as the 9 outer branches to the total surface density profile in a 9-end/linear symmetric blend. The depletion in density of the surface has a width that scales as the screening length  $\xi \sim (\rho v)^{-1/2}$ , while the spatial width of the regime showing an excess of branched polymer is determined by the extent of the outer branches, which can be seen to be farther than that of the inner arms.

A series of SCFT calculations on 9-end/linear blends with varying distance of the outer branch points to the central branch point are given in Figure 4.8a. Each 9-end polymer contains three inside arm with three branches attaching to each arm. Calculations assume the degree of polymerization of the 9-end is fixed at  $N_{\text{9end}} = N_{\text{linear}} = 1000$ , and thus the different 9-end polymers differ in the lengths of the outside branches. The SCFT results show that the 9-end molecule with longer branches produces a higher excess density close to the surface. As expected, the branch  $R_g$  scale determines the thickness of the region of

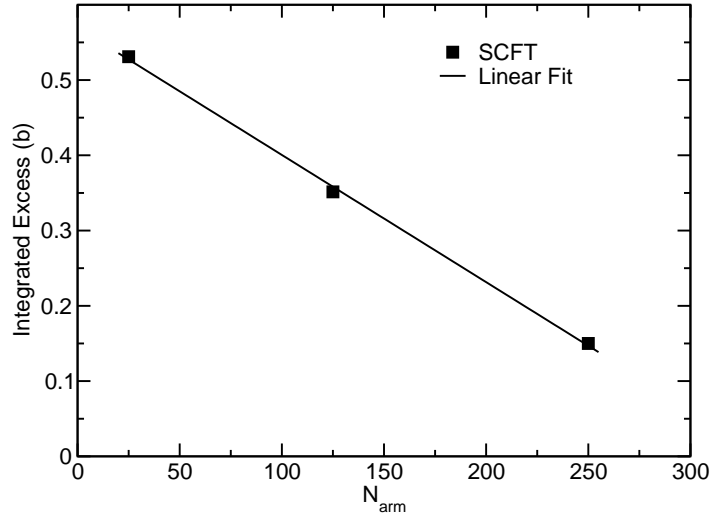


Figure 4.6: The integrated surface excess of 4-star/linear blends for different star arm lengths.  $N_{\text{linear}} = 1000$ ,  $\bar{\rho}_b = 1.0$ ,  $\phi_{\text{star}} = 0.2$ ,  $\bar{v} = 0.1$ .

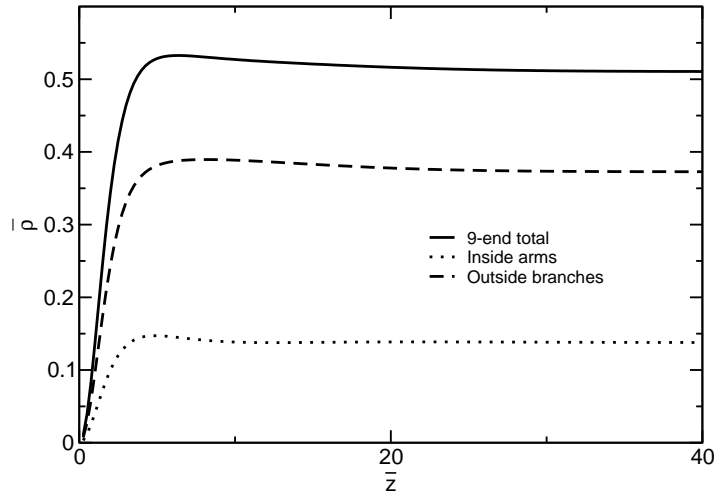


Figure 4.7: The surface density profiles of the 9-end polymer in 9-end/linear blends by SCFT, broken down into the contributions of the inside arms and outside branches.  $N_{\text{9end}} = N_{\text{linear}} = 1000$ ,  $N_{\text{arm}} = 183$  and  $N_{\text{branch}} = 50$ . In these calculations,  $\bar{\rho}_b = 1.0$ ,  $\bar{v} = 0.1$ , and  $\phi_{\text{9end}} = 0.5$ .

excess density as well. Figure 4.8b plots excess density profiles from SCFT calculations for different branched polymers with increasing number of outside branches. These branched polymers have inside arms fixed in number and length, while the number of branches (with fixed length  $N_{\text{branch}} = 50$ ) attached to each arm increases. It can be concluded that the excess can be enhanced by increasing the number of outside branches while not change the thickness of the segregation.

Figure 4.9 plots the integrated excess of the  $n$ -end component, which is found to be approximately linearly increasing with the length of the outside branch  $N_{\text{branch}}$  when the number and length of the inside arms are fixed. Two cases of  $n$ -end/linear polymer blends are studied by fixing the number of inside arms but varying the number of outside branches. In the first case, the linear molecular weight is fixed to be 1000 while the molecular weight of the nonlinear component is varied. In the second case, linear and branched components have equal molecular weight, but the outside branches consist of 30 or 50 monomers. The excess increases as the number of arms increase in both cases of equal or differing molecular weight blends. The surface excess of branched polymer in the 6-end/linear with  $N_{\text{linear}} = 1000$  is slightly greater than that found in the 6-end/linear equal molecular weight blend; however, the surface branched excess in the 21-end/linear blend shows the opposite trend. This observation can be understood as resulting from the molecular weight effect, since the 21-end has a molecular weight greater than 1000, which favors the shorter linear chain to segregate at the surface as well. It is notable that the blend of 15-end/linear ( $N_{15\text{end}} = 1000, N_{\text{branch}} = 30$ ) shows stronger segregation than the blend of 9-end/linear ( $N_{9\text{end}} = 1000, N_{\text{branch}} = 50$ ), in agreement with the experimental conclusion that increasing branched ends can enhance surface segregation [19]. This qualitative agreement implies that for end-branched architectures, the entropic effect for branching leads to the enhanced surface segregation. The comparison of Lee's experiment is discussed in a different section including the different group chemistry as the enthalpic contribution [18].

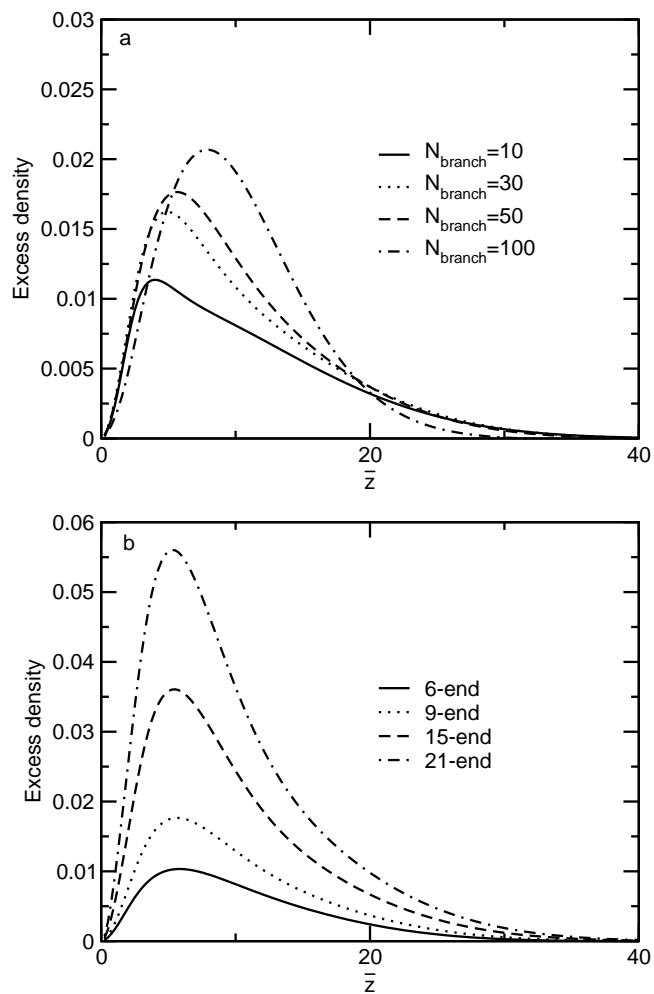


Figure 4.8: Excess density profiles of end-branched polymers in  $n$ -end/linear blends by SCFT. (a) Blends containing 9-end structures with  $N_{9\text{end}} = N_{\text{linear}} = 1000$ . (b) Blends of  $n$ -end polymers with increasing number of branches and fixed number and length of inside arms. The molecule contains 3 arms and each arm has  $N_{\text{arm}} = 183$ .  $N_{\text{branch}} = 50$ . In all calculations,  $\bar{\rho}_b = 1.0$ ,  $\bar{v}_b = 0.1$ .

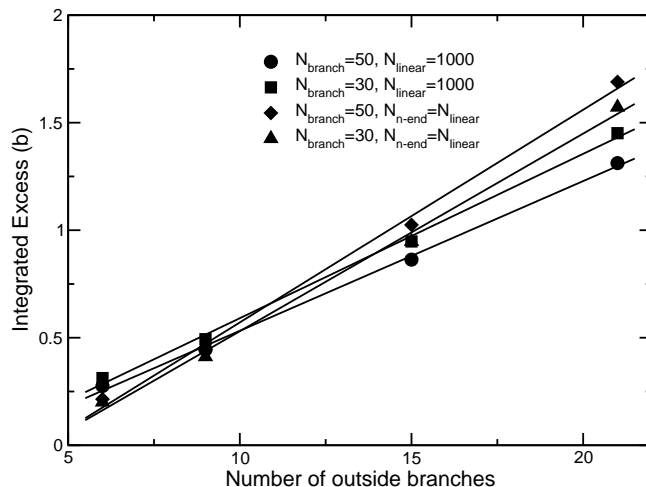


Figure 4.9: The integrated surface excess of the  $n$ -end polymers in blends with linear molecules. All  $n$ -end species have three equal inside arms,  $N_{\text{arm}} = 183$ . Two series of calculations are considered, one with fixed linear molecular weight  $N_{\text{linear}} = 1000$ , and the other one with equal molecular weight,  $N_{n\text{-end}} = N_{\text{linear}} = 1000$ . For all calculations,  $\bar{\rho}_b = 1.0$ ,  $\bar{v} = 0.1$ , and  $\phi_{n\text{-end}} = 0.2$ .

### 4.3 Surface segregation of 6-pom/linear blends: comparison between theory and experiments

Comparison using SCFT prediction and neutron reflectometry experimental results are studied for various 6-pom/linear binary blends. Foster and coworkers have synthesized pom-pom polystyrenes (PS) molecules containing six branches with about 360 total repeat units (each with molecular weight  $\sim 104$  g/mol), but varying lengths of the linear backbone [9, 16, 20]. The pom-pom molecules are named as 6pom4k, 6pom18k and 6pom34k, where the nomenclature 6pom-nk designates a molecular weight nk of the linear backbone (i.e., the monomers between the two branch points). As stated above, this series of model chain molecules provides an exquisite test of the theory, since the number and type of branch and end points are unchanged, merely the lengths of the different branches in the molecule.

Neutron reflectometry (NR) measurements were performed on the hydrogenous 6pom-nk/deuterated linear blends to determine the surface density profiles. The volume fraction

of the pom-pom polymers is 0.2 in the experiments. Note that the experiments assumed the monomer volume does not change so that the volume fraction is the same as the mole fraction of the monomers,  $\phi$ . The surface density of a series of 6pom- $n$ k/linear blends are calculated by SCFT for comparison. To match the experimental molecules, all pom-pom polymers and linear chains are assumed to have  $N = 360$  repeat units. The linear portion of the pom-pom backbone varies from 0 to 350 monomers. In particular, the 6pom0k is considered to be equivalent to a 6-star, although an ideal 6pom0k still has two branch points.  $\phi_{\text{pom}} = 0.2$  is assumed for the monomer mole fraction is equal to the volume fraction, if the monomer volume does not change. The SCFT results show that the integrated excess decreases monotonically with increasing backbone length. This is reasonable as in the limit of the backbone reaching its maximum, the molecule structurally approaches that of the linear molecule. For entropically driven segregation, there is only one adjustable parameter for the SCFT calculation, corresponding to the strength of the entropic surface potential. This parameter only acts as a multiplicative factor for the integrated excess, and was determined by a least square fit of the SCFT values for the surface excess of 6pom4k, 6pom18k and 6pom34k to the corresponding experimental results. The resulting comparison between the NR results and SCFT calculation is shown in Figure 4.10.

The agreement is fairly good between theory and experiment, with a notable difference for the 6star polymer. However, the 6star polymer was synthesized with a different chemical branch point, and is not identical with a hypothetical 6pom-0k with two pom-pom branch points separated by zero distance. Since branch points can have different surface potentials of enthalpic origin, this may be an explanation for the discrepancy seen for the 6star polymer. A similar discrepancy was seen in SANS experiments determining the entropic contribution to bulk chi values for 6-star/linear blends [20].

#### 4.4 Surface segregation in cyclic and linear polymer blends

Linear response theory predicts that cyclic molecules have a stronger preference for the surface compared with their linear analogs when considering conformational entropy effects

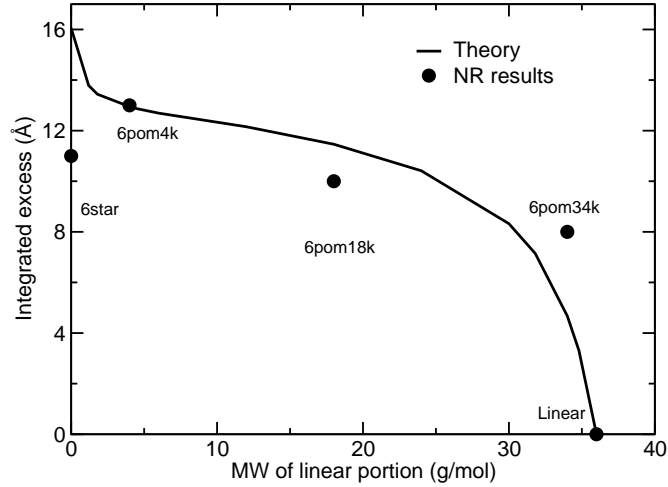


Figure 4.10: A comparison of integrated surface excess derived from neutron reflectometry measurements and SCFT calculations.  $\phi_{\text{pom}} = 0.2$  and  $N_{\text{linear}} = N_{\text{pom}} = 360$ ; for SCFT,  $\bar{v} = 0.1$ ,  $\bar{\rho}_b = 1$ .

[21]. In the limit that the cyclic molecules are infinitely dilute, the linear chains are infinitely long, and the blend is incompressible, the theory makes the provocative prediction that the cyclic topology of the molecules result in a surface concentration *exactly* twice that in the bulk. The spatial extent of the surface enrichment is predicted to be on the order of the size ( $R_g$ ) of the cyclic molecule. In this section, the SCFT algorithm for studying the surface enrichment of cyclic/linear blends without invoking these limiting conditions is introduced and applied to various blends of linear and cyclic molecules. Van Lent [141] introduced a Scheutjens-Fleer lattice model to conceptually show that the cyclic can be more absorbed to the surface layer from the athermal solvent than the linear. The pioneering work was done for small molecules  $N \sim \mathcal{O}(10)$  and 4-8 lattice layers for the system, due to the limitation of computing performance.

In this section, the surface segregation for cyclic polymers in the blend with linear species is studied firstly by compressible SCFT derived in Chapter 3, including further comparison with linear response theory and experimental data.

#### 4.4.1 Surface segregation in equal and differing molecular weight cyclic/linear blends

The first calculations focus on blends with low compositions of the cyclic polymer monomers,  $\phi_{\text{cyclic}} = 0.01$  and  $0.05$ . All calculations in this section uses total bulk density  $\bar{\rho}_b = 1$ . In this case, the linear chain has a degree of polymerization of  $N = 100$  and the degree of polymerization of the cyclic molecules are 5, 10, 20, 40, 50 and 100. Figure 4.11a shows that the density profiles of the cyclic polymers reach a similar maximum density near the surface. The decrease in the bulk density is a result of the calculation occurring with a finite number of chains in a finite box.

To account for this shift, Figure 4.11b shows the same profiles, but normalized by the bulk compositions. Compared with their bulk concentrations, the excess surface density is increased by up to approximately 80%, somewhat lower than the 100% expected by linear response theory under limiting conditions. This percentage increase is also somewhat greater than that seen so far for the branched species studied. Moreover, the width of the segregated regime is increases with increasing cyclic sizes, in qualitative agreement with linear response theory. This agrees with the prediction by linear response theory and is similar to the behavior obtained in SCFT results for end-branched/linear blends.

As with branched polymers, adding a cyclic molecule to a melt of short linear molecules presents a situation where the topological driving force for cyclics to go to the surface is competing with the driving force for lower molecular weight species to go to the surface. It can be seen that both linear and cyclic molecules can be enhanced at the surface, but over length scales corresponding to their respective sizes.

Figure 4.12 shows results for the case of a 1% additive of  $N_{\text{cyclic}} = 1000$  cyclic chains blended with a linear polymer, with the linear molecule varying in length between  $N_{\text{linear}} = 100$  to  $N_{\text{linear}} = 1000$ . Two sets of calculations are performed using cyclic bulk monomer compositions of  $\phi_{\text{cyclic}} = 0.01$  and  $\phi_{\text{cyclic}} = 0.05$ . The surface enrichment of cyclic molecules can be significantly reduced in a short linear host compared to a host with equal molecular

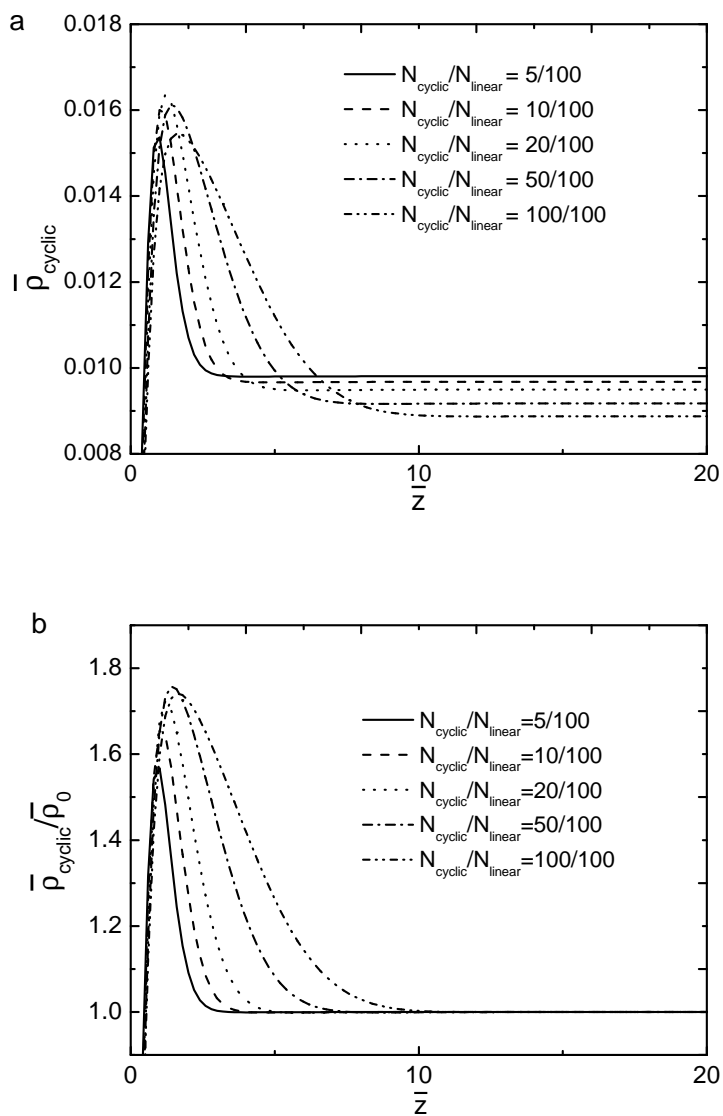


Figure 4.11: Surface density of cyclic molecules blended with linear polymer.  $N_{\text{linear}} = 100$ ,  $N_{\text{cyclic}} = 5, 10, 20, 50, \text{ and } 100$ .  $\phi_{\text{cyclic}} = 0.01$ ,  $\bar{v} = 0.1$  and  $\bar{\rho}_b = 1$ .

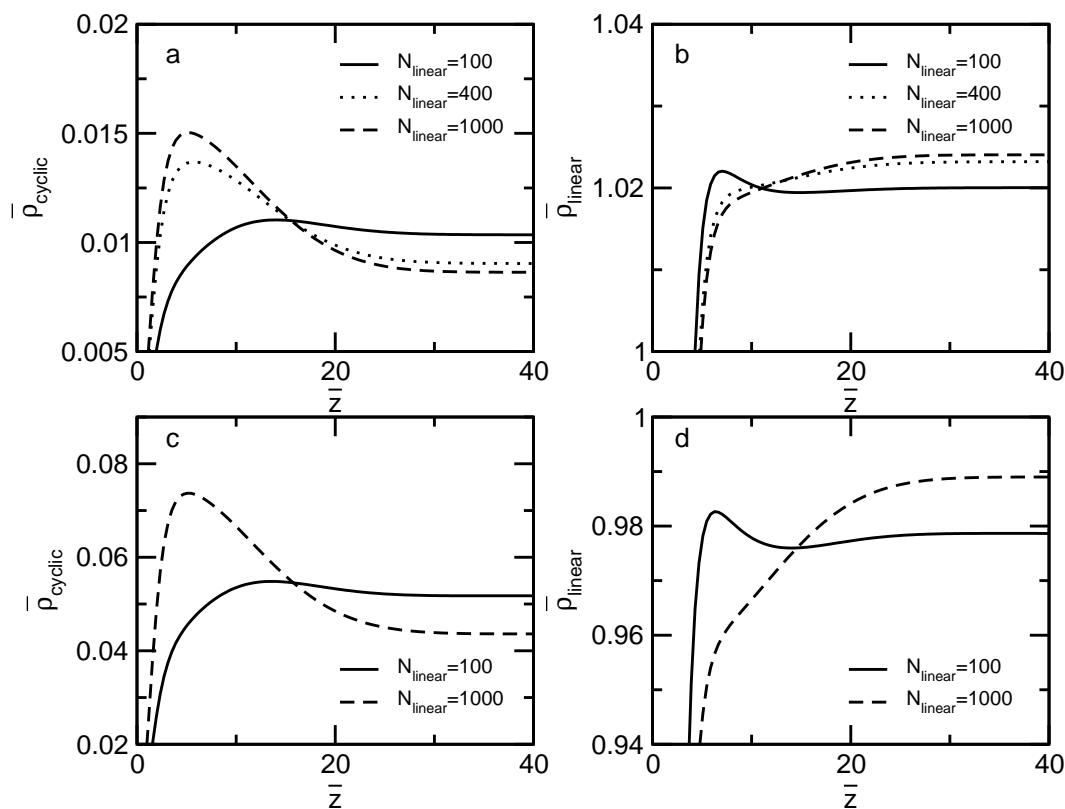


Figure 4.12: Surface density profiles of cyclic/linear blends with fixed  $N_{\text{cyclic}} = 1000$  in low cyclic concentrations. (a) Density profiles of cyclic at  $\phi_{\text{cyclic}} = 0.01$ . (b) Density profiles of linear molecules at  $\phi_{\text{cyclic}} = 0.01$ . (c) The density profiles of cyclics with initial bulk  $\phi_{\text{cyclic}} = 0.05$  and (d) The linear density profiles with initial bulk  $\phi_{\text{cyclic}} = 0.05$ . All calculations use  $\bar{v} = 0.1$ ,  $\bar{\rho}_b = 1$  and  $\bar{z} = 100$ .

weight. In blends with the shortest chains,  $N_{\text{linear}} = 100$ , the density profile  $\phi_{\text{cyclic}}(z)$  is only slightly higher at the near surface region than in the bulk. On the other hand, the corresponding linear density profiles in those blends with  $N_{\text{linear}} = 100$  are also attracted to the surface. (See panels (b) and (d)). As the polymerization of the components become equal, cyclic polymers dominate the surface region.

A similarity in the cyclic/linear and branched/linear blends is that there is an enriched layer of short linear chains in the immediate vicinity of the surface. The excess density profiles as a function of distance for unequal molecular weight blends are shown in Figure 4.13. For the blends containing  $N_{\text{linear}} = 100$ , the short linear chain is enriched at the surface over a distance scaling as  $R_{g,\text{linear}} \sim \sqrt{N_{\text{linear}}} \approx 10b$ , while the width of the enriched region for the cyclic component scales as  $R_{g,\text{cyclic}} \sim \sqrt{N_{\text{cyclic}}} \approx 30b$ .

Figure 4.14 shows the excess density profiles for blends for various higher compositions of cyclic monomers. In contrast with the branched/linear blends, the surface excess for equal molecular weight blends are not symmetric with respect to the composition. Figure 4.15 shows the dependence on  $\bar{v}$  for the integrated excess. The enriched regime appears to be roughly unchanged scaling as  $R_g$ . The height of  $\Delta\rho$  increases as the excluded volume increases. Linear response theory predicts that in the limit of incompressibility,  $\bar{v} \rightarrow \infty$ , the excess density approaches to the exact twice as the bulk density,  $\rho_{\text{cyclic}_0} = 0.2$  in this system.

The integrated surface excess is linear to the size of cyclics when fixing  $N_{\text{linear}}$ . If  $N_{\text{cyclic}} \leq N_{\text{linear}}$ , the normalized slope by the total excess by the composition of cyclic monomers is a constant, as shown in Figure 4.16 for the plots of integrated excess versus the  $\sqrt{N_{\text{cyclic}}}$  of cyclic chains.

#### 4.4.2 Comparisons between SCFT calculations and NR experiments for isotopic blends of cyclic/linear polystyrene

Experiments measuring surface compositions in a series of cyclic/linear PS blends have been performed by Wang *et al.* recently [32]. Equal molecular weight blends for long

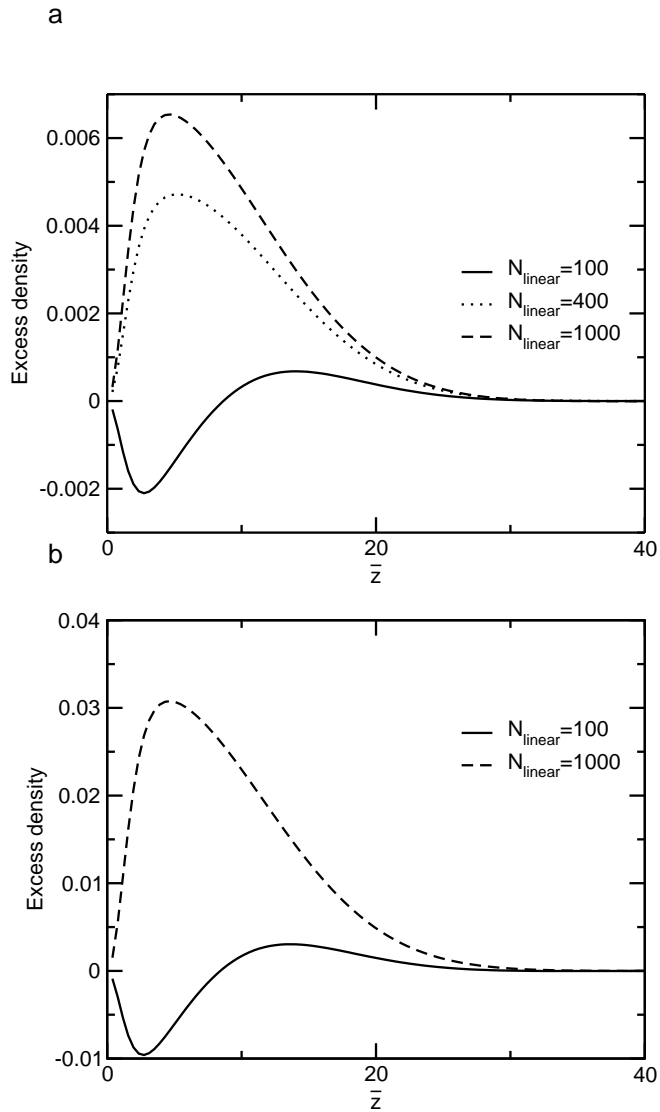


Figure 4.13: Surface excess density profile of cyclic molecules blended with linear molecules of equal and much shorter molecular weight. (a)  $\phi_{\text{cyclic}} = 0.01$ , (b)  $\phi_{\text{cyclic}} = 0.05$ .  $N_{\text{cyclic}} = 1000$ .  $\bar{v} = 0.1$  and  $\bar{\rho}_b = 1$ .

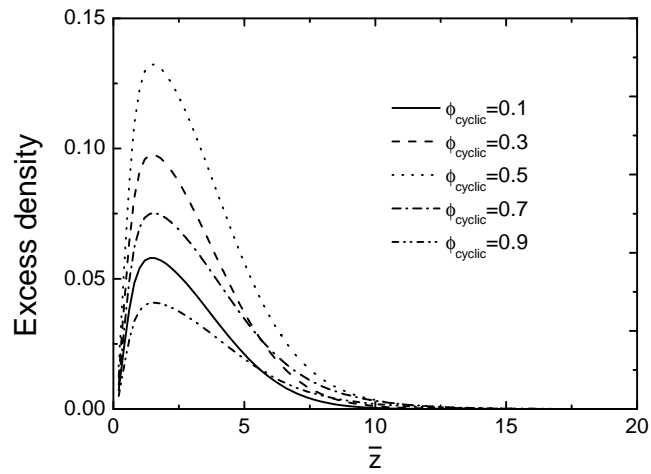


Figure 4.14: The excess surface density of cyclic polymers in cyclic/linear blends for various compositions of cyclic monomers.  $N_{\text{linear}} = N_{\text{cyclic}} = 100$ .  $\bar{v} = 0.1$ ,  $\bar{\rho}_b = 1$ .

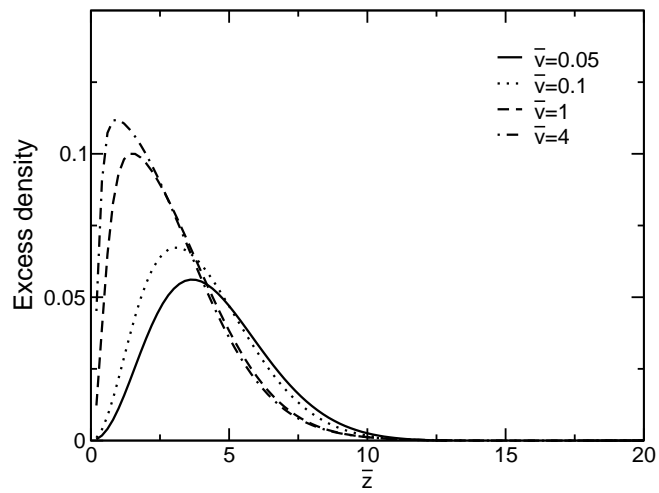


Figure 4.15: The effect of the excluded volume parameter on the cyclic excess density blended with linear chains, with  $N_{\text{linear}} = N_{\text{cyclic}} = 100$  and  $\phi_{\text{cyclic}} = 0.2$ ,  $\bar{\rho}_b = 1$ .

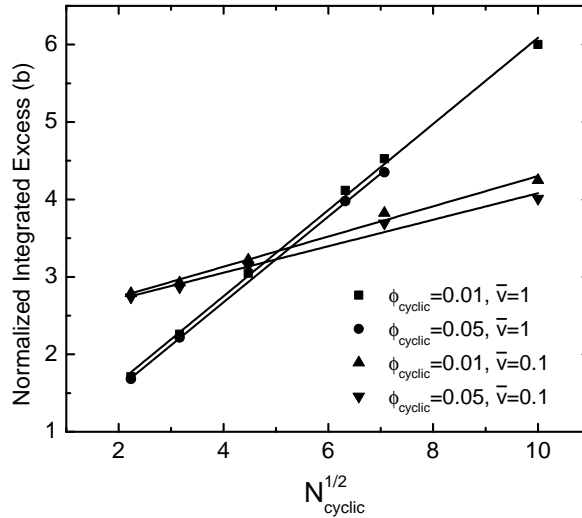


Figure 4.16: The integrated surface excess of cyclic molecules normalized by the bulk density plotted versus  $\sqrt{N_{\text{cyclic}}}$  in blends with linear chains of fixed length.  $N_{\text{linear}} = 100$ ,  $\bar{v} = 0.1$  and 1,  $\phi_{\text{cyclic}} = 0.01$  and 0.05, respectively.

chain ( $N_{\text{cyclic}} = N_{\text{linear}} \approx 370$ ) molecules at 20/80 wt% were studied. In the annealed high molecular weight blend composed of linear dPS with cyclic hPS, the composition of the macrocyclic component determined by NR shows that cyclic molecules are enriched at both air/polymer surface and polymer/substrate interface, which is consistent with the SCFT prediction, and indicates that the entropic driving force for cyclic molecules dominates the surface preference rather than the isotopic effect. Figure 4.17 gives the composition profile of cyclic hPS blended with equal molecular weight linear dPS at high molecular weight  $\approx 37\text{kg/mol}$  [62]. The height of the excess volume fraction is approximately 90% of the bulk volume fraction in Figure 4.17 and shows a good agreement with the SCFT and linear response theory predictions. One discrepancy between experiments and theories is that the enriched regime for NR data is on the order of several  $R_{g,\text{cyclic}}$ , and wider than the SCFT profiles.

In summary, the SCFT predicts that cyclic molecules (that are long enough to be considered Gaussian in conformation) can segregate to the surface when blended with lin-

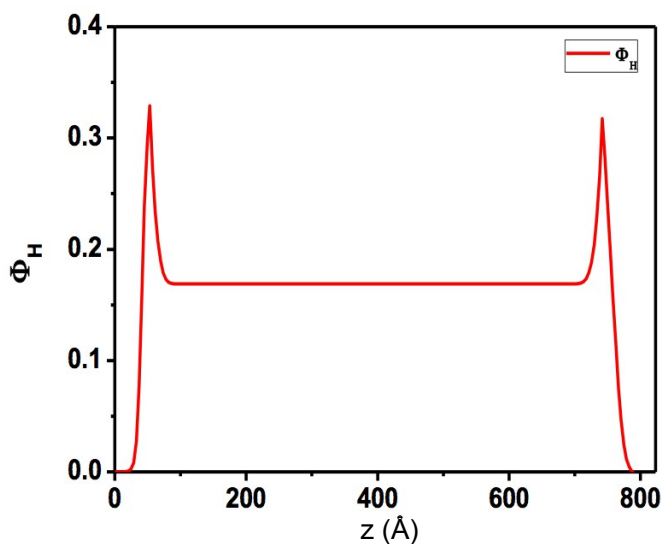


Figure 4.17: The depth profile for hydrogenous macrocyclic CPS37k blended with deuterated linear PS37k in 20/80 wt%.  $\phi_H$  corresponds to the volume fraction of the CPS37k, with molecular weight  $\approx 37$ kg/mol. The surface is at  $z \approx 0$  and the interface is at  $z \approx 800 \text{ \AA}$  [62].

ear chains that are the same molecular weight or higher than the cyclic molecules. The peak in the surface density profile of the cyclic component depends weakly on the cyclic molecular weight. SCFT calculations for the cases studied here show that the maximum value of the surface density is approximately 70 – 80% greater than the bulk density, a little less than the 100% predicted by linear response theory in a limiting case analysis. The integrated surface excess for symmetric cyclic/linear blends shows a trend that  $Z_{\phi=0.5}^* > Z_{\phi=0.3}^* > Z_{\phi=0.7}^* > Z_{\phi=0.1}^* > Z_{\phi=0.9}^*$ , which is not symmetric in the composition as was found in branched/linear blends. The integrated total excess of the cyclic molecules for  $N_{\text{cyclic}} < N_{\text{linear}}$  is also shown to be linear to the size of cyclics, for fixed length of the linear molecules. In blends composed of long cyclic but shorter linear molecules, the entropic potential depicts a surface preference on linear species which is a similar result to that in the long chain/short chain blends. These results are in qualitative agreement with the predictions of the linear response theory in limiting conditions. In particular, the prediction that cyclic chains are found at nearly twice the bulk concentration in blends with long liners was

validated by experiments on cyclic/linear blends of 37k MW polystyrene chains.

#### 4.5 Surface segregation in blends of comb and linear polymers

Previously, van der Linden *et al.* [142] studied the surface enrichment of a comb homopolymer solution using incompressible lattice SCFT. The structural parameters characterizing the comb polymer, i.e., the number of teeth,  $p$ , the number of repeat units between two teeth,  $L$ , and the number of repeat units on a tooth,  $M$ , each show different contributions to the surface adsorption of the molecule. They concluded that teeth are entropically unfavorable by the surface, but the backbone segments are favored by the surface. As a highly branched molecule, a comb structure also has a significant entropic surface preference when mixing with linear molecules. Linear response theory also provides predictions of the comb molecules in the blend with linear chains in equal and differing molecular weight. In this section, I use the compressible SCF theory, which accounts for the entropic surface potential to study the surface enrichment in blends of linear polymer with regularly branched combs, and in particular consider the case of densely branched combs.

##### 4.5.1 SCFT calculations for the surface segregation in comb/linear blends

Surface segregation in comb and linear polymer blends are generally similar to that in blends containing branched and linear molecules. For all calculations,  $\bar{v} = 0.1$  and  $\bar{\rho}_b = 1$ . An example of the entropically driven surface segregation in a comb/linear blend is given in Figure 4.18 using a comb model with  $N = 190$  total repeat units, structured according to the parameters  $L = 10$ ,  $M = 10$  and  $p = 10$ , and mixed with a linear component with varying lengths. Similar to the earlier observations in branched polymer blends, a mixture with long linear chains and short combs shows the combs to be strongly enriched at the surface. Blends containing short linear but larger combs can still have linear components enriched at the surface. For very short linear chains,  $N = 10$ , the excess density in Figure 4.18 shows that only the linear species segregates to the surface. For  $N_{\text{linear}} = 100$ , although the preferred species is the linear chain, the comb can still be enriched in a region near the surface

peaking at a distance  $z \approx R_{\text{comb}}$  from the surface. Next, comparisons between blends with

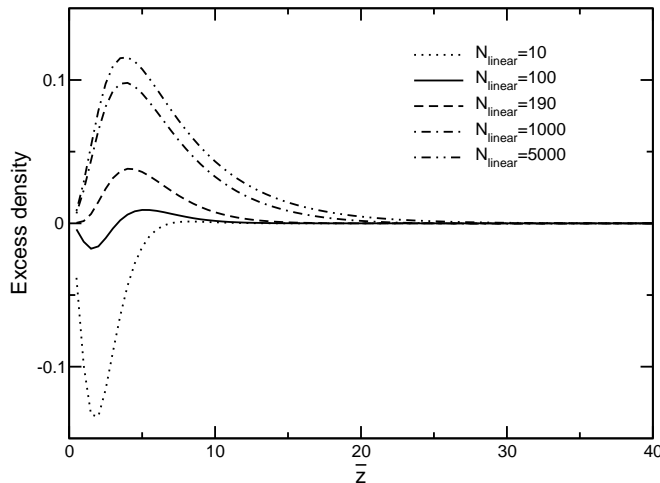


Figure 4.18: Excess density profiles of combs in comb/linear blends with  $\phi = 0.5$ .  $N_{\text{comb}} = 190$  with  $L = 10$ ,  $M = 10$  and  $p = 10$ .

equal and different molecular weights are perfumed at different compositions. The strongest surface excess among all the calculations is obtained when  $\phi_0 = 0.5$ . Comparing the cases having a linear species with  $N = 1000$  to  $N = 190$ , the excess density becomes much greater for  $\phi_{\text{comb}} = 0.7$  than  $\phi_{\text{comb}} = 0.3$ . The SCFT results for the composition dependence in comb/linear blends with equal and different molecular weights are shown respectively in Figure 4.19 and Figure 4.20.

The integrated total excess profiles do not peak at  $\phi_{\text{comb}} = 0.5$  in disparate blends. Figure 4.21 shows the integrated excess of the comb/linear blends. For short linear, the excess of comb is negative, but has a minimum at lower comb monomer composition. The blends with equal molecular weight of comb and linear can still be approximately symmetric at  $\phi = 0.5$ . When the degree of polymerization of the linear is greater than comb, the maximum total excess shifts towards higher comb concentrations around  $\phi_{\text{comb}} = 0.7$ . The directions of these shifts are consistent with predictions of the linear response theory [21], though not in quantitative agreement for every case.

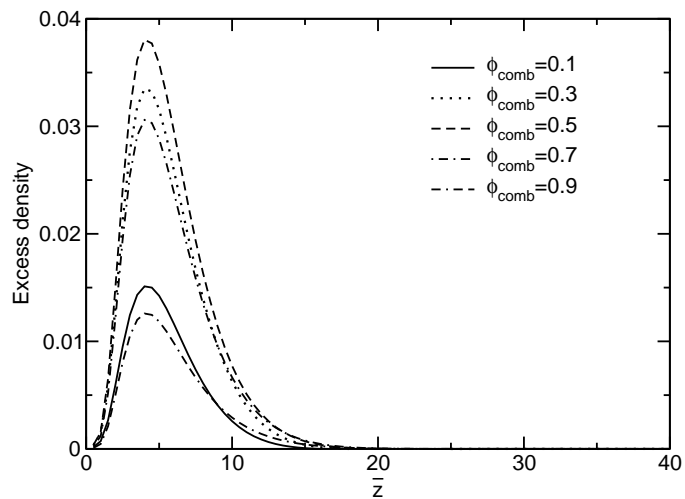


Figure 4.19: Excess density profiles of combs in comb/linear blends with equal degrees of polymerization.  $N = 190$  and the comb has parameters  $L = 10$ ,  $M = 10$  and  $p = 10$ .

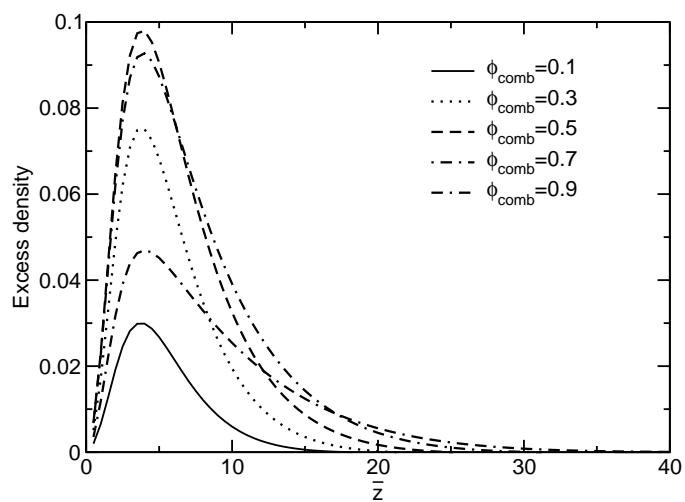


Figure 4.20: The comb density profiles for a blend of shorter comb molecules with longer linear chains.  $N_{\text{comb}} = 190$ ,  $N_{\text{linear}} = 1000$ , and the comb has parameters  $L = 10$ ,  $M = 10$  and  $p = 10$ .

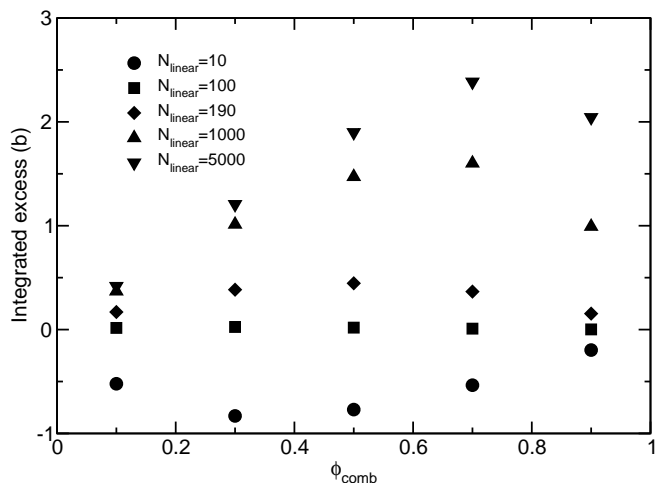


Figure 4.21: The integrated comb excess profiles for comb/linear blends with equal and different molecular weights at different compositions. The degree of polymerization of the comb is fixed at  $N_{\text{comb}} = 190$ , with  $L = 10$ ,  $M = 10$ ,  $p = 10$ .

The surface enrichment due to changes in the architectural parameters, such as the number of teeth, length and spacing are presented in Figure 4.22, with fixed linear chain length  $N_{\text{linear}} = 1000$ . In panel a, the comb has  $L = 10$  and  $M = 10$  but a changing number of teeth from  $p = 2$  to  $p = 20$ . The integrated excess is shown to be approximately linear in  $p$ , and thus linear in the total comb molecular weight, assuming fixed tooth spacing and length. Panel b indicates that the surface excess also increases with elongating the tooth length  $M$ , but saturates at longer teeth length. In contrast, the total surface excess decreases with increasing spacing between teeth, as shown in panel c. Thus the integrated excess does not depend solely on the molecular weight, but the architectural parameters of the comb as well.

#### 4.5.2 Surface segregation in blends of linear polymer and densely branched combs

As follows from the previous section, a dense comb with very small spacing,  $L$ , between branch points on the backbone can show significant surface segregation in a blend with

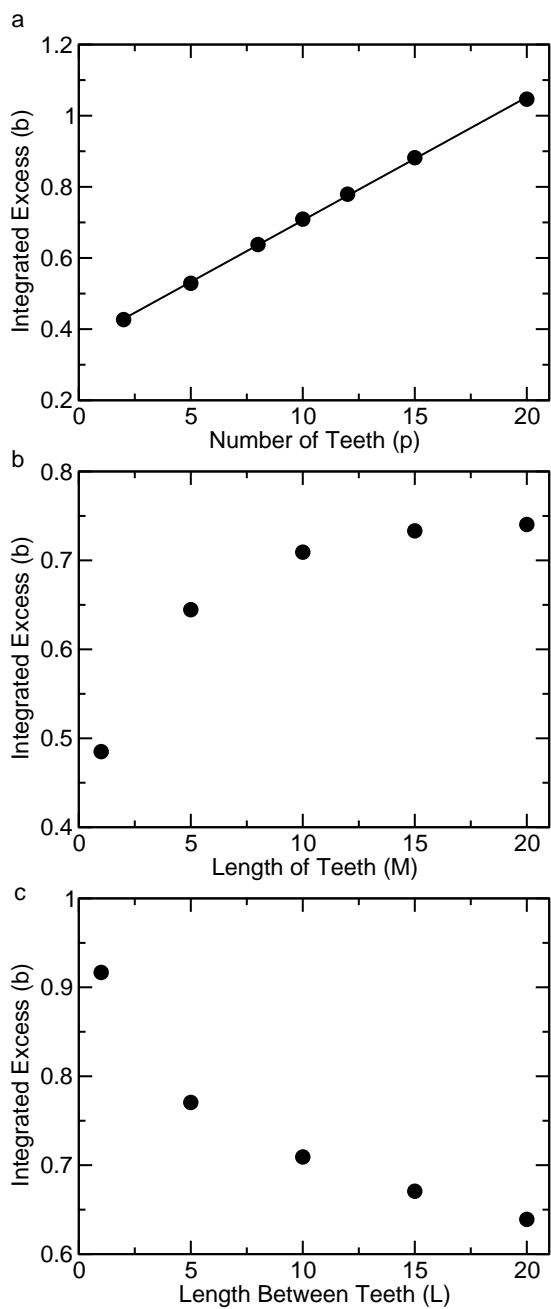


Figure 4.22: The integrated excess profiles of comb polymers with different structures blended with linear chains of fixed length  $N_{\text{linear}} = 1000$ . (a) Varying number of teeth,  $p$ , with  $L = 10$  and  $M = 10$ . (b) Varying length of teeth,  $M$ , with  $p = 10$  and  $L = 10$ . (c) Varying length between teeth,  $L$ , with  $M = 10$  and  $p = 10$ . In all calculations,  $\bar{v} = 0.1$ ,  $\phi_{\text{comb}} = 0.2$ , and  $\bar{\rho}_b = 1.0$

linear polymer. As  $L \rightarrow 0$ , the comb architecturally approaches a star polymer. SCFT is applied to model such densely branched combs in blends with linear molecules. The study uses a molecular model of comb having  $p = 100$ ,  $L = 1$  and  $M = 10$ . Choosing the linear to have similar degree of polymerization as the comb,  $N_{\text{linear}} = 1100$ , (the exact equal molecular weight is  $N_{\text{linear}} = 1099$ ), the excess density profiles are shown in Figure 4.23. Compared to the result of a comb with  $p = 10$ ,  $L = 10$  and  $N_{\text{linear}} = 190$  in Figure 4.19, the maximum excess density of dense combs at  $\phi_{\text{comb}} < 0.5$  are significantly larger than those at  $\phi_{\text{comb}} > 0.5$ . However, the depth of the segregated region for  $\phi_{\text{comb}} = 0.1$  is not as wide as for  $\phi_{text{comb}} = 0.9$ . This result suggests that for a symmetric blend with highly dense comb and linear molecules, a choice to approach strong segregation is to maintain  $\phi_{\text{comb}} < 0.5$ . Even for the case  $\phi_{\text{comb}} = 0.1$ , the excess density is close to that at  $\phi_{\text{comb}} = 0.5$ .

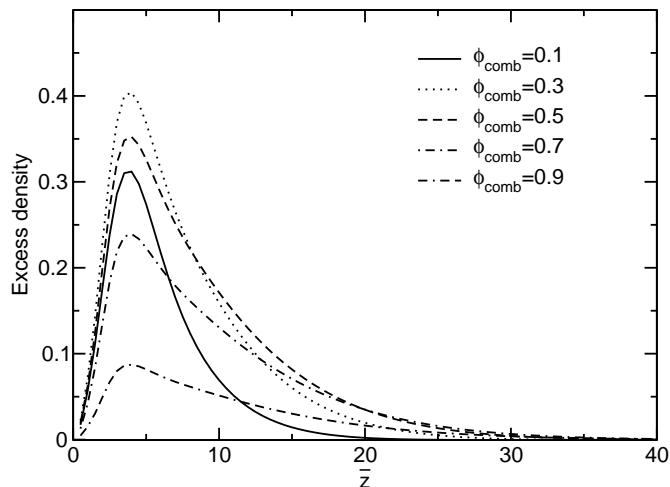


Figure 4.23: The excess density of densely branched comb molecules in a blend with linear chains.  $N_{\text{comb}} = 1099$ ,  $L = 1$ ,  $M = 10$  and  $p = 100$ . The linear chain has the same molecular weight as that of the combs,  $N_{\text{linear}} = 1100$ ,  $\bar{\rho}_b = 1$ , and  $\bar{v} = 0.1$ .

Figure 4.24 plots the excess density profiles of comb/linear blends where the length of the linear species is  $N = 100$ , which is close to the length of the linear backbone of the comb,  $(p - 1)L = 99$ . The comb molecules are still strongly favored to the surface, despite

being much heavier. At low comb compositions, e.g.,  $\phi_{\text{comb}} = 0.1$ , the short linear molecules cannot segregate to the surface. At higher comb compositions, ( $\phi_{\text{comb}} \geq 0.3$  in the figure) the molecular weight effect causes a slight segregation for short linear chains at the surface.

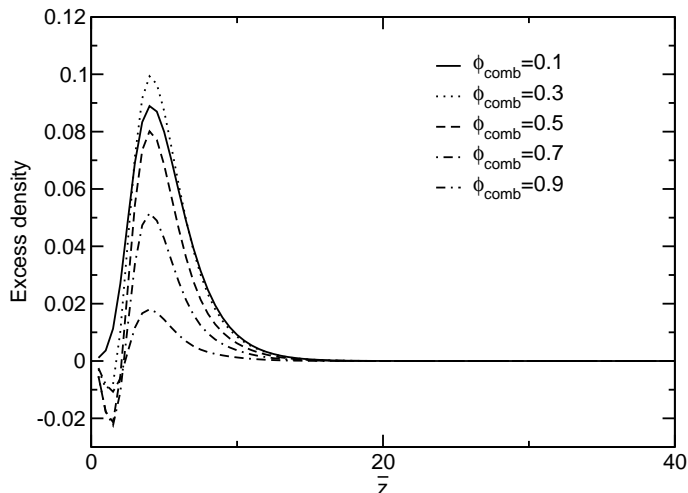


Figure 4.24: The excess density of comb molecules in a blend with linear chains.  $N_{\text{comb}} = 1099$ ,  $L = 1$ ,  $M = 10$  and  $p = 100$ .  $N_{\text{linear}} = 100$ ,  $\bar{\rho}_b = 1$ , and  $\bar{v} = 0.1$ .

#### 4.6 Surface segregation of branched/linear blends with surface potentials on ends and branch points

Up to this point in the chapter, the calculations have focussed on the entropic contributions to the driving force for surface segregation. In this section, I explore the effect of enthalpic contributions to the surface potentials for branch points and ends on surface segregation of the branched species. Derivations and notations for the modification of the SCFT can be referenced in section 3.3 of Chapter 3.

SCFT calculations of a star/linear blend with an enthalpic attraction for chain ends are performed with the incorporation of a short-ranged attractive mean-field surface potential. I consider the case of blends with equal branched and linear molecular weights and assume the strength of the surface potential for linear chain ends,  $U_1$ , is equal to that of the branched

species,  $U_e$ . The resulting surface density profiles plotted in Figure 4.25 show that the surface with  $U_e = -0.1kTb$  is enhanced slightly compared to the blend without attractive ends. As the attraction strength increases from  $U_e = -0.1kTb$  to  $-1.0kTb$ , the enrichment

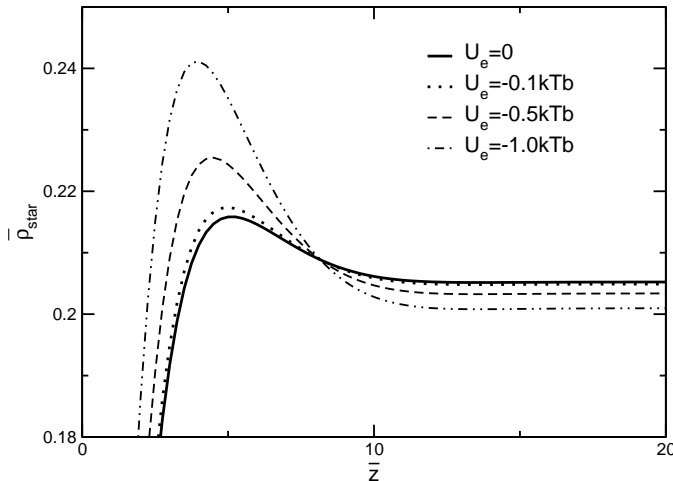


Figure 4.25: The surface density profiles of 4-star/linear blends with varying strengths of the surface attractive potential for chain ends.  $N_{\text{star}} = N_{\text{linear}} = 100$ ,  $\bar{v} = 0.1$ ,  $\bar{\rho}_b = 1.0$  and  $\phi_{\text{star}} = 0.2$ . Surface potentials for ends range from  $U_e = -0.1kTb$  to  $-1.0kTb$ .

of star molecules at the surface increases multiple-fold. The magnitude of the increase is not significant because of the competition of the attraction to ends on linear branched molecules. For  $U_e = -1.0kTb$ , it increases approximately 30% more than that for  $U_e = 0$ . The enthalpic end effect is also discussed by linear response theory in a blend of short star but long linear polymers [21]. The calculations did not account for the ends on the linear chains so that it obtains significant increase in excess density as the attractive end potential increases.

I have also performed calculations for the surface enrichment of stars as a function of increasing number of arms. As expected and shown in Figure 4.26a, the surface segregation increases with the number of arms of fixed arm length. Figure 4.26b plots the percent increase in the integrated excess with an attractive surface potential of  $U_e = -0.1kTb$  compared to the case of no enthalpic attraction to the surface, i.e.,  $U_e = 0kTb$ . As can be seen in

the figure, the percent increase in surface excess decreases slightly as the number of arms increases between 10 and 40, and thus to get the same percent increase in surface enrichment, a slightly greater surface attraction for ends is needed for stars with many arms.

The effect of a surface repulsion for branch points is shown in Figure 4.27, assuming  $U_e = U_l = 0$  while the branch point potential strength is taken to be  $U_a = 0.1kTb$  or  $1.0kTb$ . The density profile of the star species has a very small change due to  $U_a$  as compared to the significant enhancement in the surface segregation due to a change in the end potential.

In summary, the joint and end potentials can affect surface segregation in a blend. A relatively small attraction, on the order of 1 kT, for ends can have a significant impact on enriching branched polymers, particularly if it is amplified by a large number of chain ends. For the branch points, a relatively larger potential, much greater than 1 kT, is needed to influence the surface segregation of branched molecules. Under typical conditions, enthalpic interactions of chemical groups can easily exceed kT, and so it may be possible to rationalize experimentally observed surface segregation with appropriate surface potentials for specific chemical groups used as branch or end points on a branched polymer. I do so in the following section within the simpler linear response theory for the integrated surface excess and surface profiles.

#### 4.7 Linear response theory on the surface segregation of branched and linear polymer blends

Within linear response theory [21], the general formula of the integrated surface excess is controlled by the effective surface potential on branch points and ends in section 3.2

$$\int_0^\infty dz \Delta\phi(z) = \left[ \frac{1}{fN^B} + \frac{1}{(1-f)N^L} \right]^{-1} \left( \frac{2}{N^L} U_e^L - \frac{n_j^B}{N^B} U_j^B - \frac{n_b^B}{N^B} U_e^B \right), \quad (4.7)$$

where the density profile  $\Delta\rho(z)$  is written as the inverse Fourier Transform (designated a symbol of  $\mathcal{F}^{-1}$ ) of the response function:

$$\Delta\rho(z) = \rho_b \Delta\phi(z) \mathcal{F}^{-1} \left[ \left( \frac{S_{\rho\rho}^B(\mathbf{q})}{S_{\rho\rho}(\mathbf{q})} \right) S_{\rho\rho}^L(\mathbf{q}) U_e^L - \left( \frac{S_{\rho\rho}^L(\mathbf{q})}{S_{\rho\rho}(\mathbf{q})} \right) (S_{\rho e}^B(\mathbf{q}) U_e^B + S_{\rho j}^B(\mathbf{q}) U_j^B) \right]. \quad (4.8)$$

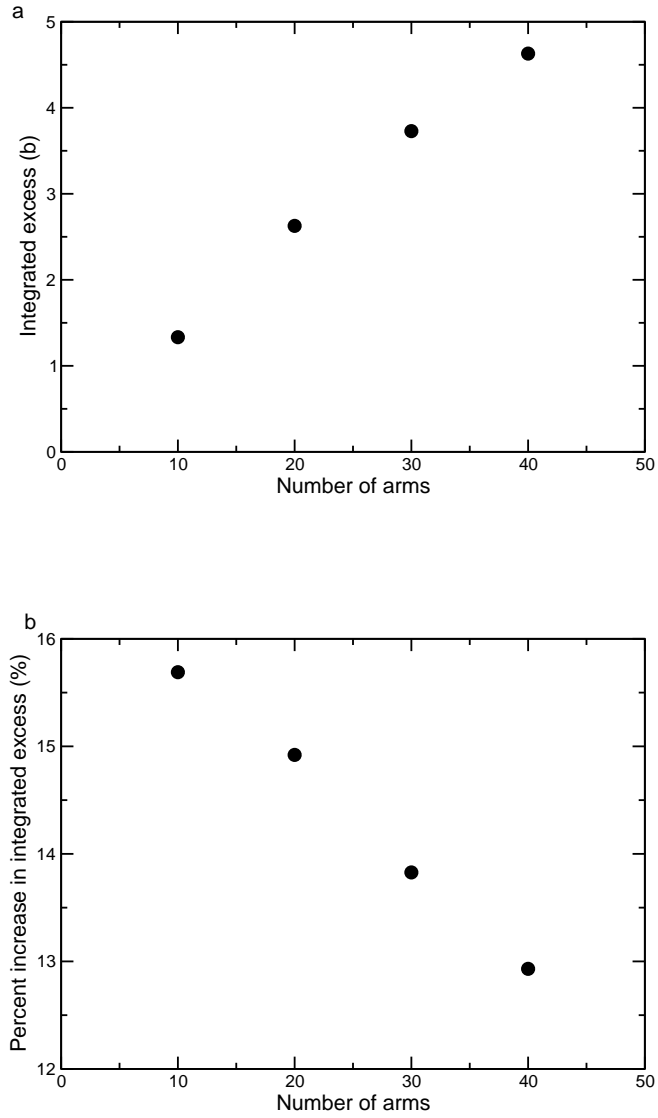


Figure 4.26: (a) The integrated surface excess of  $n$ -star/linear blends versus number of star arms by introducing an attractive surface potential  $U_e = -0.1kTb$  for chain ends. (b) The percent increase in the integrated surface excess density of stars in the same  $n$ -star/linear blends.  $N_{\text{arm}} = 25$  and  $N_{\text{linear}} = 100$ .  $\bar{v} = 0.1$ ,  $\bar{\rho}_b = 1$ , and  $\phi_{\text{star}} = 0.2$ .

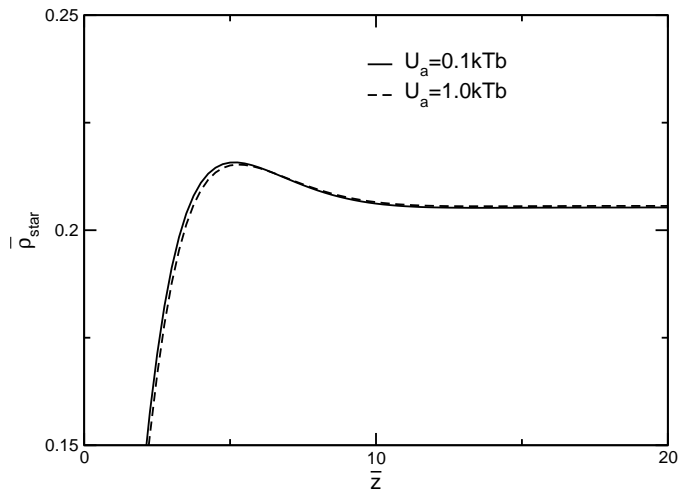


Figure 4.27: The effect of a repulsive surface potential  $U_a$  for branch points on the surface density profiles of a 4-star polymer blended with linear polymer.  $N_{\text{star}} = N_{\text{linear}} = 100$ ,  $\bar{v} = 0.1$ ,  $\bar{\rho}_b = 1$  and  $\phi_{\text{star}} = 0.2$ .

#### 4.7.1 Surface segregation of two families of branched polymers

Therefore, given the surface excess profiles, or at least the integrated excess, of a series of end-branched/linear polymer blends, one can estimate the corresponding surface potentials for each specific branch or end group. Recently Lee *et al.* [9] reported the synthesis of the end-branched polystyrene molecules described earlier, and performed experiments to measure the surface segregation in blends with their linear analog [18]. Samples were prepared with a linear monomer composition of  $\phi_{\text{linear}} = 0.8$  and coated onto a substrate. The branched structures include 6-star, 6-pom, 6-end, 9-end, and 13-end. Surface density profiles were obtained from NR experiments. The density profiles of the first family of blends of linear and branched molecules with 6 ends are plotted in Figure 4.29, and the density profiles of the second family of end-branched PS and deuterated linear PS blends, which all have 4 branch points, from NR experiments are shown in Figure 4.30.

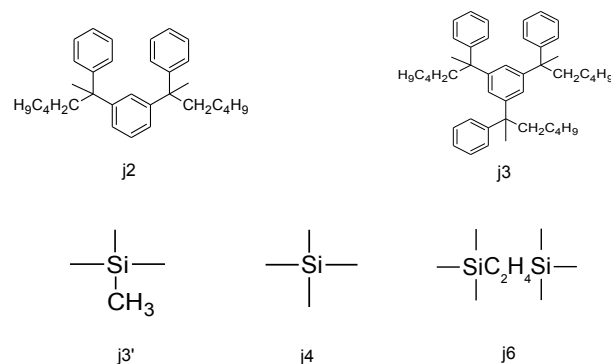


Figure 4.28: The chemical structures and nomenclature of the functional groups of joints on the branched molecules studied by Lee *et al.* [9]

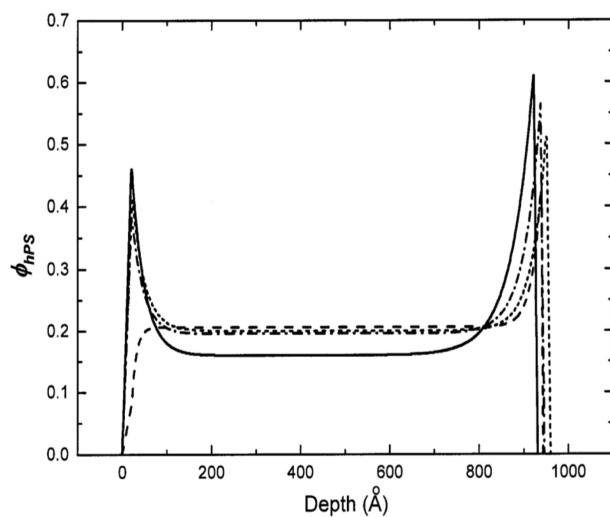


Figure 4.29: The composition profiles for a family of blends of hydrogenous branched chain structures having 6 ends with linear dPS [18]. The bulk volume fraction is 20 vol% hydrogenous branched PS. The air/polymer surface is at  $z = 0$  and polymer/substrate interface is at  $z \approx 900 \text{ \AA}$ . Dashed line: Linear/dPS. Dash-dot-Dashed line: 6-star/dPS. Dotted line: 6-pom/dPS. Solid line: 6-end/dPS.

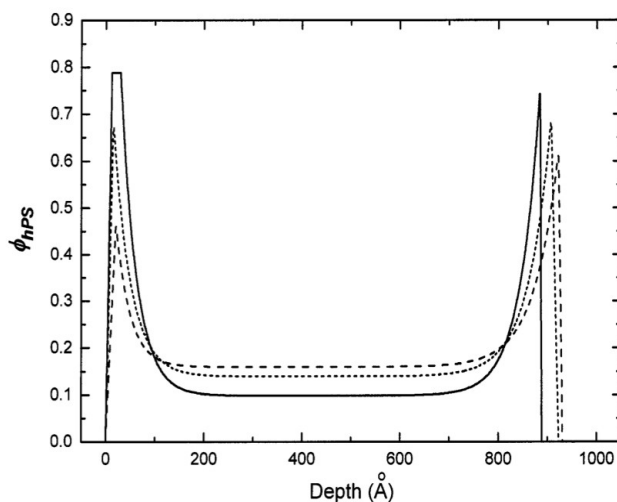


Figure 4.30: The composition profiles for a family of blends of hydrogenous end-branched chain structures having 4 branch points with linear dPS [18]. The bulk volume fraction is 20 vol% hydrogenous branched PS. The air/polymer surface is at  $z = 0$  and polymer/substrate interface is at  $z \approx 950\text{\AA}$ . Dashed line: 6-end/dPS. Dotted line: 9-end/dPS. Solid line: 13-end/dPS.

The linear dPS was enriched at the air/polymer surface in the linear/linear isotope blend due to the isotopic effect. However, all of the branched hPS with 6 ends are favored at both the surface and interface. The integrated excess on both the surface and interface increased with the number of branch points (from 1 on the 6-star to 4 on the 6-end) and the excess at the substrate interface is greater than that at the air surface for all three blends. Figure 4.30 shows that when the number of branch points are fixed, the surface and interface enrichment increases with the number of branches. In general, both the number of branch points and number of branches were found by NR to enhance the surface enrichment. The integrated surface excesses are listed in Table 4.1.

The NR excesses are used to fit surface potentials for end and branch groups using the linear response theory. There are two sets of surface potentials: one for the surface, and one for the interface. A correction is made to subtract the enthalpic contribution due to isotopic substitution in the linear hPS/dPS blend, namely  $-2\text{\AA}$  from each value of the surface excess, and  $5\text{\AA}$  from each of the interface excesses. For either the surface or the interface, the linear

Table 4.1: The integrated surface and interface excess of the hydrogenous branched PS molecule blended with deuterated linear PS by NR [18, 143]. The uncertainties are  $\pm 1\text{\AA}$ .

hPS Structure	Surface Excess( $\text{\AA}$ )	Interface Excess( $\text{\AA}$ )
Linear	-2	5
6-star	6	15
6-pom	8	12
6-end	11	19
9-end	22	28
13-end	33	29

response equations can be written as a system of 5 linear equations (one for each blend) in 7 variables (one for each branch or end group type):  $U_e, U_1, U_{j2}, U_{j3}, U_{j3'}, U_{j4}$ , and  $U_{j6}$ .

$$\begin{aligned}
& \left( \frac{1}{fN_{6\text{star}}} + \frac{1}{(1-f)N_{\text{lin}}} \right)^{-1} \left( -\frac{U_{j6}}{N_{6\text{star}}} - 6\frac{U_e}{N_{6\text{star}}} + 2\frac{U_1}{N_{\text{lin}}} \right) = Z_{6\text{star}}^*, \\
& \left( \frac{1}{fN_{6\text{pom}}} + \frac{1}{(1-f)N_{\text{lin}}} \right)^{-1} \left( -\frac{U_{j2}}{N_{6\text{pom}}} - 2\frac{U_{j3'}}{N_{6\text{pom}}} - 6\frac{U_e}{N_{6\text{pom}}} + 2\frac{U_1}{N_{\text{lin}}} \right) = Z_{6\text{pom}}^*, \\
& \left( \frac{1}{fN_{6\text{end}}} + \frac{1}{(1-f)N_{\text{lin}}} \right)^{-1} \left( -\frac{U_{j3}}{N_{6\text{end}}} - 3\frac{U_{j3'}}{N_{6\text{end}}} - 6\frac{U_e}{N_{6\text{end}}} + 2\frac{U_1}{N_{\text{lin}}} \right) = Z_{6\text{end}}^*, \\
& \left( \frac{1}{fN_{9\text{end}}} + \frac{1}{(1-f)N_{\text{lin}}} \right)^{-1} \left( -\frac{U_{j3}}{N_{9\text{end}}} - 3\frac{U_{j4}}{N_{9\text{end}}} - 9\frac{U_e}{N_{9\text{end}}} + 2\frac{U_1}{N_{\text{lin}}} \right) = Z_{9\text{end}}^*, \\
& \left( \frac{1}{fN_{13\text{end}}} + \frac{1}{(1-f)N_{\text{lin}}} \right)^{-1} \left( -\frac{U_{j3}}{N_{13\text{end}}} - 3\frac{U_{j6}}{N_{13\text{end}}} - 13\frac{U_e}{N_{13\text{end}}} + 2\frac{U_1}{N_{\text{lin}}} \right) \\
& = Z_{13\text{end}}^*.
\end{aligned} \tag{4.9}$$

The subscripts match the nomenclature for the branch group type as depicted in Figure 4.28 above;  $U_e$  and  $U_1$  are the surface potentials for ends on the branch molecule and linear molecule respectively. Actually, the linear molecule as synthesized by Lee *et al.* [9] has two types of ends, a butyl initiator and a terminal hydrogen, but since a linear molecule always presents with one of each end type, we can take  $U_1$  to be the *average* surface potential for the two linear chain ends within linear response theory.

Since the number of unknowns exceeds the number of equations by two, two extra conditions are needed to arrive at a set of surface potentials. I explore below a few physically motivated assumptions, for instance based on chemical similarity of the branch groups, shown in Figure 4.28 [9], and assess the resulting potentials for chemical and physical plausibility.

A first assumption I tested was that the chain ends have the same surface potential,  $U_e = U_1$ . However, this assumption caused a failure to fit the density profiles regardless of other assumptions on the similarity of the branch points for both the surface and interface. Therefore, I followed with the assumption that the two types of ends have different surface potentials, i.e., keep  $U_e$  and  $U_1$  independent, but assume the joints satisfy  $U_{j4} = U_{j3'}$  (each containing a Si group) and  $U_{j2} = U_{j3}$  (each containing phenyl groups). These assumed conditions lead to the result that the surface potential for the proton end of the linear chain is about three times as strong as that for a butyl end. There is a slight surface attraction for the Si containing branch points  $U_{j4}$  and  $U_{j3'}$  and a slight repulsion for  $U_{j6}$ . This may appear to be physically surprising, since the j6 branch group has two Si groups; however, the magnitude of these potentials are all very small—probably within the error bars associated with propagation of experimental uncertainties—and perhaps the best conclusion is that the Si containing groups do not have a strong interaction with the surface compared with the other groups. However, the derived potentials with the interface are not small, and the fit for the interface is less physically satisfactory.

The resulting calculated surface and interface potentials are shown in Table 4.2. The excess density profiles of the branched species can be calculated by substituting the surface potentials into Equation 4.8, and are plotted in Figure 4.31. In these calculations, I used the reported value of  $b = 6.2\text{\AA}$  for the average statistical segment length for all polymers [19].

The decay lengths found from experiment and from linear response theory are compared in Table 4.3. As can be seen, the rough magnitudes of the experimental decay lengths show some agreement, but the experimental trends are not well reproduced by the theory. The theoretical decay lengths at the surface are about  $30\text{\AA}$ , but the 6-star decay length is slightly

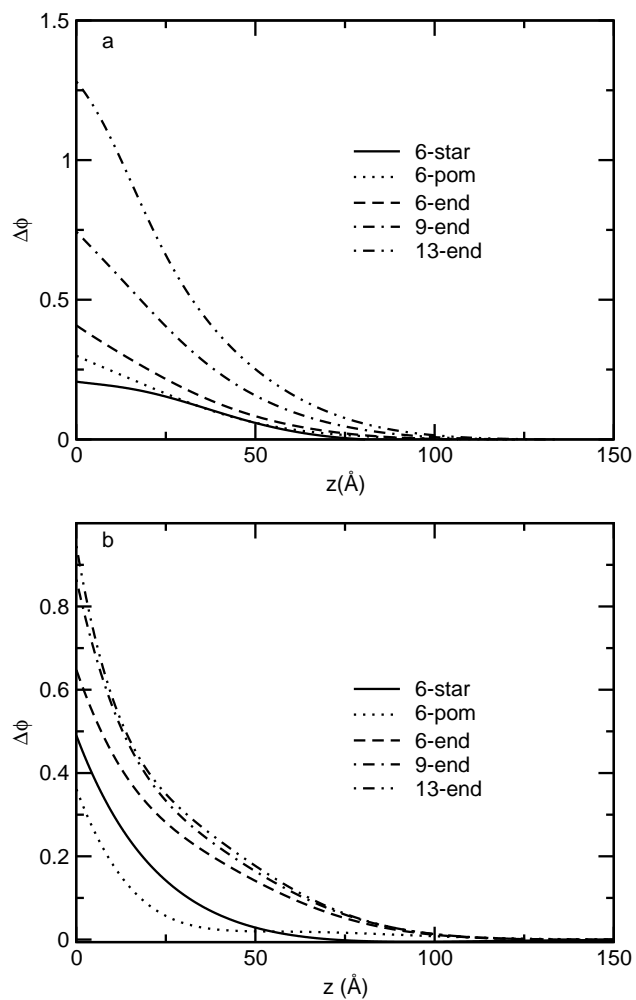


Figure 4.31: Excess density profiles of the branched/linear blends with 20 vol% branched component by linear response theory normalized by bulk density  $\rho_b$ . Surface and interface potentials on joints and ends in Table 4.2 are applied. (a) Excess density profiles at the air/polymer surface. (b) Excess density profiles at the interface. Note also that the linear response theory assumed there were 15 ends on the 13-end molecule, as 15 was the nominal target synthetically.

Table 4.2: The surface and interface potentials of functional groups of branched and linear polymers from linear response theory, under the assumptions that  $U_{j4} = U_{j3'}$  and  $U_{j2} = U_{j3}$ .

Name	Surface potential (kT Å)	Interface potential (kT Å)
$U_e$	-25.6	-10.5
$U_1$	-46.6	-29.8
$U_{j2}$	-16.0	98.1
$U_{j3}$	-16.0	98.1
$U_{j3'}$	-2.3	-71.3
$U_{j4}$	-2.3	-71.3
$U_{j6}$	4.1	55.5

larger than that of 6-pom and 6-end. At the polymer/substrate interface, the 6-star and 6-pom have smaller decay lengths when compared to those of the end-branched polymers. However, the uncertainty in the experimental decay lengths may be high enough that the exact trends are not significant. For instance, one might expect the equal molecular weight series of 6-end, 9-end, and 13-end to correspond to smaller and smaller sizes, and thus smaller and smaller decay lengths. However, the experimental decay length of the 9-end is much smaller than the other two. Another source for the discrepancy may lie in the experiments exceeding the limits of the linear response regime: Note that the composition profiles for the most highly branched species exceed 1, which reflects an unphysical over-response of the density due to the high-driving force for segregation associated with a high number of chain ends.

#### 4.7.2 Surface segregation of densely branched combs

The experiments [16] and SCFT calculations in this chapter have shown that densely branched comb polymers can strongly segregate to a surface or interface. Recently, densely branched comb polymers have been synthesized by Liu *et al.* with only one monomer between branch points on the backbone [16]. I first consider the surface segregation due to entropic effects alone. The surface concentration of the comb in a blend of  $p=28$ ,  $M=24$  and  $L=1$

Table 4.3: The decay lengths of surface density profiles in branched/linear blends from linear response theory and experiments. Surface and interface potentials in Table 4.2 are applied [18,143].

Branched polymer	Decay length (Å)			
	Experiment		Theory	
	Surface	Interface	Surface	Interface
6-star	28	25	33.0	18.7
6-pom	30	35	30.4	14.6
6-end	33	40	29.8	31.0
9-end	23	30	30.5	28.7
13-end	39	33	29.1	28.6

(namely M28P24,  $N_{\text{comb}} = 699$ ) comb molecules and  $N_{\text{linear}} = 360$  linear molecules at a volume fraction  $\phi_{\text{comb}} = 0.2$ . Figure 4.32 (corresponding to an experimentally studied system below) shows the density profile from linear response theory considering only the entropic contribution to the surface potential. The density profile is consistent with the SCFT result in Figure 4.24 in that the shorter chain is preferred at the immediate vicinity of the surface, but a weak positive surface segregation of comb polymer is obtained at larger distances ( $\sim 4b$ ) from the surface. We see that the entropic potentials are fairly weak, but are already of sufficient strength that when multiplied by the number of branch groups, can cause significant surface segregation. We anticipate then that any enthalpic contributions to the surface potential can also easily drive segregation and possibly saturation of one component at the surface.

The experimental surface concentration of this comb/linear blend measured by NR, shown in Figure 4.33, is about 0.8, which is four times the bulk concentration. This concentration and surface profile can be fit by adjusting the surface potentials, which include enthalpic and entropic contributions, for both ends and joints. A least square fit algorithm is applied to  $\phi_{\text{theory}}$  to match  $\phi_{\text{expt}}$ , while constraining the maximum surface concentration to the experimental value. In addition, it is assumed that the linear ends and comb ends are identical

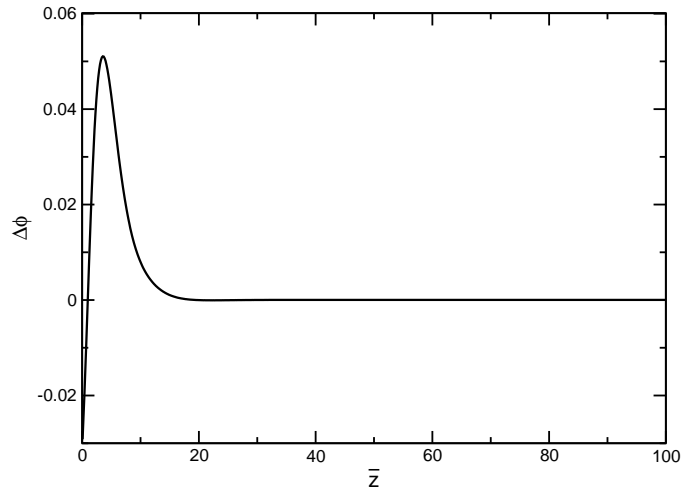


Figure 4.32: The excess density profile, in units of  $(\xi/b)$ , predicted by linear response theory for a comb/linear blend accounting for the entropic surface potential for joints ( $U_j = 0.19kT\xi$ ) and ends ( $U_e = -0.31kT\xi$ ). The mole fraction of comb polymer is  $\phi_{\text{comb}} = 0.2$ .  $N_{\text{linear}} = 360$ ,  $p = 28$ ,  $M = 24$ , and  $L = 1$ .

(neglecting isotopic differences). I consider several scenarios below regarding assumptions for the strength of the joint potential. The first assumption is that of no surface potential for the joint, i.e.,  $U_j = 0kTb$ . This single parameter fit results in a surface end potential of  $U_e = -1.27kTb$ . The integrated excess is much less than the experiments, though the exponential decay length is the right order of magnitude.

The second assumption is that the joint potential is only entropic. The calculations above on branched polymers suggest a much weaker dependence on joint potentials than end potentials. Recall the magnitude of the entropic potential in the linear response theory is proportional to  $\xi = b/\sqrt{3v\rho_b}$ . To be able to make a numerical comparison, we choose a value of  $\xi = b$  (i.e.,  $v = 1/3$ ). In this case, the best fit to the NR curve gives a value of  $U_e \approx -1.62kTb$  for the total (entropic + enthalpic) end potential. The resulting surface profile is shown in Figure 4.33. Subtracting off the entropic part of the potential then leaves the magnitude of the enthalpic attraction for ends to be less than  $1.3kTb$ .

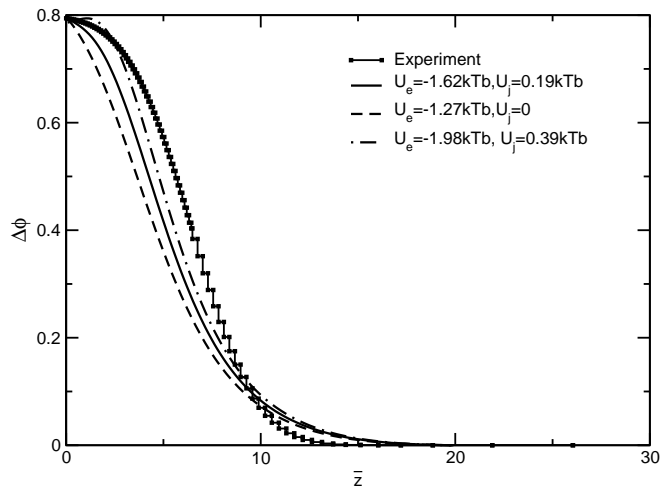


Figure 4.33: Comparison of the excess concentration profiles of comb polymer for the comb/linear blend by linear response theory fitting the surface potential of joints and ends. The mole fraction of comb polymer is  $\phi_{\text{comb}} = 0.2$ .  $N_{\text{lin}} = 360$ ,  $p = 28$ ,  $M = 24$ , and  $L = 1$ .

The third scenario makes no explicit assumption about the joint potential, and so involves a completely free fit varying both  $U_e$  and  $U_j$ . In this case,  $U_e = -1.98kTb$  and  $U_j = 0.39kTb$ . The maximum surface density is found at a distance slightly away from the wall ( $\sim 2b$ ). Such a maximum is not considered in the experimental determination of the surface profile when fitting from NR data. This profile, however, provides an integrated excess that is closer to the experimental value than the other two cases.

Exploring these three scenarios lead to some consistent observations. One conclusion is that a very weak ( $\sim 1kTb$ ) enthalpic surface attraction for ends can lead to significant surface enrichment of combs. In comparison, a moderate enthalpic repulsive potential for joints is not a significant factor affecting the surface excess. Enthalpic isotopic effects become less significant also next to the surface potentials acting on comb ends, as compared with the situation for the end-branched polymers.

In a word, the preliminary comparison between linear response theory calculation and NR experiment for surface segregation of a densely branched comb, M24P28 and linear

polystyrene blends implies that the comb strongly favors the surface even by pure entropic attraction. Because the joints are identical monomers as the backbone, the repulsive entropy does not show apparent influence on surface segregation.

## 4.8 Summary

Numerical SCFT and linear response theory are applied to study surface segregation in binary blends with linear and a variety of nonlinear polymers. This theory work was strongly motivated to help explain experimental studies of the architectural effects in surface segregation.

SCFT calculations have shown that nonlinear species can undergo surface segregation because of both enthalpic and entropic effects. Nonlinear polymer species are studied include star, pom-pom, end-branched, cyclic and comb architectures. In homogeneous binary blends containing such architectures, these architectural driving forces for segregation can occur simultaneously with driving forces based on molecular weight. I focussed first on the case of entropic driving forces alone, unless otherwise stated.

In the case of short linear molecules mixing with a larger nonlinear component, the excess density profiles of the nonlinear species have shown a negative density layer at the surface, which scales as  $R_g$  of the linear molecule. However, for mixtures with small nonlinear and long linear molecules, the nonlinear species is enriched at the surface and linear molecules are repelled when driven only by conformational entropy. In general, theoretical results indicates that the integrated excesses and surface concentrations of all types of nonlinear species increases as the molecular weight of the linear component decreases.

For equal molecular weight binary polymer blends, the nonlinear species is enriched at the surface when driven by entropic forces. Changing the architecture of the branched polymer can significantly change the amount of surface segregation. Calculations have shown that the surface excess increases linearly with additional arms to a star, and it also increases by adding more branches on end-branched molecules. The thickness and the position of the maximum excess density for star and end branched polymers are scaled to the branch

length  $R_{g\text{branch}}$ . A symmetric star/linear blend results in a parabolic relationship between the surface excess and the volume fraction.

The entropic surface enrichment of cyclic molecules due solely to the cyclic topology without extra surface interactions have been predicted by linear response theory. In cyclic/linear polymer blends, the excess density is about 70-80% of the bulk density. The maximum surface density weakly varies with the molecular weight of the cyclic when  $N_{\text{cyclic}} \leq N_{\text{linear}}$ . SCFT calculations also show that the integrated total excess for cyclic molecules linearly increases with the size of the cyclic,  $R_g$ , which is behavior that is distinctive from the branched/linear blend. The slopes of the function  $Z^*(\sqrt{N})$  against  $\sqrt{N}$  depends on excluded volume  $v$ , but independent of the concentration.

Comb polymers can be strongly enriched at the surface and interface as an additive in linear hosts. The amount of surface excess depends on structural parameters, such as the number of teeth  $p$ , the length of teeth  $M$  and the spacing  $L$ . The dependence of comb architectures are studied assuming comb/linear blends with fixed linear length. SCFT calculations indicate that if the comb degree of polymerization is increased by introducing more teeth but fixing the spacing and teeth length, the total surface excess also increases roughly linearly with the number of teeth  $p$  with fixed  $M$  and  $L$ . The segregation can be enhanced by increasing the length of teeth  $M$  without changing  $p$  and  $L$ . If the spacing  $L$  is increased while keeping  $p$  and  $M$  fixed, the surface excess will decrease.

The surface segregation for combs can be understood by considering the quantity  $pM/(p-1)L$ . When  $L \leq M$ , the comb is more like a linear molecule than a branched polymer, therefore, the entropic effect due to branching is too weak to show significant surface segregation. The integrated excess for a symmetric comb/linear is also approximately parabolic with respect to volume fractions peaking at  $\phi = 0.5$ .

SCFT calculations on a series of 6-pom/linear blends with different branch lengths are performed and compared with NR experiment results. The theory successfully predicts the trend of the total surface excess decreasing as the linear portion of the pom-pom molecule

increases. The 6-star/linear in experiment shows a weaker segregation than that in 6-pom/linear blends. However, the theory predicts 6-star should have the strongest segregation among all 6-pom like molecules since the linear portion is zero. The disagreement between theory and experiment can be resolved in terms of different enthalpic potentials acting on the different branching groups.

An application of linear response theory to the experimental data on different end-branched polymers is performed to characterize architectural effects on the surface segregation. Theoretical results predicts that the methyl end contributes an attraction to the surface which agrees with the discussion by Wu and Fredrickson [21]. On the other hand, the numerical solution of the surface excess equation system implies that the branching effect is weak for Si groups with repulsive surface potentials. The surface potentials for aromatic branching points are also attractive to the surface and interface. In addition, theoretical calculations on experimental molecules are limited by obtaining all species to solve the linear system. In the meantime, experimental profiles are related to the mathematical models to interpret the reflectivity intensity spectra, and to produce the decay lengths. The linear response theory on end-branched polymer and densely branched combs predict the trend of the surface segregation for the nonlinear molecules in the linear host qualitatively, and shows the expected effect of the branch points by attractive and repulsive surface potentials.

The entropic potential in SCFT can be modified by introducing enthalpic surface potentials for joints and ends. The attractive or repulsive potentials on chemical groups change the shape of the density profiles and the total excess. According to the strength of those potentials, the branched species can become more favored at the surface due to larger numbers of ends while the joints are repelled. The surface segregation is determined by the competition between end attraction and joint repulsion.

## CHAPTER 5

### THE INTRA- AND INTERMOLECULAR CORRELATIONS IN LINEAR AND BRANCHED POLYMER MELTS AND BLENDS

As with linear molecules, the conformations of a branched molecule can be strongly influenced by enthalpic interactions and conformational entropy. However, because of the nonlinear connectivity of a branched molecule, monomers experience different local environments or interact with different parts of the molecule, and this can lead to qualitatively different behavior compared to linear molecules. As discussed in Chapter 2, the bulk conformations of nonlinear polymers differ from those of linear molecules, and exhibit enhanced stretching near branch points [125]. To understand stretching and swelling in branched chains, it is useful to consider swelling in linear chains first. Scaling theory is one of the fundamental theories for understanding the conformations of linear chains. In the 1960's, Edwards [87] showed that in a semi-dilute solution, the crossover of the conformations from SAW to random walk is characterized by the Edwards' correlation length  $\xi_E = \sqrt{12v\rho_b}b$ , where  $b$  is the statistical segment length,  $\rho_b$  is the total bulk density, and  $v$  is the excluded volume. The excluded volume is positive for monomers with repulsive interaction, and infinite in the incompressible limit. However,  $\xi_E$  is derived assuming the overall conformation of the molecule is Gaussian. de Gennes showed the correct correlation length of the molecule with SAW statistics should scale as  $\xi = \rho_b^{-3/4}v^{-1/4}b$ . The scaling theory for the intramolecular density distributions and the monomer-monomer distances in a SAW molecule is outlined below. I focus on the scaling relationship between the density  $\rho$  and the excluded volume  $v$ . Within the length scale of  $\xi_E$ , the monomer distribution is taken to depend only on the intramolecular correlation and obey SAW statistics. At length scales beyond  $\xi_E$ , the intermolecular interaction screens the self-avoiding walk and chains obey random walk statistics. The symbol " $\cong$ " below indicates only numerical values have been omitted in the proportion-

ality relationship, while the symbol  $\sim$  indicates a proportionality possibly omitting other variables.

The scaling expression for the monomer density distribution in a single linear chain as a function of distance from a given monomer can be written

$$\bar{\rho}(r) \cong c\bar{r}^\alpha \quad (5.1)$$

up to the size of the molecule, where  $\bar{\rho} = \rho(\bar{r})b^3$  and  $\bar{r} = r/b$  are dimensionless monomer density and distance, respectively.  $c$  is independent of  $\bar{r}$  and the degree of polymerization  $N$ , but a function of the dimensionless excluded volume  $\bar{v} = v/b^3$ . The scaling exponent  $\alpha$  depends on the single chain conformation. In particular,  $\alpha = -1$  for an ideal Gaussian chain, and  $\alpha = -\frac{4}{3}$  for a swollen chain obeying SAW statistics, which is the Edwards' law [34]. The dimensionless size of the molecule,  $\bar{R}$ , scales as

$$\bar{R} \cong \bar{v}^\beta N^\gamma, \quad (5.2)$$

For a single chain at infinitely dilute concentration that obeys SAW statistics (i.e.,  $\alpha = -4/3$ ), we find  $\beta = 1/5$  and  $\gamma = 3/5$ , respectively. The integral of  $\bar{\rho}(r)$  over the range of chain length scale  $\bar{R}$  is the degree of polymerization,  $N$  of the chain:

$$N = \int_0^{\bar{R}} \bar{\rho}(\bar{r}) d\bar{r}^3 \cong \int_0^{\bar{R}} 4\pi c \bar{r}^{(\alpha+2)} d\bar{r}, \quad (5.3)$$

which gives

$$c \cong N \bar{R}^{-(\alpha+3)}, \quad (5.4)$$

where the dimensionless size of molecule  $\bar{R}$  must satisfy

$$\bar{R} \cong (\bar{v})^\beta N^{\frac{1}{(\alpha+3)}} \quad (5.5)$$

to guarantee  $c$  is independent of  $N$ . Substitute Equation 5.5 into Equation 5.4 to obtain the general form of the dimensionless prefactor  $c$  as a function of  $\bar{v}$ ,

$$c \cong (\bar{v})^{-\beta(\alpha+3)}. \quad (5.6)$$

Therefore, Equation 5.1 can be written as

$$\bar{\rho}(\bar{r}) \cong (\bar{v})^{-\beta(\alpha+3)} \bar{r}^\alpha \quad (5.7)$$

within the length scale of the molecule  $\bar{R}$ .

Equation 5.7 shows the general scaling law for a single chain with finite excluded volume. For  $\bar{v} \rightarrow 0$ , the intramolecular density profile of the molecule is expected to be a Gaussian random walk, otherwise Equation 5.7 diverges.

The crossover from SAW to random walk occurs when the intermolecular density begins to equal the dimensionless bulk density  $\bar{\rho}_b = \rho_b b^3$ . The real chain correlation length  $\bar{\xi}_{real}$  is thus defined as the distance where  $\bar{\rho}(\xi) = \bar{\rho}_b$ . The general form of the correlation length  $\bar{\xi}$  can be written as

$$\bar{\xi} \cong (\bar{v})^{\frac{\beta(\alpha+3)}{\alpha}} \bar{\rho}(\xi)^{\frac{1}{\alpha}}. \quad (5.8)$$

The screening length  $\xi_{real}$  for a Flory real chain is given as

$$\bar{\xi}_{real} \cong (\bar{\rho}_b)^{-\frac{3}{4}} (\bar{v})^{-\frac{1}{4}}, \quad (5.9)$$

and Equation 5.6 results in

$$c \cong (\bar{v})^{-\frac{1}{3}}, \quad (5.10)$$

which is consistent with the derivation by de Gennes [22].

In the following work, a two-chain SCFT approach is applied to focus on the swelling of branched polymers in melts and blends. The calculations also include the study of the mixing free energy between nonlinear and linear molecules. The two-chain SCFT captures intra- and intermolecular correlations in polymer solutions, melts and blends, and can be applied to both homogeneous and inhomogeneous polymers.

## 5.1 Two-chain SCFT for polymer bulk properties in melts and blends

One limitation of conventional SCFT is that correlations between monomers is neglected. For highly crowded branched polymers, the intra- and intermolecular correlations become more significant, and it would be desirable to extend SCFT to account for such correlations in

homogeneous systems. The two-chain self-consistent field algorithm is developed to study the bulk thermodynamics for branched molecule solutions and melts as it can capture intra- and intermolecular correlations. I note a similar but more restricted approach was implemented in a lattice-SCFT by Fleers *et al.* [66] for a homopolymer star by fixing the joint of a star polymer as a grafted monomer at a boundary and calculating the intramolecular correlations in dilute solutions [114, 144].

### 5.1.1 Modified diffusion equation in a spherically symmetric coordinate system

The two-chain SCFT focuses on a given molecule by fixing a specific monomer at the origin. In this case, the system is no longer translationally symmetric. The mean density field is a combination of that of the fixed chain and the surrounding free chains, and is thus no longer translationally invariant. Intramolecular monomer correlations can be determined by considering the density field due to the fixed chain, while intermolecular correlations are determined by the mean-field of the surrounding polymers. A schematic illustration of the two-chain algorithm is presented in Figure 5.1. The Laplacian of Equation 3.15 is reduced to be only dependent on the radius  $r$ , because of the spherical symmetry, and is given as

$$\frac{\partial q(r; t)}{\partial t} = \frac{b^2}{6} \left( \frac{\partial^2 q(r; t)}{\partial r^2} + \frac{2}{r} \frac{\partial q(r; t)}{\partial r} \right) - \mu(r)q(r; t). \quad (5.11)$$

with boundary conditions  $q(r < 0; t) = q^\dagger(r < 0; t) = 0$  and  $\frac{\partial q}{\partial r}|_{r_{\max}} = \frac{\partial q^\dagger}{\partial r}|_{r_{\max}} = 0$ , where  $r_{\max}$  represents the radius of the system.

Define  $q^{\text{fix}}(r; t; t_{\text{fix}})$  and  $q^{\dagger\text{fix}}(r; t; t_{\text{fix}})$  as the statistical weight functions of the molecule with a fixed site  $t_{\text{fix}}$ . The initial conditions are  $q^{\text{fix}}(r; 0; t_{\text{fix}}) = 1$  and  $q^{\dagger\text{fix}}(r; N; t_{\text{fix}}) = 1$ . However, when  $t = t_{\text{fix}}$ , the diffusion along the chain by Equation 3.15 is reset to solve  $q^{\text{fix}}(r; t > t_{\text{fix}}; t_{\text{fix}})$  and  $q^{\dagger\text{fix}}(r; t < t_{\text{fix}}; t_{\text{fix}})$ . The reset initial conditions at  $t_{\text{fix}}$  must satisfy  $q^{\text{fix}}(r; t = t_{\text{fix}}; t_{\text{fix}}) = \delta(r)$  and  $q^{\dagger\text{fix}}(r; t = t_{\text{fix}}; t_{\text{fix}}) = \delta(r)$ , respectively. Similarly, define  $q^{\text{free}}(r; t; t_{\text{fix}})$  and  $q^{\dagger\text{free}}(r; t; t_{\text{fix}})$  to represent the statistical weights of one of the free polymers around the fixed chain in the system. The initial conditions for the free molecule are  $q^{\text{free}}(r; 0; t_{\text{fix}}) = 1$  and  $q^{\dagger\text{free}}(r; N; t_{\text{fix}}) = 1$ .

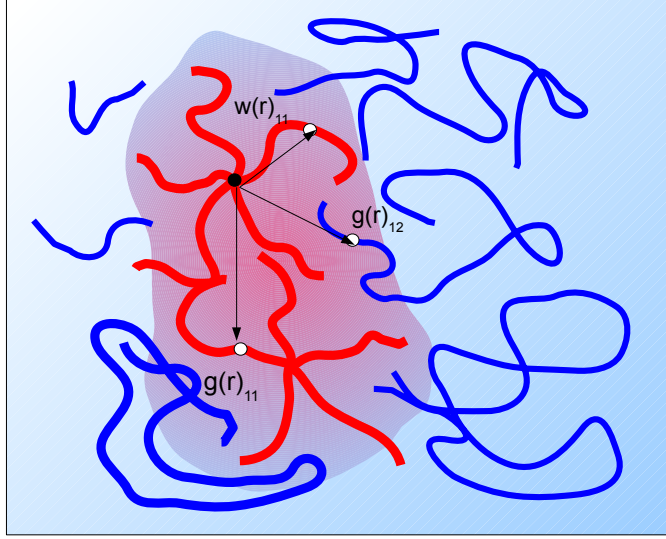


Figure 5.1: An illustration of two-chain SCFT on a star molecule fixing the joint at origin (black dot) which feels a mean-field from surrounding chains.  $\omega(r)$  is the intramolecular monomer-monomer correlations,  $g_{11}(r)$  means the intermolecular correlations between a given monomer on a different star (white dot) and the fixed joint.  $g_{12}(r)$  is the intermolecular correlation between a monomer (white dot) of linear chain and the joint.

In a polymer melt with multiple free chains and one chain with fixed monomer  $t_{\text{fix}}$ , the complete SCF potential is

$$\mu(r; t_{\text{fix}}) = v (\rho^{\text{fix}}(r; t_{\text{fix}}) + \rho^{\text{free}}(r; t_{\text{fix}})), \quad (5.12)$$

where  $\rho^{\text{fix}}$  is the intramolecular density of the chain selected to hold  $t_{\text{fix}}$  at the origin, and  $\rho^{\text{free}}$  is the density distribution of all free molecules. The intramolecular monomer radial distribution function of the chain with site  $t_{\text{fix}}$  held fixed is thus written as

$$\rho^{\text{fix}}(r; t_{\text{fix}}) = \frac{\int_0^N dt q^{\text{fix}}(r; t; t_{\text{fix}}) q^{\dagger\text{fix}}(r; t; t_{\text{fix}})}{4\pi \int_0^{r_{\text{max}}} dr q^{\text{fix}}(r; N; t_{\text{fix}}) q^{\dagger\text{fix}}(r; N; t_{\text{fix}}) r^2}, \quad (5.13)$$

and the intermolecular density  $\rho^{\text{free}}(r; t_{\text{fix}})$  is defined as

$$\rho^{\text{free}}(r; t_{\text{fix}}) = \frac{\rho_b V}{N} \frac{\int_0^N dt q^{\text{free}}(r; t; t_{\text{fix}}) q^{\dagger\text{free}}(r; t; t_{\text{fix}})}{4\pi \int_0^{r_{\text{max}}} dr q^{\text{free}}(r; N; t_{\text{fix}}) q^{\dagger\text{free}}(r; N; t_{\text{fix}}) r^2}, \quad (5.14)$$

where  $\rho_b$  is the bulk monomer density.

The general calculation of the statistical weight functions  $q$  of a branched structure is given by Fredrickson [30], but I consider a representative example here. Take a 3-arm structure labeling 1, 2, and 3 for each arm as an example. Suppose  $t_{\text{fix}}$  is located on arm 3. Let  $q1(r; t; t_{\text{fix}})$  be the weight function that diffuses from the end of arm 1, and  $q1^\dagger(r; t; t_{\text{fix}})$  diffuses towards the end of arm 1. Likewise,  $q2$  and  $q3$  diffuse from the end of arm 2 and 3 respectively, etc. If  $t_{\text{fix}} \neq t_{\text{joint}}$ , the weight function  $q1^\dagger(r; t_{\text{joint}}; t_{\text{fix}})$  is given as  $q1^\dagger(r; t_{\text{joint}}; t_{\text{fix}}) = q2(r; t_{\text{joint}}; t_{\text{fix}})q3(r; t_{\text{joint}}; t_{\text{fix}})$ . A brief illustration to calculate the density probability from  $q$  and  $q^\dagger$  is given in Figure 5.2.

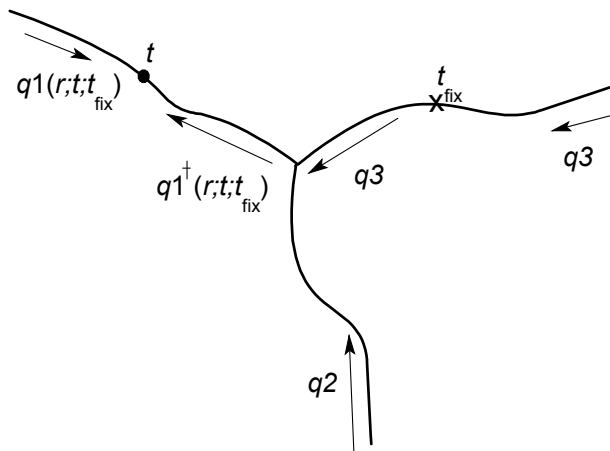


Figure 5.2: An illustration to calculate the local monomer density of a 3-star structure. In this example, the molecule is fixed at  $t_{\text{fix}}$ . As  $q3$  is solved from the end of the chain and reaches  $t_{\text{fix}}$ ,  $q3$  is reset to an initial condition  $q3(r; t = t_{\text{fix}}; t_{\text{fix}}) = \delta(r)$ .

The SCF calculation iterates by solving Equation 5.11, 5.12, 5.13 and 5.14, including two sets of modified diffusion equations to solve the fixed and free chain statistical weight functions. The segment length  $b$  is set to be 1. The Crank-Nicolson algorithm is used to solve the differential equations, and the Picard algorithm is applied in SCF iteration by updating  $\mu^i$ . A mixing ratio  $\lambda = 0.05$  ( $\lambda \in (0, 1]$ ) is applied to update  $\mu^i$  in terms of

$\mu^i = (1 - \lambda)\mu^{i-1} + \lambda v \rho^i(r)$ . Minimize  $\epsilon = \frac{\sum_j |\mu_j^i - \mu_j^{i-1}|}{\sum_j |\mu_j^i|}$  until satisfying the tolerance of the convergence  $\epsilon_t < 10^{-7}$ , where  $i$  is the index of the  $i^{\text{th}}$  iteration and  $j$  is the index of the spatial grids. Figure 5.3 introduces a typical flowchart of the two-chain SCFT problem. The numerical methods for solving the differential equation and minimization scheme are introduced in Appendix A.

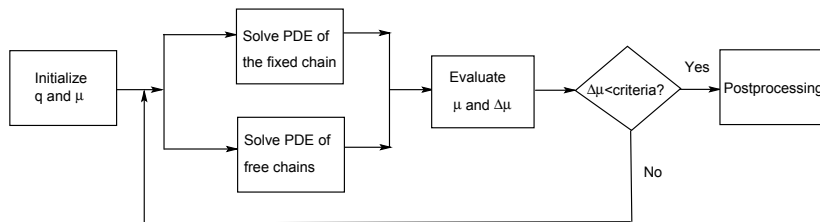


Figure 5.3: The flowchart of a two-chain SCFT algorithm.

## 5.2 Dilute solutions of linear and branched polymers

A dilute solution with a single linear chain of  $N = 50$  is studied using SCFT. Equation 5.7 and Equation 5.8 indicate that the molecular weight  $N$  is not a factor for the scaling of density and  $\xi$ . The resolution of the discretization grids is  $\Delta r = 0.02b$  unless otherwise specified. The excluded volume parameter  $\bar{v}$  ranges from 0 to 100.  $\bar{v}$  is dependent on the compressibility [26, 71].

In Figure 5.4a, the monomer density profiles show the real chain scaling of  $-4/3$  if  $v$  is sufficiently large as a result of fixing the center of the molecule at the origin. The density profiles for  $\bar{v} < \sim 0.1$  show less steep slopes, so that the weak excluded volume effect does not exhibit swelling. The plot for  $\bar{v} = 0$  is close to  $\bar{v} = 0.01$  and indistinguishable on this scale. In the cases of  $\bar{v} > \sim 1$ , the density profiles indicate that the polymers become swollen and the slope of the single chain density profile is very close to  $-4/3$  within the range of the plot when  $\bar{v} = 10$ . Another feature of strong excluded volume is that the slope changes at a length scale of  $R$ , which is likely due to weaker correlations further from the center of

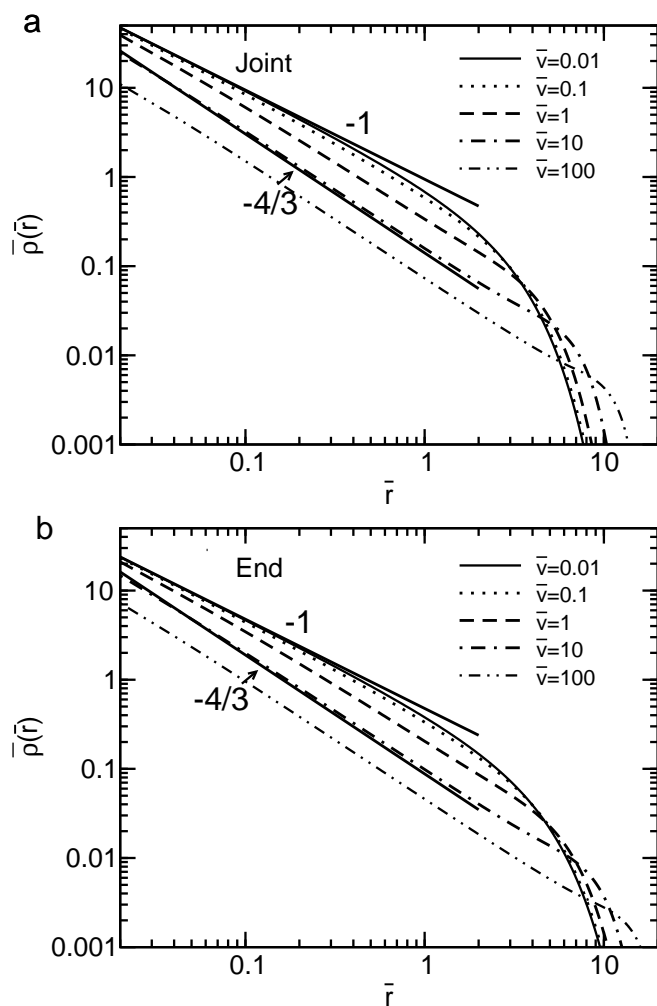


Figure 5.4: The intramolecular density profiles of a single linear molecule for different values of excluded volume  $\bar{v}$ . (a) The intramolecular density profiles of a linear molecule from the center. (b) The intramolecular density profiles of a linear molecule from the end. The length of the molecule is  $N = 50$ .

mass. For  $r \rightarrow 0$ , the molecule should be always SAW because the monomer with finite excluded volume do not interact with other monomers. The density profiles from the held end monomer of the same linear chain is plotted in Figure 5.4b. The scaling exponent is analogous to that of holding the center. Its slope close to  $-4/3$  indicates the swelling of the molecule in a dilute solution for  $\bar{v} > \sim 10$ , and a slope close to  $-1$  for  $\bar{v} < \sim 0.1$  indicates a Gaussian conformation. The density profile from the end monomer case approaches  $1/2$  of that for the held-center case, because a fixed center monomer is analogous to having two fixed ends with chains half the length.

A further study of star molecules in dilute solutions is performed using a 4-star polymer with arm length  $N_{\text{arm}} = 25$ , and total  $N = 100$ . Analogous results to the case of a single linear molecule for the density profiles from the joint and the end are shown in Figure 5.5a and b, respectively. For  $\bar{v} = 0$ , the density profile is also indistinguishable from the plot of  $\bar{v} = 0.01$ . The slope of  $\rho(r)$  from the joint, similar to a linear molecule, implies that the conformation is similar to a SAW when  $\bar{v} > \sim 1$ . Figure 5.5b shows that the molecule density from the held end behaves completely as a SAW when  $\bar{v} = 10$  until it sees the monomers near the joint at a length scale of  $R$ . Thus, a small amount of increase in density is present at long distances from the center. The scaling exponent of numerical SCFT agrees with the scaling theory for linear solutions [22] and the Monte Carlo simulations of star polymers by Cecca *et al.* [134]

A series of  $f$ -stars with identical arm lengths of  $N_{\text{arm}} = 25$  were computed. The density distributions are shown in Figure 5.6. The density profiles from the joint of  $f$ -star shown in Figure 5.6a are similar to the density in the 4-star case but with more arms. Figure 5.6b shows the density profiles from the ends of higher arm stars, e.g., 16-star increase and then a near plateau with the slope going to zero where the end monomer sees the accumulative density of the joint. The monomers close to the ends are generally in random walk conformations in dilute solutions.

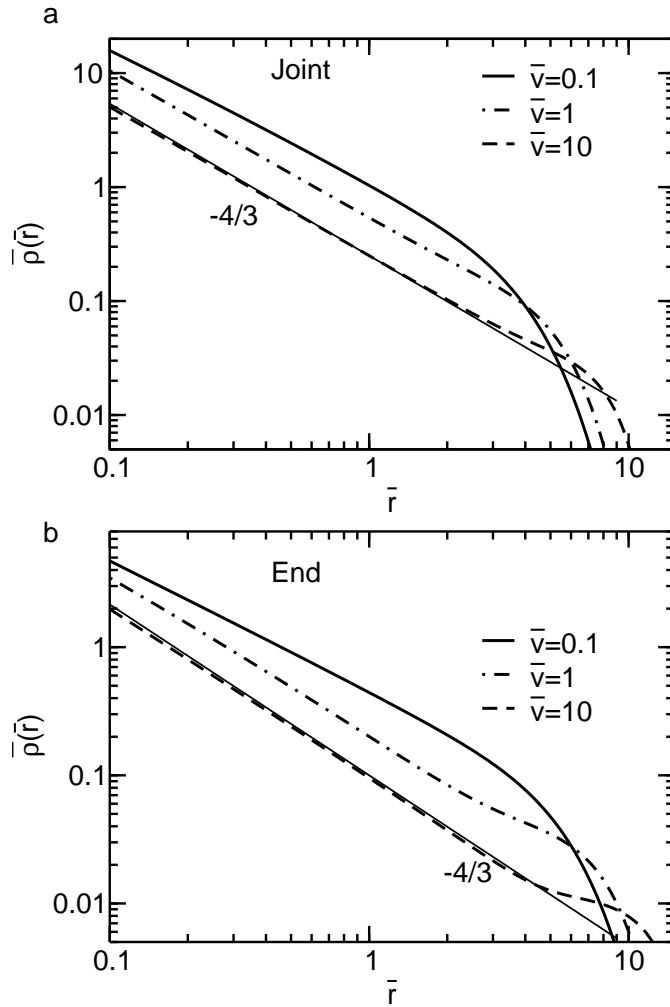


Figure 5.5: The intramolecular density profiles of a 4-star single molecule for different value of excluded volume  $\bar{v}$  in log-log scales. (a) The intramolecular density profiles of a 4-star molecule from the joint. (b) The intramolecular density profiles of a 4-star from the end.  $N_{\text{arm}} = 25$ .

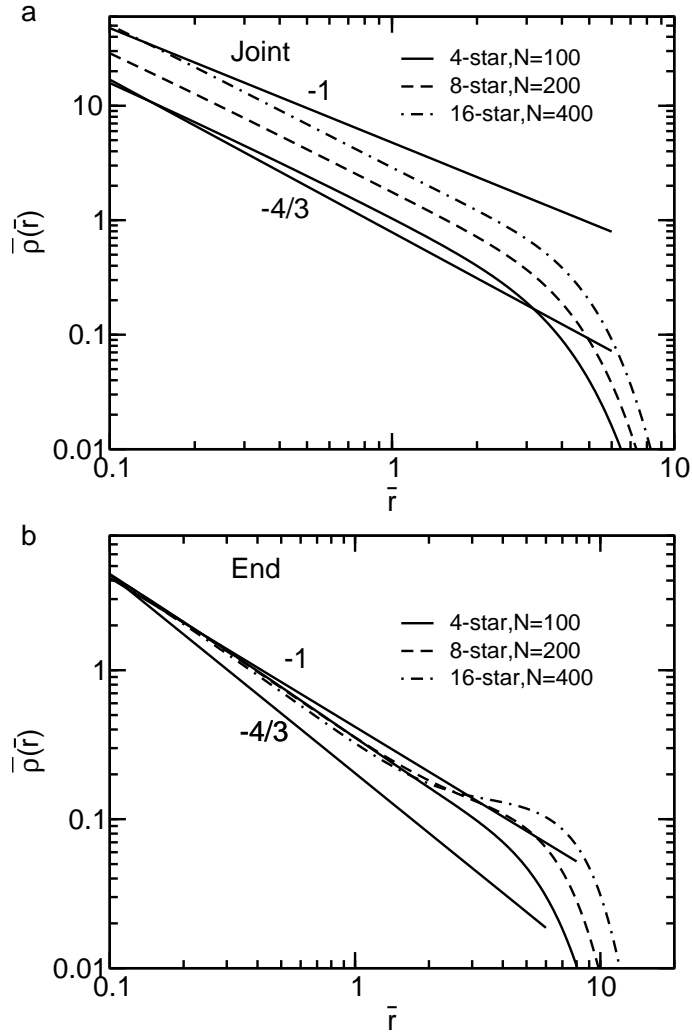


Figure 5.6: Comparisons of density distributions of  $f$ -star in a dilution solution condition with different numbers of arms.  $N_{\text{arm}} = 25$ ,  $\bar{v} = 0.1$ . (a) Density profiles from the joint and (b) Density profiles from the end.  $N_{\text{arm}} = 25$ ,  $N_{\text{star}} = 100$ .

### 5.3 The end-end distance distribution of a branched molecule

The end-to-end distance can be generated straightforwardly in the two-chain SCFT algorithm by holding one chain end fixed. This corresponds to the calculation of the end monomer distribution in 1-D single chain problems [26]. In SCFT, the distributions of the distance between two ends can be written in terms of  $q(r; N; 0)$ , where  $q(r; N; 0)$  is the statistical weight by holding the end 0 fixed and diffusing to the other end  $N$ . Thus, the three-dimensional normalized end-to-end distance distribution is

$$P(r) = \frac{q(r; N; 0)}{4\pi \int_0^\infty q(r; N; 0) r^2 dr}. \quad (5.15)$$

The SCFT result reduces to an exact Gaussian chain without the mean-field. When including the excluded volume field, the distribution function becomes that of a real chain and is comparable with des Cloizeaux's form [145]:

$$P(r) \cong \left( \frac{r}{\sqrt{\langle R^2 \rangle}} \right)^\sigma \exp \left( -G \left( \frac{r}{\sqrt{\langle R^2 \rangle}} \right)^\tau \right), \quad (5.16)$$

where the exponents and prefactors can be estimated as [146, 147]

$$P(r) \approx 0.278 \langle R^2 \rangle^{-3/2} \frac{r}{\sqrt{\langle R^2 \rangle}}^{0.28} \exp \left( -1.206 \left( \frac{r}{\sqrt{\langle R^2 \rangle}} \right)^{2.43} \right) \quad (5.17)$$

for a Flory real chain. For instance, Figure 5.7 provides the SCFT results of the monomer end-to-end distribution profiles of the linear ( $N = 100$ ) and 4-star ( $N = 100$ ) molecule in dilute solutions. In Figure 5.7a, by increasing  $v$ , the linear chain becomes non-Gaussian and narrowly distributed. The des Cloizeaux plot is close to the SCFT plot of  $\bar{v} = 1$ . The end-to-end distribution profiles for strong repulsive polymers  $\bar{v} > \sim 10$  shows that the ends are distant close to the mean end-to-end distance  $\sqrt{\langle R^2 \rangle}$ . However, the same calculation on a single 4-star with  $\bar{v} = 100$  in Figure 5.7b shows that the end-end distribution for a star is wider than that of a linear chain having the same degree of polymerization.

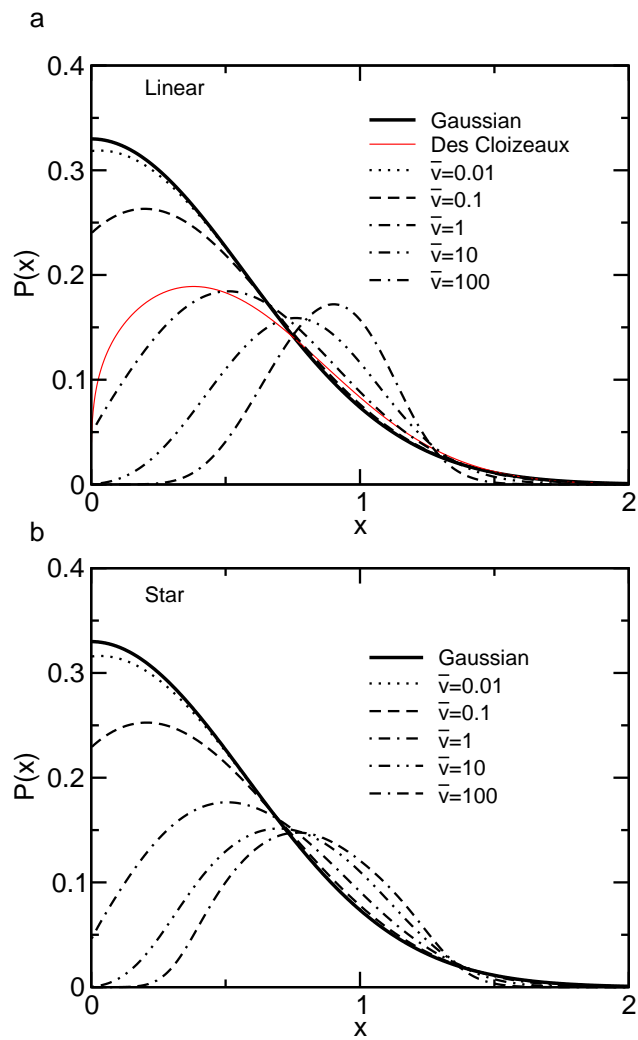


Figure 5.7: The single chain end-to-end distribution function of a linear molecule ( $N = 50$ ) and a 4-star ( $N = 100$ ) by SCFT. (a) The end-to-end distribution function of a linear molecule ( $N = 50$ ) and the comparison with Gaussian and des Cloizeaux models. (b) The end-to-end distribution function of a 4-star molecule ( $N = 100$ ) and the comparison with the Gaussian model. The reduced distance  $x = \frac{r}{\sqrt{\langle R^2 \rangle}}$ .

## 5.4 Branched chain conformations in semi-dilute solutions and melts

The two-chain SCFT can help understand the conformations of linear and non-linear polymers in a semi-dilute or concentrated system. As the density becomes finite, chains are screened due to intermolecular interactions. Equation 5.9 shows the regime where the intermolecular interaction dominates in a polymer melt with a crossover in scaling exponent from self-avoiding to random walk. The SCFT calculations are performed in a linear solution with finite density. The degree of polymerization of the linear molecule is  $N = 50$  and the reduced average bulk monomer density  $\bar{\rho}_b = \rho_b b^3$ , which is defined by the total number of monomers over volume, is variable. The excluded volume parameter  $\bar{v}$  is variable as well.

### 5.4.1 Intermolecular and total density distribution functions

The intra- and intermolecular density profiles in a linear solution with  $\bar{\rho}_b = 0.2$  from the joint and end are shown in Figure 5.8. The excluded volume parameters  $\bar{v}$  vary from 1 to 100. The intramolecular density profiles show different scaling exponents at the low  $\bar{r}$  regime at approximately  $\bar{r} < \sim 2$  in the figure. They cross over at  $\bar{r} \sim 3$ , and merge at  $\bar{r} > \sim 5$  in the range of the plot. The correlation hole is obtained on the plot of intermolecular concentration profile of free molecules. For  $\bar{v} = 100$ , less monomers approach to the short distance regime ( $\bar{r} \sim 1$ ) for the strong repulsion due to monomer excluded volume.

### 5.4.2 The swelling of linear molecules in semi-dilute solutions and melts

Figure 5.9a shows the intramolecular densities of a linear pure component,  $N = 50$ , in  $\bar{\rho}_b = 0.2$  with varying excluded volumes. In homogeneous solutions, the overlap concentration is  $c^* \cong N^{-4/5} b^{-3}$  for chains in SAW. The bulk density of  $\bar{\rho}_b = 0.2$  in Figure 5.9a can be considered above the limit of the semi-dilute solution because  $c^*$  is  $\mathcal{O}(10^{-2})b^{-3}$ . The calculations show that the monomer density decreases as the strength of monomer exclusion  $\bar{v}$  increases. However, the crossover as increasing the distance  $\bar{r}$  between SAW exponent and Gaussian exponent are not obvious.

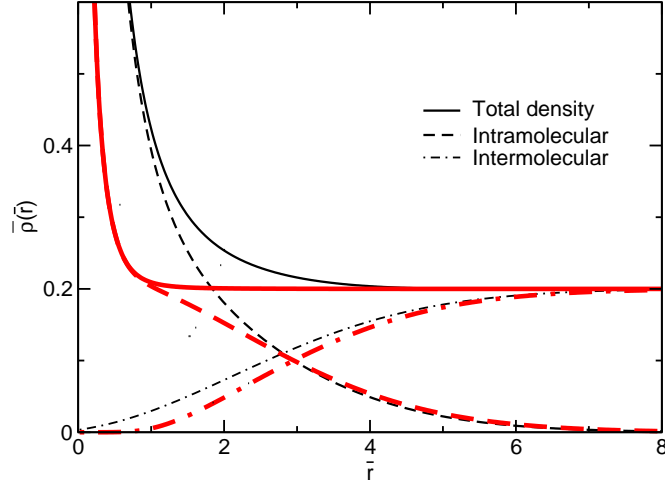


Figure 5.8: Density profiles of a linear melt from the center of the molecule, the molecular weight  $N = 50$ , and  $\bar{\rho}_b = 0.2$ . The thin solid, dash and dash-dot lines correspond to the total, intra- and intermolecular density profiles with  $\bar{v} = 1$ , respectively. The thick solid, dash and dash-dot lines are the total, intra- and intermolecular density profiles with  $\bar{v} = 100$ , respectively.

For solutions with small excluded volume (e.g.,  $\bar{v} < 0.01$ ), the molecule behaves as Gaussian random walk. This is the same to the single chain conformation in dilute solutions. Moreover, when increasing  $\bar{v}$  from 0.01 to 1, a partially screened regime can be obtained. Although the complete SAW scaling exponent,  $-4/3$ , within the blob [22] is not captured by two-chain SCFT, the calculation is still expected that at  $\bar{r} \rightarrow 0$ , the monomers are SAW. In the current resolution ( $\Delta r = 0.02b$ ), at short distances from the origin where  $\bar{r} \approx 0.1$ , the density profile has a transitional exponent between  $-4/3$  and  $-1$  and the profiles merge to Gaussian random walk exponent,  $-1$ , at long distances. However, the random walk regime is vanishing as  $\bar{v}$  becomes  $\sim 100$ . In particular, the intramolecular density profile of  $\bar{v} = 100$  does not show a random walk slope of  $-1$  but a higher density in the bulk in log-log scale. This is due to the strong repulsion among monomers. If the bulk concentration is increased while fixing the excluded volume, as is shown in Figure 5.9b, the screening of the molecules can therefore be captured at a higher concentration. When  $\bar{r}$  goes to zero, the intramolecular

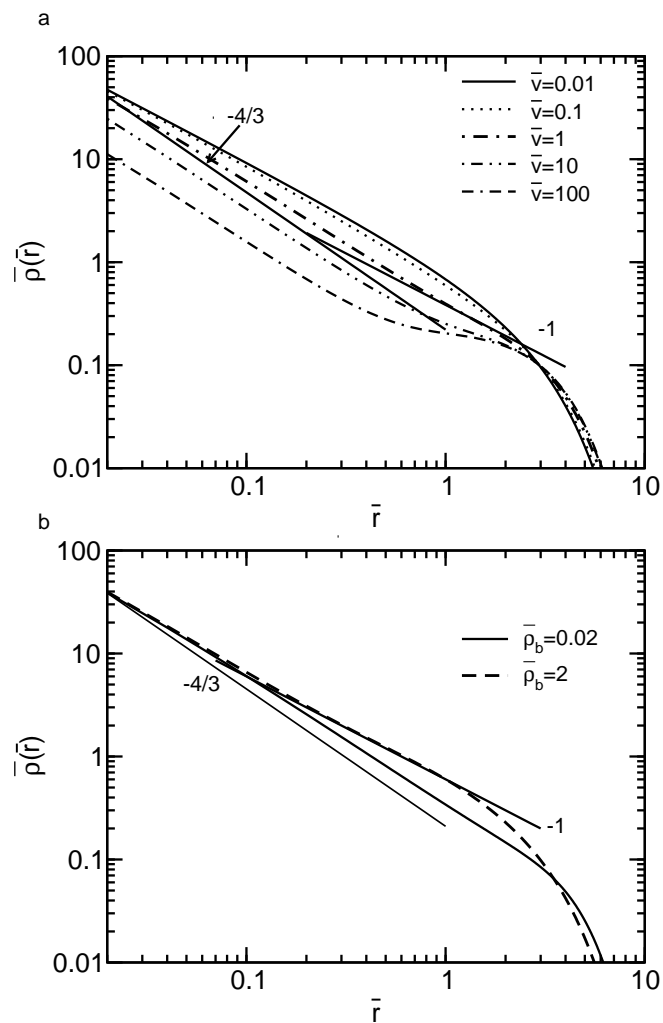


Figure 5.9: The intramolecular density profiles in linear polymer solutions from the center of the molecule. (a)  $\bar{\rho}_b = 0.2$ ,  $\bar{v}$  varies from 0.01 to 100. The slope of the density profile in the log-log scale is between  $-4/3$  and  $-1$  at  $\bar{r} \approx 0.1$ . (b)  $\bar{v} = 1$ , bulk monomer density  $\bar{\rho}_b$  increases from 0.02 to 2. The dot line shows the expected exponent for SAW.

density profiles will merge together regardless of the value of the bulk densities.

### 5.4.3 The scaling analysis

To discuss the scaling of excluded volume in the intramolecular density profile at short distances,  $\bar{\rho}(\bar{r}) \sim \bar{r}^\alpha \bar{v}^{-\beta(\alpha+3)}$ , the relationship between  $\bar{\rho}(\bar{r})/\bar{r}^\alpha$  and  $\bar{v}$  is shown in Figure 5.10a in a range of  $r < 0.1b$ . The excluded volumes vary from  $\bar{v} = 10^{-4}$  to 100, with bulk density  $\bar{\rho}_b = 0.2$ . For  $\bar{v} \leq 0.01$ ,  $\alpha = -1$  and for  $\bar{v} \geq 1$ ,  $\alpha = -4/3$ , according to the discussion of Figure 5.9a. In particular, two regimes for  $\bar{\rho}(\bar{r})/\bar{r}^\alpha$  against  $\bar{v}$  in log-log scales are obtained. For  $\bar{v} \leq 0.01$ ,  $\bar{\rho}(\bar{r})/\bar{r}^\alpha$  is independent of  $\bar{v}$ . However, for  $\bar{v} > 1$ , the scaling relationship between the monomer density and distance shows that  $\bar{\rho}(\bar{r})/\bar{r}^\alpha \sim (\bar{v})^{-1/3}$ , which is consistent to Equation 5.10 as a SAW chain. The two regimes cross over within the range of  $0.01 < \bar{v} < 1$ . The scaling analysis based on expressions from Equation 5.1 to 5.10 primarily assumes that at short distances, the intramolecular density profile in a melt is the same as it is in dilute solutions. This assumption is true at  $\bar{r} \leq 0.1$  in the above SCFT calculations, because the total monomer density at short distances is dominated by the intramolecular density (Figure 5.8). However, significant differences are seen at long distances in strong excluded volume melts by comparing Figure 5.4a and Figure 5.9a. Figure 5.10b shows the screening length  $\bar{\xi}$  against  $\bar{v}$  from  $\bar{v} = 10^{-4}$  to 100, with  $\bar{\rho}_b = 0.2$ . The inset in Figure 5.10b shows the difference of the screening lengths determined from intramolecular density profiles in a dilute solution and a melt. In the range of  $\bar{v}$  plotted in the figure,  $\bar{\xi}$  also crosses over at approximately  $\bar{v} = 1$  and the slope for  $\bar{v} > 1$  is -0.12. This is approximately half of the expected scaling exponent,  $\bar{\xi} \sim \bar{v}^{-1/4}$ , according to 5.9. If applying the single chain intramolecular density profile, which are the crossed points in Figure 5.10b, the plot of  $\bar{\xi}$  against  $\bar{v}$  shows the scaling exponent of  $\bar{\xi} \sim \bar{v}^{-1/4}$ . The crossover from weak  $v$  dependence to strong  $v$  dependence is consistent with the expected criteria of observing SAW using the  $z$  parameter:

$$z = \frac{3}{2\pi} \frac{v^{3/2}}{b^3} N^{1/2} \approx \frac{v}{b^3} N^{1/2}, \quad (5.18)$$

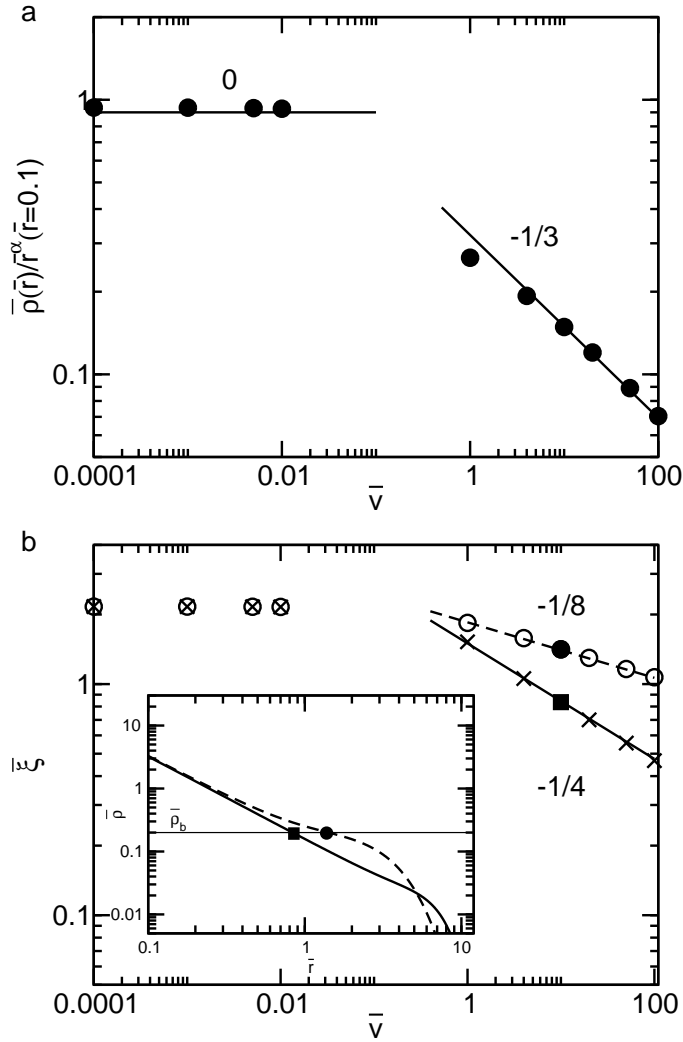


Figure 5.10: Scaling analysis of the monomer density and correlation lengths versus the excluded volume in melts of linear polymers. (a) The scaling relationship between scaled monomer density  $\bar{\rho}(\bar{r})/\bar{r}^\alpha$  and excluded volume  $\bar{v}$  at  $\bar{r} = 0.1$  in linear solutions with  $\bar{\rho}_b = 0.2$  and  $N = 50$ . (b) The scaling dependence of the correlation length  $\bar{\xi}$  on  $\bar{v}$  for linear solutions. The circles are obtained from intramolecular densities of solutions corresponding to the examples in Figure 5.9a. Crossed points are obtained assuming the intramolecular density profile in a melt is the same as in the dilute solution (as shown in Figure 5.4). The scaling exponent results agree with Equation 5.9 for  $\bar{v} > 1$ . The inset in case (b) shows the result when using the criterion  $\rho(\bar{\xi}) = \bar{\rho}_b$  from the intramolecular density profiles to obtain  $\bar{\xi}$ . The dashed line: density profile of  $\bar{v} = 10$ ,  $\bar{\rho}_b = 0.2$ . The solid line: density profile of a dilute chain,  $\bar{v} = 10$ .

where the actual excluded volume,  $v \approx b^3$  is the limit to observe SAW with a given  $N$ .

#### 5.4.4 The swelling of branched polymers in semi-dilute solutions and melts

Homogeneous melts composed of 4-star ( $N=100$ ) molecules with different monomer densities,  $\bar{\rho}_b$ , and excluded volume parameters,  $\bar{v}$ , are studied. The behavior of the chain conformation is found to be similar to that of linear melts ( $N=50$ ), because a linear chain is identical to a 2-star from its center. Figure 5.11a and b compare the intramolecular density profiles by varying  $\bar{v}$  and  $\bar{\rho}_b$ , respectively. The density distribution of the 4-star melts are expected to merge to SAW profile at  $r \rightarrow 0$ . For  $\bar{v} < 10$ , the observed exponents at short distances in the figure,  $\bar{r} < 0.1$ , are all less steep than that for  $\bar{v} = 10$ . At  $\bar{v} = 1$  with different  $\bar{\rho}_b$  from Figure 5.11b, the distance where crossover occurs increases as its density decreases. In the case of  $\bar{\rho}_b = 10$  and  $\bar{v} = 1$ , the polymer chain hardly shows any SAW behavior. On the contrary, the intramolecular density of the star solution with  $\bar{\rho}_b = 0.02$  is close to a dilute solution exhibiting an exponent close to that expected for a SAW.

In the Daoud-Cotton model [86], it predicts the size of a single  $f$ -star:

$$R_g^2 \sim f^{\frac{1}{2}} \quad (5.19)$$

in terms of  $R_g$ . The Daoud-Cotton model implies that given a star, the size of the molecule would have a corresponding constant scaling relationship  $\langle R^2 \rangle \sim f^l$ . The end-to-end distance of the same  $f$ -stars by PRISM are plotted using the data of Grayce *et al.* [125] in Figure 5.12, which approximately show  $\langle \bar{R}^2 \rangle \sim f^{0.15}$  in both low and high concentrations.

The mean squared end-to-end distances,  $\langle \bar{R}^2 \rangle$  of  $f$ -stars ( $N_{\text{arm}} = 25$ ) in dilute and semi-dilute solutions are calculated from their end-to-end distance distribution functions and shown in Figure 5.13. On a log-log plot, the scaling relationship  $\langle \bar{R}^2 \rangle \sim f^l$  shows varying exponents  $l$  with  $f$ . As the number of arms increases, the polymer size in semi-dilute solutions increases less dramatically than that in dilute solutions as increasing the number of arms. Regardless of the linear chain case (the 2-star in the calculation), the approximated scaling exponent  $l$  from 4 to 16-star in semi-dilute solutions by a linear fit results in  $l = 0.15$ .

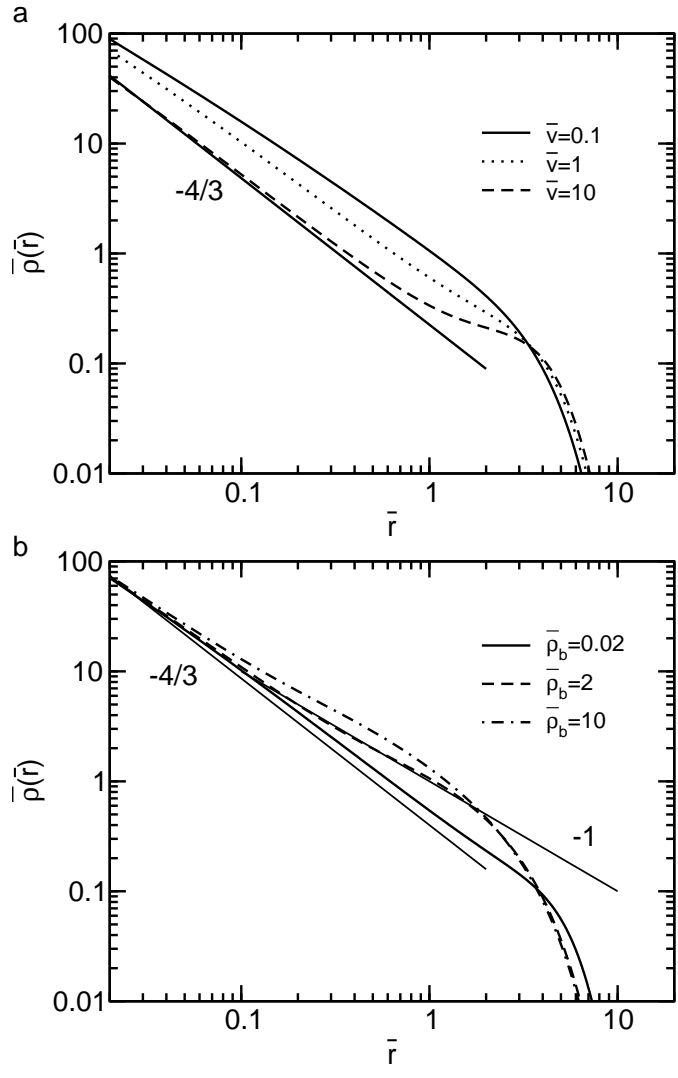


Figure 5.11: The density profiles from the joint of pure component 4-star chains.  $N = 100$ . (a) For varying excluded volume  $\bar{v} = 0.1$ ,  $\bar{v} = 1$  and  $\bar{v} = 10$ ;  $\bar{\rho}_b = 0.2$ . (b) For varying density  $\bar{\rho}_b = 0.02$ , 2, and 10;  $\bar{v} = 1$ .

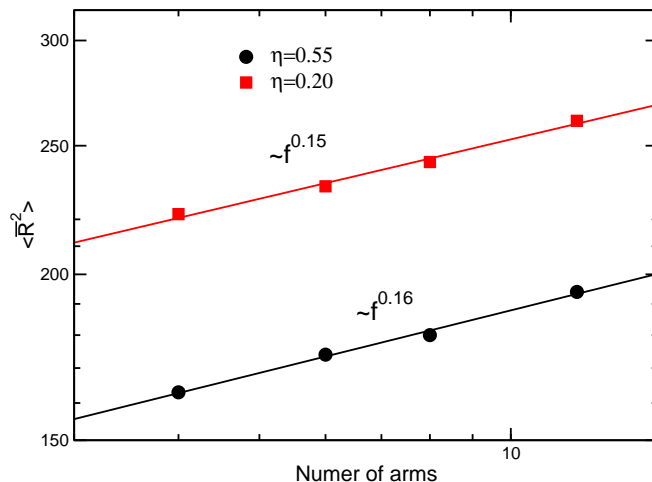


Figure 5.12: The mean squared end-to-end distances  $\langle \bar{R}^2 \rangle$  of  $f$ -stars ( $N_{\text{arm}} = 100$ ,  $f = 4, 6, 8, 12$ ) by Grayce *et al.* using PRISM theory [125].  $\eta$  is the packing density of the monomer representing the concentration of the solutions.

Therefore, although  $l$  is an  $f$  dependent factor in two-chain SCFT, the range of the values is very consistent with the PRISM theory for semi-dilute solutions. In the case of dilute solution in Figure 5.13, it gives  $l = 0.5$  as a stronger dependence on  $f$  than semi-dilute solutions.

In general, the scaling of the size of stars against the number of arms by two-chain SCFT and PRISM can show good consistency in semi-dilute solutions. The Daoud-Cotton model in semi-dilute solutions is not consistent with two-chain SCFT or PRISM, but a similar scaling exponent to the Daoud-Cotton model can be captured by two-chain SCFT in dilute solutions.

#### 5.4.5 Stretching of molecules due to branching

More complex branched polymer melts are considered with both an inner joint and outside branch points. Studies of several end-branched polymers showed how branches affect the local stretching from the joint. Branched structures such as a 6-end, 9-end and 15-end

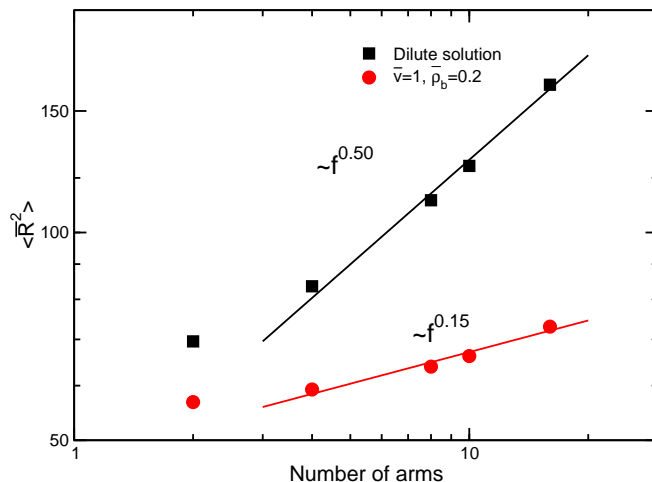


Figure 5.13: The mean squared end-to-end distances  $\langle \bar{R}^2 \rangle$  of  $f$ -stars ( $N_{\text{arm}} = 25$ ,  $f = 4, 8, 10, 16$ ) in dilute and semi-dilute solutions. The 2-star is the linear chain with  $N = 50$ . For dilute solutions,  $\bar{v} = 1$ .

are illustrated in Figure 4.1. As given in Figure 5.14, calculations on various type of end-branched melts are performed using  $\bar{v} = 1$  and  $\bar{\rho}_b = 0.2$  for the higher molecular weight molecules. The conformation and local stretching due to branching can be analyzed by the following steps.

First, the intermolecular density profiles of different 9-end melts with fixed arm length  $N_{\text{arm}} = 70$  and varying branch length  $N_{\text{branch}}$  in Figure 5.14a show, within the range of the figure, that increasing the length of outside branches simply increases the intramolecular density at long distances, ( $\bar{r} > 1$ ), while at short distances from the joint, the density distributions merge on a log-log scale, and are expected to exhibit SAW scaling at  $\bar{r} \rightarrow 0$ .

Second, keep the length of the inside arms and the branches unchanged while increasing branch points  $f$ . As shown in Figure 5.14b, the density behavior at short distances is similar to Figure 5.14a. Higher branching slightly increases the density at long distances as well. In general, either the length or the number of branches directly affects the chain conformations at short distances from the inside joint.

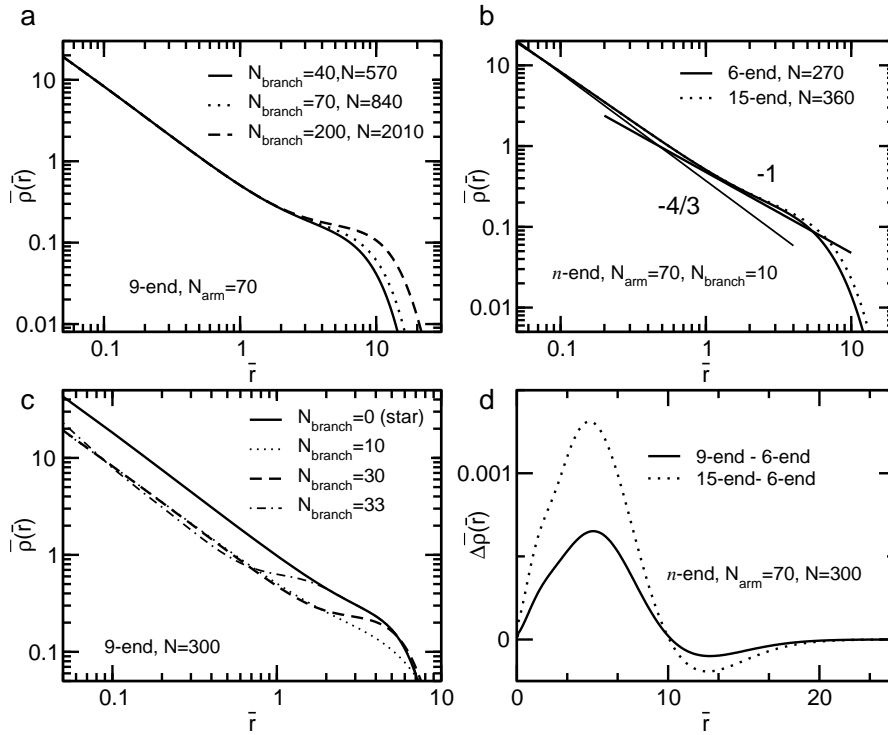


Figure 5.14: The intramolecular density profiles of various branched polymer melts from the inside joint. ( $\bar{v} = 1$  and  $\bar{\rho}_b = 0.2$ ) (a) The density profiles of 9-end melts with the inside arm length of  $N_{\text{arm}} = 70$  and with varying lengths of the outside branches. (b) Density profiles of branched molecules with varying numbers of outside branches by fixing the length of the inside arm  $N_{\text{arm}} = 70$  and the outside branch,  $N_{\text{branch}} = 10$ . (c) Density profiles of different 9-end molecules by changing the length of the outside branch  $N_{\text{branch}}$  with fixed degree of polymerization of  $N = 300$ . The lengths of the inside arms are  $N_{\text{arm}} = 1$  for  $N_{\text{branch}} = 33$  and  $N_{\text{arm}} = 10$  for  $N_{\text{branch}} = 30$ . (d) The difference of density profiles of 6, 9 and 15-end by fixing the total degree of polymerization  $N = 300$  and the length of the inside arms  $N_{\text{arm}} = 70$ .

Third, the density profile of a 9-end melt in Figure 5.14c when  $N = 300$  with shortening inside arms is shown. As the length of branch increases, the crossover from self-avoiding to random walk can be screened by condensed branches, and strong stretching of the arms at short distances is observed if the lengths of branches are longer than that of the arm in the case of  $N_{\text{branch}} = 30$ , where the arm length,  $N_{\text{arm}} = 10$ . Similarly, in the extreme case where  $N_{\text{branch}} = 33$ , which has one monomer between the joint and branch point, the local intramolecular density is slightly lower than that in the case of  $N_{\text{branch}} = 10$ . In the meantime, completely different density profiles are obtained compared to an ideal 9-star. The two plots merge at  $\bar{r} \sim 2$  from the origin. However, the monomers on the branches are stretched away from the joint. At very short distances, where  $\bar{r} \rightarrow 0$ , the density of 9-end ( $N_{\text{branch}} = 33$ ) and the 9-star decay to the same line.

Finally, I change the number of outside branches, while keeping both the degree of polymerization of the molecule  $N = 300$  and the inside arm  $N_{\text{arm}} = 70$  fixed. The intramolecular density profiles of all the melts merge together on a log-log plot, given the density profile of the 9-end,  $N_{\text{branch}} = 10$  (the dotted line) as the example in Figure 5.14c. Figure 5.14d shows the difference of the density profiles of 9- and 15-end molecules from the reference density profile of 6-end molecules. Changes in the density profiles  $\Delta\bar{\rho}(r)$  on a linear plot show that the swelling is slightly enhanced at short distances for higher branching, however the monomers near the enhanced swollen regime are stretched out and exhibit lower density. e.g.,  $\bar{r} \sim 10$  in Figure 5.14b. In addition, the differences in the density profiles of different melts in Figure 5.14a and Figure 5.14b also show the similar effect that increasing the number or length of outside branches slightly enhances the swelling at short distances, though they are not plotted in this thesis.

#### 5.4.6 Structure factors of polymers in solutions and melts

The two-chain SCFT is done on a chain by holding each monomer fixed in sequence, and then averaging to calculate the radial distribution functions. The radial distribution for the intramolecular correlation,  $\omega(r)$  and the intermolecular correlation,  $g(r)$  of a polymer melt

can be written directly as

$$\omega(r) = \frac{1}{N} \sum_{t_{\text{fix}}=0}^N \rho^{\text{fix}}(r; t_{\text{fix}}) \quad (5.20)$$

and

$$g(r) = \frac{1}{N\rho_b} \sum_{t_{\text{fix}}=0}^N \rho^{\text{free}}(r; t_{\text{fix}}). \quad (5.21)$$

Considering a polymer melt with  $\rho_b$  and the degree of polymerization  $N$ , the total structure factor includes both intra- and intermolecular contributions, i.e.,

$$S(k) = \rho_b N \omega(k) + \rho_b^2 h(k) \quad (5.22)$$

where  $\omega(k)$  is the intramolecular structure factor and  $h(k)$  is the intermolecular contribution.  $\omega(k)$  and  $h(k)$  are three-dimensional Fourier transforms of pair correlation functions in spherical coordinates of the spherically symmetric functions,  $\omega(r)$  and  $h(r) = g(r) - 1$ . The structure factors are written as

$$\omega(\bar{k}) = 4\pi \int_0^\infty d\bar{r} \frac{\bar{r} \sin(\bar{k}\bar{r})}{\bar{k}} \omega(\bar{r}), \quad (5.23)$$

and

$$h(\bar{k}) = 4\pi \int_0^\infty d\bar{r} \frac{\bar{r} \sin(\bar{k}\bar{r})}{\bar{k}} (g(\bar{r}) - 1), \quad (5.24)$$

where  $\bar{k} = kb$ .

$\omega(\bar{k})$  of the 4-star molecule in a dilute solution and in two melts with  $\bar{\rho}_b = 0.2$  and  $\bar{\rho}_b = 10$ , respectively, are shown in Figure 5.15a. In homogeneous melts, (e.g.,  $\bar{\rho}_b = 10$ ),  $\omega(\bar{k})$  is similar to the profile of a Gaussian chain.  $\omega(\bar{k})$  of a swollen molecule is intermediate between the dilute solution and the ideal chain. In Figure 5.15b, the intermolecular structure factor  $h(\bar{k})$  in four typical 4-star solutions are shown. In the case of  $\bar{\rho}_b = 10$ ,  $h(\bar{k})$  is almost zero indicating weak intermolecular correlations in high density melts.

Figure 5.16 shows the total static structure factors of the 4-star molecules in different solutions. The peaks at low  $\bar{k}$  correspond to melts with high bulk density and strong contribution of intermolecular structure factors,  $\rho_b^2 h(\bar{k})$ . The condition to show a peak in  $S(\bar{k})$

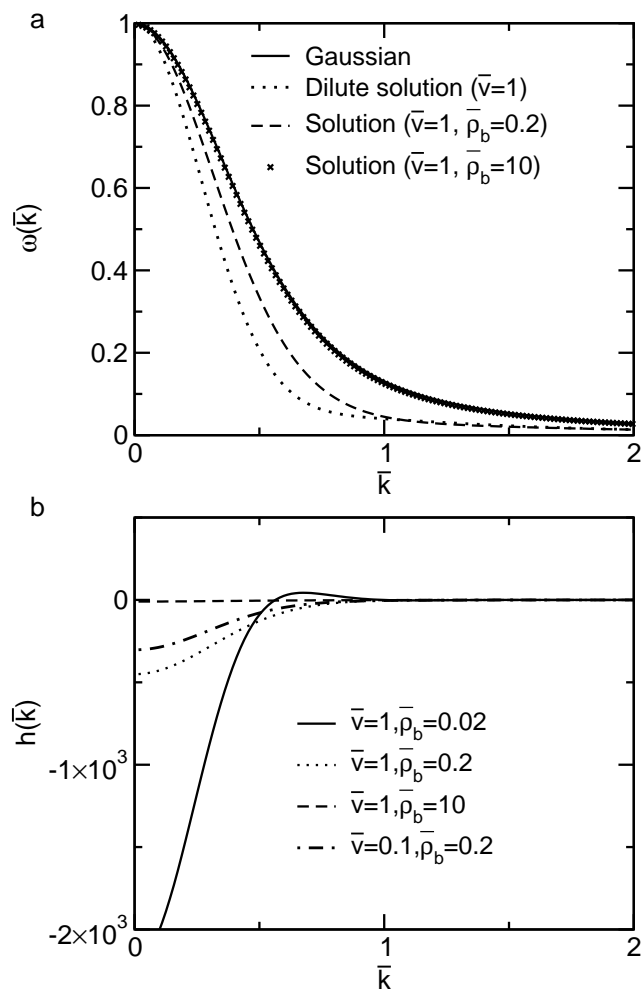


Figure 5.15: The intramolecular  $\omega(k)$  and intermolecular  $h(k)$  structure factors of 4-star molecules ( $N_{\text{star}} = 100$ ). (a) Comparison with the Gaussian chain, with a chain in dilute solution with  $\bar{v} = 1$ , and with 4-star solutions with  $\bar{\rho}_b = 0.2$  and 10, respectively, and  $\bar{v} = 1$ . (b) Comparison with various  $\bar{v}$  and  $\bar{\rho}_b$ .

only depends on  $\bar{\rho}_b$  but not  $\bar{v}$ . It is unusual in SANS experiments on homogeneous polymer melts and blends, which remains an interesting question to explain the two-chain SCFT  $S(\bar{k})$  at high density. The placement of peaks depends on  $\bar{\rho}_b$  comparing the thick solid line ( $\bar{v} = 0.1$ ) and the dot-dash-dot line ( $\bar{v} = 1$ ).

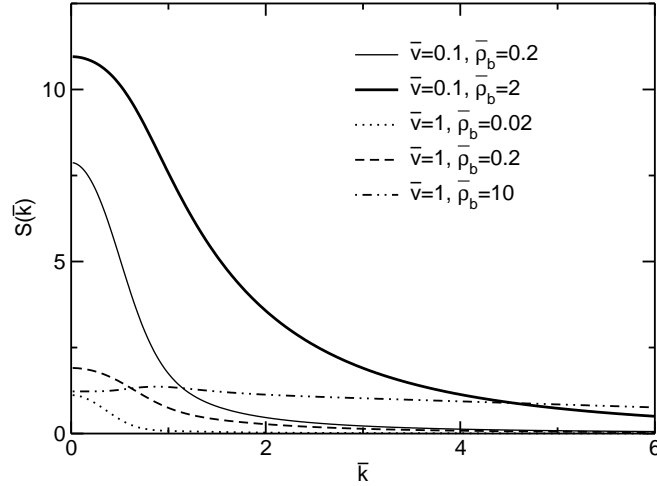


Figure 5.16: Structure factors of 4-star molecules in different solutions.  $N_{\text{star}} = 100$ .

The Kratky plots,  $\bar{k}^2\omega(\bar{k})$  against  $\bar{k}$ , of the star molecules in solutions are shown in Figure 5.17 in the linear-logarithm scales. The star in the dilute solution shows a smaller low- $k$  peak than does the Gaussian star. This is due to the cancellation by the stretching of the arms. In a semi-dilute solution, i.e.,  $\bar{v} = 1$  and  $\bar{\rho}_b = 0.2$ , the stretching of the monomers is not as strong as that in the dilute solution, and the low- $k$  peak has a maximum higher than the dilute solution curve. As the bulk density increases from 0.2 to 2, the maximum of the peak in Kratky plot increases to be closer to the ideal star since the stretching are screened in a concentrated polymer solution or melt. The results by two-chain SCFT are consistent with the PRISM study by Grayce *et al.* [125] A small  $\bar{v}$  weakens the excluded volume effect of the monomers as well as the stretching. The curve of  $\bar{v} = 0.1$ ,  $\bar{\rho}_b = 2$  shows a slightly larger low- $k$  peak than that of  $\bar{v} = 1$  and  $\bar{\rho}_b = 2$ .

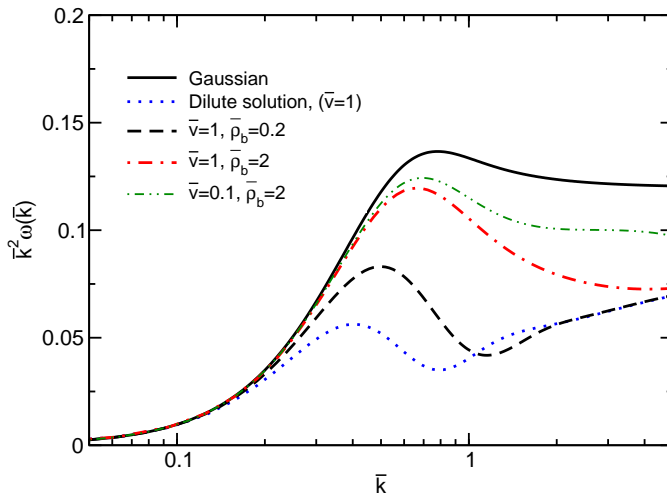


Figure 5.17: The Kratky plots of the intramolecular structure factors  $\omega(k)$  of 4-star molecules ( $N_{\text{star}} = 100$ ). Comparisons are performed among the Gaussian chain, the single chain in dilute solution with  $\bar{v} = 1$ , and 4-star in different solutions with  $\bar{v} = 1$ ,  $\bar{\rho}_b = 0.2$  and  $2$ , respectively.  $\bar{v} = 0.1$ , and  $\bar{\rho}_b = 2$ .

Figure 5.18 shows the intramolecular structure factors of a series of  $f$ -star ( $N_{\text{arm}} = 25$ ) solutions in the Kratky form. The low- $k$  peaks of the Kratky plots decrease as the number of arms increases with fixed arm length, indicating enhanced stretching in highly branched solutions.

## 5.5 The intra- and intermolecular correlations in branched/linear polymer blends

The two-chain SCFT is extended for binary blends containing linear and branched molecules. The conformations for branched molecules in blends and melts are discussed in this section. Within the mean-field approximation, the mixing free energy of the polymer blends can be calculated by two-chain SCFT for predictions of monomer interaction parameters of the homogeneous blends of branched and linear molecules.

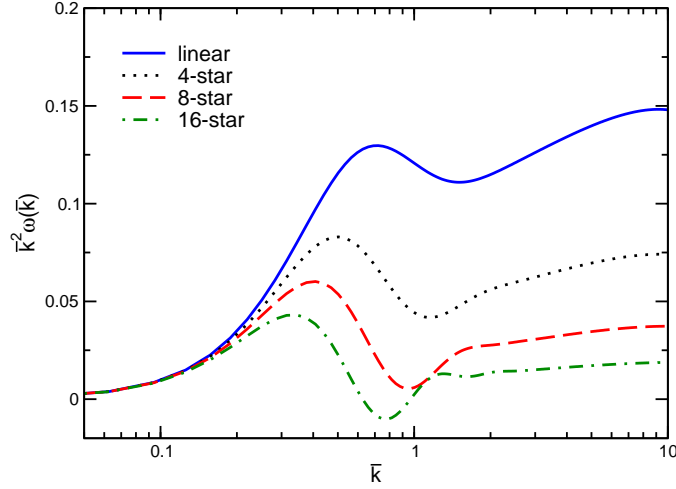


Figure 5.18: The Kratky plots of the intramolecular structure factors  $\omega(k)$  of  $f$ -star solutions.  $N_{\text{arm}} = 25$ ,  $\bar{v} = 1$  and  $\bar{\rho}_b = 0.2$ .

### 5.5.1 Swelling in homogeneous star and linear polymers blends

The molecular conformation in melts and blends is compared using the 4-star melt and blends of 4-star and linear molecules. Given  $N_{\text{star}} = 100$ , the first two-chain SCFT calculation studies an athermal mixture with linear molecules,  $N_{\text{linear}} = 50$ . The excluded volume is  $\bar{v} = 1$ , and the bulk density is  $\bar{\rho}_b = 0.2$  for all calculations unless otherwise specified. The difference in the intramolecular density of the star between a melt and a blend is shown in Figure 5.19 in different compositions. The difference of the density in blends and melts,  $\Delta\bar{\rho} = \bar{\rho}_{\text{melt}} - \bar{\rho}_{\text{blend}}$  is shown on a linear-linear plot, since they are too close to distinguish in a log-log plot. If  $\Delta\bar{\rho} > 0$ , the molecule is more stretched in the blend; if  $\Delta\bar{\rho} < 0$ , the molecule is more stretched as a melt. Figure 5.19 shows that the monomers of the star polymers are more stretched in a blend of linear chains. The peak scaling as  $R_g$  of the arm represents the most enhanced swollen regime in the blend.  $\Delta\bar{\rho}_{\text{star}}$  in all samples are negative close to the joint and it implies that the intramolecular densities in melt and blend converge to different finite limits in SCFT. The compositions of two components also affect swelling. In blends

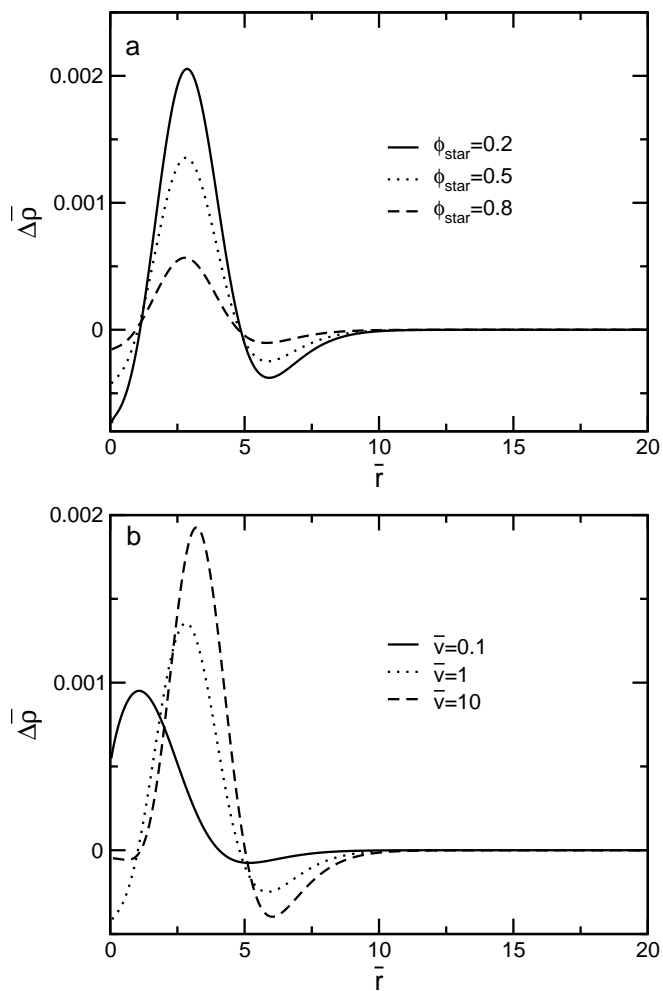


Figure 5.19: Comparisons of the intramolecular density profiles of a 4-star polymer in a melt and a 4-star/linear blend,  $\Delta \bar{\rho}_{\text{star}}$ . Density profiles are calculated by fixing the joint at the origin.  $N_{\text{star}} = 100$  and  $N_{\text{linear}} = 50$ . (a) The comparison of  $\Delta \bar{\rho}_{\text{star}}$  in different compositions. The total monomer density  $\bar{\rho}_b = 0.2$  and  $\bar{v} = 1$ . (b) The intramolecular density of the 4-star components in the 4-star/linear blend by varying excluded volume parameters. The composition of the star monomers,  $\phi_{\text{star}} = 0.5$ ,  $\bar{\rho}_b = 0.2$ .

with lower linear composition, e.g.,  $\phi_{\text{linear}} = 0.2$ , the swelling of stars is weakly enhanced because the system is similar to a star melt. In addition, the stars become more swollen as more linear molecules are added. Figure 5.19b shows that the peaks shift to longer distances by increasing  $\bar{v}$ .

The swelling of the conformation with a fixed end monomer of the star is studied and shown in Figure 5.20a, where the conformations of end regime in a melt is nearly random walk. In the presence of the linear species, the swelling near the end is more enhanced than near the joint. Figure 5.20b shows that the enhancement of swelling is also controlled by the molecular weight of the two components. The mixture with a shorter linear species, i.e., the blends with degree of polymerizations of  $N_{\text{star}} = 100/N_{\text{linear}} = 50$  and  $N_{\text{star}} = 200/N_{\text{linear}} = 100$ , result in a stronger swollen regime. On the contrary, if  $N_{\text{star}} < N_{\text{linear}}$ , the swelling of the star chain is weakly enhanced. Figure 5.20b also shows that the swelling regime depends on the length of arm  $N_{\text{arm}}$ .

Figure 5.21 gives the density profiles of blends with a fixed degree of polymerization ( $N = 300$ ) of linear and 9-end polymers, with different outside branch lengths. As the length of outside branches increases, the 9-end molecule behaves as expected by enhancing swelling. The 9-star ( $N_{\text{arm}} = 30$ ) blends are less stretched than 9-ends with 9-ends with  $N_{\text{branch}} = 30$  and  $N_{\text{arm}} = 10$ . The length of the inside arm has a significant effect on the change in swelling. Note that the height of  $\Delta\bar{\rho}_{9\text{end}}(r)$  does not always increase with increasing the length of the outside branches as shown in Figure 5.21. The strongest swelling enhancement is found in blends of  $N_{\text{branch}} = 20$  among five samples. The swelling is likely stronger when the length of the inside arms and outside branches are close.

### 5.5.2 The intermolecular correlation functions and static structure factors

The intra- and intermolecular correlation functions obtained using two-chain SCFT for a 4-star/linear blend with a fixed joint on the star molecule are shown in Figure 5.22. As discussed in section 5.4.6, the structure factor of the polymer blends can be evaluated from the averaged pair correlation functions. Consider a binary polymer blend of species  $\alpha$  and

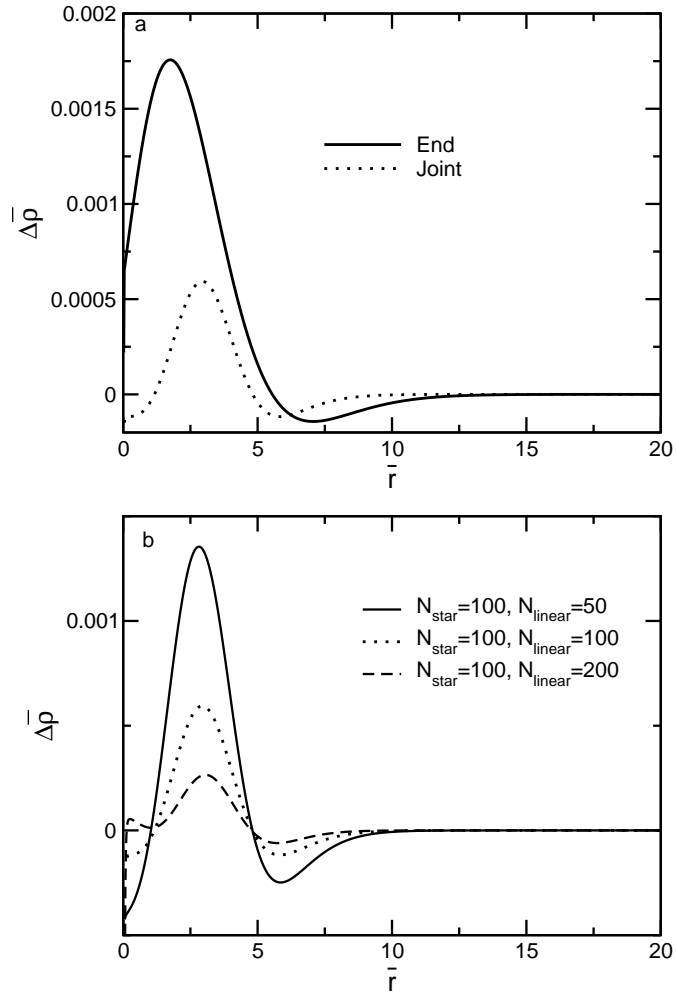


Figure 5.20: A comparison of the intramolecular density profiles between 4-star/linear blends and the 4-star melt. (a) Comparisons of  $\Delta\bar{\rho}_{\text{star}}$  from the joint and end in the 50/50 blend.  $N_{\text{star}} = N_{\text{linear}} = 100$ . (b) Comparison of  $\Delta\bar{\rho}_{\text{star}}$  from the joint of star polymer by changing the molecular weight of the linear polymer. In both cases,  $\bar{\rho}_b = 0.2$  and  $\bar{v} = 1$ .

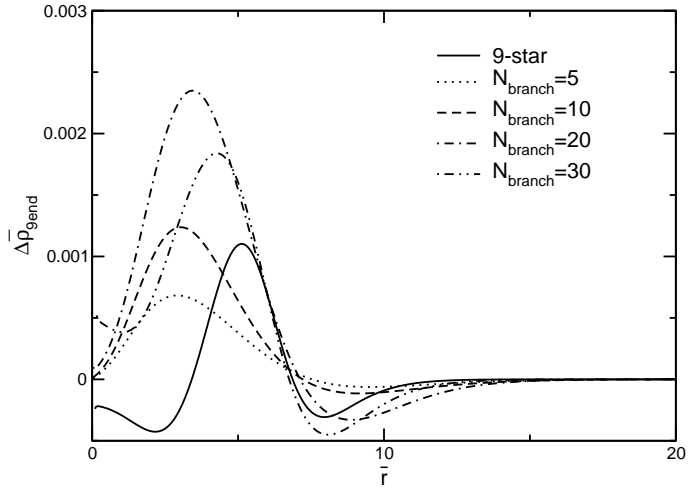


Figure 5.21: A comparison of the intramolecular 9-end density profiles between various 9-end/linear blends and the 9-end melt. The plots locate the joint of the 9-end molecule at the origin. The polymerization index of the 9-end and linear molecules are fixed to be  $N = 300$ . The 9-star is equivalent to a 9-end molecule with  $N_{\text{arm}} = 0$ .  $\bar{\rho}_b = 0.2$  and  $\bar{v} = 1$ .

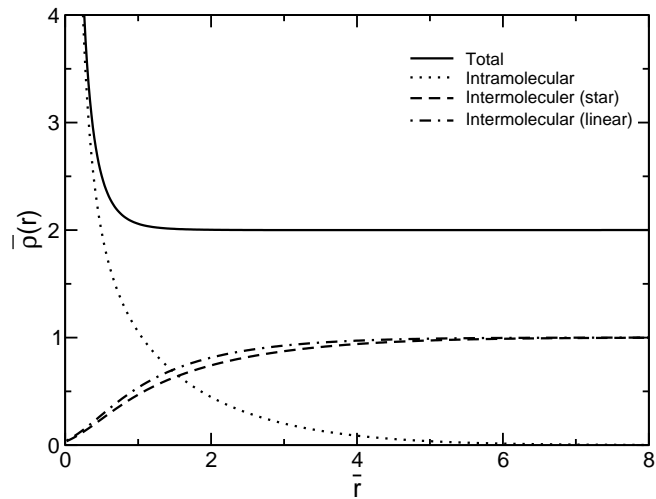


Figure 5.22: The intra- and intermolecular density distribution function of a 4-star/linear binary blend from the joint of a 4-star by SCFT.  $N_{\text{star}} = 100$  and  $N_{\text{linear}} = 50$ .  $\bar{\rho}_b = 2.0$ ,  $\bar{v} = 1$ , and  $\phi = 0.5$ .

$\beta$  with densities of  $\rho_\alpha$  and  $\rho_\beta$ , and polymerization degree  $N_\alpha$  and  $N_\beta$ . The total structure factor is composed of portion of intramolecular and intermolecular contributions defined by:

$$S(\mathbf{k}) = \sum_{i(i=\alpha,\beta)} \rho_i N_i \omega_i(\mathbf{k}) + \sum_{i,(i=\alpha,\beta)} \sum_{j,(j=\alpha,\beta)} \rho_i \rho_j h_{ij}(\mathbf{k}), \quad (5.25)$$

where  $\omega_i(\mathbf{k})$  is the intramolecular structure factor of component  $i$  and  $h_{ij}(\mathbf{k})$  is the intermolecular correlation function for capturing correlations between chains in species  $i$  and  $j$ . Figure 5.23 shows the structure factor of a series of 4star/linear blends ( $\phi = 0.5$ ) in different molecular weight. All calculations use  $\bar{v} = 1$  and  $\bar{\rho}_b = 0.2$ .

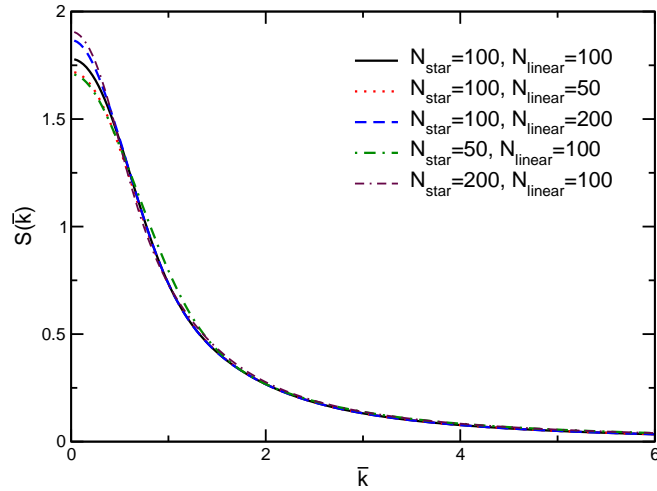


Figure 5.23: The structure factors of a series of 4-star/linear binary blends for various molecular weights.  $\bar{v} = 1$ ,  $\bar{\rho}_b = 0.2$ , and  $\phi = 0.5$ .

## 5.6 The free energy of binary blends by two-chain SCFT

The free energy functional of a binary blend can be written in terms of the monomer density operator shown in Equation 5.26:

$$\hat{W}_{\text{int}} = \int dr \frac{v}{2} (\hat{\rho}_A(r) + \hat{\rho}_B(r))^2 + \int dr \chi \hat{\rho}_A(r) \hat{\rho}_B(r), \quad (5.26)$$

where the parameter  $\chi$  represents the repulsive interaction between species A and B. The canonical ensemble partition function of a binary blend A and B can be written as

$$\begin{aligned} Z_C = Z_0 \int \mathcal{D}\rho_A \mathcal{D}\rho_B \mathcal{D}\mu_A \mathcal{D}\mu_B & (\exp[-W_{\text{int}}] + \exp\left[\int dr(\mu_A \rho_A + \mu_B \rho_B)\right]) \times \\ & \int \mathcal{D}r \exp[-H_0] \exp\left[-\int dt(\mu_A(r(t)) + \mu_B(r(t)))\right], \end{aligned} \quad (5.27)$$

as discussed in Chapter 3. The Helmholtz free energy functional is thus,

$$\begin{aligned} F_C = & -\int dr \left( \chi \rho_A \rho_B + \frac{v}{2} (\rho_A + \rho_B)^2 \right) - \int dr (\mu_A \rho_A + \mu_B \rho_B) \\ & - (n_A \ln(VQ_A) + n_B \ln(VQ_B)) \\ & + (n_A \ln(n_A) + n_B \ln(n_B)) - (n_A + n_B), \end{aligned} \quad (5.28)$$

where  $Q_i$  is the single chain partition function of species  $i$ . With a fixed A polymer, this term includes single chain partition functions in this formula is thus  $(n_A - 1) \ln Q_A + \ln Q_{\text{fix}} + n_B \ln Q_B$ . The saddle point method is applied to find the mean-field free energy, which is given as

$$\mu_A(r) = v(\rho_A(r) + \rho_B(r)) + \chi \rho_B(r), \quad (5.29)$$

and similarly the mean-field potential for B polymer is

$$\mu_B(r) = v(\rho_A(r) + \rho_B(r)) + \chi \rho_A(r). \quad (5.30)$$

Substitute  $\mu_A$  and  $\mu_B$  into Equation 5.28, and the mean-field free energy is written as

$$\begin{aligned} F_C = & -\int dr \left( \chi \rho_A \rho_B + \frac{v}{2} (\rho_A + \rho_B)^2 \right) \\ & - ((n_A - 1) \ln(VQ_A) + \ln(VQ_{\text{fix}}) + n_B \ln(VQ_B)) \\ & + (n_A \ln(n_A) + n_B \ln(n_B)) - (n_A + n_B). \end{aligned} \quad (5.31)$$

### 5.6.1 The mixing free energy of branched/linear blends in canonical ensemble

The free energy of a blend with one fixed molecule in Equation 5.31 can be written in terms of the interaction contribution

$$F_{\text{int}} = -\int dr \left( \chi \rho_A \rho_B + \frac{v}{2} (\rho_A + \rho_B)^2 \right), \quad (5.32)$$

and the entropy

$$F_{\text{ent}} = -(n_A \ln(Q_A) + \ln(Q_{\text{fix}}) + n_B \ln(Q_B)) + n_A \ln(n_A/V) + n_B \ln(n_B/V) - (n_A + n_B). \quad (5.33)$$

In this work, I only consider cases as athermal blends and  $\chi$  is zero. The calculation of the mixing free energy using two-chain SCFT requires some consideration. In an A/B blend composed of two components with the same bulk density, the two-chain SCFT calculates the free energy of the blend in volume  $V$ , with a fixed A or B molecule. Although two-chain SCFT can capture conformational changes at short distances, it only shows the bulk density at long distances (greater than its  $R_g$ ). The subtraction of the free energy between the blend and melt,  $F_{\text{intblendA}} - F_{\text{intmeltA}}$  results in the change of the mixing free energy for a single molecule A correlated to the environment. For instance, in the athermal blend, the expression

$$\begin{aligned} \Delta \bar{F}_{\text{intA}} &= F_{\text{intblendA}} - F_{\text{intmeltA}} \\ &= -\frac{v}{2} \int_V d^3r (\rho_{\text{blend}}(r)^2 - \rho_A(r)^2) \end{aligned} \quad (5.34)$$

gives the change of the enthalpic free energy for a molecule A in the melt and blend. Similarly,

$$\begin{aligned} \Delta \bar{F}_{\text{intB}} &= F_{\text{intblendB}} - F_{\text{intmeltB}} \\ &= -\frac{v}{2} \int_V d^3r (\rho_{\text{blend}}(r)^2 - \rho_B(r)^2). \end{aligned} \quad (5.35)$$

is the change of the interaction free energy of a B molecule. The mixing enthalpic free energy of a binary blend *per monomer* is thus given as

$$\Delta \bar{F}_{\text{intblend}} = \frac{\phi_A}{N_A} \Delta F_{\text{intA}} + \frac{\phi_B}{N_B} \Delta F_{\text{intB}} \quad (5.36)$$

by assuming the volume of each monomer does not change.

The number of molecules  $n_A$  and  $n_B$  are written in terms of compositions,  $\phi_A = V_A/V$  and  $\phi_B = V_B/V$ :

$$n_A = \frac{(n_A N_A + n_B N_B)}{N_A} \phi_A \quad (5.37)$$

and

$$n_B = \frac{(n_A N_A + n_B N_B)}{N_B} \phi_B, \quad (5.38)$$

where  $V_A$  and  $V_B$  are volumes occupied by A and B polymer in the blend.

The entropic contribution is divided into configurational entropy and the ideal mixing entropy:

$$\Delta \bar{F}_{\text{ent}} = \Delta \bar{F}_{\text{conf}} + \Delta \bar{F}_{\text{ideal}}, \quad (5.39)$$

where

$$\Delta \bar{F}_{\text{ideal}} = \frac{\phi_A}{N_A} \ln(\phi_A) + \frac{\phi_B}{N_B} \ln(\phi_B). \quad (5.40)$$

$\Delta \bar{F}_{\text{conf}}$  can be calculated from

$$\Delta \bar{F}_{\text{conf}_A} = -n_A \ln(Q_{\text{blend}_A}/Q_{\text{melt}_A}) - \ln(Q_{\text{blend}_{\text{fix}_A}}/Q_{\text{melt}_{\text{fix}_A}}) \quad (5.41)$$

and

$$\Delta \bar{F}_{\text{conf}_B} = -n_B \ln(Q_{\text{blend}_B}/Q_{\text{melt}_B}) - \ln(Q_{\text{blend}_{\text{fix}_B}}/Q_{\text{melt}_{\text{fix}_B}}), \quad (5.42)$$

where  $Q_{\text{blend}_A}$  and  $Q_{\text{blend}_B}$  are the partition functions of the free chains in the blend, and  $Q_{\text{melt}_A}$  and  $Q_{\text{melt}_B}$  are their partition functions as melts.  $Q_{\text{melt}_{\text{fix}_A}}$  is the partition function of the fixed A molecule in the melt, and  $Q_{\text{blend}_{\text{fix}_A}}$  is the fixed chain partition function in the blend. The partition functions of the same type of the free polymers should be equal in melt or blends with the same bulk density, because

$$\begin{aligned} Q &= \exp(-\mu N) \\ &= \exp(-v\rho_b N). \end{aligned} \quad (5.43)$$

Thus, Equations 5.41 and 5.42 evaluate the difference of the configurational entropy of the fixed molecule in the melt and blend, which is

$$\Delta \bar{F}_{\text{conf}} = \frac{\phi_A}{N_A} \Delta \bar{F}_{\text{conf}_A} + \frac{\phi_B}{N_B} \Delta \bar{F}_{\text{conf}_B}, \quad (5.44)$$

and it can be written as

$$\Delta \bar{F}_{\text{conf}} = -\frac{\phi_A}{N_A} \ln(Q_{\text{blend}_{\text{fixA}}}/Q_{\text{melt}_{\text{fixA}}}) - \frac{\phi_B}{N_B} \ln(Q_{\text{blend}_{\text{fixB}}}/Q_{\text{melt}_{\text{fixB}}}). \quad (5.45)$$

A two-chain SCFT calculation is performed by changing the fixed sites  $t_{\text{fix}}$  on the fixed molecule. The free energy also varies with different  $t_{\text{fix}}$ . The mean value of  $\bar{F}(t_{\text{fix}})$  is taken because every fixed monomer in the SCFT calculations has the same weight, which gives

$$\bar{F} = \frac{1}{N} \sum_{t_{\text{fix}}=0}^N \bar{F}(t_{\text{fix}}), \quad (5.46)$$

where  $N$  is the number of monomers of the molecule.

The SCFT in NVT ensemble has a finite size effect. The difference of the free chain configurational entropy  $\ln(Q_{\text{blend}}/Q_{\text{melt}})$  goes to zero when  $r_{\text{max}} \rightarrow \infty$ . Otherwise, it is nonzero because the bulk concentrations are dependent on the size of the box. This excess effect is also understood as below: The partition function  $Q$  of the free polymer can be expressed as

$$Q = Q_b \frac{(V - V_b)}{V}, \quad (5.47)$$

where  $Q_b$  is the bulk value of the weight function,  $q^{\text{free}}(r, N)$ .  $V_b$  is defined as the finite volume of the correlation hole of  $q^{\text{free}}(r, N)$  at short distance, which also depends on  $V$ .

Therefore,

$$\frac{Q_{\text{blend}}}{Q_{\text{melt}}} = \frac{Q_{b_{\text{blend}}}}{Q_{b_{\text{melt}}}} \left( \frac{V - V_{b_{\text{blend}}}}{V - V_{b_{\text{melt}}}} \right), \quad (5.48)$$

and it implies that this excess term always changes with  $V$ , unless when  $V \rightarrow \infty$ .

$$\lim_{V \rightarrow \infty} Q = Q_b = \exp(-\rho_b(\infty)v).$$

The size effect cannot be corrected by explicit expressions because of the finite  $V_b$ . In order to eliminate the finite size effect, the grand-canonical SCFT is applied to force the bulk concentration to be constant, while allowing fluctuations to the number of monomers.

### 5.6.2 The mixing free energy in semi-grand canonical ensemble

The mixing free energy in a semi-grand canonical ensemble two-chain SCFT can be calculated by modeling the A/B blend and melt A and B, respectively. The A/B blend is modeled by fixing an A molecule first, and then fixing a B polymer. The chemical potentials,  $\mu_A^0$  and  $\mu_B^0$  in both melts and blends are given. The total free energy for a blend in the semi-grand canonical two-chain SCFT can be written as

$$\begin{aligned}
 F_{\text{SGblend}}(n_A + n_B, V) &= -\frac{v}{2} \int_V \rho_{\text{blend}}(r)^2 d^3r - \ln(VQ_{\text{fix}}) \\
 &\quad - z_{\text{Ablend}} VQ_A - z_{\text{Bblend}} VQ_B \\
 &\quad + (\mu_{\text{Ablend}}^0 n_A + \mu_{\text{Bblend}}^0 n_B).
 \end{aligned} \tag{5.49}$$

Similarly, the Helmholtz free energy in melt A with a fixed A molecule in  $V_A$  is written as

$$\begin{aligned}
 \bar{F}_{\text{SGA}}(n_A, V_A) &= -\frac{v}{2} \int_{V_A} \rho_A(r)^2 d^3r \\
 &\quad - (z_{\text{Amelt}} V_A Q_A + \ln(V_A Q_{\text{Afix}})) \\
 &\quad + \mu_{\text{Amelt}}^0 n_A.
 \end{aligned} \tag{5.50}$$

The free energy in melt B can be obtained by replacing A with B in Equation 5.50.

The free energy of the mixture includes the contribution by the fluctuation of the number of molecules,  $\Delta n_A$  and  $\Delta n_B$ , due to mixing. The mixing free energy of an A/B blend including the number fluctuations  $F_{\text{SG}}(n_A + \Delta n_A, n_B + \Delta n_B, V)$  is written in terms of an approximate correction for small  $\Delta n_A$  and  $\Delta n_B$ , which is

$$\begin{aligned}
 F_{\text{SG}}(n_A + \Delta n_A, n_B + \Delta n_B, V) &= F_{\text{SG}}(n_A, n_B, V) + \Delta n_A \frac{\partial F_{\text{SG}}}{\partial n_A} + \Delta n_B \frac{\partial F_{\text{SG}}}{\partial n_B} \\
 &\quad + \mathcal{O}(\Delta n_A^2, \Delta n_B^2, \Delta n_A \Delta n_B) \\
 &\approx F_{\text{SG}}(n_A, n_B, V) + \Delta n_A \mu_A^0 + \Delta n_B \mu_B^0,
 \end{aligned} \tag{5.51}$$

where  $F_{\text{SG}}(n_A, n_B, V)$  is the approximate mixing free energy of the A/B blend from melts A and B with  $n_A$  and  $n_B$  molecules, respectively. With the correction of

$$F_{\text{SG}}(n_{\text{A}}, n_{\text{B}}, V) \approx F_{\text{SG}}(n_{\text{A}} + \Delta n_{\text{A}}, n_{\text{B}} + \Delta n_{\text{B}}, V) - \Delta n_{\text{A}} \mu_{\text{A}}^0 - \Delta n_{\text{B}} \mu_{\text{B}}^0, \quad (5.52)$$

the number of molecules in the blend will be the same as they are in the melts.

The chemical potential  $\mu_{\text{A}}^0$  of an A molecule with  $\phi_{\text{A}}$  can be determined from the expression

$$\begin{aligned} \rho_{\text{A}}^0 &= \phi_{\text{A}} \rho_{\text{b}} \\ &= z_{\text{A}} \int q_{\text{A}}(r; N_{\text{A}}) q_{\text{A}}^\dagger(r; N_{\text{A}}) d^3 r \\ &= e^{\mu_{\text{A}}^0} e^{-\rho_{\text{b}} v N_{\text{A}}}. \end{aligned} \quad (5.53)$$

i.e.,

$$\mu_{\text{A}}^0 = \ln(\phi_{\text{A}} \rho_{\text{A}}^0) \rho_{\text{b}} v N_{\text{A}}, \quad (5.54)$$

and similarly,

$$\mu_{\text{B}}^0 = \ln(\phi_{\text{B}} \rho_{\text{B}}^0) \rho_{\text{b}} v N_{\text{B}}. \quad (5.55)$$

For polymers with the same bulk density,  $\rho_{\text{b}} = \rho_{\text{A}}^0 = \rho_{\text{B}}^0$ , they have  $z_{\text{Ablend}}/z_{\text{Amelt}} = \phi_{\text{A}}$  and  $z_{\text{Bblend}}/z_{\text{Bmelt}} = \phi_{\text{B}}$ . The grand canonical configurational entropy  $zVQ$  is equivalent to the total number of the free monomers, with a correction of  $\Delta n$  canceling the polymer number fluctuation. Thus, the mixing configurational entropy only accounts for change of the fixed molecule from a melt to a blend:

$$\Delta F_{\text{SG,conf}} = -\ln(Q_{\text{fixblend}}/Q_{\text{fixmelt}}), \quad (5.56)$$

and the change of the configurational entropy *per monomer* is

$$\Delta \bar{F}_{\text{SG,conf}} = \frac{\phi_{\text{A}}}{N_{\text{A}}} \ln(Q_{\text{fixAblend}}/Q_{\text{fixAmelt}}) + \frac{\phi_{\text{B}}}{N_{\text{B}}} \ln(Q_{\text{fixBblend}}/Q_{\text{fixBmelt}}). \quad (5.57)$$

Finally, the ideal mixing entropy *per monomer* can be written in terms of

$$\begin{aligned}
\Delta\bar{F}_{\text{SG,ideal}} &= \frac{1}{n_{\text{A}}N_{\text{A}} + n_{\text{B}}N_{\text{B}}}(\mu_{\text{A,blend}}^0 n_{\text{A}} + \mu_{\text{B,blend}}^0 n_{\text{B}}) \\
&\quad - \frac{\phi_{\text{A}}}{n_{\text{A}}N_{\text{A}}}(\mu_{\text{A,melt}}^0 n_{\text{A}}) - \frac{\phi_{\text{B}}}{n_{\text{B}}N_{\text{B}}}(\mu_{\text{B,melt}}^0 n_{\text{B}}) \\
&= \frac{\phi_{\text{A}}}{N_{\text{A}}}\ln(\phi_{\text{A}}) + \frac{\phi_{\text{B}}}{N_{\text{B}}}\ln(\phi_{\text{B}})
\end{aligned} \tag{5.58}$$

by substituting  $\mu_{\text{A,blend}}^0 = \ln(\phi_{\text{A}}) + \mu_{\text{A,melt}}^0$  and  $\mu_{\text{B,blend}}^0 = \ln(\phi_{\text{B}}) + \mu_{\text{B,melt}}^0$  to the first line of the above equation.

The free energy for several 4-star/linear athermal blends is studied by semi-grand canonical two-chain SCFT. In those blends,  $N_{\text{star}} = 100$  is fixed, and the polymerization degrees of the linear molecules vary. The star and linear polymers have the same bulk density,  $\bar{\rho}_{\text{b}} = 0.2$  and  $\bar{v} = 1$ . Note that the excluded volume parameter for a polymer melt is different from that in solutions, this preliminary calculation uses the value of  $\bar{v}$  as the semi-dilute solutions since the appropriate  $\bar{v}$  in melts or blends is not well-compared. The size of the system is given  $r_{\text{max}} = 100b$ . The diagrams of the excess mixing free energy  $\Delta\bar{F}_{\text{ex}} = \Delta\bar{F}_{\text{int}} + \Delta\bar{F}_{\text{conf}}$  for different 4-star/linear blends are shown in Figure 5.24. For the blend with equal polymerization degree,  $N = 100$ , the free energy diagram is approximately symmetric to  $\phi_{\text{star}} = 0.5$ , and exhibits weak immiscibility. For other blends in different polymerization degrees, i.e.,  $N_{\text{linear}} = 50$ , and  $N_{\text{linear}} = 200$ , the excess free energy is increased for a stronger immiscibility compared to the symmetric case. Furthermore, the free energy diagrams are not parabolic or symmetric at  $\phi_{\text{star}} = 0.5$ , but are dependent on the compositions.

Flory-Huggins theory defines the interaction energy of the mixture as  $\Delta\bar{F}_{\text{ex}} = \chi_{\text{eff}}\phi_{\text{A}}\phi_{\text{B}}$ .  $\chi_{\text{eff}}$  can also be estimated from the mixing free energy by semi-grand canonical SCFT. In two-chain SCFT,  $\chi_{\text{eff}}$  is also defined as

$$\chi_{\text{eff}} = \Delta\bar{F}_{\text{ex}}/(\phi_{\text{A}}\phi_{\text{B}}). \tag{5.59}$$

$\chi_{\text{eff}}$  for the 4-star/linear ( $\phi = 0.5$ ) blends are listed in Table 5.1 by SCFT. Results indicate that for a binary blend composed of the same type monomers, the excess mixing free energy

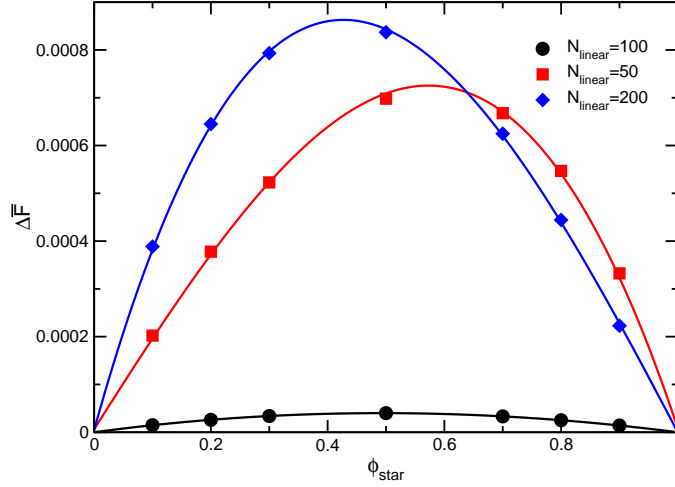


Figure 5.24: The excess free energy  $\Delta\bar{F}$  of the 4-star/linear homogeneous blend in semi-grand canonical SCFT.  $N_{\text{star}} = 100$ , and  $N_{\text{linear}}$  are 50, 100 and 200, respectively.  $\bar{v} = 1$ , and  $\bar{\rho}_b = 0.2$ . The size of the system,  $\bar{r}_{\text{max}} = 100$ .

depends on the molecular weight of the two species.  $\chi_{\text{eff}}$  depends on the compositions and the weakest  $\chi_{\text{eff}}$  is obtained in the symmetric blend for the best miscibility. On the other hand, the interaction parameter significantly increases in blends of disparate molecular weight by a factor of 10 compared to the symmetric blend with equal monomer compositions in the tested blends.

Table 5.1: The effective Flory-Huggins interaction parameters of different 4-star/linear blends with equal monomer compositions, based on the free energy diagrams in Figure 5.24.

Blends $N_{\text{star}}/N_{\text{linear}}$	$\chi_{\text{eff}} (\times 10^{-4})$
100/50	28
100/100	2
100/200	33

The interaction parameters for blends of several symmetric end-branched and linear polymers are evaluated by two-chain SCFT, and compared with experimental values. Re-

cently, Lee *et al.* [19] performed experiments on the bulk thermodynamics of a series of end-branched/linear isotopic polystyrene by SANS.  $\chi_{\text{eff}}$  was evaluated using RPA and Gaussian field theory. For blends ( $\phi = 0.5$ ) of linear and 6-end, 9-end, and 13-end ( designed as 15-ends ) polystyrene with symmetric molecular weight and equal number of branch points, the experiments shows that  $\chi_{\text{eff}}$  increases as the number of outer branches increases. I apply the two-chain SCFT to calculate the mixing free energy and  $\chi_{\text{eff}}$  of the blends of end-branched and linear polymers by Lee and coworkers. The molecules follow the molecular characterization from the reference [19], which are listed in Table 5.2.

Table 5.2: The molecular characterization of n-end/linear blends in two-chain SCFT.

Polymer	$N_{\text{arm}}$	$N_{\text{branch}}$	$N_{\text{total}}$
Linear			360
6-end	60	30	360
9-end	48	24	360
15-end*	55	13	360

\*The molecule studied in the experiment is 13-end; two ends are missing.

Figure 5.25 plots the diagrams of the excess mixing free energy against the composition of the end-branched component of the n-end/linear blends. The  $\chi_{\text{eff}}$  by SCFT are smaller than the SANS  $\chi_{\text{eff}}$  by RPA theory for all three blends, although two of them (6-end and 9-end) are still within the same order of magnitude. SCFT  $\chi_{\text{eff}}$  is close to the Gaussian field theory only for 6-end/linear blend, but much smaller for 9-end/linear and 15-end/linear blends. The excess mixing free energy for the tested end-branched polymer blends increases with increasing outside branches due to enhanced crowding of the branched species. The effective  $\chi_{\text{eff}}$  also increases as the number of branches increases, which is listed and compared with the experiments and Gaussian theory in Figure 5.26.

A reason for the discrepancy for  $\chi_{\text{eff}}$  between SCFT and Gaussian field theory is the parameter  $\bar{v}$  representing the excluded volume effect and the compressibility. It controls the intra- and intermolecular correlations of the polymer blends. Both RPA and Gaussian

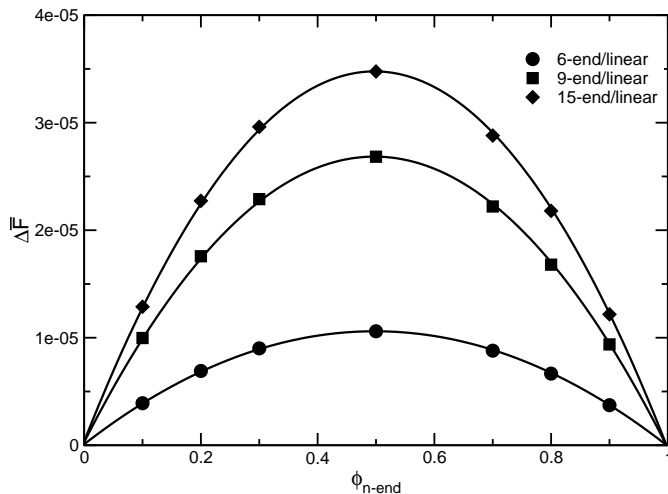


Figure 5.25: The excess free energy  $\Delta\bar{F}$  of n-end/linear homogeneous blends in semi-grand canonical SCFT.  $N = 360$ ,  $\bar{v} = 1$ ,  $\bar{\rho}_B = 0.2$ , and the size of the system,  $\bar{r}_{\max} = 200$ .

field theories have assumed Gaussian conformations in the blend. The SANS spectra also depends on temperature. In particular, the experimental results in Figure 5.26 are measured at 120°C [19]. Gaussian field theory assumes incompressibility corresponding to  $\bar{v} \rightarrow \infty$  in SCFT, and the Gaussian chain conformation corresponds to  $\bar{v} \rightarrow 0$  in SCFT. In addition, the actual monomer volume is considered as a factor of  $\chi_{\text{eff}}$  by Gaussian field theory, but not applied in two-chain SCFT. Future study will focus on the application of two-chain SCFT with appropriate  $\bar{v}$  for different complex architectures with comparisons to the experimental and theoretical results.

### 5.6.3 Gaussian field theory on the approximation of Flory-Huggins parameter for comb/linear blends

Gaussian field theory can estimate the Flory-Huggins interaction parameters of binary blends in terms of mixing entropy. The expressions of the theory is given briefly below. More details of Gaussian field theory can be found in reference [38]. The excess free energy

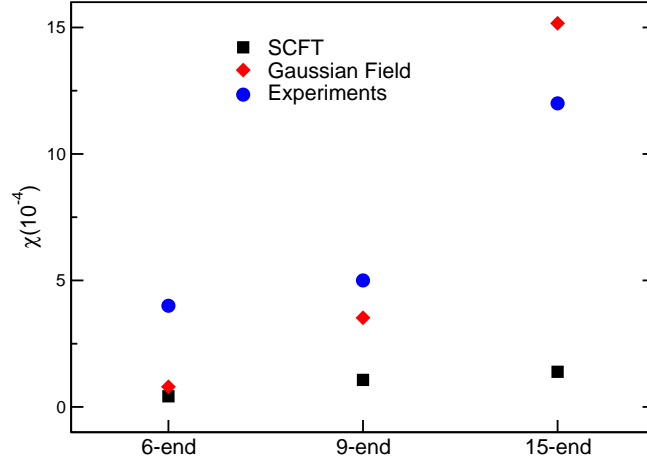


Figure 5.26: The effective interaction parameter  $\chi_{\text{eff}}$  in the n-end/linear homogeneous blends by semi-grand canonical two-chain SCFT, Gaussian field theory and SANS experiments. The experimental  $\chi_{\text{eff}}$  is determined by SANS at  $120^\circ\text{C}$ . The uncertainty in  $\chi_{\text{eff}}$  of  $\pm 0.3 \times 10^{-4}$  for characterizing a linear/linear blend using the same method is reported. Gaussian field theory assumes the statistical segment length  $b = 6.2\text{\AA}$  [19]. In SCFT,  $\bar{v} = 1$ ,  $\bar{\rho}_b = 0.2$ .

is written as

$$\frac{F_E}{kT} = \frac{1}{8\pi^3} \int dk \ln[\phi_1 S_1(k) + \phi_2 S_2(k)], \quad (5.60)$$

where  $S_1$  and  $S_2$  are Gaussian single chain structure factors of the two components. The total free energy of mixing in a mean-field is thus

$$\frac{\Delta F}{kT} = \frac{\phi_1}{V_1} \ln \phi_1 + \frac{\phi_2}{V_2} \ln \phi_2 + \frac{F_E}{kT}, \quad (5.61)$$

where the monomer composition satisfies the incompressibility  $\phi_1 = 1 - \phi_2$ . The second derivative of the excess free energy with respect to  $\phi_1$

$$\begin{aligned} \alpha_E &= -\frac{1}{2kT} \frac{\partial^2 F_E}{\partial \phi_1^2} \\ &= \frac{1}{8\pi^2} \int_0^\infty dk k^2 \left[ \frac{S_1(k) - S_2(k)}{\phi_1 S_1(k) + (1 - \phi_1) S_2(k)} \right]^2, \end{aligned} \quad (5.62)$$

can be applied to estimate the effective monomer-monomer interaction parameter  $\chi_{\text{eff}}$

$$\chi_{\text{eff}} = \alpha_E(v_1 v_2)^{1/2}, \quad (5.63)$$

where  $v_1$  and  $v_2$  are monomer volumes of two components.  $\chi_{\text{eff}}$  for a series of comb/linear of 50vol%/50vol% polystyrene blends are estimated using Gaussian field theory. An example where it is used in the calculation is based on polymers synthesized by Liu *et al* with dense teeth [16]. Two types of linear polymer is used with 360 and 1270 repeat units, respectively. For all combs, the spacing has only one repeat unit between two teeth ( $L = 1$ ). The structural characterization of the comb and liner molecules are listed in Table 5.3.

Table 5.3: The molecular characterization of comb polymers for Gaussian field theory.

Name	Spacing (L)	Length of teeth (M)	Number of teeth (P)
M24P14	1	24	14
M24P28	1	24	28
M24P50	1	24	50
M15P34	1	15	34
M15P105	1	15	105

The Gaussian structure factor of the comb and linear polymer are given in B. Using a reported statistical segment length of  $6.2\text{\AA}$  and the experimentally determined segment volume  $V = 100 \text{ cm}^3/\text{mol}$  [19], the theoretical effective interaction parameters versus the number of teeth  $p$  are given in Figure 5.27.

## 5.7 Summary

A modified two-chain SCFT is developed to study polymer systems for linear and non-linear architectures. Intra- and intermolecular correlations are accounted for by holding one monomer on one chain fixed and allowing surrounding chains to be free. Density distribution profiles of a single molecule from both joints and ends show SAW behavior. This algorithm also captures the crossover in molecular conformation from SAW to Gaussian behavior in polymer solutions with finite densities. The swelling exponent for the monomer density in

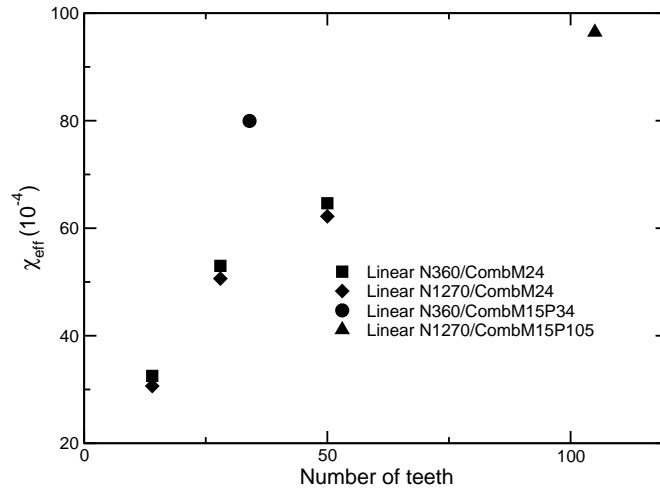


Figure 5.27: The effective thermodynamic interaction parameters  $\chi_{\text{eff}}$  of blends of linear and densely branched comb polymers calculated by Gaussian field theory. The segment length is assumed to be  $b = 6.2\text{\AA}$  as previously reported for branched polystyrene [19].

polymer solutions approaches but is not exactly  $-4/3$ , and varies depending on the excluded volume parameter. A stronger monomer repulsion and relatively low concentrations produce crossovers in the intramolecular density profiles which are most clearly in the scaling regimes.

At short distances, the monomer densities do not depend on excluded volume. However, this dependence becomes stronger as the excluded volume parameter  $v$  increases, so that it finally shows the scaling  $\bar{\rho} \sim \bar{v}^{-1/3}$  when  $\bar{v} > 1$ , consistent with de Gennes' scaling description of polymers in semi-dilute solution. Two regimes of the dependence between  $\bar{v}$  and the correlation length  $\bar{\xi}$  are obtained, and they cross over at approximately  $\bar{v} \approx 1$  in the SCFT calculation. In the strong dependence regime,  $\bar{\xi} \sim \bar{v}^{-1/8}$  is obtained in a semi-dilute solution, compared to  $\bar{\xi} \sim \bar{v}^{-1/4}$  when assuming conformations are given by dilute solution conditions. The intermolecular distribution function displays the expected correlation hole as controlled by excluded volume. This effect is weakened as the excluded volume decreases to a level close to that of a noninteracting chain. Local stretching of monomers can be observed when the monomer exclusion is strong (e.g.,  $\bar{v} = 100$ ). End-branched molecules

such as a 9-end polymer molecule can also exhibit enhanced swelling at short distances near the joint due to the steric and entropic effect of outside branches when  $N_{\text{branch}}/N_{\text{arm}} > 1$ . Lastly, the complete SCFT calculation holding every monomer on one molecule fixed can also generate the structure factors of polymer systems.

In binary blends of star and linear molecules, the swelling of branched molecules are enhanced at short distances compared to melts. The presence of short linear chains results in a stronger swelling for star molecules than for long linear additives. The Helmholtz mixing free energy determined by canonical ensemble SCFT comprises the interaction (excluded volume), configurational entropy and ideal mixing entropy contributions. A semi-grand canonical SCFT calculation is performed to eliminate the finite-size effect in canonical ensemble. The effective Flory-Huggins parameter  $\chi_{\text{eff}}$  by two-chain SCFT is estimated based on the excess free energy. A series of 4-star/linear blends differing in degree of polymerization are tested by the theory. The results indicate that in homogeneous blends, the interaction parameter is dependent on the relative degree of polymerization of the components, with a minimum for blends of equal molecular weight. A series of end-branched/linear ( $\phi = 0.5$ ) polystyrene blends with equal molecular weights are compared by two-chain SCFT, Gaussian field theory and experiments. Based on the calculations using  $\bar{v}$  for semi-dilute solutions, the two-chain SCFT provides the same trends of  $\chi_{\text{eff}}$  for end-branched polymers as RPA and Gaussian field theory. The magnitude of the values from two-chain SCFT are generally smaller, but may be improved by applying  $\bar{v}$  values appropriate for polymer blends.

## CHAPTER 6

### CONCLUSIONS AND FUTURE WORK

My research leads to original contributions in two major topics related to the knowledge of conformations and thermodynamics of nonlinear polymers. The first topic focuses on the surface segregation in blends of nonlinear and linear polymers, including branched, comb and cyclic architectures. The SCFT calculation successfully predicted the surface segregation of the nonlinear architectures due to both entropic and enthalpic effects. Furthermore, the SCFT calculation on the surface segregation for cyclic/linear blends is the first time this has been studied. The results were in excellent agreement with the NR experiments for high molecular weight blends. The second topic focussed on studies of bulk conformations and thermodynamics for branched polymer melts and blends. To attack the problem, a novel two-chain SCFT approach is developed to capture bulk intra- and intermolecular correlations, and to evaluate the mixing free energy for homogeneous polymer blends containing complex branched architectures.

Chapter 3 presents a conceptual overview of SCFT for the surface segregation in blends of linear and nonlinear structures. The SCFT is modified to include surface potentials on ends and joints. In Chapter 4, surface segregation in binary blends containing linear and nonlinear architectures, including star, multiple-end branched, and comb-branched polymers are studied by compressible SCFT. The calculations indicate that the effect of the topology and the excluded volume can cause surface enrichment of the nonlinear components in blends with symmetric degrees of polymerization. The SCFT calculation produces good agreement with the neutron reflectivity experiments on the surface excess of 6-end/linear polystyrene symmetric blends. In disparate blends, the short linear chain exhibits a preference for the immediate vicinity of the surface. However, the nonlinear molecules show a positive integrated excess in the near-surface regime. The dependence of integrated excess on molecular

size differs with different architectures. For star/linear blends, the excess increases linearly as the number of arms increases, but decreases linearly as the length of the arms increases. In striking contrast, for cyclic molecules, the integrated excess is increasing, and linear with  $\sqrt{N_{\text{ring}}}$ . SCFT calculations by adding surface potentials on ends and branch points show surface density profiles for molecules containing particular chemical groups. The density profiles are determined by the competition between the repulsive branch points and attractive ends. In addition, linear response theory is performed to compare with experiments on various end-branched/linear blends by neutron reflectivity. The comparison provides a qualitative understanding of the surface potentials for functional groups, and could aid in guiding the synthesis of surface-active branched polymers.

Chapter 5 documents the development of a novel two-chain SCF theory to study the bulk conformations, correlations, and thermodynamic properties of linear and nonlinear polymers. The two-chain SCFT is applied in canonical and semi-grand canonical ensemble to study the branched melt and mixtures with linear molecules. The intramolecular density profiles of star and branched melts exhibit self-avoiding walk conformations at short distances,  $\bar{r} \rightarrow 0$ , and random walk conformations at long distances  $\bar{r} \rightarrow \bar{R}$ . In semi-dilute solutions, the intramolecular density at short distance is independent of  $\bar{v}$  for  $\bar{v} < 1$ . When  $\bar{v}$  is large, ( $\bar{v} \gg 1$ ) a strong dependence between  $\bar{v}$  and  $\bar{\rho}(\bar{r})$  can be obtained in terms of  $\bar{\rho} \sim \bar{v}^{-1/3}$ . The reduced correlation length  $\bar{\xi}$  by SCFT shows that in polymer melts, it satisfies  $\bar{\xi} \sim \bar{v}^{-1/8}$ . Assuming the conformation of the molecule in a melt is the same as in the dilute solution, the relation  $\bar{\xi} \sim \bar{v}^{-1/4}$  is obtained, and agrees with the scaling analysis by de Gennes for the real chain screening length. The conformation of end-branched molecules such as a 9-end molecule can also exhibit stretching of the inside arms due to the steric and entropic effects of outside branches in a melt when  $N_{\text{branch}} > N_{\text{arm}}$ .

The enhanced swelling for branched molecules is seen in the binary blends of nonlinear and linear molecules. For a blend with short and long chains, the conformation of the long molecule is more swollen by adding short molecules. On the other hand, the conformation

of the short molecule is not affected by the addition of long chains. A short chain is much easier to fill into the space between long chains so that the monomers are crowded. In two-chain SCFT at long distances, the short chain feels a mean-field that equally involves contributions of the large molecule or many short chains, thus the density profiles for short chains does not change significantly under the influence of long chains. The Helmholtz free energy of branched/linear polymer blends can be evaluated using two-chain SCFT. For calculations performed in an NVT ensemble, the two-chain SCFT derived mixing free energy has noticeable finite-size effects that require correction. The semi-grand canonical two-chain SCFT is developed to minimize the finite-size effect. The semi-grand canonical SCFT successfully calculated the mixing free energy of the blend of linear and branched polymers. From the mixing free energy, one can determine a value for the effective monomer (segment) interaction parameter,  $\chi_{\text{eff}}$ , of the homogeneous blend. The free energy diagrams plotted against the volume fraction for the 4-star/linear blends indicate that the interaction parameter is dependent on the volume fraction in disparate molecular weight blends. In the equal molecular weight blend, the free energy is approximately symmetric with respect to  $\phi = 0.5$ . Blends with symmetric molecular weights show a small  $\chi_{\text{eff}}$  compared to disparate molecular weight blends. While a proper choice for the excluded volume parameter for polymer blends has not been well defined for two-chain SCFT, I used values of  $\bar{v}$  typical for semi-dilute solutions to obtain preliminary results for the end-branched polymer blends. While the trend are in agreement with the Gaussian field theory, the magnitude of the  $\chi_{\text{eff}}$  values are low compared to Gaussian field theory and RPA theory. The choice of the excluded volume parameter should be carefully considered in future applications.

The SCFT is still a coarse-grained theory, and is limited by the validity of the Gaussian assumption. It is thus expected to better predict properties for polymers with large molecular weight; but begin to fail for short molecules or rigid structures. For surface studies on short molecules, packing effects at surfaces is missing in SCFT, which will also influence the results of the prediction. In the two-chain theory, the calculation for molecular conformations at

very short distances,  $r \rightarrow 0$  increases numerical difficulties. In calculations for long range intermolecular correlations, SCFT results in a uniform bulk density, and misses information of the correlation between two specific molecules far from the test molecule being held fixed. As such, binary correlations are accounted for in the two-chain SCFT, but higher order correlations are still neglected. In principle, it is possible to extend the methodology to multi-chain SCFT, but at an increased computational cost.

Further comparison with Flory-Huggins theory, Gaussian field theory and random phase approximation theory should be carried out to test the two-chain SCFT for  $\chi_{\text{eff}}$  parameters in branched/linear PS blends in the future. Studies of the bulk conformations of various molecular topologies, for instance understanding which parts of a highly complex branched molecule is stretched or under stress, is also a promising direction for study using these two-chain algorithms. The two-chain SCFT can also be extended to fixing multiple molecules, to capture higher order correlations. In particular, this would be of interest in studying the topological consequences of non-crossing in a system of ring polymers. The new algorithm also provides the solution of the modified diffusion equations in more complicated coordinates. To sample the conformations in a multiple-chain SCF theory, it may be necessary to consider hybrid algorithms including self-consistent field and Monte Carlo sampling (SCF-MC). Such an algorithm generates the configurations of molecules using Monte Carlo method instead of the Gaussian chain assumption. The free polymers contribute a mean-field potential satisfying self-consistency with the mean density. It can be expected to capture the intermolecular correlations between two specific molecules, and could be more efficient than a full Monte Carlo simulation. In addition, it is also possible to study a variety of polymer architectures beyond star, pom-pom and end-branched polymers. The understanding of the bulk correlation of macrocyclic molecular melts is proposed as a future topic for study using a hybrid SCF-MC approach. The molecules can be simple rings or more complicated structures containing loops, such as those shown in Figure 6.1.



Figure 6.1: Cyclic, balloon, dumbbell, and rings on a rope topologies.

In conclusion, conventional SCFT and the novel two-chain SCFT have been demonstrated to successfully predict many conformational, segregation, and thermodynamic properties for nonlinear macromolecules at surfaces and in the bulk. These theories can be applied to guide future experiments and hopefully the commercialization of nonlinear polymers.

## REFERENCES CITED

- [1] D. R. Paul and C. B. Bucknall, *Polymer Blends*, vol. 1 and 2. Wiley-Interscience, 2000.
- [2] L. A. Utracki, *Polymer Blends Handbook*, vol. 1. Springer-Verlag, 2002.
- [3] L. A. Utracki, *Commercial Polymer Blends*. Chapman and Hall, 1998.
- [4] C. K. Ober, S. Z. D. Cheng, P. T. Hammond, M. Muthukumar, E. Reichmanis, K. L. Wooley, and T. P. Lodge, "Research in macromolecular science: Challenges and opportunities for the next decade," *Macromolecules*, vol. 42, no. 2, pp. 465–471, 2009.
- [5] H. Hsieh and R. P. Quirk, *Anionic Polymerization: Principles and Practical Applications*. CRC Press, 1996.
- [6] L. A. Archer and S. K. Varshney, "Synthesis and relaxation dynamics of multiarm polybutadiene melts," *Macromolecules*, vol. 31, no. 18, pp. 6348–6355, 1998.
- [7] J. S. Lee, R. P. Quirk, M. D. Foster, K. M. Wollyung, and C. Wesdemiotis, "A new methodology for the synthesis of star polymers utilizing the reaction of living polymers with alkoxysilyl-functionalized polymers," *Macromolecules*, vol. 37, no. 17, pp. 6385–6394, 2004.
- [8] M. G. McKee, S. Unal, G. L. Wilkes, and T. E. Long, "Branched polyesters: recent advances in synthesis and performance," *Progress in Polymer Science*, vol. 30, no. 5, pp. 507 – 539, 2005.
- [9] J. S. Lee, R. P. Quirk, and M. D. Foster, "Synthesis and characterization of well-defined, regularly branched polystyrenes utilizing multifunctional initiators," *Macromolecules*, vol. 38, no. 13, pp. 5381–5392, 2005.
- [10] H. Gao and K. Matyjaszewski, "Synthesis of star polymers by a combination of atip and the "click" coupling method," *Macromolecules*, vol. 39, no. 15, pp. 4960–4965, 2006.
- [11] Y. Chen, Z. Shen, E. Barriau, H. Kautz, and H. Frey, "Synthesis of multiarm star poly(glycerol)-block-poly(2-hydroxyethyl methacrylate)," *Biomacromolecules*, vol. 7, no. 3, pp. 919–926, 2006.

- [12] L. Wang and W. P. Weber, "Synthesis and properties of novel comb polymers: unsaturated carbosilane polymers with pendent oligo(oxyethylene) groups," *Macromolecules*, vol. 26, no. 5, pp. 969–974, 1993.
- [13] J. Yoo, M. B. Runge, and N. B. Bowden, "Synthesis of complex architectures of comb block copolymers," *Polymer*, vol. 52, no. 12, pp. 2499 – 2504, 2011.
- [14] T. F. Schaub, G. J. Kellogg, A. M. Mayes, R. Kulasekere, J. F. Ankner, and H. Kaiser, "Surface modification via chain end segregation in polymer blends," *Macromolecules*, vol. 29, no. 11, pp. 3982–3990, 1996.
- [15] R. Mason, C. A. Jalbert, P. A. O. Muisener, J. T. Koberstein, J. F. Elman, T. E. Long, and B. Z. Gunesin, "Surface energy and surface composition of end-fluorinated polystyrene," *Advances in Colloid and Interface Science*, vol. 94, no. 1–3, pp. 1 – 19, 2001.
- [16] B. Liu, *Synthesis and Surface Dynamics of Comb Polystyrenes and Their Interfacial Segregation and Bulk Thermodynamics in Blends with Linear Polystyrenes*. PhD thesis, The University of Akron, 2012.
- [17] A. Asatekin, S. Kang, M. Elimelech, and A. M. Mayes, "Anti-fouling ultrafiltration membranes containing polyacrylonitrile-graft-poly(ethylene oxide) comb copolymer additives," *Journal of Membrane Science*, vol. 298, no. 1–2, pp. 136 – 146, 2007.
- [18] J. S. Lee, *Synthesis and Characterization of Novel, Highly Branched Polystyrenes and Their Interfacial Segregation and Bulk Thermodynamics in Blends with Linear Polystyrenes*. PhD thesis, The Univeristy of Akron, 2005.
- [19] J. S. Lee, M. D. Foster, and D. T. Wu, "Effects of branch points and chain ends on the thermodynamic interaction parameter in binary blends of regularly branched and linear polymers," *Macromolecules*, vol. 39, no. 15, pp. 5113–5121, 2006.
- [20] S. Yang, *Thermodynamics and Dynamics of Branched Polystyrenes and Their Mixtures*. PhD thesis, The University of Akron, 2008.
- [21] D. T. Wu and G. H. Fredrickson, "Effect of architecture in the surface segregation of polymer blends," *Macromolecules*, vol. 29, no. 24, pp. 7919–7930, 1996.
- [22] P. G. de Gennes, *Scaling Concepts in Polymer Physics*. Cornell University Press, 1 ed., 1979.

- [23] E. Helfand and Y. Tagami, "Theory of the interface between immiscible polymers," *Journal of Polymer Science Part B: Polymer Letters*, vol. 9, pp. 741–746, 1971.
- [24] E. Helfand and Y. Tagami, "Theory of the interface between immiscible polymers," *The Journal of Chemical Physics*, vol. 57, no. 4, pp. 1812–1813, 1972.
- [25] E. Helfand and Y. Tagami, "Theory of the interface between immiscible polymers. ii," *The Journal of Chemical Physics*, vol. 56, no. 7, pp. 3592–3601, 1972.
- [26] E. Helfand, "Theory of inhomogeneous polymers: Fundamentals of the gaussian random-walk model," *The Journal of Chemical Physics*, vol. 62, no. 3, pp. 999–1005, 1975.
- [27] A. Hariharan, S. K. Kumar, and T. P. Russell, "Surface segregation in binary polymer mixtures: a lattice model," *Macromolecules*, vol. 24, no. 17, pp. 4909–4917, 1991.
- [28] D. G. Walton and A. M. Mayes, "Entropically driven segregation in blends of branched and linear polymers," *Physical Review E*, vol. 54, no. 3, pp. 2811–2815, 1996.
- [29] P. G. Ferreira and L. Leibler, "Copolymer brushes," *The Journal of Chemical Physics*, vol. 105, no. 20, pp. 9362–9370, 1996.
- [30] G. Fredrickson, *The Equilibrium Theory of Inhomogeneous Polymers*. Oxford University Press, 2006.
- [31] M. W. Matsen, *Self-Consistent Field Theory and Its Applications*, vol. 1, ch. 2, pp. 87–178. Wiley-VCH Verlag GmbH & Co. KGaA, 2007.
- [32] S.-F. Wang, *Synthesis and Characterization of Surface Relaxations of Macrocyclic Polystyrenes and Interfacial Segregation in Blends with Linear Polystyrenes*. PhD thesis, The University of Akron, 2011.
- [33] A. Ghosh, *Relaxation Dynamics of Branched Polymers*. PhD thesis, The Pennsylvania State University, 2007.
- [34] S. F. Edwards, "The statistical mechanics of polymers with excluded volume," *Proceedings of the Physical Society*, vol. 85, no. 4, p. 613, 1965.
- [35] G. S. Grest, K. Kremer, and T. A. Witten, "Structure of many arm star polymers: a molecular dynamics simulation," *Macromolecules*, vol. 20, no. 6, pp. 1376–1383, 1987.

- [36] M. L. Huggins, "Solutions of long chain compounds," *The Journal of Chemical Physics*, vol. 9, no. 5, pp. 440–440, 1941.
- [37] P. J. Flory, "Thermodynamics of high polymer solutions," *The Journal of Chemical Physics*, vol. 9, no. 8, pp. 660–660, 1941.
- [38] G. H. Fredrickson, A. J. Liu, and F. S. Bates, "Entropic corrections to the flory-huggins theory of polymer blends: Architectural and conformational effects," *Macromolecules*, vol. 27, no. 9, pp. 2503–2511, 1994.
- [39] T. D. Martter, M. D. Foster, T. Yoo, S. Xu, G. Lizzaraga, R. P. Quirk, and P. D. Butler, "Nonuniversal behavior of the thermodynamic interaction parameter in blends of star and linear polybutadiene," *Macromolecules*, vol. 35, no. 26, pp. 9763–9772, 2002.
- [40] L. S. Bartell and R. R. Roskos, "Isotope effects on molar volume and surface tension: Simple theoretical model and experimental data for hydrocarbons," *The Journal of Chemical Physics*, vol. 44, no. 2, pp. 457–463, 1966.
- [41] F. S. Bates and G. D. Wignall, "Isotope-induced quantum-phase transitions in the liquid state," *Physical Review Letters*, vol. 57, pp. 1429–1432, 1986.
- [42] F. S. Bates, J. H. Rosedale, G. H. Fredrickson, and C. J. Glinka, "Fluctuation-induced first-order transition of an isotropic system to a periodic state," *Physical Review Letters*, vol. 61, pp. 2229–2232, 1988.
- [43] A. Hariharan, S. K. Kumar, and T. P. Russell, "Reversal of the isotopic effect in the surface behavior of binary polymer blends," *The Journal of Chemical Physics*, vol. 98, no. 5, pp. 4163–4173, 1993.
- [44] A. Hariharan, S. K. Kumar, and T. P. Russell, "A lattice model for the surface segregation of polymer chains due to molecular weight effects," *Macromolecules*, vol. 23, no. 15, pp. 3584–3592, 1990.
- [45] A. Hariharan, S. K. Kumar, and T. P. Russell, "Surface segregation in binary polymer mixtures: a lattice model," *Macromolecules*, vol. 24, no. 17, pp. 4909–4917, 1991.
- [46] W. Zhao, X. Zhao, M. H. Rafailovich, J. Sokolov, R. J. Composto, S. D. Smith, T. P. Russell, W. D. Dozier, T. Mansfield, and M. Satkowski, "Segregation of chain ends to polymer melt surfaces and interfaces," *Macromolecules*, vol. 26, no. 3, pp. 561–562, 1993.

- [47] L. J. Norton, E. J. Kramer, F. S. Bates, M. D. Gehlsen, R. A. L. Jones, A. Karim, G. P. Felcher, and R. Kleb, "Neutron reflectometry study of surface segregation in an isotopic poly(ethylenepropylene) blend: Deviation from mean-field theory," *Macromolecules*, vol. 28, no. 25, pp. 8621–8628, 1995.
- [48] I. Hopkinson, F. T. Kiff, R. W. Richards, S. Affrossman, M. Hartshorne, R. A. Pethrick, H. Munro, and J. R. P. Webster, "Investigation of surface enrichment in isotopic mixtures of poly(methyl methacrylate)," *Macromolecules*, vol. 28, no. 2, pp. 627–635, 1995.
- [49] J. Sokolov, M. H. Rafailovich, R. A. L. Jones, and E. J. Kramer, "Enrichment depth profiles in polymer blends measured by forward recoil spectrometry," *Applied Physics Letters*, vol. 54, no. 6, pp. 590–592, 1989.
- [50] R. A. L. Jones, E. J. Kramer, M. H. Rafailovich, J. Sokolov, and S. A. Schwarz, "Surface enrichment in an isotopic polymer blend," *Physical Review Letters*, vol. 62, pp. 280–283, 1989.
- [51] U. Steiner, J. Klein, E. Eiser, A. Budkowski, and L. J. Fetters, "Complete wetting from polymer mixtures," *Science*, vol. 258, pp. 1126–1129, 1992.
- [52] P. P. Hong, F. J. Boerio, and S. D. Smith, "Effect of annealing time, film thickness, and molecular weight on surface enrichment in blends of polystyrene and deuterated polystyrene," *Macromolecules*, vol. 27, no. 2, pp. 596–605, 1994.
- [53] D. G. Walton, P. P. Soo, A. M. Mayes, S. J. Sofia Allgor, J. T. Fujii, L. G. Griffith, J. F. Ankner, H. Kaiser, J. Johansson, G. D. Smith, J. G. Barker, and S. K. Satija, "Creation of stable poly(ethylene oxide) surfaces on poly(methyl methacrylate) using blends of branched and linear polymers," *Macromolecules*, vol. 30, no. 22, pp. 6947–6956, 1997.
- [54] C. Jalbert, J. T. Koberstein, I. Yilgor, P. Gallagher, and V. Krukoniš, "Molecular weight dependence and end-group effects on the surface tension of poly(dimethylsiloxane)," *Macromolecules*, vol. 26, no. 12, pp. 3069–3074, 1993.
- [55] S. Affrossman, M. Hartshorne, R. Jerome, R. A. Pethrick, S. Petitjean, and M. R. Vilar, "Surface concentration of chain ends in polystyrene determined by static secondary ion mass spectroscopy," *Macromolecules*, vol. 26, no. 23, pp. 6251–6254, 1993.
- [56] K. Tanaka, D. Kawaguchi, Y. Yokoe, T. Kajiyama, A. Takahara, and S. Tasaki, "Surface segregation of chain ends in  $\alpha$ -fluoroalkyl-terminated polystyrenes films," *Polymer*, vol. 44, no. 15, pp. 4171 – 4177, 2003.

- [57] A. Hariharan, S. K. Kumar, and T. P. Russell, “Free surfaces of polymer blends. ii. effects of molecular weight and applications to asymmetric polymer blends,” *The Journal of Chemical Physics*, vol. 99, no. 5, pp. 4041–4050, 1993.
- [58] M. Sikka, N. Singh, A. Karim, F. S. Bates, S. K. Satija, and C. F. Majkrzak, “Entropy-driven surface segregation in block copolymer melts,” *Physical Review Letters*, vol. 70, pp. 307–310, 1993.
- [59] F. Scheffold, A. Budkowski, U. Steiner, E. Eiser, J. Klein, and L. J. Fetters, “Surface phase behavior in binary polymer mixtures. ii. surface enrichment from polyolefin blends,” *The Journal of Chemical Physics*, vol. 104, no. 21, pp. 8795–8806, 1996.
- [60] A. Budkowski, J. Rysz, F. Scheffold, J. Klein, A. Bernasik, and J. Jedliński, “Surface segregation in the minority component of the binary polymer mixture,” *Vacuum*, vol. 54, no. 1–4, pp. 273 – 277, 1999.
- [61] M. D. Foster, C. C. Greenberg, D. M. Teale, C. M. Turner, S. Corona-Galvan, E. Cloutet, P. D. Butler, B. Hammouda, and R. P. Quirk, “Effective and surface segregation in blends of star and linear polystyrene,” *Macromolecular Symposia*, vol. 149, no. 1, pp. 263–268, 2000.
- [62] M. D. Foster, D. T. Wu, S.-F. Wang, and R. Hu. Private communication.
- [63] V. S. Minnikanti and L. A. Archer, “Surface migration of branched molecules: Analysis of energetic and entropic factors,” *The Journal of Chemical Physics*, vol. 123, no. 14, pp. 144902–1–144902–9, 2005.
- [64] V. S. Minnikanti and L. A. Archer, “Entropic attraction of polymers toward surfaces and its relationship to surface tension,” *Macromolecules*, vol. 39, no. 22, pp. 7718–7728, 2006.
- [65] H. J. Ploehn, W. B. Russel, and C. K. Hall, “Self-consistent field model of polymer adsorption: generalized formulation and ground-state solution,” *Macromolecules*, vol. 21, no. 4, pp. 1075–1085, 1988.
- [66] J. M. H. M. Scheutjens and G. J. Fleer, “Statistical theory of the adsorption of interacting chain molecules. 1. partition function, segment density distribution, and adsorption isotherms,” *The Journal of Physical Chemistry*, vol. 83, no. 12, pp. 1619–1635, 1979.
- [67] J. M. H. M. Scheutjens and G. J. Fleer, “Interaction between two adsorbed polymer layers,” *Macromolecules*, vol. 18, no. 10, pp. 1882–1900, 1985.

- [68] C. C. van der Linden and F. A. M. Leermakers, “On the self-similar structure of adsorbed polymer layers: dependence of the density profile on molecular weight and solution concentration,” *Macromolecules*, vol. 25, no. 13, pp. 3449–3453, 1992.
- [69] G. K. Stratouras and M. K. Kosmas, “On the density profile of ring chains interacting with a surface,” *Macromolecules*, vol. 24, no. 25, pp. 6754–6758, 1991.
- [70] G. H. Fredrickson and J. P. Donley, “Influence of broken conformational symmetry on the surface enrichment of polymer blends,” *The Journal of Chemical Physics*, vol. 97, no. 12, pp. 8941–8946, 1992.
- [71] D. T. Wu, G. H. Fredrickson, and J.-P. Carton, “Surface segregation in conformationally asymmetric polymer blends: Incompressibility and boundary conditions,” *The Journal of Chemical Physics*, vol. 104, no. 16, pp. 6387–6397, 1996.
- [72] J. P. Donley and G. H. Fredrickson, “Influence of conformational asymmetry on the surface enrichment of polymer blends II,” *Journal of Polymer Science Part B: Polymer Physics*, vol. 33, no. 9, pp. 1343–1351, 1995.
- [73] J. P. Donley, D. T. Wu, and G. H. Fredrickson, “On the control of surface enrichment in polymer blends and copolymers,” *Macromolecules*, vol. 30, no. 7, pp. 2167–2174, 1997.
- [74] M. A. Carignano and I. Szleifer, “Surface segregation in diblock copolymers and polymer blend thin films,” *EPL (Europhysics Letters)*, vol. 30, no. 9, p. 525, 1995.
- [75] Z. Qian, V. S. Minnikanti, and L. A. Archer, “Surface segregation of highly branched polymer additives in linear hosts,” *Journal of Polymer Science Part B: Polymer Physics*, vol. 46, no. 17, pp. 1788–1801, 2008.
- [76] A. Yethiraj, S. Kumar, A. Hariharan, and K. S. Schweizer, “Surface segregation in polymer blends due to stiffness disparity,” *The Journal of Chemical Physics*, vol. 100, no. 6, pp. 4691–4694, 1994.
- [77] S. K. Kumar, A. Yethiraj, K. S. Schweizer, and F. A. M. Leermakers, “The effects of local stiffness disparity on the surface segregation from binary polymer blends,” *The Journal of Chemical Physics*, vol. 103, no. 23, pp. 10332–10346, 1995.
- [78] A. Yethiraj, “Integral equation theory for the surface segregation from blends of linear and star polymers,” *Computational and Theoretical Polymer Science*, vol. 10, no. 1–2, pp. 115 – 123, 2000.

- [79] S. K. Nath, J. D. McCoy, J. P. Donley, and J. G. Curro, "A modified self-consistent-field theory: Application to a homopolymer melt near a hard wall," *The Journal of Chemical Physics*, vol. 103, no. 4, pp. 1635–1640, 1995.
- [80] P. Cifra, E. Nies, and F. E. Karasz, "Free surface profile and surface tension in a polymer melt: A monte carlo study," *Macromolecules*, vol. 27, no. 5, pp. 1166–1171, 1994.
- [81] P. Cifra, F. E. Karasz, and W. J. MacKnight, "Surface segregation in polymer blends: a monte carlo simulation," *Macromolecules*, vol. 25, no. 19, pp. 4895–4901, 1992.
- [82] P. Cifra, F. Bruder, and R. Brenn, "Surface segregation in a polymer blend. comparison between monte carlo simulation and mean-field theory," *The Journal of Chemical Physics*, vol. 99, no. 5, pp. 4121–4127, 1993.
- [83] A. Yethiraj, "Entropic and enthalpic surface segregation from blends of branched and linear polymers," *Physical Review Letters*, vol. 74, pp. 2018–2021, 1995.
- [84] M. Daoud, J. P. Cotton, B. Farnoux, G. Jannink, G. Sarma, H. Benoit, C. Duplessix, C. Picot, and P. G. de Gennes, "Solutions of flexible polymers. neutron experiments and interpretation," *Macromolecules*, vol. 8, no. 6, pp. 804–818, 1975.
- [85] B. Farnoux, F. Boue, and J. P. Cotton, "Cross-over in polymer solutions," *Journal de Physique*, vol. 39, no. 1, pp. 77–86, 1978.
- [86] M. Daoud and J. P. Cotton, "Star shaped polymers : a model for the conformation and its concentration dependence," *Journal de Physique*, vol. 43, no. 3, pp. 531–538, 1982.
- [87] S. F. Edwards, "The theory of polymer solutions at intermediate concentration," *Proceedings of the Physical Society*, vol. 88, no. 2, pp. 265–280, 1966.
- [88] W. Burchard, "Static and dynamic light scattering from branched polymers and biopolymers," *Advances in Polymer Science*, vol. 48, pp. 1–124, 1983.
- [89] H. Benoit, M. Benmouna, and W. L. Wu, "Static scattering from multicomponent polymer and copolymer systems," *Macromolecules*, vol. 23, no. 5, pp. 1511–1517, 1990.
- [90] A. T. Boothroyd, G. L. Squires, L. J. Fetters, A. R. Rennie, J. C. Horton, and A. M. B. G. De Vallera, "Small-angle neutron scattering from star-branched polymers in dilute solution," *Macromolecules*, vol. 22, no. 7, pp. 3130–3137, 1989.

- [91] B. Hammouda, R. M. Briber, and B. J. Bauer, "Small angle neutron scattering from deuterated polystyrene/poly(vinylmethyl ether)/protonated polystyrene ternary polymer blends," *Polymer*, vol. 33, no. 8, pp. 1785 – 1787, 1992.
- [92] B. Hammouda, "SANS from homogeneous polymer mixtures: A unified overview," *Advances in Polymer Science*, vol. 106, pp. 87–133, 1993.
- [93] E. Wendt and J. Springer, "Screening and excess low-angle scattering in semidilute solutions of polystyrene in benzene," *Polymer*, vol. 29, no. 7, pp. 1301 – 1306, 1988.
- [94] D. Richter, O. Jucknischke, L. Willner, L. J. Fetters, M. Lin, J. S. Huang, J. Roovers, C. Toporovski, and L. L. Zhou, "Scaling properties and ordering phenomena of star polymers in solution," *J. Phys. IV France*, vol. 03, pp. 3–12, 1993.
- [95] M. Warner, J. S. Higgins, and A. J. Carter, "Chain dimensions and interaction parameters in neutron scattering from polymer blends with a labeled component," *Macromolecules*, vol. 16, no. 12, pp. 1931–1935, 1983.
- [96] F. S. Bates, G. D. Wignall, and W. C. Koehler, "Critical behavior of binary liquid mixtures of deuterated and protonated polymers," *Physical Review Letters*, vol. 55, pp. 2425–2428, 1985.
- [97] F. S. Bates, G. D. Wignall, and S. B. Dierker, "Phase behavior of amorphous binary mixtures of perdeuterated and normal 1,4-polybutadienes," *Macromolecules*, vol. 19, no. 7, pp. 1938–1945, 1986.
- [98] F. S. Bates, L. J. Fetters, and G. D. Wignall, "Thermodynamics of isotopic polymer mixtures: poly(vinylethylene) and poly(ethylene)," *Macromolecules*, vol. 21, no. 4, pp. 1086–1094, 1988.
- [99] W. W. Graessley, R. Krishnamoorti, N. P. Balsara, L. J. Fetters, D. J. Lohse, D. N. Schulz, and J. A. Sissano, "Effect of deuterium substitution on thermodynamic interactions in polymer blends," *Macromolecules*, vol. 26, no. 5, pp. 1137–1143, 1993.
- [100] F. S. Bates, M. F. Schulz, J. H. Rosedale, and K. Almdal, "Correlation of binary polyolefin phase behavior with statistical segment length asymmetry," *Macromolecules*, vol. 25, no. 20, pp. 5547–5550, 1992.
- [101] R. Krishnamoorti, W. W. Graessley, N. P. Balsara, and D. J. Lohse, "Structural origin of thermodynamic interactions in blends of saturated hydrocarbon polymers," *Macromolecules*, vol. 27, no. 11, pp. 3073–3081, 1994.

- [102] J. D. Londono, A. H. Narten, G. D. Wignall, K. G. Honnell, E. T. Hsieh, T. W. Johnson, and F. S. Bates, "Composition dependence of the interaction parameter in isotopic polymer blends," *Macromolecules*, vol. 27, no. 10, pp. 2864–2871, 1994.
- [103] F. S. Bates, "Measurement of the correlation hole in homogeneous block copolymer melts," *Macromolecules*, vol. 18, no. 3, pp. 525–528, 1985.
- [104] T. P. Russell, L. J. Fetters, J. C. Clark, B. J. Bauer, and C. C. Han, "Concentration fluctuations in mixtures of linear and star-shaped polymers," *Macromolecules*, vol. 23, no. 2, pp. 654–659, 1990.
- [105] B. Hammouda and M. Benmouna, "Neutron scattering from polymer blends under pressure," *Journal of Polymer Science Part B: Polymer Physics*, vol. 33, no. 17, pp. 2359–2364, 1995.
- [106] M. G. Brereton, E. W. Fischer, C. Herkt-Maetzky, and K. Mortensen, "Neutron scattering from a series of compatible polymer blends: Significance of the Flory  $\chi$  parameter," *The Journal of Chemical Physics*, vol. 87, no. 10, pp. 6144–6149, 1987.
- [107] J. T. Cabral and J. S. Higgins, "Small angle neutron scattering from the highly interacting polymer mixture tmpc/psd: No evidence of spatially dependent parameter," *Macromolecules*, vol. 42, no. 24, pp. 9528–9536, 2009.
- [108] R. G. Alamo, J. D. Londono, L. Mandelkern, F. C. Stehling, and G. D. Wignall, "Phase behavior of blends of linear and branched polyethylenes in the molten and solid states by small-angle neutron scattering," *Macromolecules*, vol. 27, no. 2, pp. 411–417, 1994.
- [109] R. G. Alamo, W. W. Graessley, R. Krishnamoorti, D. J. Lohse, J. D. Londono, L. Mandelkern, F. C. Stehling, and G. D. Wignall, "Small angle neutron scattering investigations of melt miscibility and phase segregation in blends of linear and branched polyethylenes as a function of the branch content," *Macromolecules*, vol. 30, no. 3, pp. 561–566, 1997.
- [110] M. Agamalian, R. G. Alamo, M. H. Kim, J. D. Londono, L. Mandelkern, and G. D. Wignall, "Phase behavior of blends of linear and branched polyethylenes on micron length scales via ultra-small-angle neutron scattering," *Macromolecules*, vol. 32, no. 9, pp. 3093–3096, 1999.
- [111] Y. Y. Chen, T. P. Lodge, and F. S. Bates, "Influence of long-chain branching on the miscibility of poly(ethylene-*r*-ethylene) blends with different microstructures," *Journal of Polymer Science Part B: Polymer Physics*, vol. 40, no. 5, pp. 466–477, 2002.

- [112] C. C. Greenberg, M. D. Foster, C. M. Turner, S. Corona-Galvan, E. Cloutet, R. P. Quirk, P. D. Butler, and C. Hawker, “Effective interaction parameter between branched and linear polystyrene,” *Journal of Polymer Science Part B: Polymer Physics*, vol. 39, no. 21, pp. 2549–2561, 2001.
- [113] D. T. Wu, G. H. Fredrickson, J.-P. Carton, A. Ajdari, and L. Leibler, “Distribution of chain ends at the surface of a polymer melt: Compensation effects and surface tension,” *Journal of Polymer Science Part B: Polymer Physics*, vol. 33, no. 17, pp. 2373–2389, 1995.
- [114] J. K. Wolterink, F. A. M. Leermakers, G. J. Fler, L. K. Koopal, E. B. Zhulina, and O. V. Borisov, “Screening in solutions of star-branched polyelectrolytes,” *Macromolecules*, vol. 32, no. 7, pp. 2365–2377, 1999.
- [115] J. K. Wolterink, J. van Male, M. A. Cohen Stuart, L. K. Koopal, E. B. Zhulina, and O. V. Borisov, “Annealed star-branched polyelectrolytes in solution,” *Macromolecules*, vol. 35, no. 24, pp. 9176–9190, 2002.
- [116] J. G. Curro and K. S. Schweizer, “Theory of polymer melts: an integral equation approach,” *Macromolecules*, vol. 20, no. 8, pp. 1928–1934, 1987.
- [117] K. S. Schweizer and J. G. Curro, “Integral equation theory of the structure and thermodynamics of polymer blends,” *The Journal of Chemical Physics*, vol. 91, no. 8, pp. 5059–5081, 1989.
- [118] K. G. Honnell, J. G. Curro, and K. S. Schweizer, “Local structure of semiflexible polymer melts,” *Macromolecules*, vol. 23, no. 14, pp. 3496–3505, 1990.
- [119] J. G. Curro and K. S. Schweizer, “Integral equation theory for compressible polymer alloys: thermodynamics, scattering, and miscibility of gaussian chains,” *Macromolecules*, vol. 24, no. 25, pp. 6736–6747, 1991.
- [120] K. G. Honnell, J. D. McCoy, J. G. Curro, K. S. Schweizer, A. H. Narten, and A. Habenschuss, “Local structure of polyethylene melts,” *The Journal of Chemical Physics*, vol. 94, no. 6, pp. 4659–4662, 1991.
- [121] J. G. Curro, “Intermolecular structure and thermodynamics of vinyl polymer liquids: Freely-jointed chains,” *Macromolecules*, vol. 27, no. 17, pp. 4665–4672, 1994.
- [122] C. J. Grayce and K. S. Schweizer, “Solvation potentials for macromolecules,” *The Journal of Chemical Physics*, vol. 100, no. 9, pp. 6846–6856, 1994.

- [123] C. J. Grayce, A. Yethiraj, and K. S. Schweizer, "Liquid-state theory of the density dependent conformation of nonpolar linear polymers," *The Journal of Chemical Physics*, vol. 100, no. 9, pp. 6857–6872, 1994.
- [124] K. Schweizer and J. Curro, "Prism theory of the structure, thermodynamics, and phase transitions of polymer liquids and alloys," *Advances in Polymer Science*, vol. 116, pp. 319–377, 1994.
- [125] C. J. Grayce and K. S. Schweizer, "A liquid-state theory of dense star polymer fluids," *Macromolecules*, vol. 28, no. 22, pp. 7461–7478, 1995.
- [126] D. G. Gromov and J. J. de Pablo, "Structure of binary polymer blends: Multiple time step hybrid monte carlo simulations and self-consistent integral-equation theory," *The Journal of Chemical Physics*, vol. 103, no. 18, pp. 8247–8256, 1995.
- [127] A. Yethiraj, "Theory for chain conformations and static structure of dilute and semidilute polyelectrolyte solutions," *The Journal of Chemical Physics*, vol. 108, no. 3, pp. 1184–1192, 1998.
- [128] R. Patil, K. S. Schweizer, and T.-M. Chang, "Stretching, packing, and thermodynamics in highly branched polymer melts," *Macromolecules*, vol. 36, no. 7, pp. 2544–2552, 2003.
- [129] M. Murat and G. S. Grest, "Molecular dynamics study of dendrimer molecules in solvents of varying quality," *Macromolecules*, vol. 29, no. 4, pp. 1278–1285, 1996.
- [130] Y. Rouault and O. V. Borisov, "Comb-branched polymers: Monte carlo simulation and scaling," *Macromolecules*, vol. 29, no. 7, pp. 2605–2611, 1996.
- [131] I. Carmesin and K. Kremer, "The bond fluctuation method: a new effective algorithm for the dynamics of polymers in all spatial dimensions," *Macromolecules*, vol. 21, no. 9, pp. 2819–2823, 1988.
- [132] H. P. Deutsch and K. Binder, "Interdiffusion and self-diffusion in polymer mixtures: A monte carlo study," *The Journal of Chemical Physics*, vol. 94, no. 3, pp. 2294–2304, 1991.
- [133] H.-P. Wittmann and K. Kremer, "Vectorized version of the bond fluctuation method for lattice polymers," *Computer Physics Communications*, vol. 61, no. 3, pp. 309 – 330, 1990.

- [134] A. Di Cecca and J. J. Freire, “Monte carlo simulation of star polymer systems with the bond fluctuation model,” *Macromolecules*, vol. 35, no. 7, pp. 2851–2858, 2002.
- [135] A. Yethiraj, “A monte carlo simulation study of branched polymers,” *The Journal of Chemical Physics*, vol. 125, no. 20, p. 204901, 2006.
- [136] F. A. M. Leermakers, M. Ballauff, and O. V. Borisov, “Counterion localization in solutions of starlike polyelectrolytes and colloidal polyelectrolyte brushes: A self-consistent field theory,” *Langmuir*, vol. 24, no. 18, pp. 10026–10034, 2008.
- [137] C. C. van der Linden, B. van Lent, F. A. M. Leermakers, and G. J. Fleer, “Adsorption of polymers on heterogeneous surfaces,” *Macromolecules*, vol. 27, no. 7, pp. 1915–1921, 1994.
- [138] C. C. van der Linden, F. A. M. Leermakers, and G. J. Fleer, “Adsorption of comb polymers,” *Macromolecules*, vol. 29, no. 3, pp. 1000–1005, 1996.
- [139] M. Charlaganov, P. Kosovan, and F. A. M. Leermakers, “New ends to the tale of tails: adsorption of comb polymers and the effect on colloidal stability,” *Soft Matter*, vol. 5, pp. 1448–1459, 2009.
- [140] M. Doi and E. SF, *The Theory of Polymer Dynamics*. Oxford University Press, 1988.
- [141] B. Van Lent, J. Scheutjens, and T. Cosgrove, “Self-consistent field theory for the adsorption of ring polymers from solution,” *Macromolecules*, vol. 20, no. 2, pp. 366–370, 1987.
- [142] C. C. van der Linden, F. A. M. Leermakers, and G. J. Fleer, “Adsorption of comb polymers,” *Macromolecules*, vol. 29, no. 3, pp. 1000–1005, 1996.
- [143] M. D. Foster, D. T. Wu, and R. Hu. Private communication.
- [144] J. M. P. van den Oever, F. A. M. Leermakers, G. J. Fleer, V. A. Ivanov, N. P. Shusharina, A. R. Khokhlov, and P. G. Khalatur, “Coil-globule transition for regular, random, and specially designed copolymers: Monte Carlo simulation and self-consistent field theory,” *Physical Review E*, vol. 65, p. 041708, Apr 2002.
- [145] J. des Cloizeaux, “Lagrangian theory for a self-avoiding random chain,” *Physical Review A*, vol. 10, pp. 1665–1669, 1974.

- [146] M. Bishop, J. H. R. Clarke, A. Rey, and J. J. Freire, “Investigation of the end-to-end vector distribution function for linear polymers in different regimes,” *The Journal of Chemical Physics*, vol. 95, no. 6, pp. 4589–4592, 1991.
- [147] S. Caracciolo, M. S. Causo, and A. Pelissetto, “End-to-end distribution function for dilute polymers,” *The Journal of Chemical Physics*, vol. 112, no. 17, pp. 7693–7710, 2000.
- [148] J. E. Dennis and R. B. Schnabel, *Numerical Methods for Unconstrained Optimization and Nonlinear Equations*. SIAM, 1996.
- [149] S. W. Sides and G. H. Fredrickson, “Parallel algorithm for numerical self-consistent field theory simulations of block copolymer structure,” *Polymer*, vol. 44, no. 19, pp. 5859 – 5866, 2003.
- [150] Z. Baolin and L. Wenzhi, “On alternating segment Crank-Nicolson scheme,” *Parallel Computing*, vol. 20, no. 6, pp. 897 – 902, 1994.
- [151] S. Zhu and J. Zhao, “The alternating segment explicit-implicit scheme for the dispersive equation,” *Applied Mathematics Letters*, vol. 14, no. 6, pp. 657 – 662, 2001.
- [152] M. J. Quinn, *Parallel Programming in C with MPI and OpenMP*. McGraw-Hill, 2004.

## APPENDIX A - THE NUMERICAL ALGORITHMS IN SCFT

The numerical SCFT and two-chain SCFT are developed to study the surface and bulk thermodynamic properties of polymer systems containing linear and nonlinear architectures. In this section, the details of the numerical algorithms are discussed including the discretization of the partial differential equations and the minimization of SCF potential.

### A.1 Numerical method for modified diffusion equation

The SCFT modified diffusion equation is solved by finite difference method. In this project, the differential equation have been solved in terms of discretized form using the explicit scheme and the Crank-Nicolson implicit scheme.

#### A.1.1 The explicit and implicit method

For instance, the typical 1-D heat equation (diffusion equation)

$$\frac{\partial u(z; t)}{\partial t} = a \frac{\partial^2 u(z; t)}{\partial z^2} \quad (\text{A.1})$$

can be discretized by the classic explicit scheme:

$$\frac{u(j; k+1) - u(j; k)}{\Delta t} = a \frac{u(j+1; k) - 2u(j; k) + u(j-1; k)}{\Delta z^2}. \quad (\text{A.2})$$

where  $z = j\Delta z$  and  $t = k\Delta t$ . The space is divided into  $j_{\max}$  grids,  $j = 0, 1, 2, \dots, j_{\max} - 1$ .  $k$  is the index of the time step. The stability of solution requires

$$\frac{a\Delta t}{\Delta z^2} < 0.5. \quad (\text{A.3})$$

Equation A.1 can also be written in terms of the implicit scheme:

$$\frac{u(j; k+1) - u(j; k)}{\Delta t} = a \frac{u(j+1; k+1) - 2u(j; k+1) + u(j-1; k+1)}{\Delta z^2}. \quad (\text{A.4})$$

which is unconditionally stable.

### A.1.2 The Crank-Nicolson algorithm

The Crank-Nicolson algorithm is known well as a unconditionally stable method with second-order accuracy of truncation error.

$$\frac{u(j; k+1) - u(j; k)}{\Delta t} = \alpha \left( \frac{u(j+1; k+1) - 2u(j; k+1) + u(j-1; k+1)}{2\Delta z^2} + \frac{u(j+1; k) - u(j; k) + u(j-1; k)}{2\Delta z^2} \right). \quad (\text{A.5})$$

This is rewritten from  $j = 1$ , to  $j_{\max} - 2$  as

$$-\alpha u(j+1; k+1) + (1+2\alpha)u(j; k+1) - \alpha u(j-1; k+1) = \alpha u(j+1; k) + (1-2\alpha)u(j; k) + \alpha u(j-1; k), \quad (\text{A.6})$$

where  $\alpha = \frac{a\Delta t}{2\Delta z^2}$ . The differential equation then becomes solving a tri-diagonal problem in a linear system.

## A.2 Discretization of the modified diffusion equation

For a 1-D modified diffusion equation:

$$\frac{\partial q(z; t)}{\partial t} = \frac{b^2}{6} \frac{\partial^2 q(z; t)}{\partial z^2} - \mu(z)q(z; t), \quad (\text{A.7})$$

the explicit scheme can be written as

$$\frac{q(j; k+1) - q(j; k)}{\Delta t} = \frac{b^2}{6} \frac{q(j+1; k) - 2q(j; k) + q(j-1; k)}{\Delta z^2} - \mu(j)q(j; k). \quad (\text{A.8})$$

where  $j = 0, 1, 2, \dots, j_{\max} - 1$  is the index of the grids, and  $k = 0, 1, 2, \dots, N_{\max} - 1$  is the discretized monomer index of the polymer.

In two-chain SCFT, the modified diffusion equation describes the single chain distribution in a spherical coordinate system. The modified diffusion equation

$$\frac{\partial q}{\partial t} = \frac{b^2}{6} \nabla^2 q - \mu q, \quad (\text{A.9})$$

can be written in terms of

$$\frac{\partial q(r; t)}{\partial t} = \frac{b^2}{6} \frac{\partial}{r^2 \partial r} \left( r^2 \frac{\partial q(r; t)}{\partial r} \right) - \mu(r)q(r; t). \quad (\text{A.10})$$

or

$$\frac{\partial q(r; t)}{\partial t} = \frac{b^2}{6} \left( \frac{\partial^2 q(r; t)}{\partial r^2} + \frac{2}{r} \frac{\partial q(r; t)}{\partial r} \right) - \mu(r)q(r; t). \quad (\text{A.11})$$

Equation A.11 is therefore discretized as

$$\begin{aligned} \frac{q(j; k+1) - q(j; k)}{\Delta t} &= \frac{b^2}{6} \left( \frac{q(j+1; k) - 2q(j; k) + q(j-1; k)}{\Delta r^2} \right. \\ &\quad \left. + \frac{q(j+1; k) - q(j-1; k)}{r_j \Delta r} \right) - \mu(j)q(j; k), \end{aligned} \quad (\text{A.12})$$

where  $r_j$  is  $(j+1)\Delta r$ . Using the Crank-Nicolson algorithm, the modified diffusion equation for  $0 < j < j_{\max} - 1$  is rearranged to be

$$\begin{aligned} & -\left(\alpha + \frac{\alpha}{j+1}\right)q(j+1; k+1) + (1 + 2\alpha + 0.5\Delta t\mu(j))q(j; k+1) \\ & + \left(-\alpha + \frac{\alpha}{j+1}\right)q(j-1; k+1) \\ = & \left(\alpha + \frac{\alpha}{j+1}\right)q(j+1; k) + (1 - 2\alpha - 0.5\Delta t\mu(j))q(j; k) \\ & + \left(\alpha - \frac{\alpha}{j+1}\right)q(j-1; k), \end{aligned} \quad (\text{A.13})$$

where the prefactor  $\alpha = \frac{b^2 \Delta t}{12 \Delta r^2}$ . At  $j = 0$  and  $j = j_{\max} - 1$ , the discretized equation is constrained by the boundary condition.

### A.3 The boundary conditions

The bulk density profile is uniform in a polymer melt. Therefore, it satisfies the reflective boundary condition at  $r = r_{\max}$ , which is

$$\frac{\partial q}{\partial r} \Big|_{r=r_{\max}} = 0. \quad (\text{A.14})$$

The boundary condition at  $r = 0$  satisfies

$$q(r < 0; t) = 0, \quad (\text{A.15})$$

and the Crank-Nicolson form of Equation A.11 at  $r = 0$  is

$$\begin{aligned} & -2\alpha q(1; k+1) + (1 + 2\alpha + 0.5\Delta t\mu(0))q(0; k+1) = \\ & 2\alpha q(1; k) + (1 - 2\alpha - 0.5\Delta t\mu(0))q(0; k). \end{aligned} \quad (\text{A.16})$$

At  $r = r_{\max}$ , Equation A.11 is written as

$$\begin{aligned} & \left(-\frac{\alpha}{j_{\max}} + 1 + \alpha + 0.5\Delta t\mu(j_{\max} - 1)\right)q(j_{\max} - 1; k+1) \\ & + \left(-\alpha + \frac{\alpha}{j_{\max}}\right)q(j_{\max} - 2; k+1) \\ = & \left(\frac{\alpha}{j_{\max}} + 1 - \alpha - 0.5\Delta t\mu(j_{\max} - 1)\right)q(j_{\max} - 1; k) \\ & + \left(\alpha - \frac{\alpha}{j_{\max}}\right)q(j_{\max} - 2; k). \end{aligned} \quad (\text{A.17})$$

#### A.4 The Picard method and Newton-Broyden algorithm

The SCFT algorithm shown in Chapter 3 is solved by updating the field potential  $\boldsymbol{\mu}$  from the density distribution  $\boldsymbol{\rho}$  self-consistently. The condition of self-consistency also requires that  $\boldsymbol{\rho}[\boldsymbol{\mu}(\mathbf{r})]$  is solved from the modified diffusion equation given  $\boldsymbol{\mu}(\mathbf{r})$ . Next, the new  $\boldsymbol{\mu}(\mathbf{r})$  is proportional to the density  $\boldsymbol{\rho}(\mathbf{r})$ :

$$\boldsymbol{\mu}[\boldsymbol{\rho}(\mathbf{r})] = v\boldsymbol{\rho}(\mathbf{r}), \quad (\text{A.18})$$

where  $v$  is the excluded volume parameter.  $\boldsymbol{\rho}$  and  $\boldsymbol{\mu}$  both have  $j_{\max}$  elements.

The differential equation can be solved in a linear system. In particular, the Picard algorithm is applied to update  $\mu^t$  and minimize  $\epsilon = \frac{|\mu^t - \mu^{t-1}|}{|\mu^t|}$ , where  $t$  is the index of the  $t^{\text{th}}$  iteration. A mixing ratio  $\lambda \in (0, 1]$  is applied to update  $\mu^t$  in terms of  $\mu^t = (1 - \lambda)\mu^{t-1} + \lambda v\rho^t$ . The tolerance of the convergence is  $\epsilon_{\text{tor}} = 10^{-7}$ .

An advanced minimizing algorithm, Newton's algorithm can also solve the SCFT non-linearly [30, 148]. Construct a function  $\mathbf{F}$

$$\mathbf{F}(\boldsymbol{\mu}) = \boldsymbol{\mu} - v\boldsymbol{\rho}, \quad (\text{A.19})$$

minimizing  $\mathbf{F} \rightarrow 0$  results in the solution of the nonlinear systems where  $\mathbf{F}$ ,  $\boldsymbol{\mu}$  and  $\boldsymbol{\rho}$  are vectors containing  $j_{\max}$  elements. The Newton-Raphson method is often the standard method to solve such a nonlinear system by solving

$$-\mathbf{F} = \mathbf{J} \cdot \delta\boldsymbol{\mu}, \quad (\text{A.20})$$

where  $\delta\boldsymbol{\mu}$  is the small difference from the goal of solution and the *Jacobian Matrix*,  $\mathbf{J}$  is a  $j_{\max} \times j_{\max}$  matrix with elements of  $J_{ij} = \partial F_i / \partial \mu_j$ . The Newton-Raphson method solves

$$-\mathbf{F}^t = \mathbf{J}^t \cdot \delta\boldsymbol{\mu}^t \quad (\text{A.21})$$

by updating

$$\boldsymbol{\mu}^{t+1} = \boldsymbol{\mu}^t \quad (\text{A.22})$$

until  $\boldsymbol{\mu}$  and  $\mathbf{F}$  satisfy the expected precision of tolerance. The superscript  $t$  is the index of the  $t^{\text{th}}$  iteration.

Instead of evaluating the exact Jacobian matrix, an approximation scheme so called the quasi-Newton algorithm can be applied to reduce the number of total operations. In SCFT, the Broyden's method can be used as an alternative technique. The brief steps are given as below:

The approximated Jacobian matrix  $\mathbf{B}$  is introduced to solve

$$-\mathbf{F} = \mathbf{B} \cdot \delta\boldsymbol{\mu}. \quad (\text{A.23})$$

$\mathbf{B}$  is initially guessed and an iterating procedure to update  $\mathbf{B}$  from the  $t^{\text{th}}$  to  $t + 1^{\text{th}}$  iteration is given as

$$\mathbf{B}^{t+1} = \mathbf{B}^t + \frac{(\delta\mathbf{F}^t - \mathbf{B}^t \cdot \boldsymbol{\mu}^t) \otimes \delta\boldsymbol{\mu}^t}{\delta\boldsymbol{\mu}^t \cdot \delta\boldsymbol{\mu}^t}, \quad (\text{A.24})$$

where  $\otimes$  denotes the tensor product, and  $\delta\mathbf{F}^t = \mathbf{F}^{t+1} - \mathbf{F}^t$ . Eventually  $\mathbf{B}$  should converge to  $\mathbf{J}$  matrix as well as the linear system converges to the solution. Fredrickson [30] discussed the nature of evaluating the Jacobian and gave the approximated initial guess of the elements

of  $\mathbf{B}$ :

$$B(r_i, r_j) \approx \frac{1}{v} \delta(r_i, r_j) + \rho_0 N \omega(|r_i - r_j|), \quad (\text{A.25})$$

where  $\rho_0$  is the bulk monomer density and  $N$  is the chain length.  $\omega(r)$  is the Gaussian single chain intramolecular density. This approximation works successfully when  $\mu(r)$  is weakly inhomogeneous [30].

The Picard iteration is implemented in the SCFT programs. The Newton-Broyden algorithm is also implemented as a test based on the reference [30]. The flowchart of SCFT by Picard iteration and Newton-Broyden method are given in Figure A.1 and Figure A.2, respectively. In this project, Crank-Nicolson method and Picard iteration are applied to SCFT and two-chain SCFT calculations.

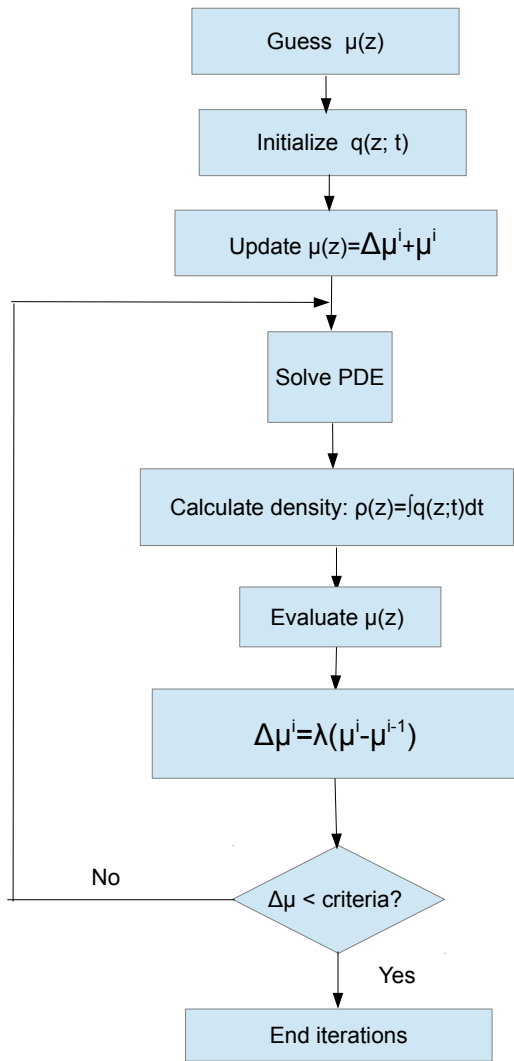


Figure A.1: The flowchart of SCFT iterations by Picard method.

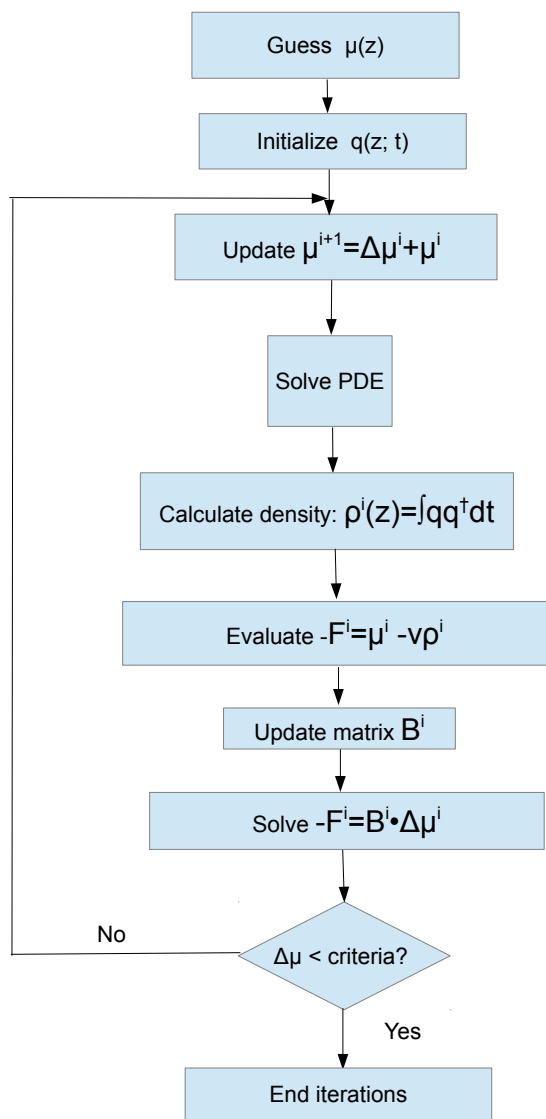


Figure A.2: The flowchart of SCFT iterations by Newton-Broyden method.

APPENDIX B - GAUSSIAN STRUCTURE FACTORS OF BRANCHED AND COMB  
POLYMERS

**B.1 Structure factors of branched molecules**

The Debye function is the total intramolecular pair correlations of a Gaussian random walk linear structure:

$$D[x] = \frac{2(e^{-x} - 1 + x)}{x^2}, \quad (\text{B.1})$$

in terms of  $x$ , which is defined as

$$x(N) = N \frac{q^2 b^2}{6}, \quad (\text{B.2})$$

where  $\frac{Nb^2}{6}$  is the  $R_g^2$  of the linear Gaussian chain.

The total pair correlation from one point to all the other points on a linear chain is given as

$$F[x] = \frac{1 - e^{-x}}{x}, \quad (\text{B.3})$$

and the correlation of one pair of points is simply:

$$E[x] = e^{-x}. \quad (\text{B.4})$$

The structure factor of a  $f$ -star is composed of two types of contributions, the correlations between monomers in the same arm ( $S_1$ ) and monomers between two arms ( $S_2$ ):

$$S_1(q) = N_A^2 D[x(N_A)] \quad (\text{B.5})$$

and

$$S_2(q) = N_A^2 F[x(N_A)]^2, \quad (\text{B.6})$$

where  $N_A$  is the length of the inner arm ( $N_{\text{arm}}$ ), and the  $N_B$  is the length of the outer branch ( $N_{\text{branch}}$ ). The normalized structure factor of the star is thus

$$S_{\text{star}}(q) = \frac{1}{N_{\text{star}}} (fS_1 + f(f-1)S_2). \quad (\text{B.7})$$

Note that the total number of monomers  $N_{\text{star}} = fN_A$ .

Similarly, the structure factor of an end-branched molecule is derived in pieces.  $S_1$  accounts for the correlations between two monomers on the same branch, which is written as

$$S_1 = f_A [N_A^2 D[x(N_A)] + f_B N_B^2 D[x(N_B)]]. \quad (\text{B.8})$$

The correlations between two monomers on two different outside branches,  $S_2$ , is given by

$$S_2 = f_A \left[ f_B N_B F[x(N_B)] ((f_B - 1) N_B F[x(N_B)] + (f_A - 1) f_B N_B E[x(2N_A)] F[N_B]) \right]. \quad (\text{B.9})$$

The last portion,  $S_3$ , contains the contribution between a monomer on the inside arm and another monomer on the outside branch, plus the correlation between monomers on two separate inside arms:

$$S_3 = f_A \left[ N_A F[x(N_A)] \times \left( (f_A - 1) (N_A F[x(N_A)] + 2f_B N_B F[x(N_B)] E[x(N_A)]) + 2f_B N_B F[x(N_B)] \right) \right]. \quad (\text{B.10})$$

Finally, the structure factor of an end-branched molecule is the summation of  $S_1$ ,  $S_2$  and  $S_3$ :

$$S_{\text{endbr}} = \frac{1}{N} (S_1 + S_2 + S_3), \quad (\text{B.11})$$

where  $N$  is the total number of the molecule:  $N = f_A f_B N_B + f_A N_A$ .

The partial structures factors for the ends and joints of a polymer are listed below: For linear chains, it gives

$$S_{\text{lin}}^e = 2F[x(N_{\text{lin}})]. \quad (\text{B.12})$$

For star structures, they are given

$$S_{\text{star}}^e = F[x(N_A)] + (f - 1) E[x(N_A)] F[N_A], \quad (\text{B.13})$$

and

$$S_{\text{star}}^j = F[x(N_A)], \quad (\text{B.14})$$

respectively.

For end-branched polymers, the end structure factor is written as

$$\begin{aligned} S_{\text{endbr}}^e = & \frac{1}{N} f_A f_B \left[ N_B F[x(N_B)] \right. \\ & + E[x(N_B)] \left( (f_B - 1) N_B F[x(N_B)] + N_A F[x_A] \right) \\ & + (f_A - 1) \left( N_A E[x(N_A + N_B)] F[x(N_A)] \right. \\ & \left. \left. + f_B N_B E[x(2N_A + N_B)] F[x(N_B)] \right) \right]. \end{aligned} \quad (\text{B.15})$$

The structure factor for the inside joint is

$$S_{\text{endbr}}^j = \frac{1}{N} f_A \left[ N_A F[x(N_A)] + f_B N_B E[x(N_A)] F[x(N_B)] \right], \quad (\text{B.16})$$

and the outside joint structure factor is given by

$$\begin{aligned} S_{\text{endbr}}^{j'} = & \frac{1}{N} f_A \left[ N_A F[x(N_A)] + f_B N_B F[x(N_B)] \right. \\ & + (f_A - 1) N_A E[x(N_A)] F[x(N_A)] \\ & \left. + f_B (f_A - 1) N_B E[x(2N_A)] F[x(N_B)] \right]. \end{aligned} \quad (\text{B.17})$$

Note that by this definition, the molecular structure factor  $S(0)$  converges to  $N$ , while the end and joint structure factors converge to  $f_A/N$  and  $f_B/N$ .

## B.2 Structure factors of comb molecules

For a comb structure, the Gaussian structure factor is derived in terms of three pieces  $S_1, S_2$  and  $S_3$  as well:  $S_1$  is simply Debye's functions for all linear pieces:

$$S_1(q) = pM^2 D[M] + ((p-1)L)^2 D[L(p-1)]. \quad (\text{B.18})$$

$S_2$  counts from one monomer on the tooth,

$$S_2(q) = 2 \sum_{i=2}^p \sum_{j=1}^i M^2 F[M]^2 E[(i-j)L]. \quad (\text{B.19})$$

Note that the factor of 2 represents the indistinguishable counts by switching index  $i$  and  $j$ .

$S_2$  can be expanded as

$$S_2 = 2M^2 F[M]^2 \frac{(E[-L])}{1 - E[-L]} \left( E[L]^2 \frac{1 - E[(p-1)L]}{1 - E[L]} - (p-1)E[L] \right). \quad (\text{B.20})$$

$S_3$  is written as

$$S_3 = 2MF[M] \left( \left( \sum_{i=1}^p (i-1)L F[(i-1)L] \right) + (p-1)LF[(p-1)L] \right), \quad (\text{B.21})$$

which is simplified as

$$S_3 = 2M \frac{F[M]}{k} \left( 2p - 2 \frac{1 - E[pL]}{1 - E[L]} \right), \quad (\text{B.22})$$

where

$$k = \frac{q^2 b^2}{6}. \quad (\text{B.23})$$

The total static structure factor of a comb molecule is thus

$$S_{\text{comb}} = N_{\text{comb}}^{-1} (S_1 + S_2 + S_3). \quad (\text{B.24})$$

Moreover, the end and joint partial structure factors of a comb are given in terms of four portions, respectively:

$$S_{\text{comb}_1}^e = MF[M] + (p-1) \frac{(1 - E[M]E[L])}{k}, \quad (\text{B.25})$$

$$S_{\text{comb}_2}^e = \frac{1 - E[L+M]}{k} \frac{E[M]}{E[L] - 1} \left( \frac{E[L] - E[pL]}{1 - E[L]} - (p-1) \right), \quad (\text{B.26})$$

$$S_{\text{comb}_3}^e = E[M] \frac{(2 - E[L] - E[M]) (p-2) - (E[L]^{p-2} - 1)}{k(1 - E[L]) (1 - E[-L])}, \quad (\text{B.27})$$

$$S_{\text{comb}_4}^e = \frac{(E[L]^{p-1} - 1) E[L+M] (1 - L[M])}{E[L] - 1 k}, \quad (\text{B.28})$$

and finally,

$$S_{\text{comb}}^e = N_{\text{comb}}^{-1} (S_{\text{comb}_1}^e + S_{\text{comb}_2}^e + S_{\text{comb}_3}^e + S_{\text{comb}_4}^e). \quad (\text{B.29})$$

Similarly, the end and joint structure factor on a comb are written as

$$S_{\text{comb}_1}^j = p \frac{(2 - E[M] - E[L]) - \frac{1 - E[L]}{k}}{k}, \quad (\text{B.30})$$

$$S_{\text{comb}_2}^j = \frac{1 - E[L + M]}{k(E[L] - 1)} \left( \frac{E[L] - E[pL]}{1 - E[L]} - (p - 1) \right), \quad (\text{B.31})$$

$$S_{\text{comb}_3}^j = \frac{(2 - E[L] - E[M])}{k(1 - E[L])} \left( (p - 2) - \frac{E[(p - 2)L] - 1}{1 - E[-L]} \right), \quad (\text{B.32})$$

$$S_{\text{comb}_4}^j = \frac{(E[pL] - E[L])(1 - E[M])}{k(E[L] - 1)}, \quad (\text{B.33})$$

$$S_{\text{comb}}^j = N_{\text{comb}}^{-1} (S_{\text{comb}_1}^j + S_{\text{comb}_2}^j + S_{\text{comb}_3}^j + S_{\text{comb}_4}^j). \quad (\text{B.34})$$

## APPENDIX C - PARALLELIZATION OF SELF-CONSISTENT FIELD CALCULATIONS

Sides and Fredrickson discussed the parallelization of SCFT in pseudo-spectral method [149]. The density propagator  $q(z; t)$  by the explicit method can be spatially decomposed into multiple processors in parallel as well. Crank-Nicolson method could not be straightforwardly parallelized. An alternating segment Crank-Nicolson (ASC-N) algorithm has been developed as a parallelizable algorithm [150, 151]. The ASC-N algorithm is not applied in this project. In this section, a parallel explicit method is tested as an example.

### C.1 Parallel scheme for 1-D diffusion equation using explicit method

The explicit method can be parallelized by decomposing the data into multiple processors by adding ghost points to the boundary of each processors [152]. The ghost points store the data sent/received from the neighbor processors. Figure C.1 shows the scheme of the domain decomposition to solve a diffusion equation.

The performance of the domain decomposition strongly depends by the grid size of the space. The speedup of parallelization is defined as

$$S_p = \frac{T_1}{T_p} \quad (\text{C.1})$$

where  $T_1$  is the wall time for the sequential program and  $T_p$  is the wall time when running on  $p$  CPUs in parallel.

The performance of using the explicit method to solve the diffusion equation in parallel is tested on computing clusters containing 12 cores on each node. For a system containing totally 512 spatial grids, only approximately 4 times of speedup can be obtained using 8 cores. If using more processors, the performance is slowed down by the frequent data communication. However, for an array containing 10240 elements, the speedup is better if using more processors, in the test using 16 processors, the speedup is approximately 10

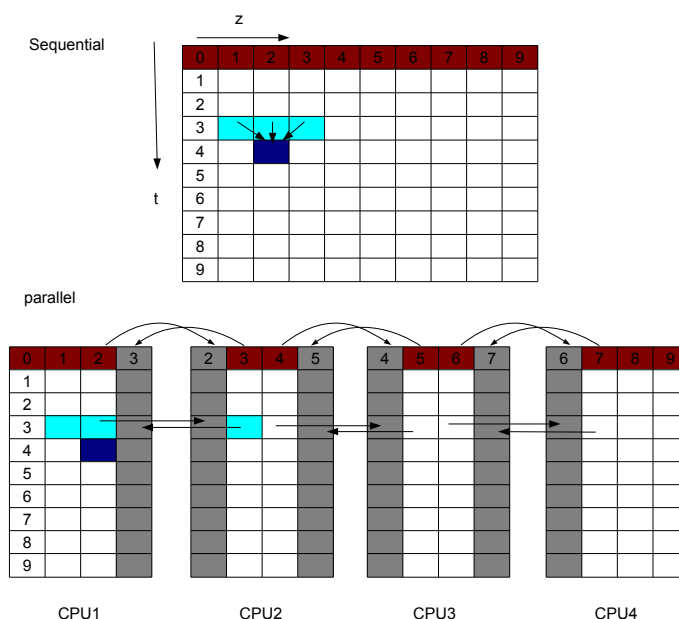


Figure C.1: An illustration of the domain decomposition algorithm using ghost points for an explicit method scheme on 4 CPUs.

times faster. In general, the parallel algorithm can achieve better speedup for larger size of the system, compared to the frequently data exchange between CPUs, including a much less narrow band width for data passing between each machine through infiniband. The plot of the speedup depending on the size of the grid matrices is shown in Figure C.2.

In SCFT iterations, the array of the density weight function,  $q(z;t)$  and  $q^\dagger(z;t)$  can be solved in each CPUs. The value of the partition function  $Q$  is obtained by gathering  $q(r;N)$  from all processors. It is then passed to all processors immediately to calculate the monomer density  $\rho(r)$ . The self-consistent potential  $\mu(r)$  only depends on the local values of  $\rho(r)$ . It stays in the subtask and does not communicate with other processors. The one-dimensional problem achieves limited speedup by parallelization, but it has better performance for multiple-dimensional problems.

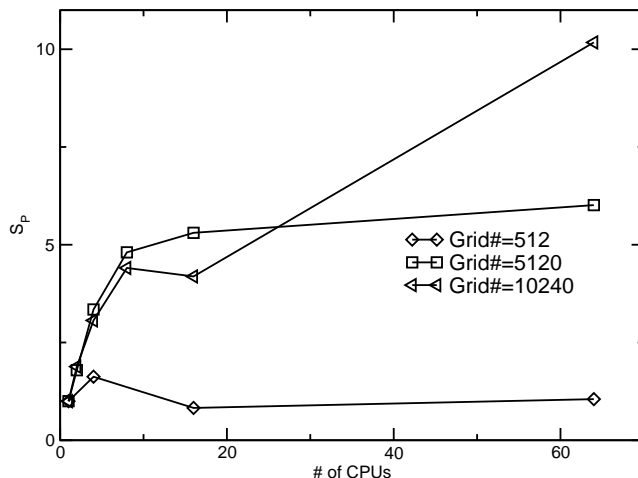


Figure C.2: The speedup test for solving the 1-D diffusion equation using parallel explicit method.

## C.2 The implementation of parallelized SCFT for cyclic molecules

In SCFT for cyclic problems, the Green's function  $G(z', z''; 0, t)$  has independent dimensions  $z'$  and  $z''$ . A parallelization on the first array dimension  $z'$  is very efficient in speeding the SCFT calculation. Figure C.4 gives an example that  $G(z', z''; 0, t)$  is distributed equally as four sub-matrices to four processors. Because there is no data exchange between processors, CPU time is consumed to solve the differential equation. The parallel SCFT starts with an initial guess of self-consistent potential  $\mu$ . It distributes the main matrix of  $G$  to each processors and solve the differential equations and gathers  $G$  to calculate the density profile  $\rho$  to update  $\mu$ . For cyclic polymers,  $G(z, z; 0, N)$  is needed to update the density  $\rho(z)$ . The useful data are just the diagonal values of  $G$  at  $t = N$ .

The convergence of  $\mu$  is determined by the master processor. Once the updated  $\mu$  is known, it will be passed to all processors and start a new loop. The complete SCF process is shown as a flowchart in Figure C.5.

A test of the speedup is performed for a cyclic molecule with  $N = 100$ . The  $G(z', z''; t)$  is discretized into a  $256 \times 256 \times 1000$  ( $z' \times z'' \times t$ ) grids and  $512 \times 512 \times 1000$  grids, respectively.

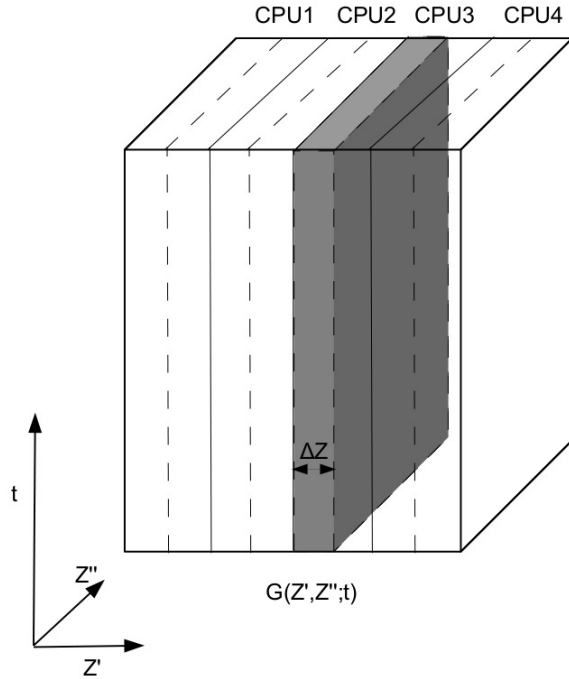


Figure C.3: The schematic illustration of a parallel matrix of function  $G(z', z''; 0, t)$ . The first dimension  $z'$  is split into eight steps and split into four processors. The filled area represents a separate solution of diffusion equation at a specified  $z$

The error of tolerance is  $10^{-5}$  with a Picard algorithm using the Crank-Nicolson method. For other parameters,  $\phi_{\text{ring}} = \phi_{\text{linear}} = 0.5$ ,  $\bar{v} = 1$ . All computations are done on a supercomputer cluster. Each node contains two Intel Xeon 6-core processors working at a clock of 3.06GHZ and connected by infiniband. The wall time for a complete self-consistent iteration is shown in Figure C.6. The parallelization achieves better speeding when using more processors (Figure C.7).

Calculations using CPU number more than 64 have better performance if the grid size is larger. As is shown in Figure C.8, the efficiency  $E_p = \frac{T_p}{p}$  of the 128 CPUs job with

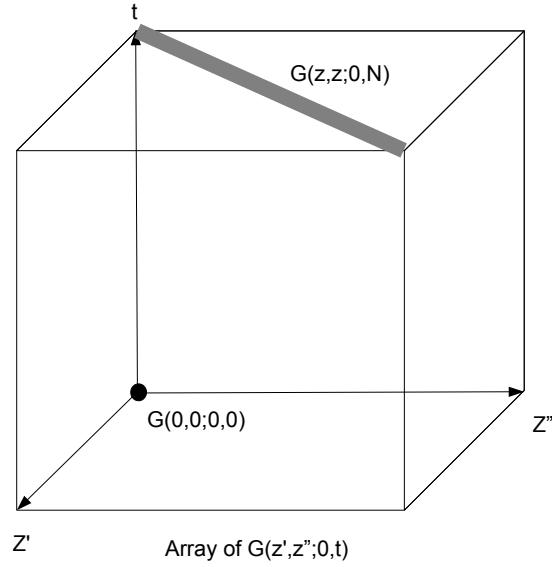


Figure C.4: The values to be gathered in the array of  $G(z', z''; 0, t)$ .

512×512×1000 grids system is approximately 0.6, compared to 0.4 on a 256×256×1000 system. The Karp-Flatt metric analysis [152] estimates the serial fraction  $f$  in the parallel algorithm, which is defined as

$$f = \frac{\frac{1}{E_p} - \frac{1}{p}}{1 - \frac{1}{p}}. \quad (\text{C.2})$$

Figure C.9 indicates that the parallelization has a small serial portion. The serial fraction decreases as the grids increases. For the system of 512×512×1000 grids, the parallelization is more than 99%.

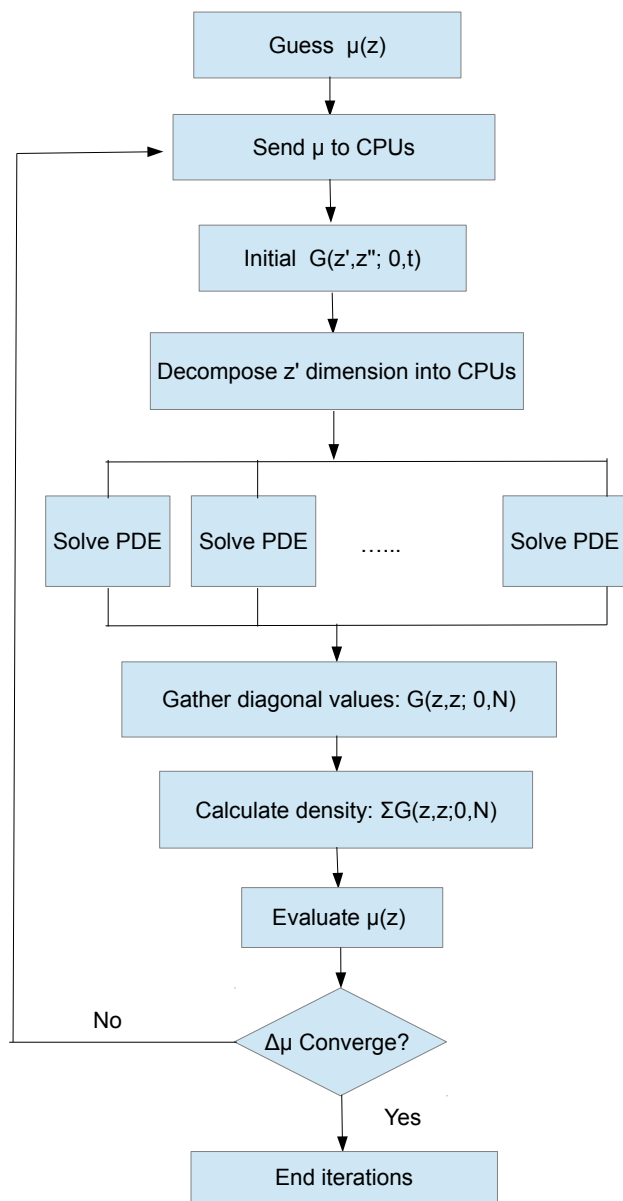


Figure C.5: The flowchart of an SCFT program for cyclic molecules.

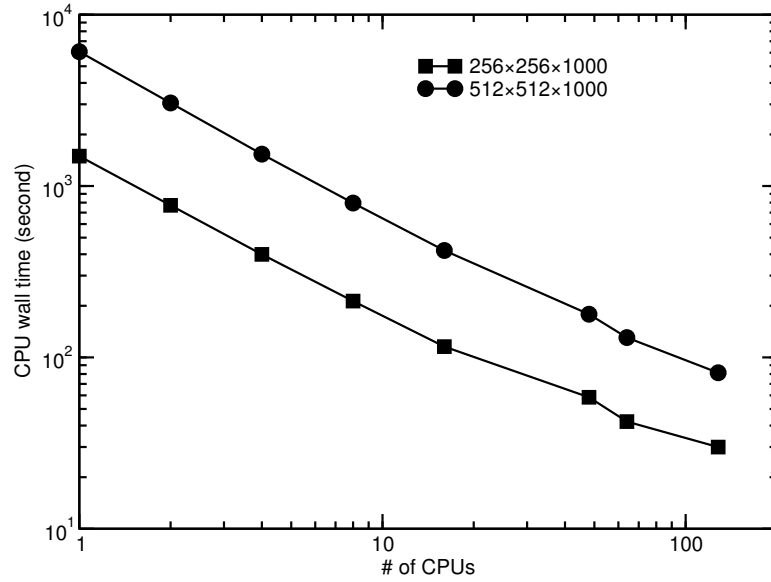


Figure C.6: CPU wall time of SCF calculations in parallel of a cyclic/linear ( $\phi = 0.5$ ) blend.  $N_{\text{ring}} = N_{\text{linear}} = 100$ ,  $\bar{v} = 1$ .

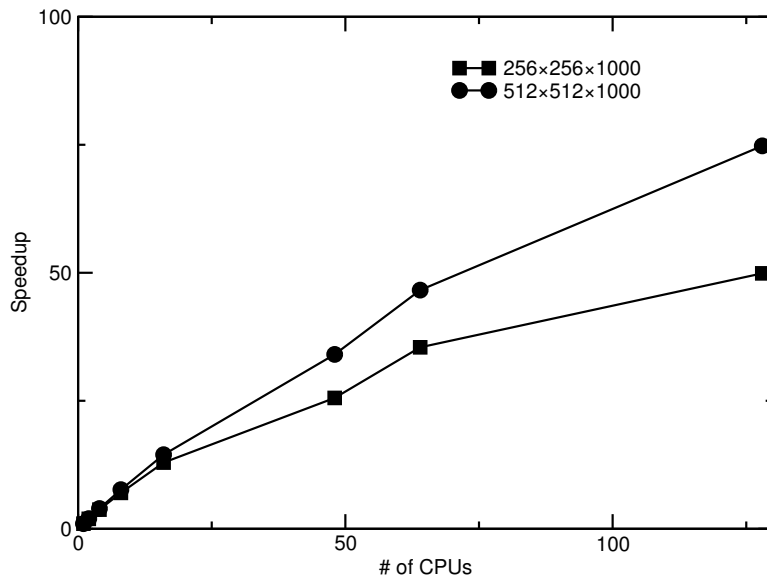


Figure C.7: The speedup of parallel computation of a cyclic/linear ( $\phi = 0.5$ ) blend in the calculations in Figure C.6.

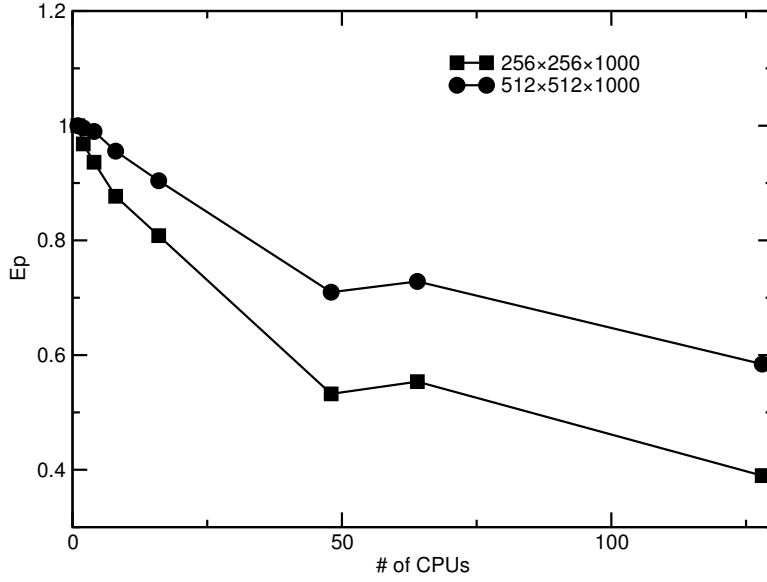


Figure C.8: The efficiency of the parallel computation of a cyclic/linear ( $\phi = 0.5$ ) blend. The dimension of the matrix is the same as Figure C.6.

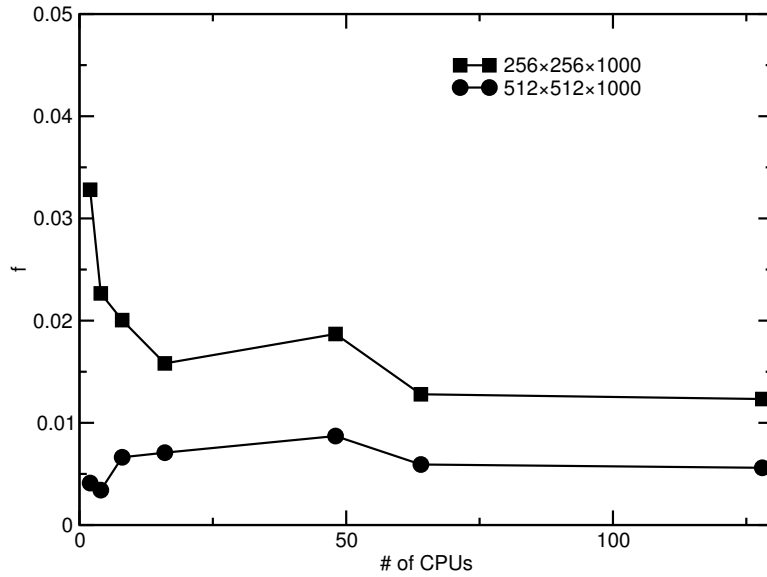


Figure C.9: Sequential fraction  $f$  in parallel computation of a cyclic/linear ( $\phi = 0.5$ ) blend. The dimension of the matrix is the same as Figure C.6.